Linking fluvial dynamics to white sturgeon habitat in the Nechako River, BC

by

Simon Gauthier-Fauteux

BA, Geography, Concordia University, 2013

A THESIS SUBMITTED IN PARTIAL FULFILLMENT
OF THE REQUIREMENTS FOR THE DEGREE OF

Master of Science

in

THE FACULTY OF GRADUATE AND POSTDOCTORAL STUDIES
(Geography)

The University of British Columbia
(Vancouver)

February 2017

Abstract

Considerable effort has been dedicated to restoring sturgeon habitat within dammed rivers. However, sedimentation causes long-term failure because interstitial voids provide critical habitat during early life-stages. Based on the premise that a better understanding of geomorphic processes will improve restoration design, this study characterizes flow and sediment transport dynamics through a white sturgeon spawning reach on the Nechako River, BC.

An extensive dataset was collected throughout the 2015 flood. Bedload transport was sampled on 36 days with flows ranging from 44 m^3/s to 656 m^3/s. During a high flow of 525 m^3/s, channel bathymetry and water surface elevation were surveyed and velocity profiles were collected across 9 transects. Banklines, bars and island topography were later surveyed during low flow.

Sediment transport into the reach was positively related with discharge. This relation was non-linear and transport rates increased rapidly once flows exceeded 400 m^3/s. The relation weakened with downstream distance and sediment transport peaked progressively later throughout the year. No relation was observed at the downstream end of the reach, where transport rates remained low and constant relative to upstream.

Sediment was primarily transported through secondary channels conveying a disproportionate amount of sediment compared to flow. Within the single-thread channel, the locations conveying the greatest amount of sediment remained spatially consistent over time.

Hydrodynamic modelling indicates the Burrard Ave. Bridge causes backwatering once discharge exceed 225-275 m^3/s. Velocity, shear stress and transport capacity at the downstream end of the reach do not increase with discharge because of the backwatering and the expansion in channel width through the island complex. The locations of maximum shear stress and transport capacity shift upstream with increasing discharge, but shear stress does not exceed 23 N/m^2 for flows up to 775 m^3/s.

The fluvial dynamics within the spawning reach create challenges and opportunities for habitat restoration. Backwatering is problematic because it causes mid-reach deposition during high flows and limits shear stress magnitude over the downstream spawning substrate. Meanwhile, the presence of sediment transport pathways through secondary channels and within the mainstem can be used to site restoration projects in areas apt to maintain suitable habitat.

Preface

This thesis is a continuation of geomorphic research conducted within the framework of the Nechako White Sturgeon Recovery Initiative. Portions of fieldwork and analysis were done in collaboration with Northwest Hydraulic Consultants Ltd. (NHC) and have been published elsewhere (*2015 Sediment Transport Investigation on the Vanderhoof Reach of the Nechako River*, available at www.nechakowhitesturgeon.org). All thesis work was completed under the guidance of a supervisory committee that included supervisor Dr. Brett Eaton (University of British Columbia), Dr. Andre Zimmermann (Northwest Hydraulic Consultants) and Dr. Steve McAdam (BC Ministry of Environment).

Table of Contents

List of Tables

List of Figures

Acknowledgments

I would like to thank my supervisor, Dr. Brett Eaton, for creating an excellent learning environment for me to develop as a geomorphologist. Dr. Eaton is an excellent teacher who supports his students' development through the stimulation of curiosity and critical thought. I am also very grateful to have had Dr. Andre Zimmermann and Dr. Steve McAdam on my committee. Both of these committee members provided me with incredible insight, attention and support along the way. It is no surprise that I have forged great relationships, both personal and professional, with all three of these people.

I would also like to thank all the members of the Nechako White Sturgeon Recovery Initiative. This team is accomplishing incredible work and I feel very lucky to be a part of the effort. The Nechako White Sturgeon Conservation Center was very welcoming and provided assistance, personnel and equipment, which made the project possible.

I am also grateful to have had the opportunity to collaborate with Northwest Hydraulic Consultants throughout the project. NHC provided me with the necessary resources to accomplish this research and allowed me to gain valuable professional experience.

My work would not have been possible without the help of the Carrier-Sekani Tribal Council. Their generosity and effort is something I have rarely come across. I could never have expected to make such good friends along the way.

The district of Vanderhoof, BC, was a great place to work. I thank Wayne Salewski and the community for their help and interest. I also thank Dr. Michael Church for his generosity.

Finally, I gratefully acknowledge the financial support from the Natural Sciences and Engineering Research Council of Canada, the Province of British Columbia through the Ministry of Environment and the Government of Canada through the department of Fisheries and Oceans.

Chapter 1

Introduction

1.1 Context

At present, the Nechako, Columbia and Kootenay River populations of white sturgeon (*Acipenser transmontanus*) are experiencing recruitment failure primarily caused by the effects of flow regulation (DFO, 2014). Geomorphic effects, including changes in substrate composition, occur in response to flow regulation as the fluvial system adjusts to the imposed flow and sediment regimes (Church, 1995; Grant et al., 2003). White sturgeon are susceptible to these changes because of their reproductive life-history traits (Winemiller, 2005; Lytle and Poff, 2004) and because substrate characteristics determine survival during early life-stages (McAdam, 2011; McAdam et al., 2005).

In response to declining sturgeon populations, considerable effort has been dedicated to rehabilitate habitat within degraded river systems (NWSRI, 2012; KTOI, 2009; Crossman and Hildebrand, 2014). However, the functionality of restored habitat has often been short-lived because altered fluvial dynamics continue to produce geomorphic change that is non-conducive to sturgeon survival (Crossman and Hildebrand, 2014; Johnson et al., 2006; NHC, 2012). This study uses a biogeomorphic approach to understand how sturgeon habitat is affected by sediment transport through a critical spawning reach of the Nechako River near Vanderhoof, BC. The premise of this research is that a better understanding of geomorphic processes within the spawning reach will increase the effectiveness of habitat restoration by allowing projects to be designed in accordance with the changing fluvial system.

1.2 White sturgeon spawning and habitat

White sturgeon are a slow growing, long-lived species of fish found within the Fraser, Columbia and Sacramento River systems of western North America (Hildebrand et al., 2016). In Canada, they inhabit the Fraser, Nechako, Columbia and Kootenay Rivers. Females may require 15-30 years to reach sexual maturity, but once mature, they can spawn multiple times throughout their lives at intervals of 3 years or more (Hildebrand et al., 2016). This species has a *periodic*

life-history strategy, where high fecundity spawners reproduce periodically over time in a form of intergenerational bet-hedging (Winemiller, 2005). This life-history trait is suited to large-scale environmental variations because recruitment can be achieved through episodic reproductive success despite long periods with unfavorable conditions (Winemiller, 2005; Coutant, 2010).

Although the environmental/physiological cues that trigger spawning are poorly understood, water temperature has been described as a relatively good predictor of spawn timing (Hildebrand et al., 2016). In the snowmelt-dominated fluvial systems of western Canada, water temperature typically rises to produce favorable spawning conditions in late spring or early summer. This timing generally corresponds to the spring freshet, creating a strong temporal association between the period of peak flow and sturgeon spawning activity. Spawning typically occurs in relatively deep, moderate to high velocity flow and has been documented along meander bends (Paragamian et al., 2009), within side-channels (Perrin et al., 2003), at tributary confluences (Hildebrand et al., 1999) and below dam tailraces (Parsley and Beckman, 1994). Sturgeon spawn by broadcasting negatively buoyant eggs into the water column that adhere to the substrate surface until hatch (Hatfield et al., 2013). Once the eggs hatch, yolksac larvae immediately seek refuge within the interstitial pore spaces, where they must remain hidden for approximately 12-15 days until the onset of exogenous feeding to increase survival (McAdam, 2011). After this period, larvae emerge from the substrate and drift towards lower velocity rearing habitat (Hatfield et al., 2013).

Larvae cannot access interstitial refuge habitat if the gravel substrate has been infilled or covered by sand. Sedimentation and lack of interstitial habitat results in pre-mature drift, higher larval mortality and higher predation (Kock et al., 2006; McAdam, 2011). The infilling of larval habitat has been identified as a cause of population decline within the Nechako (McAdam et al., 2005), Columbia (McAdam, 2015) and Kootenay Rivers (Paragamian, 2012). Substrate conducive to larval survival therefore consists of medium to coarse gravel (Bennett et al., 2007) with no more than a minimal proportion of fine sediment within the upper layer.

1.3 Bedload sediment transport in relation to sturgeon habitat

Sediment transport determines the quality and availability of substrate habitat through its influence on bed surface composition (Hassan and Church, 2000), grain stability (Hassan et al., 2007) and intergravel flow (Greig et al., 2005; Zimmermann and Lapointe, 2005; Lisle, 1989). The interaction between local hydrodynamics, substrate characteristics and sediment mobility can produce geomorphic adjustment within spawning reaches (Eaton and Lapointe, 2001; Lapointe et al., 2000) that cause egg/larvae burial and suffocation (Kock et al., 2006). Although fluvial dynamics driving sediment transport are inherently variable (Ashmore, 1991) and influenced by external factors including sediment supply (Buffington and Montgomery, 1999), hydrograph shape (Hassan et al., 2006) and the superimposition of sedimentological features (Hoey, 1992; Nicholas et al., 1995), certain regularities and characteristics can be used to identify how suitable habitat is naturally maintained within a spawning reach.

Channel morphology directly influences habitat availability by generating flow dynamics capable of spatially sorting, or segregating, sediment based on size. Suitable habitat found along the outer bank of large meander bends (McDonald et al., 2010) can result from lateral sediment sorting if inward acting, near-bed secondary flow circulation is sufficient to move fine grained sediment upwards along the point-bar slope (Dietrich and Smith, 1984; Dietrich and Whiting, 1989; Powell, 1998). Areas of flow convergence can also provide coarse substrate habitat as water super-elevation generates helicoidal vortices acting to excavate and maintain scour holes (Ashmore and Parker, 1983; Rhoads and Kenworthy, 1995). The junction angle and discharge ratio of confluent channels also influences how bedload is transported through, or around, such scour holes (Best, 1988; Roy and Bergeron, 1990).

Habitat characteristics also vary depending on cross-channel location because a relatively small proportion of the total channel width can convey most of the bedload sediment (Gomez, 1991; Habersack et al., 2008; Ashmore et al., 2011). The channel width conveying bedload sediment and undergoing short-term morphological change is known as the *active width* (Ashmore et al., 2011). Even for a nearly straight, single-thread reach, slight asymmetry in the channel bed can cause cross-sectional variation in transport rates and bedload transport may be highest along topographic lows (Habersack et al., 2008).

Although the active width of a channel can increase with stream power, it commonly remains only a fraction of the total channel width (Ashmore et al., 2011). Significant areas of grain immobility remain due to the development of high intensity transport zones (Lisle et al., 2000) and due to the feedback between partially mobile coarse fractions and bed structuring (Church and Hassan, 2002). Sediment immobility can be beneficial or problematic for larval sturgeon depending on the pre-existing substrate characteristics and the composition of the bedload sediment. Poor correlation between bed shear stress and particle size during bankfull flow (Lisle et al., 2000) can be beneficial because coarse, stable substrate located in areas with low shear stress can provide refuge habitat for larvae during the high flow spawning period.

The surficial composition of substrate in regulated rivers is often not conducive to larval survival because bed texture adjusts to changing sediment input, stream power and hydrograph shape (Church, 1995; Hassan et al., 2006; McDonald et al., 2010). Decreased stream competence under a regulated flow regime can result in a bed surface composed of coarse, immobile particles (Church, 1995) that progressively infills with fine sediment depending on sediment supply, flow conditions and substrate to bedload grain size ratio (Gibson et al., 2009). Medium to coarse sand is especially apt to infill a static surface layer because it is large enough to resist suspension and fine enough to bridge inter-gravel spaces; creating a sand seal within the upper framework (Beschta and Jackson, 1979; Lisle, 1989). Once a sand seal has been formed, increasing flow and deceasing sediment supply does not entrain infilled fines to a significant depth (Beschta and Jackson, 1979). Therefore, periodic mobility of coarse grains during high flow is a key mechanism in flushing stream gravels and providing suitable larval habitat.

Sediment transport dynamics influence the availability and quality of sturgeon habitat

within the four major Canadian rivers they inhabit. In the Kootenay River, critical spawning habitat has been identified along meander bends (Paragamian et al., 2009) where pre-regulation flows could maintain suitable larval habitat by sorting sediment and scouring the bed (McDonald et al., 2010). Within the Columbia River, sturgeon spawn immediately downstream of a tributary confluence (Golder, 2006) which has complex hydrodynamic circulation (Fissel and Jiang, 2008). The relative discharge between confluent channels affects eddy circulation and influences the path of sediment transport, where pre-regulation flows may have effectively routed bedload around the spawning substrate rather than overtop of it (McAdam, 2015). In the lower Fraser River, spawning occurs (not exclusively) within side-channels (Perrin et al., 2003). This type of spawning habitat is interesting because bedload can be conveyed through braided reaches by a subset of anabranches (Bertoldi et al., 2010; Ashmore et al., 2011), suggesting that some spawning sites may not be exposed to active bedload transport during the spawning period. Finally, in the Nechako River, sturgeon spawn downstream of an anabranching reach where bedload sediment transport affects the availability of interstitial habitat and limits the effectiveness of restorative measures (McAdam et al., 2005; NHC, 2012). Overall, the presence and maintenance of high quality spawning habitat within each of these rivers is determined by the dynamics linking flow and sediment conveyance through the spawning area.

1.4 Restoring white sturgeon habitat

Sturgeon habitat restoration typically attempts to re-create or remediate natural spawning habitat in regulated river systems (Dumont et al., 2011; Gendron et al., 2002; LaHaye et al., 1992). The most commonly employed technique is to increase the availability of interstitial voids for egg and larval incubation by adding coarse sediment overtop the non-functional habitat (NWSRI, 2012; Crossman and Hildebrand, 2014; Dumont et al., 2011; Gendron et al., 2002; LaHaye et al., 1992; Trencia and Collin, 2006). Considering both white sturgeon and lake sturgeon habitat rehabilitation projects, the grain size of placed substrate has varied widely (0.02-1.5 m) and spawning area design has included the construction of mid-channel shoals, outer bank ridges, riffles, boulder cells and circular pads (Kerr et al., 2011).

White sturgeon habitat restoration has been conducted on the Columbia, Kootenay and Nechako Rivers, where sedimentation of the native substrate had occurred in response to flow regulation (DFO, 2014). In the Columbia river, a 1,000 m^2 area of substrate was added within the thalweg at a known spawning location to increase complexity and availability of interstitial habitat (Crossman and Hildebrand, 2014). The restored habitat, consisting of 90% large cobbles and boulders to resist displacement and 10% coarse to very coarse gravel, proved successful in providing refuge habitat for larval fish. Restoration on the Nechako system has consisted of adding 2,100 m^2 of spawning substrate in two locations within a critical spawning reach (NWSRI, 2012), the details of which are presented in Section 2.3. Recent efforts on the Kootenay system have adopted an ecosystem-based approach intended to restore fluvial dynamics and the ecological functionality of three interconnected reaches (KTOI, 2009). Restorative measures

included bank-stabilization through grading and reestablishment of riparian vegetation, increasing floodplain and side-channel connectivity and the installation of instream structures to create scour pools, route bedload sediment and generate hydraulic complexity (KTOI, 2009).

Restoration projects have often resulted in initial spawning success followed by long-term failure attributed to progressive sedimentation (NHC, 2012; Kerr et al., 2011; Johnson et al., 2006; Gendron et al., 2002). To prolong the functionality of restored habitat, instream works must be designed in accordance with the fluvial and sedimentological dynamics of the spawning reach while remaining within the habitat requirements of the species. Pre-project hypothesis testing (Wheaton et al., 2004a; Wheaton et al., 2004b) and post-project monitoring are key in understanding spawning site selection and in determining the sustainability of instream works. While mechanical or hydraulic remediation can be used to maintain the quality of restored habitat, designs that require minimal maintenance, for example periodic substrate augmentation, are clearly more desirable.

1.5 Numerical modelling and its role in sturgeon habitat restoration

Flow and sediment transport models are extensively applied to understand fluvial processes, link fluvial processes with stream ecology and evaluate channel restoration designs (e.g. Pasternack et al., 2004; Biron et al., 2012; McDonald et al., 2010). While numerous hydrodynamic models are currently available, selecting an appropriate one depends on the purpose of modelling, the spatial scale of analysis and the resolution of input and output data (Brown and Pasternack, 2009; Gard, 2009; Lane et al., 1999; Shen and Diplas, 2008).

Depth-averaged, 2-dimensional (2D) models can be an effective means to simulate meso-scale hydrodynamics and evaluate restoration design based on sediment entrainment, flow complexity and habitat suitability (Crowder and Diplas, 2000; Shen and Diplas, 2008; Pasternack et al., 2006; Wheaton et al., 2004b). However, 2D model performance can be negatively affected by Digital Elevation Model (DEM) interpolation, mesh refinement and the presence of submerged instream obstacles (Crowder and Diplas, 2000; Pasternack et al., 2004; Shen and Diplas, 2008). Surveyed point density and DEM inaccuracy have been found to be primary factors causing error in predicted depth, velocity and shear velocity; however model output may still be within the range of measurement error in the field (Pasternack et al., 2006). Achieving representative hydrodynamics is critical in testing restoration design because error in simulated depth and velocity propagates directly into habitat suitability metrics (Boavida et al., 2013).

Given that local velocity refugia provided by submerged instream structures are often integral to habitat restoration design, fully 3-dimensional simulations may be more appropriate despite their greater cost, computational demand and required data collection. These models have been successful in reproducing complex hydrodynamics around instream structures and represent a more accurate treatment of bed shear stress (Lane et al., 1999; Shen and Diplas, 2008; Biron et al., 2012). However, the predictive ability of complex 3D models remains lim-

ited by methodological issues arising from sensitivity to initial hydraulic conditions, channel curvature and bed topography (Wheaton et al., 2004a; Lane et al., 1999). Acknowledging that predictive accuracy is fundamentally limited by the complexity of a fluvial system, the better process representation achieved by 3D models can increase their utility in hydraulically complex areas, especially if restoration designs are being compared relative to each other (Lane et al., 1999; Shen and Diplas, 2008; Wheaton et al., 2004a).

Hydrodynamic modelling has been used on the Nechako, Columbia and Kootenay systems within the context of sturgeon habitat use and restoration. On the Nechako River, a 2D model (RIVER2D) of the 6-km spawning reach predicted secondary channel flow conveyance and cross-sectional velocity fairly well, with discrepancies attributed to the resolution of topographic input data and possible effects of submerged vegetation (NHC, 2008). Simulations revealed that as discharge increases, a greater proportion of the flow becomes conveyed through secondary channels and that the two highest velocity areas within the reach potentially correspond to historical sturgeon spawning sites.

In the Kootenay River, a 2D flow and sediment transport model (FaSTMECH) was used to determine hydraulic cues for spawning site selection, assess how flow regulation may affect these cues and to determine the effects of pre- and post-dam flow conditions on substrate condition within the 18-km spawning reach downstream of the Libby dam (McDonald et al., 2010). Results from the modelling suggest a strong spatial correlation between spawning location and area of maximum cross-sectional depth and velocity and revealed that pre-regulation flows could have maintained suitable substrate habitat at these locations through strong sediment sorting and vertical scour. Modelling was also used in the Kootenay system to evaluate a proposed channel restoration design intended to convey high flows, transport available sediment, reduce bank erosion, improve flood plain connectivity and provide greater depth and velocity for spawning fish (Logan et al., 2011). Simulations proved useful in identifying several design flaws, including the inability to mobilize sediment within the channel and the failure to achieve flood plain connectivity.

On the Columbia system, three-dimensional modelling (COCIRM) was used to simulate complex hydrodynamics at a tributary confluence used by spawning sturgeon (Golder, 2006; Fissel and Jiang, 2008). The model domain incorporated a dam spillway into the upstream boundary and was able to simulate standing waves reasonably well within the supercritical outflow region (Fissel and Jiang, 2008). Modelling revealed the presence of a highly dynamic circulation pattern at the channel confluence, where the presence of up to three gyres circulating in opposite directions dominate the eddy depending on the discharge ratio between channels (Golder, 2006; Fissel and Jiang, 2008). The effects of flow regulation on the local hydrodynamics are likely to have caused geomorphic change within the spawning area which contributed to recruitment failure (McAdam, 2015).

1.6 Study rationale

The research presented herein was conducted within the framework of the Nechako White Sturgeon Recovery Initiative as a continuation of geomorphic investigations (NHC, 2014; NHC, 2015). The goal of this study was to advance our understanding of fluvial dynamics within the critical spawning reach, based on the premise that an increased understanding of geomorphic processes will improve future habitat restoration design. Specifically, this study sought to characterize the spatial and temporal pattern of sediment transport through the reach and to identify the drivers of geomorphic change affecting sturgeon habitat. To accomplish this, an intensive sampling program was conducted throughout the 2015 flood hydrograph and the dataset was analyzed in conjunction with 2D hydrodynamic modelling to supplement the interpretation of results.

Chapter 2

Study Site

2.1 Description

The Nechako River at Vanderhoof, BC has been identified as a critical spawning reach for Nechako white sturgeon. The river at this location has an anabranching morphology (*type-3* channel using classification from Nanson and Knighton (1996)) that flows through a complex of stable, densely vegetated islands (Figure 2.1). Prior to the onset of flow regulation in the early 1950's, the low-lying islands and bars were largely devoid of vegetation suggesting the periodic mobility of sediment at high flow.

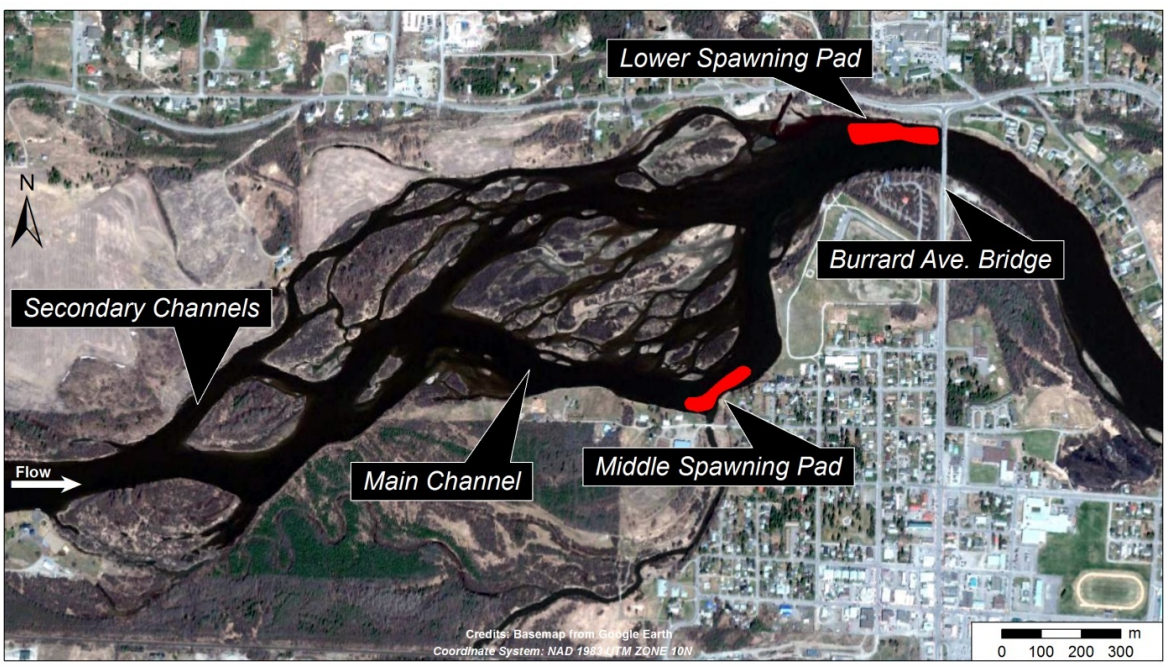

Figure 2.1: White sturgeon spawning reach on the Nechako River near Vanderhoof, BC.

The location of the spawning reach corresponds to a transition where the river is gravel-

bedded upstream and sand-bedded downstream (NHC, 2006). This section of river is a depositional zone situated on a gradient break with an upstream channel slope of 0.06% and downstream slope of 0.03% (NHC, 2013). Within the study area, substrate generally fines with downstream distance starting from a pebble, gravel and imbricated cobble bed at the upstream extent to a bed composed largely of sand, granules and infilled gravel at the downstream extent (NHC, 2012; NHC, 2014).

Regarding the glacial legacy of the region, the Nechako River occupies a large meltwater channel valley produced during the Pleistocene glaciation (Rood, 1999). During deglaciation, remnant ice impounded large glacial lakes in the area that deposited a thick surficial layer of fine glaciolacustrine sediment (Plouffe and Levson, 2001). The river has since incised into this deposit, resulting in terrace scarps that rise 30 m above the current floodplain elevation along the outside of meander bends (NHC, 2006). The two major sediment sources upstream of the study site are actively eroding terrace scarps and incising tributaries and the dominant size-class of the sediment input is sand or finer (Rood, 1999).

Overall, the Nechako River is relatively gravel-poor. Historically, this was because of the large proportion of fine sediment within the glaciolacustrine deposit, the lake headed nature of the fluvial system and the presence of gradient breaks which act as depositional zones along the mainstem and tributary channels (Rood, 1999; NHC, 2006). Since flow regulation, however, the amount of gravel input to the channel has further decreased due to vegetation encroachment and bank stabilization (Rood and Neill, 1987; NHC and McAdam, 2003a).

2.2 Hydrology

Flow regulation on the Nechako River began in 1952 with the construction of the Kenney Dam and flow diversion tunnel to the Kemano Generating Station near Kitimat, BC. Historically, the natural hydrograph of the Nechako River was driven by spring snowmelt on the leeward side of the Coast Range and the Interior Plateau (NHC and McAdam, 2003a). Peak annual flow typically occurred in June, with the receding limb of the annual hydrograph periodically re-supplied by large frontal rainstorms during the latter portion of summer and into fall (NHC and McAdam, 2003a). Spring flows exceeding 1000 m^3/s at Vanderhoof were not uncommon and the estimated mean annual peak daily discharge was 658 m^3/s (NHC and McAdam, 2003a).

The Nechako Reservoir was filled from 1952 to 1956, reducing the mean annual peak daily discharge to only 233 m^3/s (Figure 2.2). Since then, two water management strategies have been implemented; the first from 1957 to 1979 and the second from 1980 to present. The mean annual peak daily discharge during these periods has been 426 m^3/s and 360 m^3/s, respectively, which represents an approximate 45% reduction from historic flows. The timing of peak flow has also been changed from June to August because the current management plan was developed to control stream temperature during the sockeye salmon migration. The 2015 peak daily flow of 677 m^3/s was the 3rd highest discharge since the onset of flow regulation in 1952.

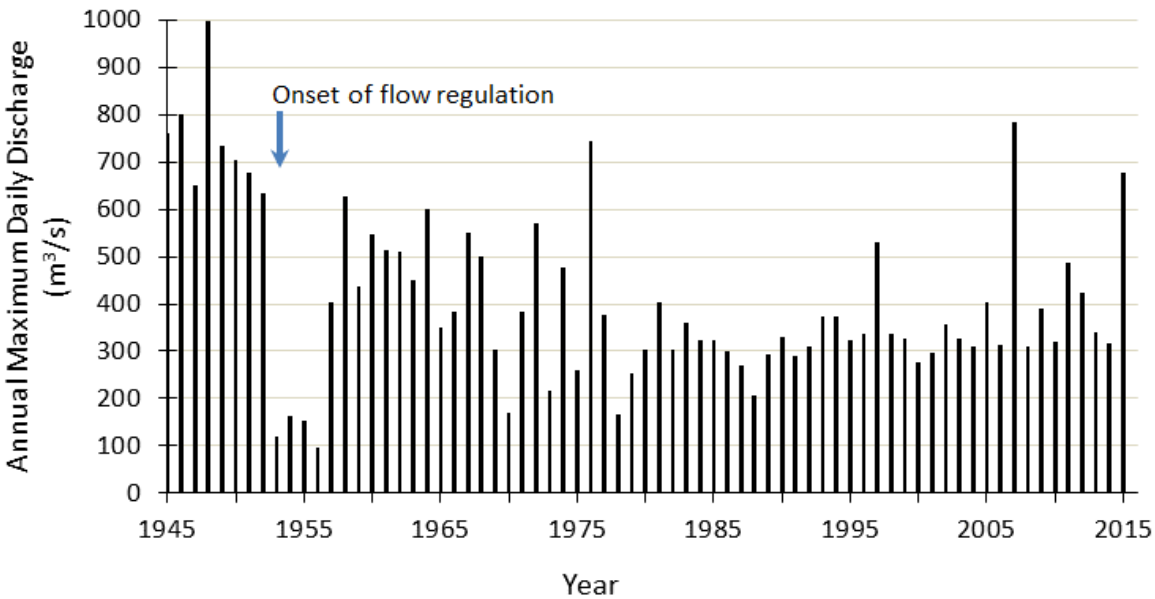

Figure 2.2: Pre- and post-regulation annual maximum daily discharge.

2.3 History

In May 2011, as part of the Nechako White Sturgeon Recovery Initiative (NWSRI), coarse substrate was placed at two locations within the spawning reach to increase the availability of suitable larval incubation habitat (labelled *Middle Spawning Pad* and *Lower Spawning Pad* on Figure 2.1) (NWSRI, 2012). The two spawning pads are approximately 20 cm thick, with 20-30% of the placed material sized between 20-40 mm and 30-50% between 150-200 mm (NHC, 2012). The cobble-gravel interstices of the downstream spawning pad, located downstream of the island complex, began to infill with coarse sand and fine gravel shortly after placement (NHC, 2012). Subsequent monitoring has confirmed that the downstream spawning pad continues to infill due to the immobility of coarse grains and because bedload is consistently transported over the pad (NHC, 2016). The upstream spawning pad has remained largely free of fine sediment deposition and infilling has only occurred in local areas near a tributary confluence and along pad margins (NHC, 2012; NHC, 2016).

A series of geomorphic assessments (Rood, 1998; Rood, 1999; NHC and McAdam, 2003a; NHC and McAdam, 2003b) and sediment transport studies (NHC, 2014; NHC, 2015; NHC, 2016) have been completed to gain insight into reach-scale sediment dynamics. Biological monitoring programs focused on spawning behavior and population dynamics have been ongoing for over a decade and have included juvenile indexing, spawn monitoring, and telemetry (reports available at www.nechakowhitesturgeon.org). Additional work completed in recent years has included investigating the use of low-relief bedforms and mechanical remediation to maintain/restore the quality of substrate habitat. This study represents a continuation of geomorphic research intended to increase the knowledge-base supporting future habitat restoration design.

Chapter 3

Methods

3.1 Bathymetry, topography and water surface elevation

A Trimble Real-Time Kinematic (RTK) GPS was used to survey bathymetry, water surface elevation, banklines and bar topography within the study reach. A static observation from Geodetic Control Monument (GCM) 653659, located approximately 8 km southeast of Vanderhoof, and Post-Processing Kinematic (PPK) procedures were used to position the GPS base-station near the study site. To provide a measure of quality assurance between days, five pre-and post-survey points were routinely logged on fixed markers located 300-500 m from the base-station.

Channel bathymetry was surveyed from May 12-15th, 2015, during a relatively high discharge of approximately 525 m^3/s. Surveying at high flow allowed access to a large wetted extent within secondary channels. To conduct the survey, the RTK GPS was mounted on top of a survey-grade SonarMite echo sounder and configured to take point measurements at equal frequency intervals. This configuration resulted in simultaneous measurement of bed and water surface elevation.

Bathymetric data were collected systematically from upstream to downstream with a typical transect spacing of approximately 30 m (Figure 3.1). The maximum transect spacing was 80 m and occurred downstream of the Burrard Ave. Bridge. Two longitudinal profiles of bed and water surface elevation were also measured on May 14th, one collected along the southern mainstem channel and the other collected along the northern-most secondary channel.

Top-of-bank and bottom-of-bank banklines, as well as bar surfaces and island topography were surveyed during low-flow (64-118 m^3/s) from August 25th to September 6th, 2015. Surveying was done with an irregular point spacing as determined by breaks in the natural topography. Island topography was surveyed somewhat opportunistically due to the high level of radio and satellite signal interference caused by the tree canopy. Consequently, surveyed point density on some vegetated islands remains relatively sparse.

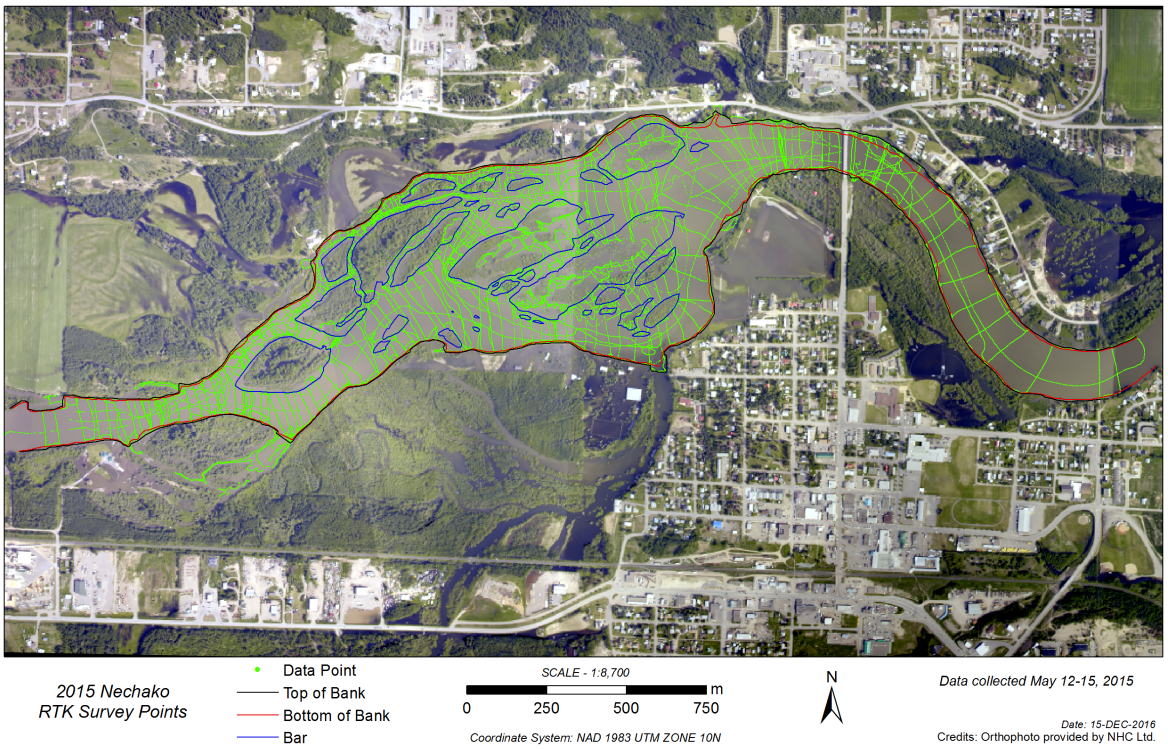

Figure 3.1: Surveyed bathymetry, bar contours and bankline topography.

The base-station coordinates initially obtained from the GCM 653659 baseline were verified against Precise Point Positioning (PPP) reports generated for the four longest duration base-station observations (CSRS-PPP service offered by the Geodetic Survey Division of Natural Resources Canada) (Appendix A). This comparison showed that post-processing of the survey data was warranted and as a result, the base-station coordinates were shifted 0.359 m south and 0.786 m east to match the Northing and Easting obtained from the PPP results averaged over 33 hours of data logging. The PPP results were considered more accurate than the GCM baseline location because GCM 653659 had not been recently maintained. The GCM baseline and PPP results were in good agreement regarding the elevation of the base-station, but for consistency, it too was corrected to match the PPP results by decreasing it 0.007 m. For further detail about the survey methodology, see Appendix A.

3.2 Flow velocity and discharge

A Teledyne RDI RiverRay Acoustic Doppler Current Profiler (ADCP) was used to collect velocity profiles and discharge estimates across nine transects distributed throughout the reach (Figure 3.2). Velocity measurements were taken from May 12-15th, 2015, at a discharge of approximately 525 m^3/s. To collect the data, an RTK GPS receiver was mounted to the ADCP raft and set to transmit real-time position to the ADCP software via Bluetooth. This makes it

possible to detect whether moving bed conditions are present by comparing the GPS location to the ADCP location referenced to the Bottom Track (BT). The ADCP raft was tethered to the side of a motorized boat operating at a slow and constant speed. Average boat speed during data collection was 0.40 m/s (SD = 0.17 m/s). Each transect was repeated a minimum of four times. If the estimated discharge from consecutive transect passes differed by over 5%, the pass would be flagged as an outlier, discarded and repeated. Only 3 out of 41 passes were flagged as outliers. The percent difference between consecutive discharge estimates averaged 1.6% (SD = 1.2%), with a maximum error of 4.2%. Four compass calibrations were performed and error values ranged between 0.6° and 1.8°.

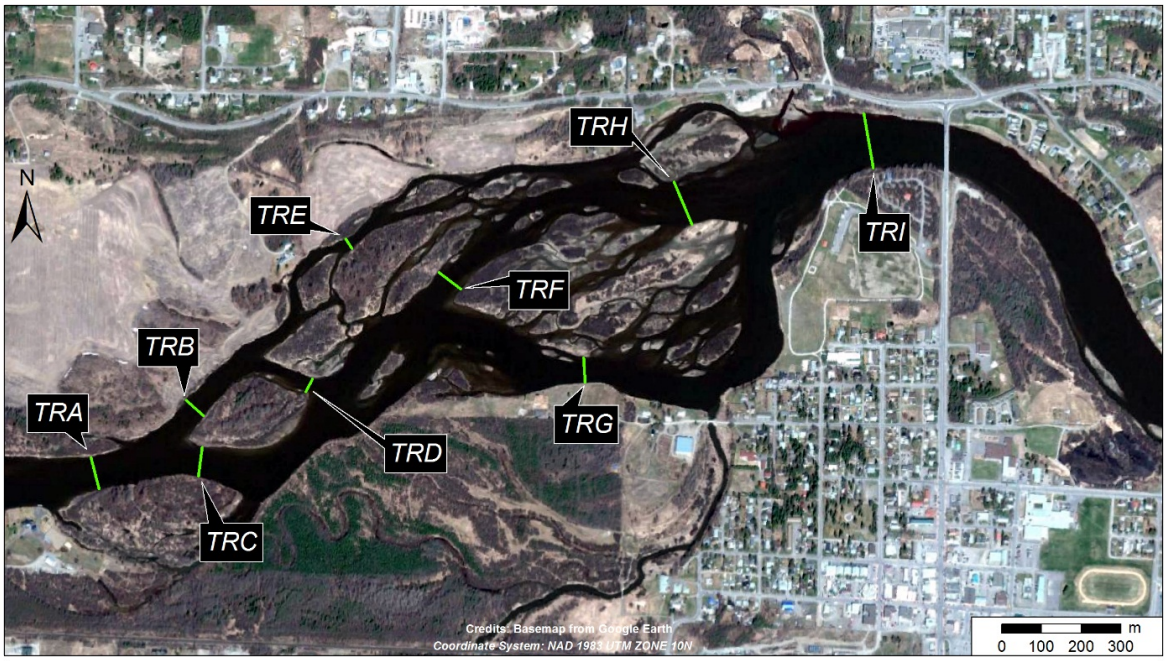

Figure 3.2: ADCP velocity transects.

The ADCP data were post-processed using the Teledyne RDI WinRiver II software. Magnetic variation was set at 17.3° for all transects. This value was determined by aligning the GPS ship track with the ADCP BT referenced track along transects that were highly unlikely to have moving bed conditions. Discharge and velocity were referenced to the ADCP BT for all transects except TRA and TRB, which had sufficient bed mobility to offset the two ship tracks (Figure 3.3). For these two transects, discharge and velocity was referenced to the National Marine Electronics Association (NMEA) GGA sentence from the GPS receiver. All transects were then cropped to exclude poor quality data nearest the banks. The post-processed data for each of the nine transects was exported, depth-averaged and binned into 5-m cross-channel distance intervals. Further information about the post-processing is presented in Appendix B.

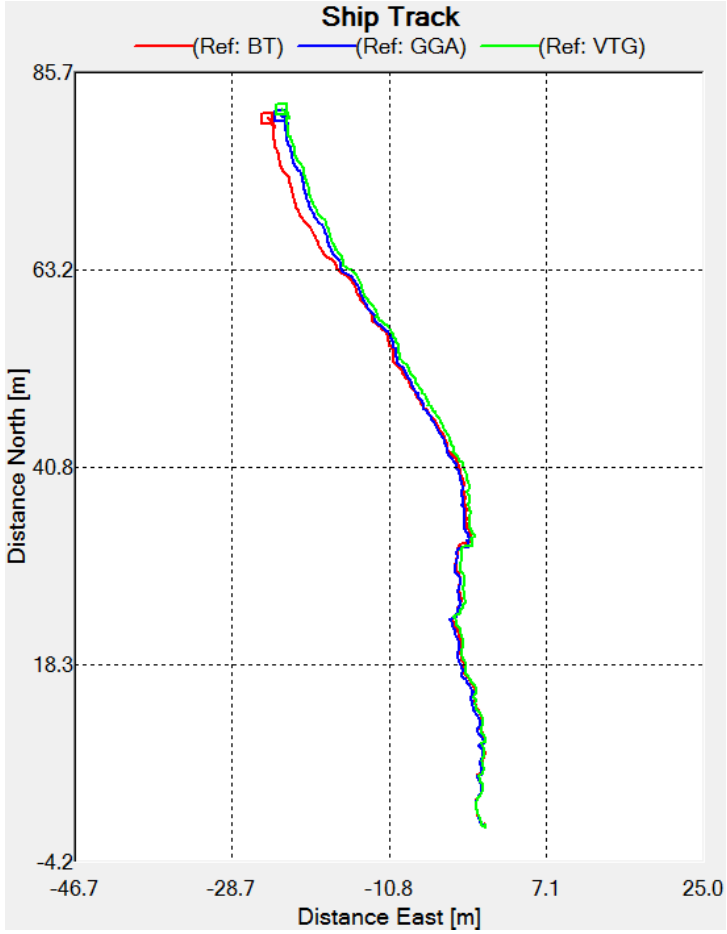

Figure 3.3: Moving bed at TRA causing offset between GPS sentences (green and blue lines) and Bottom Track positioning (red line).

3.3 Bedload sediment transport

Bedload transport rates were sampled at 10-m intervals across a total of 12 transects (Figure 3.4). Two of the sampling transects, US and LP, were previously established from ongoing sampling programs (NHC, 2015; NHC, 2016). Sampling began two days after ice-off on March 22nd and ended once flows receded below 45 m^3/s on October 17th, 2015. A total of 36 days were sampled throughout the annual hydrograph and samples were collected during flows ranging from 44 m^3/s to 656 m^3/s (Figure 3.5). On average, sampling was conducted once every 38 m^3/s change in discharge. No samples could be collected from June 3rd to June 28th because the access to the river was restricted by the municipality due to flooding risk.

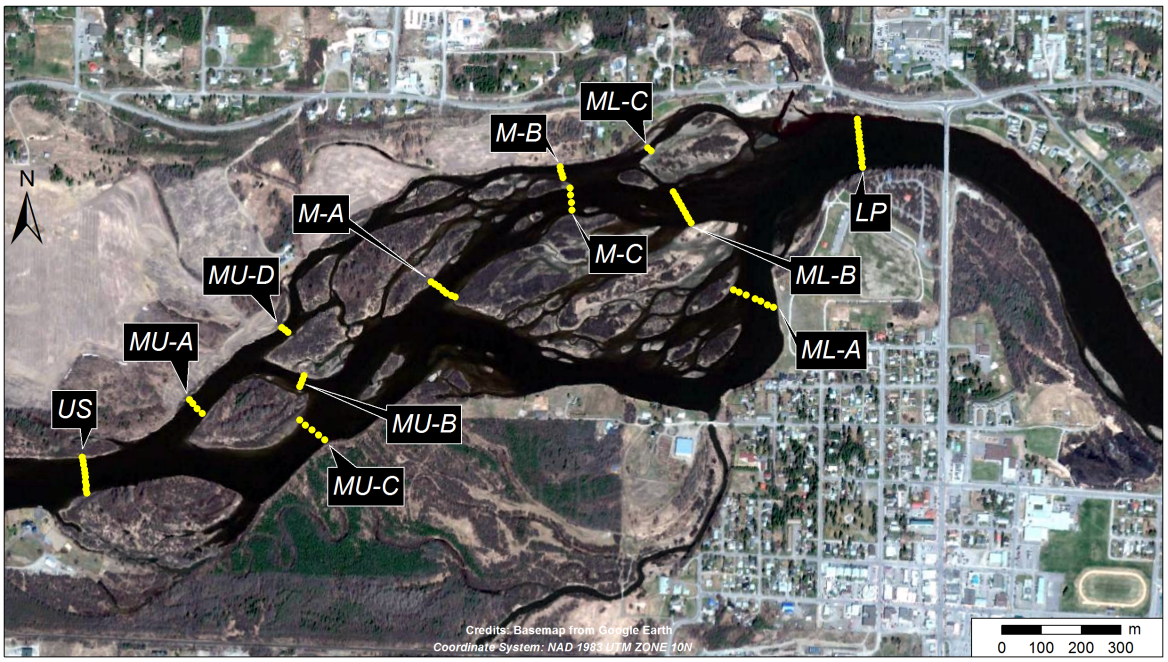

Figure 3.4: Bedload sampling locations in 2015.

Samples were collected using a Helley-Smith bedload sampler with a 76.2 mm wide opening and 0.125 mm mesh bag. A larger Elwha River Sampler with a 203.2 mm wide opening was used during the period of peak flow when discharge exceeded 600 m^3/s to reduce under-sampling of coarse bedload grains (Vericat et al., 2006). Each sample was collected over a duration of 300 s, unless high transport rates caused overfilling of the sampler. In this case, two 150-second samples were collected. Additional details about the sampling protocol are provided in Appendix C.

All bedload samples were dried and individually weighed. This allowed for a unit transport rate, or transport rate per meter width, to be calculated at each location by dividing the mass of each sample by the sampling duration and the width of the opening on the sampler. Measured transport rates were then used to estimate the total transport rate for each 10-m segment of cross-channel distance as well as the total transport rate for each sampling transect.

Samples collected on 13 dates were additionally sieved using phi sieves. Sieving was done to obtain the composition of the bedload sediment, to determine whether the grain size distribution changed as flow increased from 62 m^3/s to 656 m^3/s, to identify any downstream trends in bedload composition and to see if coarse gravel became mobile during high flow. Due to time constraints, all samples from a transect were combined prior to sieving; results from the sieving therefore represent the mean cross-sectional grain size distribution. All sieved samples were either from the US or LP transects.

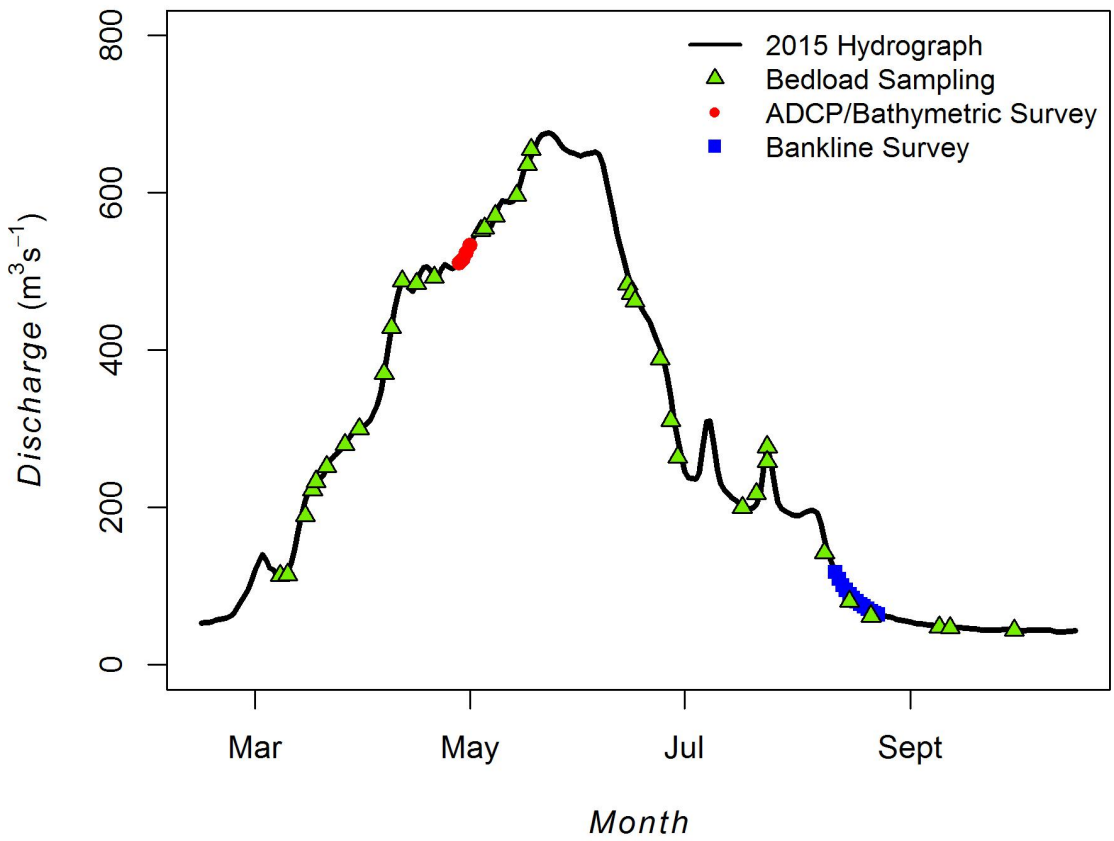

Figure 3.5: 2015 hydrograph with bedload sampling and surveying dates.

Chapter 4

Results

4.1 Bathymetry and water surface elevation

A 1-m resolution DEM of the study area was created in a geographic information system using the bathymetry, topography and bankline data (Figure 4.1). The DEM clearly defines the thalweg along the southern mainstem channel with deeper pools located at channel constrictions, along bends and in areas of flow convergence. North of the mainstem, a complex of secondary channels flows through the anabranching reach. Secondary channels within the northern portion of the island complex are seen to bifurcate at high angles, reaching 90 degrees in some locations, due to the vegetated, cohesive nature of the banks.

Water surface elevation (WSE) was interpolated and used to map depth throughout the reach for the time it was surveyed, which was from May 12-15th at a flow of about 525 m^3/s (Appendix D). The mean and maximum depths within the mainstem channel were 3.07 m (SD = 0.78 m) and 6.32 m, respectively, while the mean and maximum depths within secondary channels were 2.22 m (SD = 0.40 m) and 3.87 m. The deepest area within the entire reach was located downstream of the anabranching reach in the mainstem channel. Secondary channels had a narrow distribution of depths, with 50% of the total secondary channel area being 2.0-2.5 m deep. In comparison, the most frequent range of depths within the mainstem was 2.5-3.0 m, but covered only 26% of the total mainstem area. The total areas covered by secondary channels and the mainstem channel were approximately 0.28 km^2 and 0.55 km^2, respectively.

The longitudinal profile of bed and water surface elevations collected along the mainstem channel indicates that flow was non-uniform within the reach during high discharge (Figure 4.2). At the upstream extent of the reach, the steep water surface slope corresponds to high velocity flow through a relatively narrow channel width. Roughly 1 km downstream, the hydraulic gradient begins to decrease, indicative of backwatered flow conditions. Backwatering appears to be controlled by the Burrard Ave. Bridge because water surface slope increases once again downstream of the bridge. At a discharge of about 525 m^3/s, the backwater is seen to extend approximately 1.5 km upstream from the bridge.

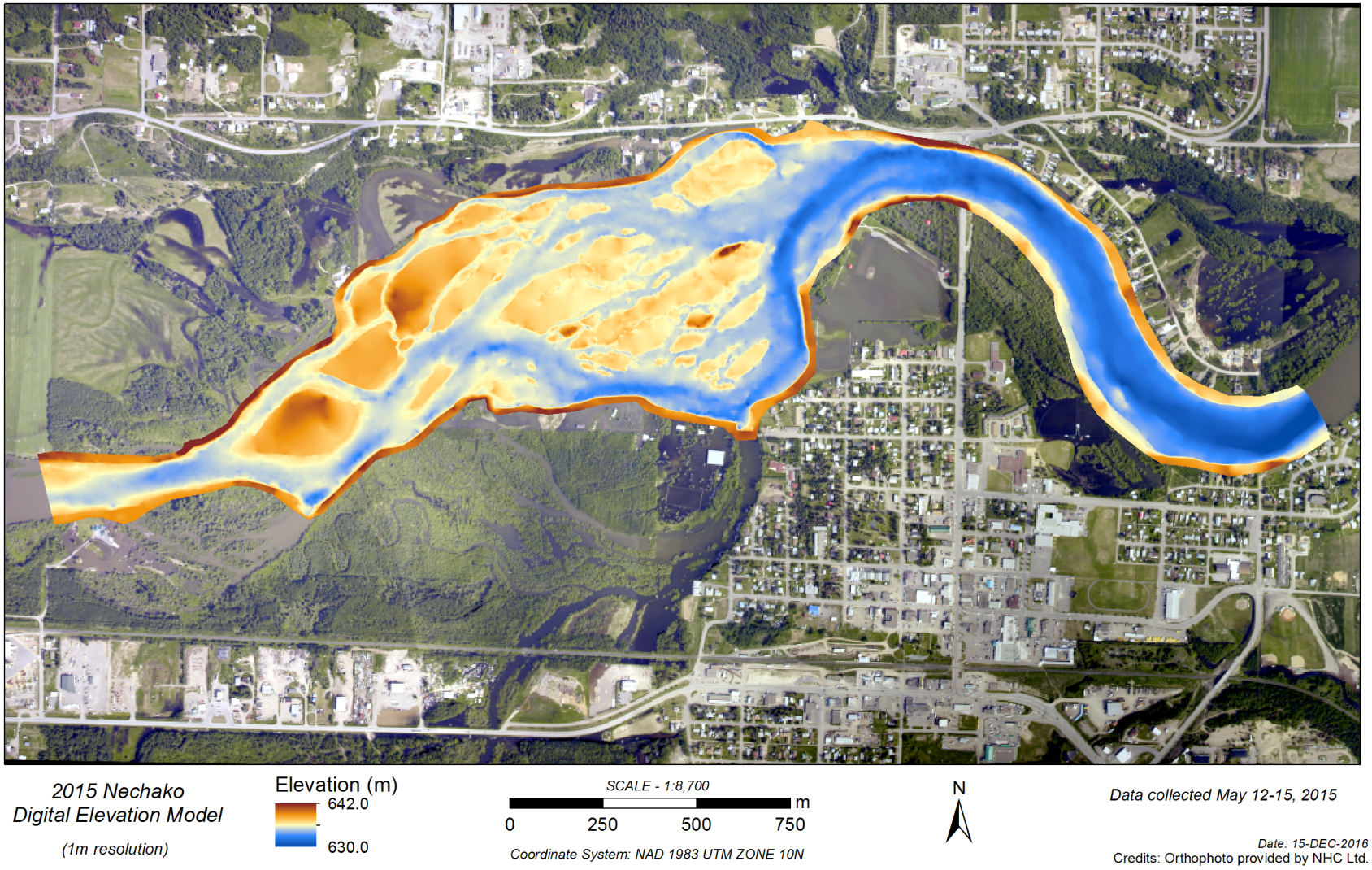

Figure 4.1: Digital elevation model of the spawning reach.

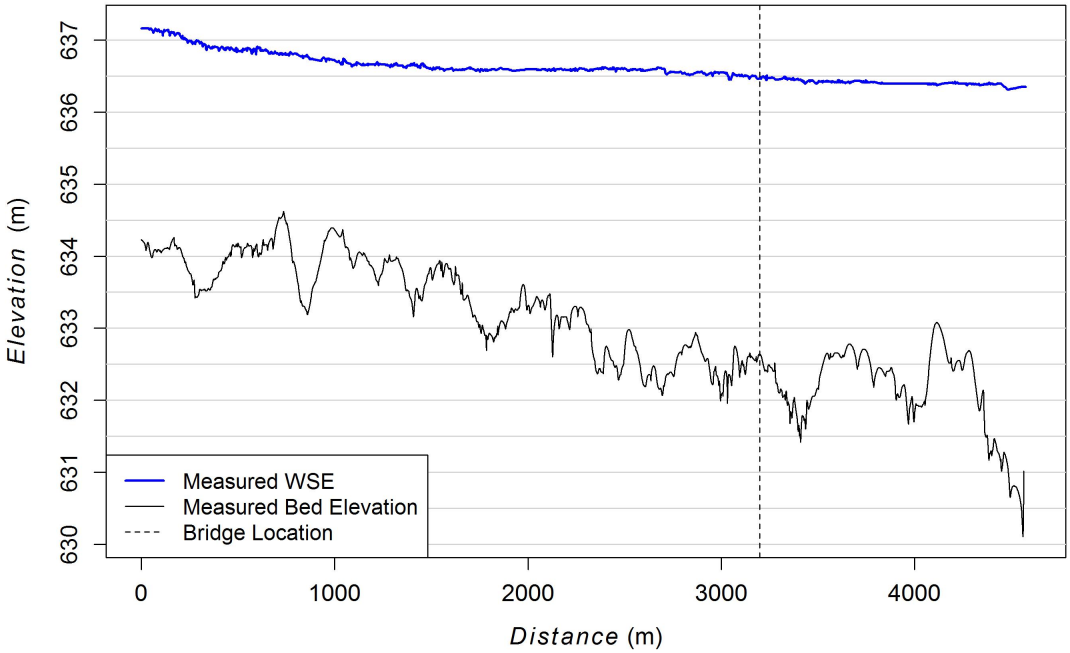

Figure 4.2: Bed and WSE profile along the mainstem channel during a flow of approximately 525 m^3/s.

4.2 Velocity and flow conveyance

The cross-channel velocity profile taken across the upstream transect TRA (Figure 3.2) during a discharge of about 525 m^3/s shows high-velocity flow through a relatively simple, parabolic-shaped channel (Figure 4.3) (see Appendix B for all velocity profiles). The mean cross-sectional flow velocity at this location was the highest within the study area, reaching 2.17 m/s. Mean velocity then decreased downstream to a minimum of 0.57 m/s at transect TRH, located at the downstream extent of the island complex approximately 675 m upstream from the Burrard Ave. Bridge (Table 4.1). At this location, the channel shape is roughly rectangular and higher velocity flow is concentrated within a 40-m wide section beginning about 30 m from the left bank (Figure 4.3). Approximately 200 m upstream from the bridge, mean velocity increases once again to 1.01 m/s at transect TRI. This location corresponds to the upstream portion of the Lower spawning pad (Figure 2.1). The cross-sectional profile at this transect is relatively complex with slower, deeper flow through the thalweg and higher velocity flow concentrated along the inside of the meander about 40 m from the right bank (Figure 4.3). The downstream spawning pad is located within the thalweg, about 40 m from the left bank.

Bed mobility was detected at Transect TRA and Transect TRB due to the offset between GPS and Bottom Track (BT) referenced ship tracks (Figure 3.3). At the upstream transect TRA, the bed was mobile between about 10-20 m from the left bank and the greatest mobility

occurred near the 20-m mark. High sediment mobility at this location was also observed during bedload sampling (US) on May 19th, seven days after the ADCP data were collected. On that day, the highest cross-sectional transport rate of 138.62 g/s/m was sampled directly at the 20-m mark; a rate corresponding to 58.4% of the total cross-sectional sediment transport on that day. At transect TRB, the GPS and BT ship tracks became offset between 15-25 m from the left bank. When bedload transport was sampled across this channel (MU-A), two days before and six days after the velocity profiles were taken, the highest transport rates also occurred at a 20-m distance from the left bank. The sampled rates at this location on both days were 44.8 g/s/m and 19.6 g/s/m, respectively, representing 67.9% and 48.6% of the total cross-sectional bedload transport for each date. These findings suggests that bedload sediment is laterally concentrated into lanes of higher sediment transport, rather than being evenly distributed across the channel.

Around the time of data collection (500-550 m^3/s), the amount of flow was not proportional to the amount of bedload being conveyed through the different channels. On May 18th, 93% of the channel-wide bedload sediment was conveyed by 39% of the total flow through secondary channel MU-A (see Figure 3.4) (bedload transect MU-A corresponds to ADCP transect TRB in Table 4.1). Further downstream, on May 5th, the sediment transport rate across transect ML-A was only 0.3 g/s compared to 34.8 g/s at transect ML-B. The difference in bedload conveyance between both transects occurred despite both channels conveying almost equal amounts of flow (bedload transects ML-A and ML-B correspond to ADCP transects TRG and TRH in Table 4.1). The disproportionate amount of sediment compared to flow being conveyed through different channels further supports that preferential pathways of sediment transport exist within the reach, both at the cross-sectional and reach-planform scales.

Overall, a wide range of flow velocities were present within the reach during the time of data collection. The decreasing trend in mean flow velocity from upstream to downstream (Figure 4.4) is consistent with the longitudinal profile of water surface slope (Figure 4.2); TRA is in the high gradient section at the upstream extent, TRH is within the backwatered area of the island complex and TRI is just upstream of the bridge where the hydraulic gradient increases once again. It is interesting that results from the ADCP provided insight into bedload conveyance as well, as bed mobility was detected within narrow cross-channel widths.

Table 4.1: Proportional flow conveyance and mean velocity across 9 ADCP transects (data collected May 12-15th, 2015 at a discharge of approximately 525 m^3/s).

Transect	Percent of Total Discharge	Mean Velocity (m/s)
TRA	100	2.17
TRB	39	1.56
TRC	61	1.74
TRD	19	1.02
TRE	12	1.02
TRF	31	1.00
TRG	38	0.10
TRH	39	0.57
TRI	100	1.01

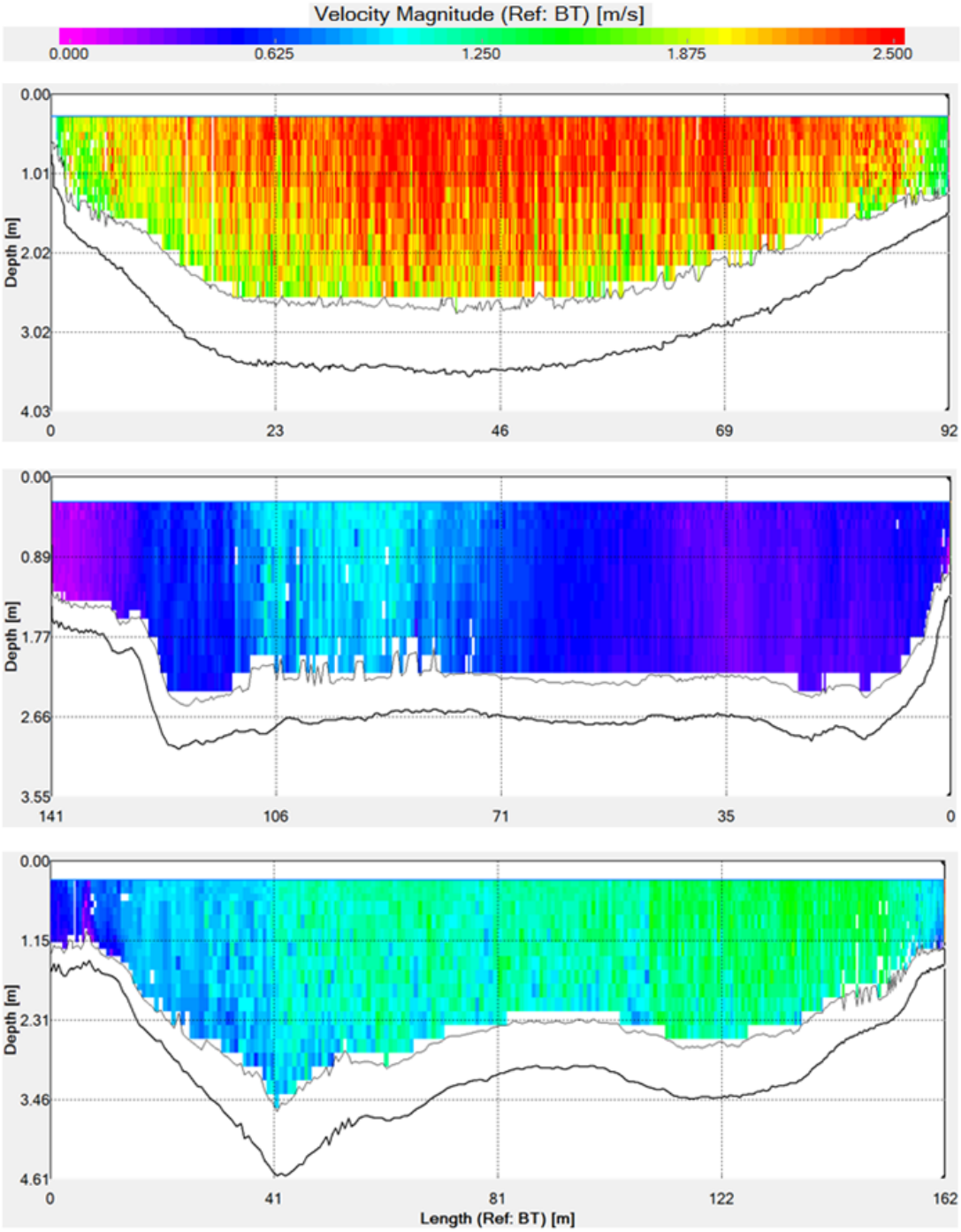

Figure 4.3: Cross-channel velocity profiles at transects TRA (top), TRH (middle) and TRI (bottom) during a discharge of approximately 525 m^3/s between May 12-15th, 2015.

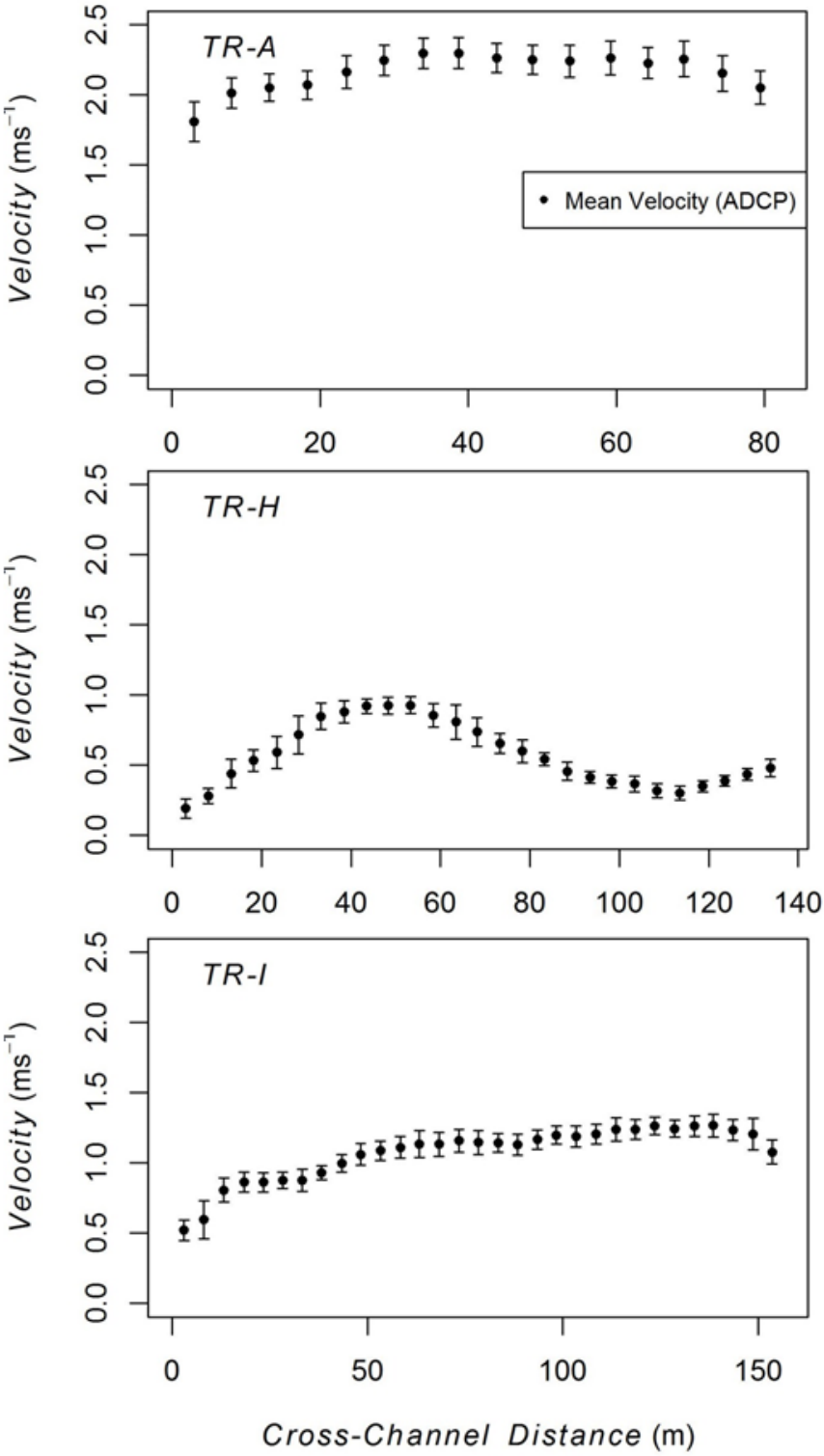

Figure 4.4: Depth-averaged velocity across transects TRA, TRH and TRI during a discharge of approximately 525 m^3/s between May 12-15th, 2015 (whiskers indicate standard deviation within each cross-channel bin).

4.3 Bedload sediment composition and transport rates

The bedload being transported throughout the spawning reach was almost entirely composed of sand finer than 2 mm. The grain size distribution of the bedload showed no relation with increasing discharge or transport rate and did not vary significantly between sampling locations. The coarsest D_{84} grain size sampled within the entire reach reached only 3 mm, and the D_{84} at the US transect did not exceed 2 mm even when flow velocities were over 2.00 m/s during high flow (Figure 4.5). In fact, only 3.4% and 6.7% of the total sampled mass at the US transect was coarser than 8 mm gravel during the two highest flows sampled; 597 m^3/s on May 28th and 656 m^3/s on June 2nd. Very coarse gravel in the 45-64 mm range constituted only 1.4% and 4.4% of the total sampled mass on these respective dates.

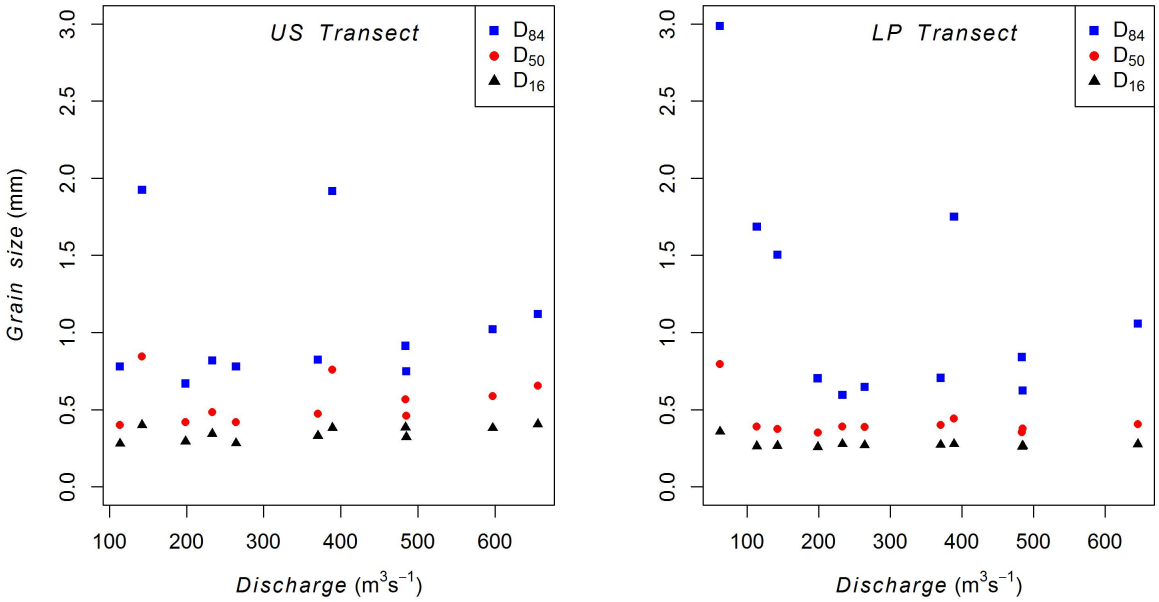

Figure 4.5: D_{84}, D_{50} and D_{16} grain sizes of bedload sediment.

The rate of bedload transport at the US transect was positively correlated with discharge (Figure 4.6). However, this relation was non-linear and transport rates increased markedly once discharge exceeded about 400 m^3/s. Using this threshold to split the data into two linear relations, bedload transport increased with a slope of 1.48 below 400 m^3/s ($R^2 = 0.39$) and a slope of 8.97 above 400 m^3/s ($R^2 = 0.79$). The mean cross-sectional transport rate was 225.6 g/s (SD = 203.1 g/s) for flows between 80-400 m^3/s compared to 1,753.5 g/s (SD = 724.1 g/s) for flows of 400-656 m^3/s. The maximum cross-sectional transport rate past this sampling transect reached 2,599.4 g/s during a discharge of 656 m^3/s, on June 2nd, 2015. This date nearly corresponds to the timing of peak annual flow, that reached 677 m^3/s on June 6th. After this date, hysteresis was observed in the bedload-discharge relation. The lower transport rates

during the falling limb of the hydrograph suggest that the supply of bedload sediment upstream of the US transect became limited during the period of peak flow.

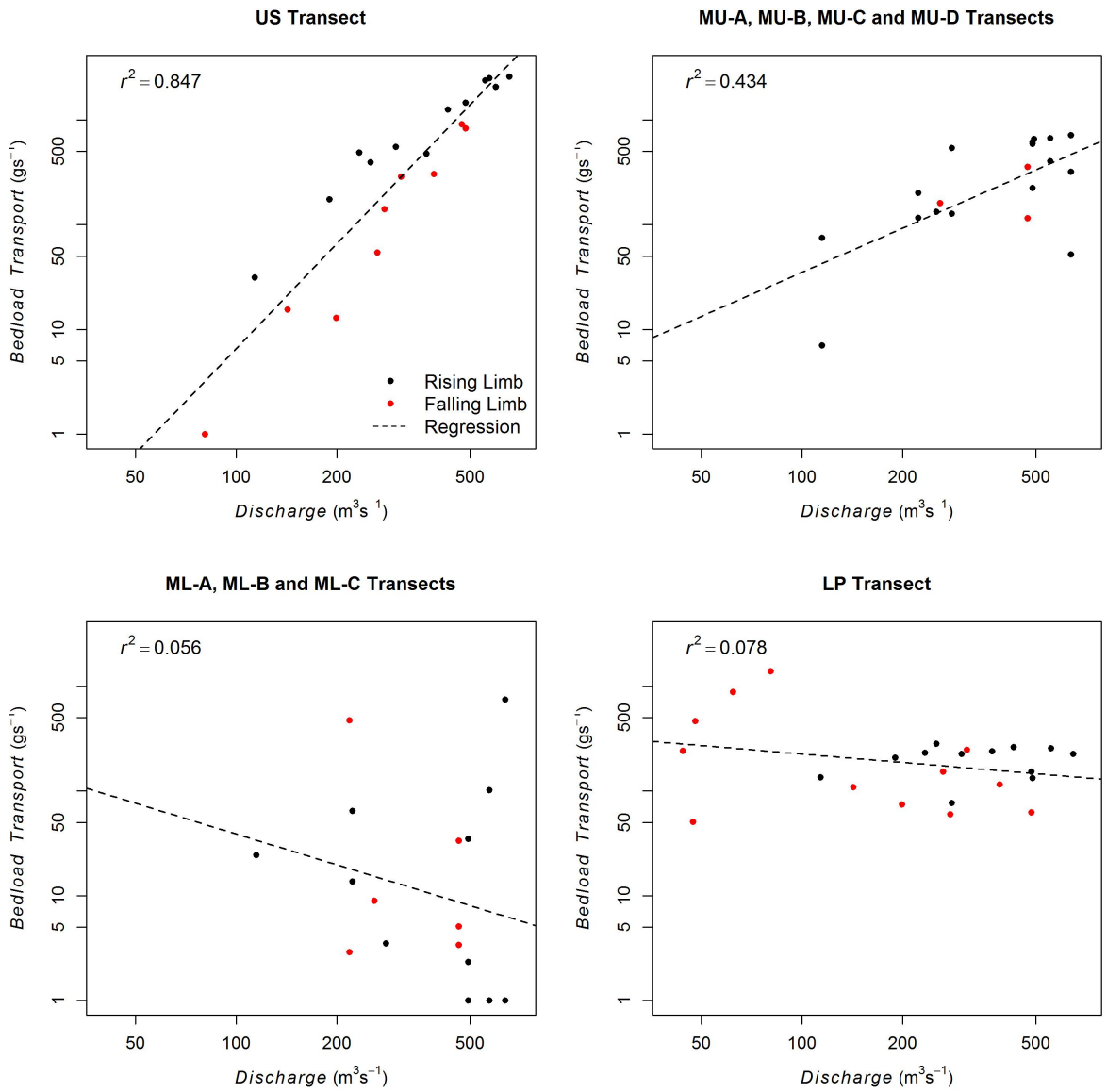

Figure 4.6: Relation between bedload transport and discharge at progressively downstream sampling locations (Note: only regressions at the US and MU transects are significant).

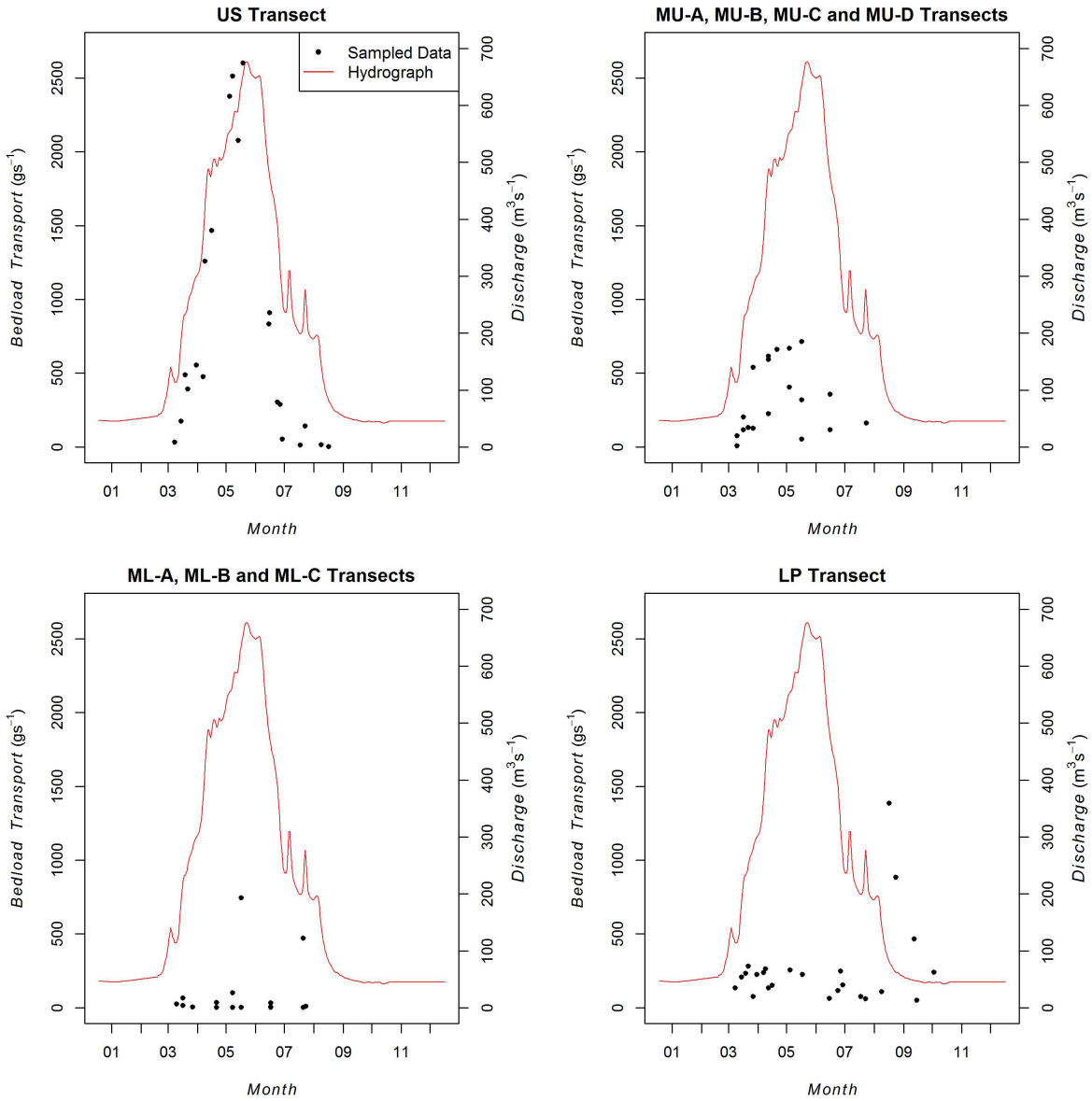

Figure 4.7: Sampled bedload transport rates throughout the 2015 hydrograph.

In contrast, the rate of bedload transport past the LP transect was not related to discharge. The maximum cross-sectional transport rate was only 1,384.8 g/s, or roughly half of the maximum transport rate past the US transect. Peak sediment transport across transect LP occurred on August 31st at a relatively low discharge of 81 m^3/s during the tailing end of the receding hydrograph limb. Cross-sectional transport rates were also relatively constant compared to the rates sampled upstream. The mean and standard deviation of bedload transport at the LP transect was 261.2 g/s and 288.1 g/s, compared to the US transect where the mean and standard deviation was 807.7 g/s and 865.4 g/s. Overall, the relation between discharge and bedload transport weakened with downstream distance (Figure 4.6) and the timing of maximum

sediment transport occurred progressively later throughout the year (Figure 4.7).

As part of the ongoing Nechako Sediment Transport Investigations, framed within the Nechako White Sturgeon Recovery Initiative, an analysis was done to quantify the sediment loads moving through the reach. The details of the analysis are not presented as part of this thesis, but are provided for completeness in Appendix E and are summarized below.

A bedload-discharge rating curve was used to derive the annual sediment load transported into the study area past the US transect; predicted and observed bedload rates were in good agreement. The incoming sediment load was then compared to the amount of bedload being transported out of the reach past the LP transect. This output sediment load was estimated by interpolating daily transport rates between sampled dates since transport was uncorrelated with discharge. The predicted bedload transport rate across the US transect reached a maximum of 190 m^3/day during peak flow, exceeding the maximum transport rate across the LP transect of 75 m^3/day for 61 consecutive days between April 25th and June 24th, 2015. The total annual loads for the upstream and downstream locations were estimated at 9,250 m^3 and 3,050 m^3, suggesting net deposition of over 6,000 m^3 of sediment within the reach.

4.4 Patterns of sediment transport through the study reach

Bedload sediment was primarily transported downstream through the spawning reach by a subset of active secondary channels (Appendix F). As bedload entered the reach, a large portion of it was routed into the first secondary channel immediately downstream of the US transect, labelled *MU-A* in Figure 4.8. Transport rates within this channel ranged from 12.7% to 111.6% of the US cross-sectional transport rate while the amount of sediment transported in the mainstem channel MU-C was only 1.2% to 19.3% (Table 4.2) [1]. Throughout the monitoring period, secondary channel MU-A transported on average 8 times more sediment than the mainstem channel. Roughly 280 m downstream, the amount of bedload transported in channel MU-D was 97% and 224% of the upstream cross-sectional transport rate at MU-A on April 26th and May 31st, respectively. For these same dates, the transport rate in channel MU-B which leads back into the mainstem channel was 37% and 16% of the upstream transport rate at MU-A.

Further downstream within the anabranching section, bedload was primarily conveyed by channel ML-B through the middle of the island complex (Figure 4.8). The amount of sediment being transported through channel ML-B increased with discharge, as well as over time, with the two maximum rates occurring during the peak of the hydrograph and during the receding limb (Table 4.3). Compared to channel ML-B, transport rates were very low within the mainstem channel ML-A and within the northern secondary channel ML-C. The two highest transport rates in channel ML-A were sampled during the rising and falling limbs of the flood hydrograph and transport dropped to zero during the period of peak flow.

[1] If transects were not sampled on the same date, values were obtained by interpolating transport rates between sampled days.

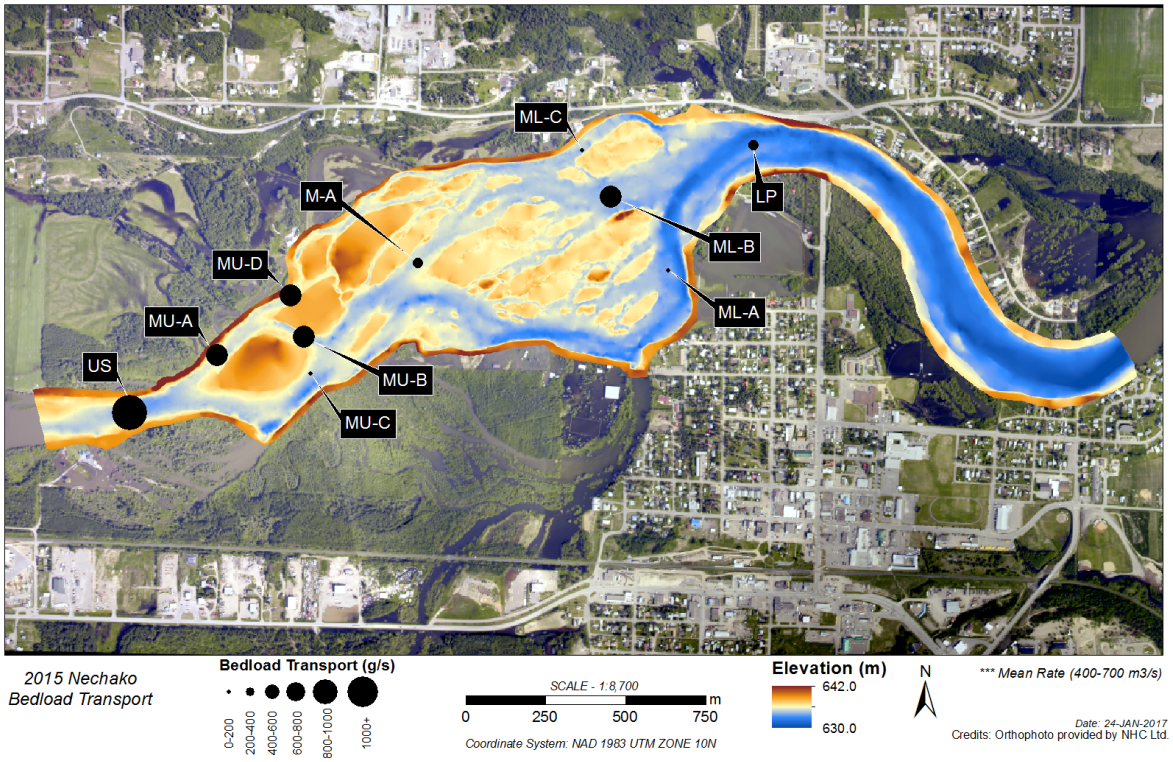

Figure 4.8: Mean bedload transport rate through different channels (sampled between 400-700 m^3/s).

Table 4.2: Bedload tranport through secondary channel MU-A and mainstem channel MU-C in the upstream portion of the study reach.

Date	Discharge (m^3/s)	MU-A % of US	MU-C % of US
3/24/2015	115	104.0	8.7
3/31/2015	223	60.6	13.5
4/10/2015	280	111.6	19.3
4/26/2015	488	45.6	3.8
5/18/2015	552	17.4	1.2
5/31/2015	636	13.3	5.4
6/30/2015	473	12.7	3.7

Table 4.3: Bedload tranport through mainstem channel ML-A compared to secondary channels ML-B and ML-C within the island complex.

Discharge (m^3/s)	Hydrograph Limb	ML-A (g/s)	ML-B (g/s)	ML-C (g/s)
100 - 200	Rising	24.5	No Data	No Data
200 - 300	Rising	8.6	64.4	No Data
400 - 500	Rising	0.3	34.9	2.3
500 - 600	Rising	No Data	101.9	0.0
600 - 700	Rising	0.0	743.2	0.0
500 - 400	Falling	5.1	33.6	3.4
300 - 200	Falling	9.0	470.7	2.9

The location of highest sediment transport past the US and LP transects remained spatially consistent over time (Figure 4.9). At the US transect, where the total channel width is approximately 100 m, bedload was typically transported within 50 m of the left bank and the highest transport rates were located 15-35 m from the bank. This narrow 20-m width had the highest transport rates of the entire cross-section on 16 of the 21 sampled days. The eleven highest transport rates sampled across the US transect in 2015 were located within this 20-m width and ranged from 32.6 g/s/m to 181.3 g/s/m. At the LP transect, the highest transport rate on 21 of 24 sampled days was located 15- 65 m from the left bank. The total channel width at this location is roughly 150 m. The six highest transport rates across this transect were sampled 15-35 m from the left bank and ranged from 15.2 g/s/m to 134.1 g/s/m. Four of these peak transport rates were sampled between August 31st and October 17th when discharge was between 44 m^3/s and 80 m^3/s. The consistency in cross-channel location with high sediment transport corroborates results from the ADCP (described in Section 4.2) stating that bedload is laterally concentrated within discrete lanes at the US transect. In addition, the sampling results described above confirm that preferential pathways of sediment transport also exist at the LP transect, a spatial dynamic which was undetected by the ADCP due to the lower intensity transport rates.

Overall, bedload was conveyed through the reach in a relatively consistent pattern. Sediment is primarily transported through the island complex by a subset of active secondary channels with comparatively minimal bedload transported along the mainstem channel. At the US and LP sampling transects, where the channel is single-thread, bedload is conveyed within a 50-m portion of the total channel width and highest transport occurs within a 20-m subsection near the left bank.

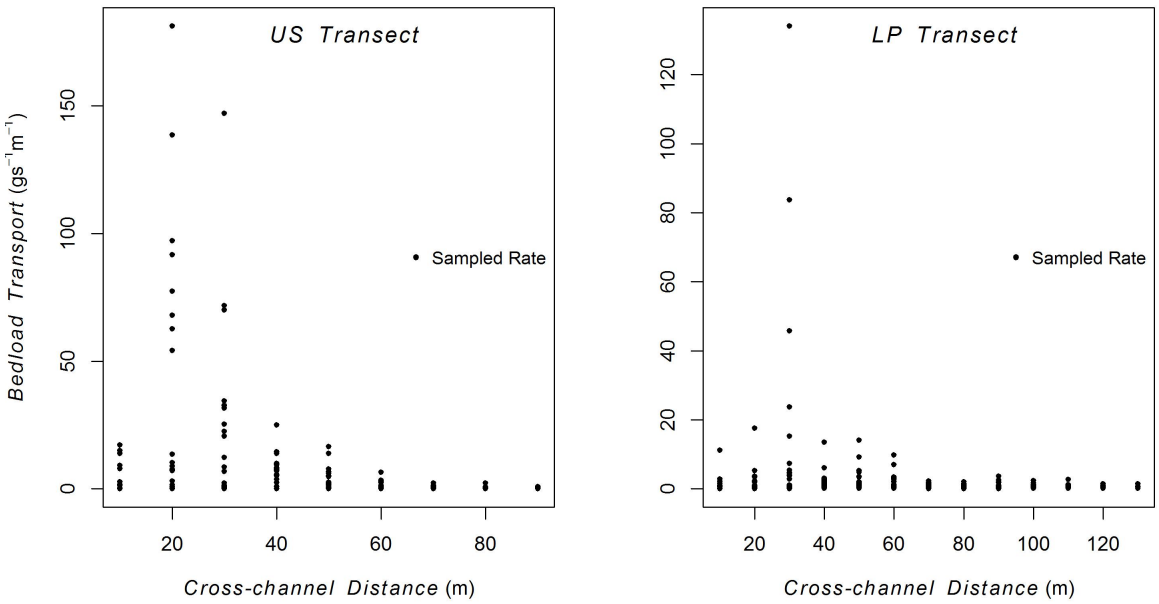

Figure 4.9: Cross-channel bedload transport rates sampled in 2015 at the US and LP transects, distances provided relative to a fixed location on the left bank.

Chapter 5

Modelling

5.1 Initialization

The Nays2DH hydrodynamic model, accessed through the International River Interface Cooperative (iRIC) platform, was used to conduct all simulations. Details about the 2-dimensional solver are not presented herein and can be found elsewhere (www.i-ric.org). Nays2DH was selected over alternative models due to its numerical stability, flexibility in setting the initial water surface profile and because the effect of vegetation can be introduced separately from Mannings roughness as an additional drag force. For further detail regarding the model data, configurations and results presented below, see Appendix G.

Topography was input to the model using the reach-scale DEM (Appendix D) coarsened to a resolution of 2 m. The modelling mesh, composed of 5 x 5 m grid cells, was created from a polygonal channel center-line and specified domain width of 900 m. Simulations were run for 10,000 seconds and the time-step was adjusted between 0.10-0.15 seconds depending on the simulated discharge to achieve model stability. Solution results were output at 10 second intervals and the last 1,000 seconds were averaged to generate the final simulation result.

Discharge and water surface elevation at the downstream boundary were held constant for each simulation. Simulations were run for every 50 m^3/s discharge increment between 75 m^3/s and 775 m^3/s, with an additional low flow simulation of 45 m^3/s. Preliminary runs using a uniform flow calculation to set the downstream boundary condition revealed that flow is non-uniform downstream of the bridge during moderate to high discharges. Consequently, a stage-discharge rating curve was developed to specify WSE at the downstream boundary. This was done by iteratively adjusting the input WSE until good agreement was achieved between modelled output and measured stage at Water Survey of Canada (WSC) Gauge 08JC001 (Figure 5.1). This WSC gauge is located approximately 1 km upstream of the model boundary. Including the entire range of simulated flows, the mean absolute error of modelled WSE at the gauge location was 0.066 m.

Manning's roughness coefficient (n) was varied during model calibration to achieve agree-

ment between simulated and observed WSE profiles. Calibration resulted in a low Manning's roughness value of 0.0215 assigned to the channel, with a slightly higher roughness of 0.024 assigned to a localized area of flow convergence to reduce instability at high flow. Bar contours, bottom-of-bank and top-of-bank shapefiles were imported to the model and assigned additional drag to account for vegetation. Bar tops and bank slopes were assigned a vegetation density of 0.1 stems/m^2 and all overbank areas were assigned a vegetation density of 2.0 stems/m^2. These values were determined by comparing simulation output with water surface elevation and velocity data.

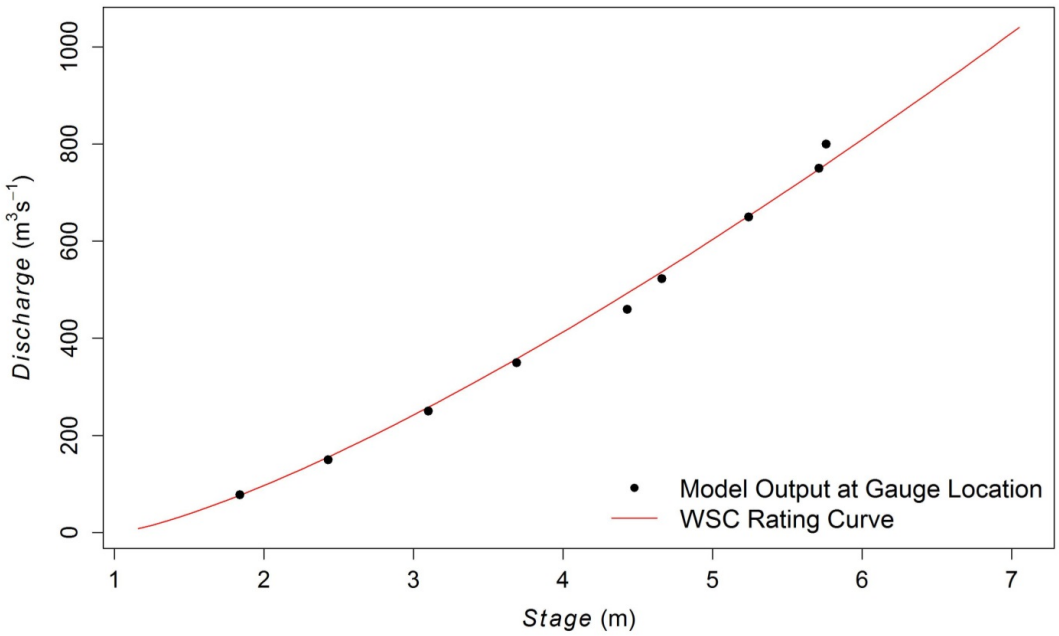

Figure 5.1: Measured versus modelled stage at WSC gauge location (simulations were run using a rating curve to specify the downstream WSE boundary condition).

The grain size distribution imported to the model was obtained by photo-sieving a series of 30 underwater images taken across the US, MU-A, MU-B, MU-D, M-A and LP bedload sampling transects (Figure 3.4). Image resolution was 1.76 pixels per 1.0 mm and the surface area captured in each image was about 627 cm^2. The photo-sieving code used a Wolman Pebble Count approach where 100 grains within the image were digitally measured at gridded intervals. The finest size class used for classification was sand and all grains finer than 2 mm were included within the sand fraction. The grain size distribution of the bed surface was determined for each photo and combined by transect to generate averaged cross-channel results. The averaged grain size distributions were used to create five polygons, corresponding to the substrate characteristics of channels US, MU-A, MU-B/MU-D, M-A and LP. The grain size distribution showed a trend of downstream fining from the US transect (D_{50} = 36 mm, 12% sand) to the LP transect (D_{50} = 8 mm, 28% sand).

For all simulations, the model was run with a fixed bed and the output flow parameters were used to calculate the sediment transport capacity for each grid cell. Transport capacity was calculated using the Wilcock and Crowe (2003) transport function. This surface-based sediment transport model is defined by Eqs.5.1, 5.2 and 5.3:

$$W_i^* = \begin{cases} 0.002\Phi^{7.5} & \text{for } \Phi < 1.35 \\ 14\left(1 - \frac{0.894}{\Phi^{0.5}}\right)^{4.5} & \text{for } \Phi \geq 1.35 \end{cases} \tag{5.1}$$

$$\tau_{rm}^* = 0.021 + 0.015 \exp[-20F_s] \tag{5.2}$$

$$\frac{\tau_{ri}}{\tau_{rm}} = \left(\frac{D_i}{D_{sm}}\right)^b \tag{5.3}$$

where,

$$b = \frac{0.67}{1 + \exp\left(1.5 - \frac{D_i}{D_{sm}}\right)} \tag{5.4}$$

$$\tau_{rm}^* = \frac{\tau_{rm}}{(s-1)\rho g D_{sm}} \tag{5.5}$$

W_i^* is the dimensionless transport rate of size fraction i, $\Phi = \tau/\tau_{ri}$, τ is the shear stress, τ_{ri} is the reference shear stress of size fraction i, τ_{rm}^* is the reference dimensionless Shields stress for the mean size of the bed surface, τ_{rm} is the reference shear stress of the mean size of the bed surface, F_s is the proportion of sand in the surface size distribution, D_i is the grain size of fraction i, D_{sm} is the mean grain size of the bed surface, s is the ratio of sediment to water density, ρ is water density and g is gravitational acceleration.

For the calculation, each cell within the model domain was attributed a grain size distribution by interpolating between the six locations where underwater images had been collected and photo-sieved (Appendix G).

5.2 Calibration and validation

The low channel roughness (n = 0.0215) calibrated to a discharge of approximately 525 m^3/s achieved good agreement between simulated and observed WSE profiles in both the southern mainstem channel and the northern-most secondary channel (Figure 5.2). Minimum, maximum and mean absolute error in the mainstem channel and secondary channel was -0.033 m, 0.082 m and 0.025 m, and -0.061 m, 0.100 m and 0.015 m, respectively. Such a low roughness value suggests that the wetted channel boundary is hydraulically smooth, lacking bedforms and vegetation. This seems possible given the D_{50} of the substrate within the study reach is typically immobile medium to coarse gravel (8-36 mm) infilled with 12-28% sand. While no clear spatial trend in the error was observed within the secondary channel, a downstream trend

does exist within the mainstem channel where simulated WSE around the island complex is slightly higher than measured elevations.

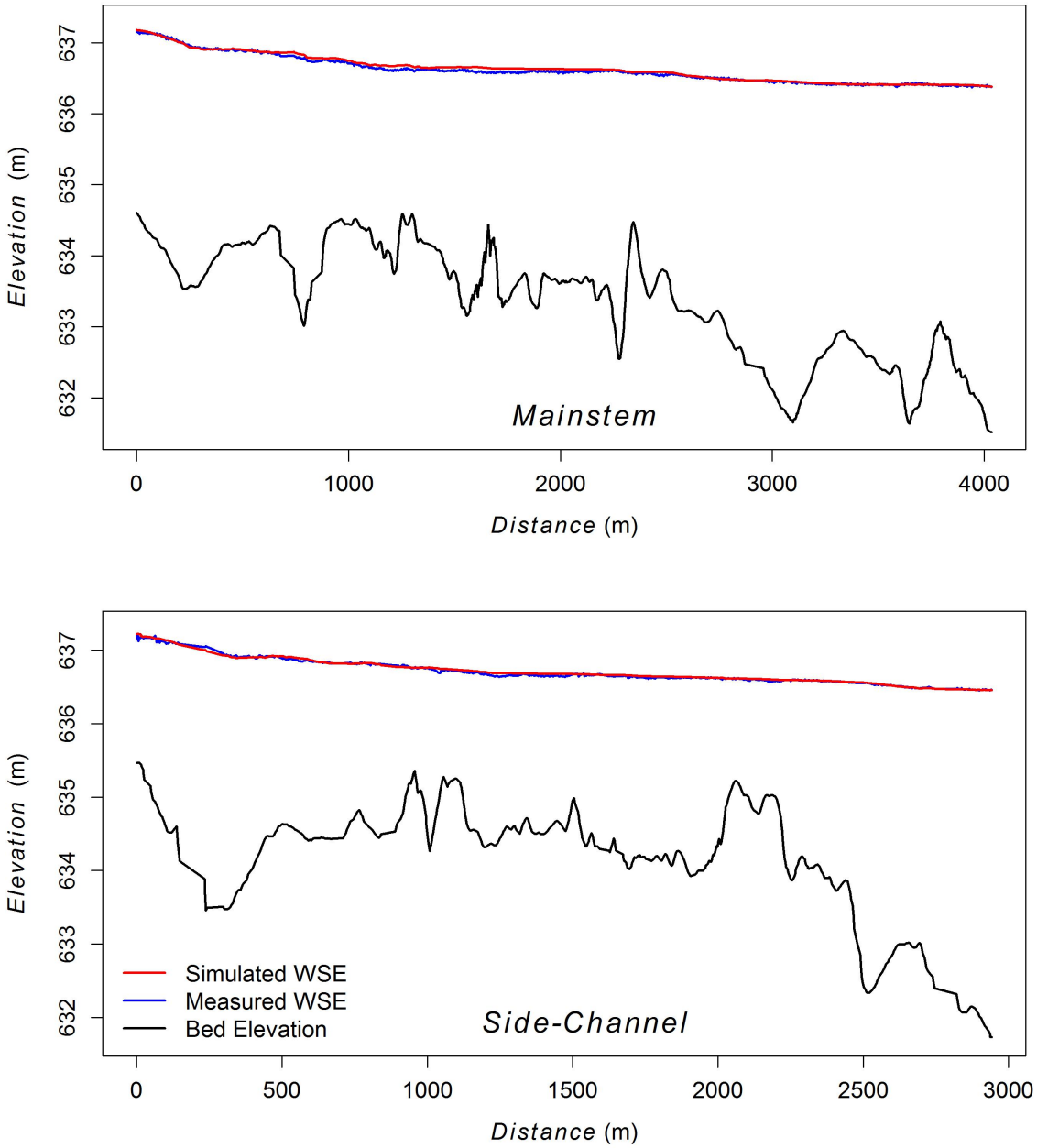

Figure 5.2: Measured (May 12-15th, 2015) and simulated WSE profiles for a discharge of 525 m^3/s after calibration of channel roughness.

The model was validated against velocity and depth data collected across nine transects (Figure 3.2). The mean absolute error in simulated velocities across each transect ranged from 0.09 m/s to 0.19 m/s (Table 5.1). The most accurate simulation results were obtained within the mainstem channel, while poorest results occurred within relatively narrow secondary channels.

Mean absolute percent error was lowest at transects TRA and TRC where flow velocity was the highest (Table 4.1). Regarding modelled depth, mean absolute error was less than 0.10 m for all transects except TRA, but the mean absolute percent error at this location was still less than 5%. Overall, modelled patterns of cross-channel velocity (Figure 5.3) and depth were in close agreement with measured data given the complexity of channel. Data from all 9 ADCP transects are compared to simulated results in Appendix G.

Table 5.1: Simulated velocity and depth compared to ADCP data collected May 12-15th during a discharge of approximately 525 m^3/s

Transect	Velocity MAE (m/s)	Velocity MAE (%)	Depth MAE (m)	Depth MAE (%)
TRA	0.14	6.7	0.13	4.6
TRB	0.17	15.5	0.04	2.2
TRC	0.14	8.7	0.06	2.6
TRD	0.17	28.0	0.07	2.8
TRE	0.19	17.8	0.08	4.1
TRF	0.19	19.5	0.07	3.3
TRG	0.11	11.7	0.09	3.1
TRH	0.09	17.0	0.10	3.6
TRI	0.10	11.5	0.09	3.0

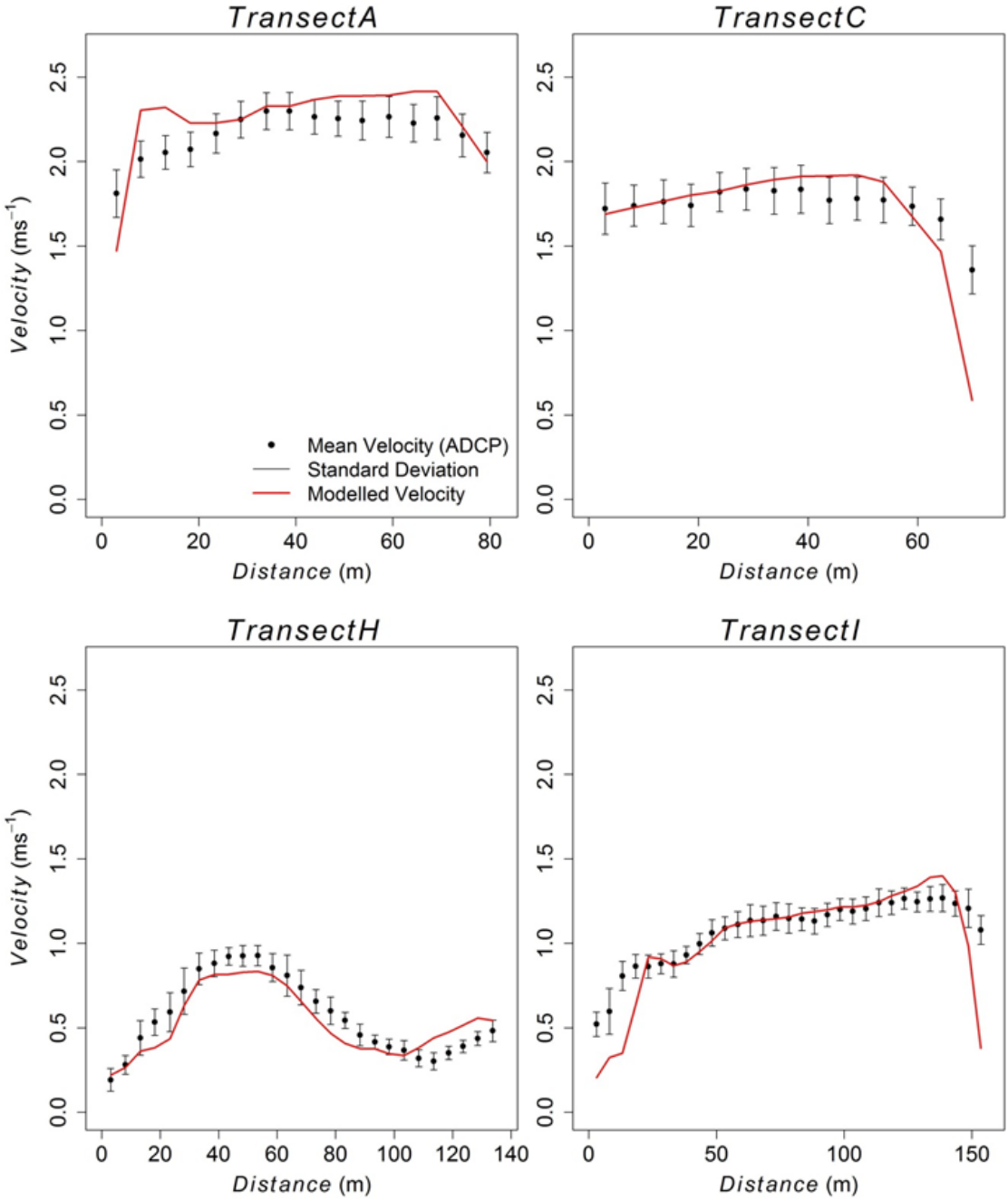

Figure 5.3: Measured (May 12-15th, 2015) versus simulated cross-channel velocity for a discharge of 525 m^3/s.

Additional data collected in 2006-07 by NHC (NHC, 2006; NHC, 2008) were used to evaluate model performance for discharges of 78 m^3/s, 460 m^3/s and 800 m^3/s. At 78 m^3/s, modelled WSE was generally high with a mean absolute error of 0.107 m (Figure 5.4). However, this error may be due to changes in channel topography which have occurred since the data were collected about 10 years ago. Results from the 460 m^3/s simulation are closer to observed values with a mean absolute error of 0.038 m and the 800 m^3/s simulation can be considered in general agreement with the data, given that the data represent estimates of the high-water mark from the 2007 freshet (NHC, 2008). Overall, these comparisons confirm the validity of the modelling approach and are likely to overestimate simulation error due to the effects of potential changes in channel bathymetry.

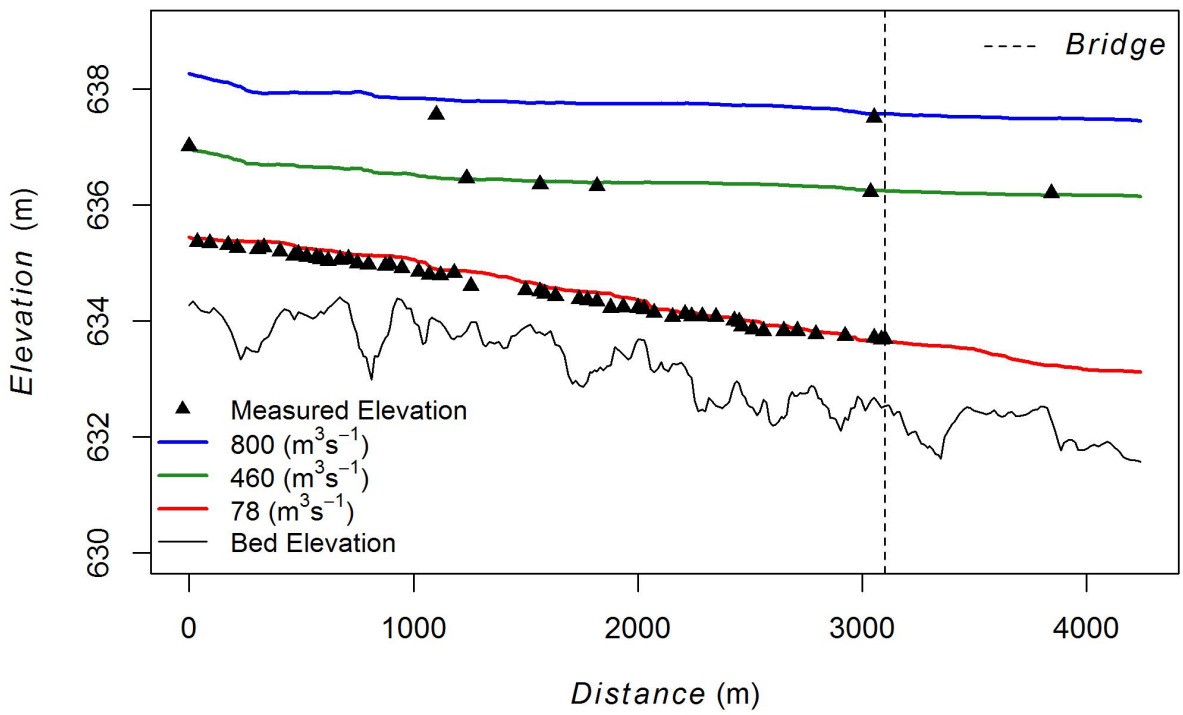

Figure 5.4: Simulated versus measured water surface profiles (data collected by NHC in 2006-07).

5.3 Simulation results

Discharge and velocity show a positive relation within the mainstem channel at the upstream extent of the reach and downstream of the bridge. However, they are negatively related within the downstream portion of the island complex (Figure 5.5). At the upstream extent of the

reach, velocity reached a maximum of 2.54 m/s during a simulated discharge of 775 m^3/s and a minimum of 0.62 m/s during a 45 m^3/s simulation. Comparatively, velocity reached a maximum of 1.35 m/s within the downstream portion of the island complex during low flow simulation of 45 m^3/s and a minimum of 0.37 m/s during a high flow of 775 m^3/s. Velocity varied with the greatest magnitude within the upstream reach, changing by 1.92 m/s over the range of flows compared to more moderate variations of 0.67 m/s, 0.98 m/s and 0.76 m/s for three progressively downstream locations.

The negative relation between discharge and velocity within the island complex agrees with measured WSE data indicating a non-uniform flow profile upstream of the Burrard Ave. Bridge during moderate to high flows (Figure 4.2). The reversal from a negative to a positive relation downstream of the bridge (Figure 5.5) further supports that the bridge is controlling the backwater within the reach. Model results suggest that backwatering begins at a discharge of approximately 225-275 m^3/s and that a clear non-uniform flow profile develops once discharge exceeds 325 m^3/s (Figure 5.6).

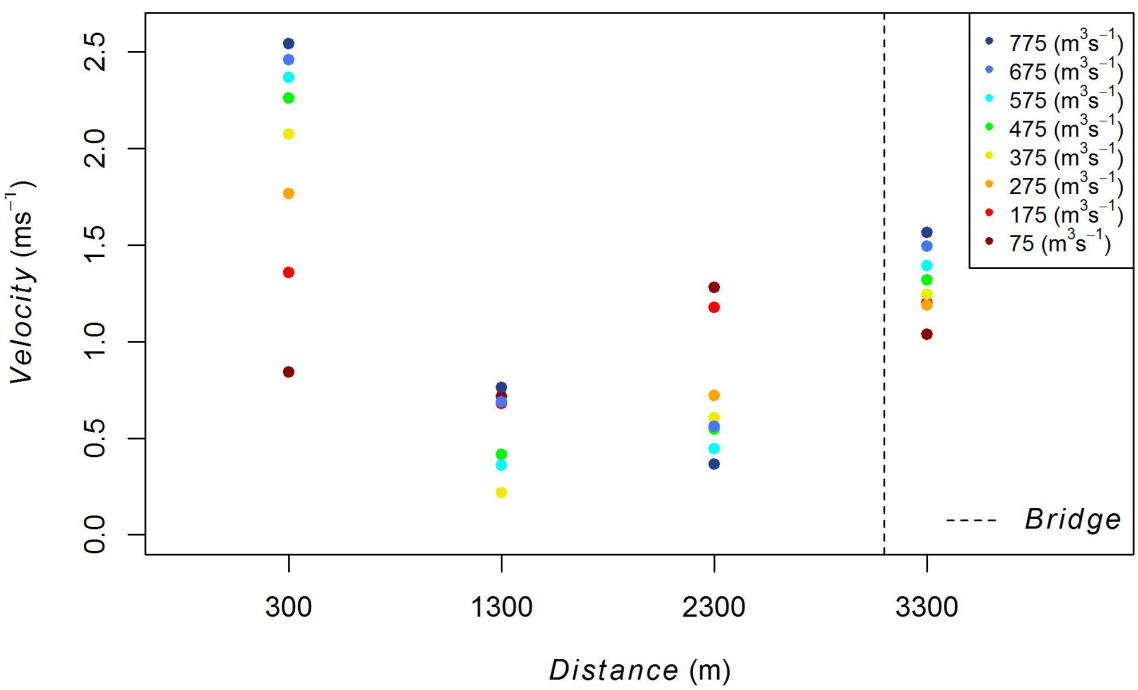

Figure 5.5: Relation between discharge and velocity within the mainstem channel (plotted by 100 m^3/s discharge intervals).

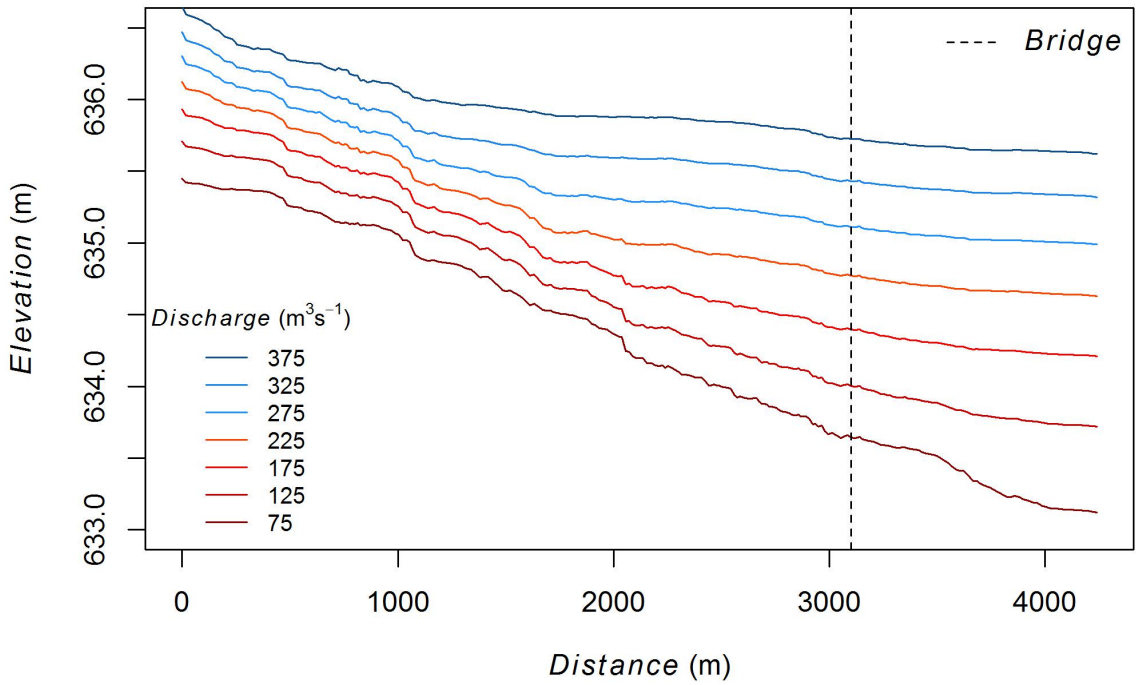

Figure 5.6: Simulated WSE profiles along the mainstem channel showing the development of backwater upstream of the Burrard Ave. Bridge.

The maximum shear stress within the reach increased with discharge, reaching 22.6 N/m^2 at 775 m^3/s. Maximum shear stress for all simulated flows varied only within a narrow range, between 22.6 N/m^2 and 16.2 N/m^2 (Table 5.2). Similarly, mean shear stress within the mainstem channel increased with discharge but only from 3.2 N/m^2 to 4.4 N/m^2. The location of maximum shear stress shifts as discharge increases from mid-reach channel constrictions and meanders to the upstream, mainstem channel (Figure 5.7).

Similar to the pattern of maximum shear stress, the area of highest transport capacity shifts upstream as discharge increases from 45 m^3/s to 375 m^3/s (Figure 5.8). The spatial pattern of high transport remains constant once discharge exceeds 425 m^3/s, although the magnitude of the transport capacity continues to increase. At a discharge of 75 m^3/s, the total cross-sectional transport capacity reaches a maximum of 8.7 kg/s at the downstream extent of the island complex (Figure 5.9). At this flow, the cross-sectional capacity at US and LP are 0.0 kg/s and 2.8 kg/s, respectively. As discharge increases to 375 m^3/s, the transport capacity becomes similar at US and LP, with rates of 2.1 kg/s and 1.2 kg/s, while capacity within the island complex drops to 0.0 kg/s. For a discharge of 775 m^3/s, the transport rate at US, within the island complex and at LP are 5.7 kg/s, 0.0 kg/s and 3.2 kg/s, respectively.

Table 5.2: Simulated shear stresses within the reach with increasing discharge (mean shear stress calculated using the mainstem channel).

Discharge (m^3/s)	Max Shear Stress (N/m^2)	Mean Shear Stress (N/m^2)
45	16.9	3.2
75	19.3	3.5
175	20.9	3.9
275	19.7	4.1
375	16.2	4.0
475	18.8	4.0
575	20.2	4.1
675	21.3	4.2
775	22.6	4.4

Sampled bedload transport rates were less than the estimated transport capacity at both the US and LP transects. This overestimation may have been produced because the modelled shear stress used to calculate the capacity represented the total shear stress, rather than only the skin drag, which is the proportion of the total shear stress responsible for grain mobility in sediment transport functions. In addition, transport capacity may have been overestimated because grain size distribution has a strong influence on estimated rates and significant interpolation was required to attribute a substrate composition to the entire model domain (further discussed in Section 6.4). While it is possible that the difference between transport capacity and observed transport at the US transect could indicate supply limited conditions, this is unlikely to be the case at the LP transect given the large supply of sand within the island complex located immediately upstream. Despite the discrepancy between observed and predicted transport rates, the ranges of flows producing the highest sampled rates correspond to the ranges of flows with the highest transport capacity at each location (Figure 5.10).

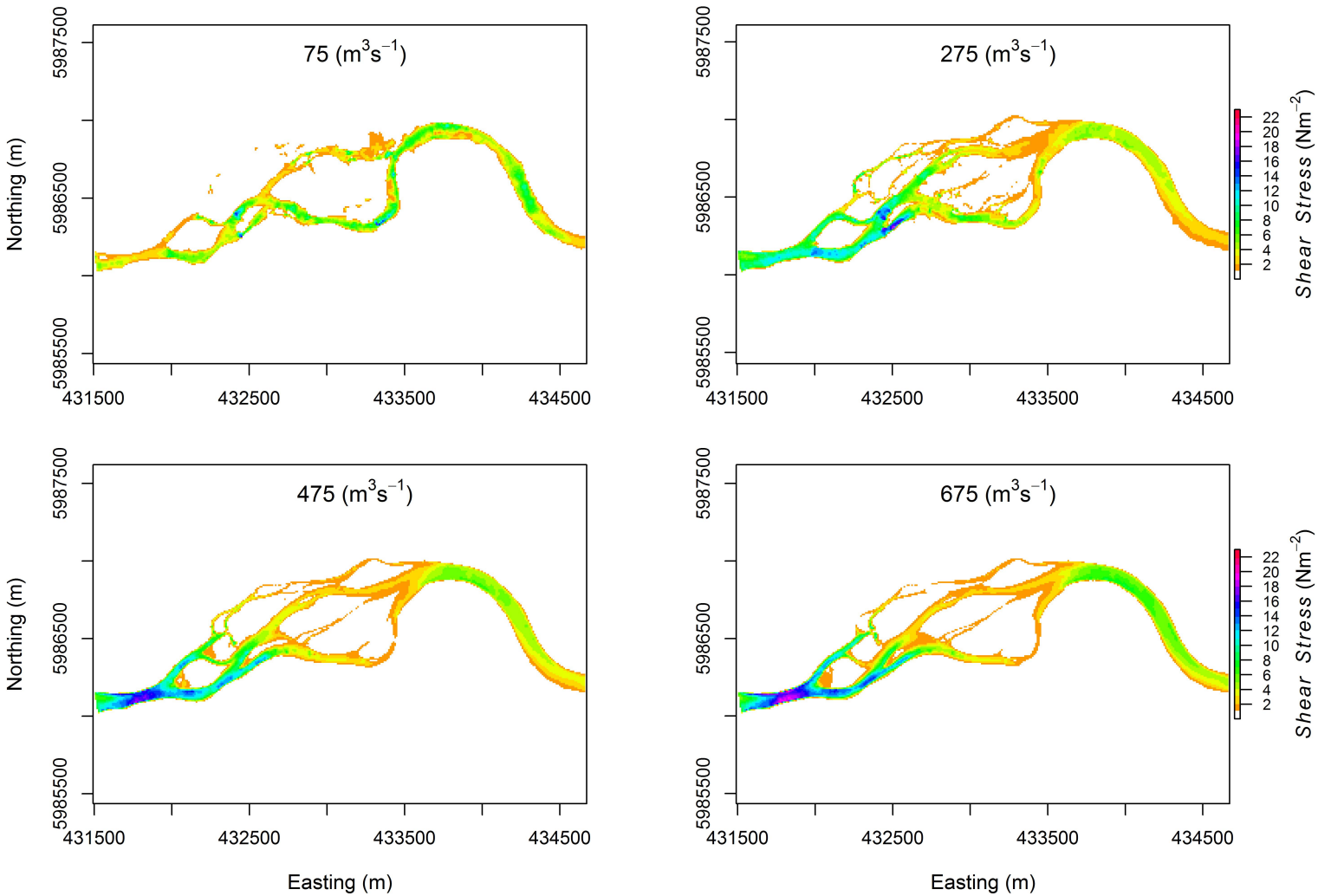

Figure 5.7: Reach-scale distribution of shear stress with increasing discharge; areas with shear stress less than 1 N/m^2 not shown (colored white).

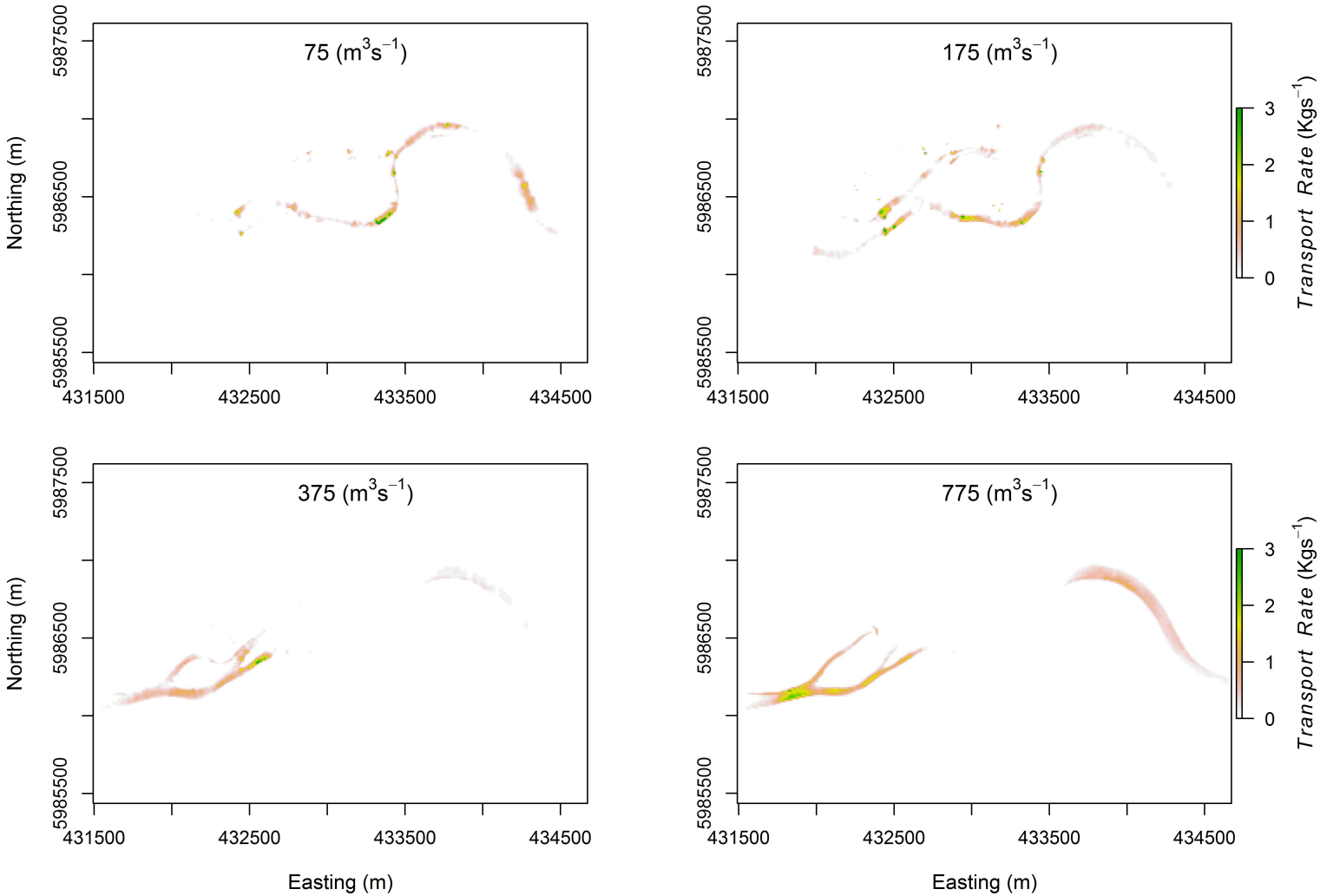

Figure 5.8: Reach-scale sediment transport capacity with increasing discharge.

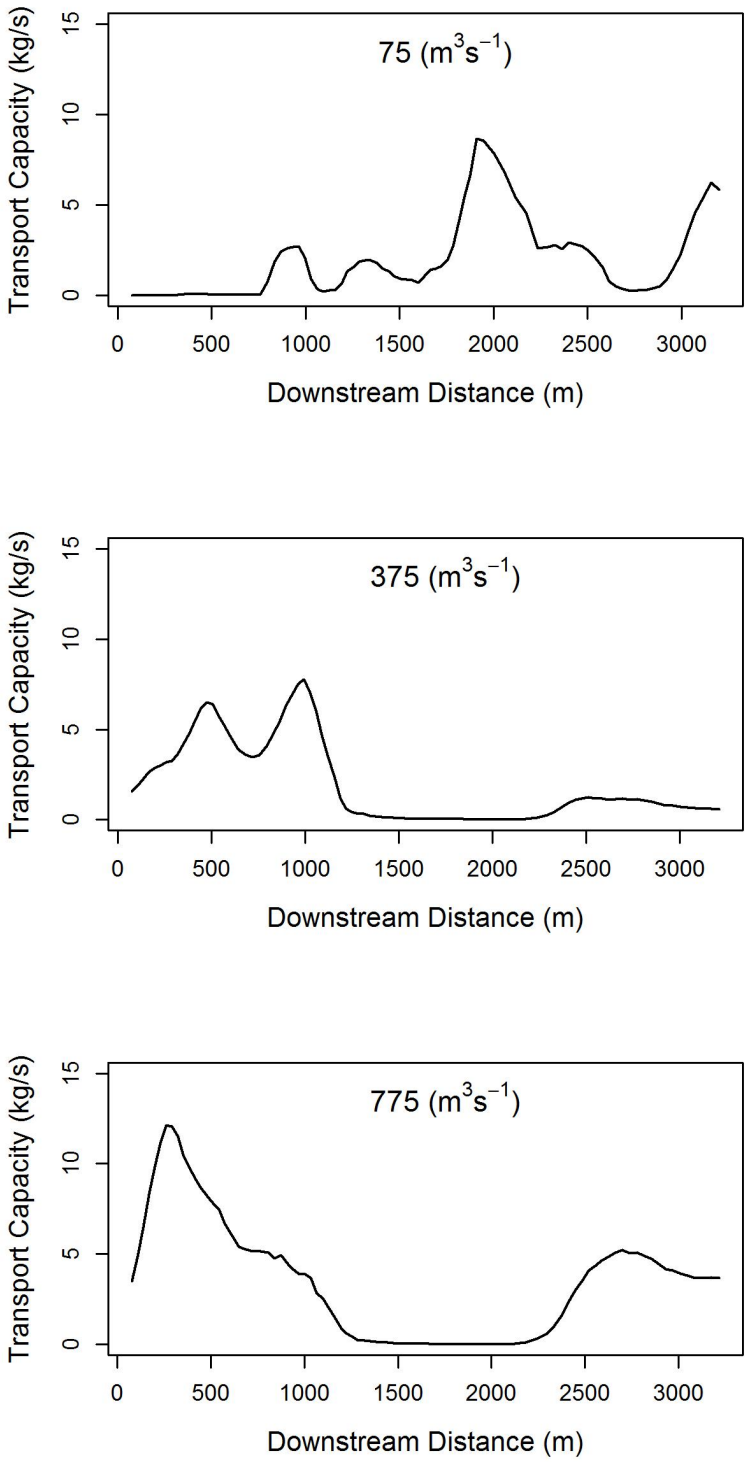

Figure 5.9: Total cross-channel transport capacity with increasing discharge.

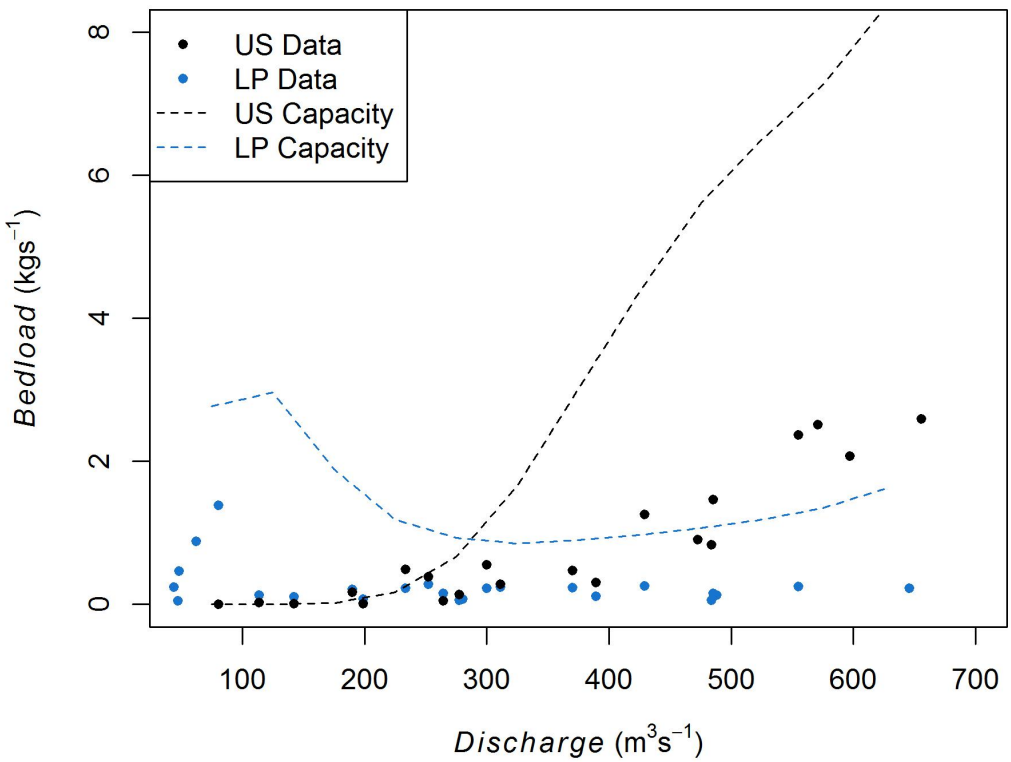

Figure 5.10: Calculated transport capacity and sampled bedload transport at the US and LP transects plotted as a function of discharge.

Chapter 6

Discussion

6.1 Variation in flow dynamics with discharge

Increasing discharge produces very different responses in hydraulic conditions depending on location within the spawning reach. Within the anabranching portion of the reach, shear stress increases with discharge from 45 m^3/s to approximately 325 m^3/s (Appendix G). The relatively uniform depths and rectangular channel geometries of the secondary channels (Appendix B) suggest that total wetted width increases rapidly once the water surface reaches a threshold elevation. Most secondary channels across the middle of the island complex have bed elevations that are 1.0-1.3 m higher than the thalweg elevation within the mainstem. This initial wetting stage produces an increase in the total surface area exposed to moderate shear stress without causing a major increase in shear stress within the mainstem despite higher flows (Table 5.2). Velocities within the mainstem channel near the island complex even decrease slightly once secondary channels become wetted due to the increase in total channel width (Figure 5.5).

As discharge begins to exceed 225-275 m^3/s, the Burrard Ave. Bridge reduces flow conveyance enough to cause backwatering. Backwatering decreasing the water surface slope progressively further upstream as discharge increases (Figure 5.6). The near-zero hydraulic gradient reaches the downstream extent of the island complex once flows reach 275 m^3/s, causing mainstem velocities to decrease abruptly by 39% from 1.18 m/s to 0.72 m/s (Figure 5.5). Backwatering further extends into the island complex as discharge increases from approximately 275 m^3/s to 525 m^3/s, resulting in decreased shear stresses (Figure 5.7).

Velocity (Table 4.1) and shear stress (Figure 5.7) over the downstream spawning pad remain higher than within the island complex during backwatered conditions. Higher velocities are maintained because the local hydraulic gradient increases with discharge immediately upstream of the bridge as backwatered flow passes through the constriction (Figure 5.6). The spatial distribution of shear stresses over the spawning pad remains relatively constant once discharge exceeds 325 m^3/s, as does the magnitude of shear stress, varying between 3 N/m^2 and 8 N/m^2. Shear stress at this location peaks at a flow of 125 m^3/s, reaching just over 8 N/m^2.

At the upstream extent of the study reach, velocity and shear stress are positively correlated with discharge. At this location, flow through the single-thread, parabolic-shaped channel is nearly uniform over a wide range of flows. Flow is described as nearly uniform because the hydraulic gradient through this section increases locally once discharge exceeds about 475 m^3/s, an effect caused by the relatively narrow channel slightly constricting high flows. This area is located far enough upstream from the bridge constriction that the water surface profile remains unaffected by backwater, even during the highest simulated discharge of 775 m^3/s.

Results from the hydrodynamic model suggest that flow downstream of the bridge is also non-uniform during periods of high discharge. When simulating a discharge of 525 m^3/s with uniform flow as the downstream boundary condition, the simulated WSE is 1.22 m lower than the measured elevation at the downstream extent of the model domain. Under these same conditions, the simulated WSE is 1.00 m lower than measured values at the WSC gauge located immediately downstream of the bridge. Though the model does not extend far enough downstream to simulate the origin of backwatering, a large meander downstream of the study area is suspected to be the cause. The uniform flow boundary condition is only valid for discharges below 125 m^3/s, confirmed by accurate prediction of WSE at the WSC gauge location.

Backwatering that occurs downstream of the Burrard Ave. Bridge raises the question of where fish may have spawned and what the hydrodynamics of the spawning reach were prior to bridge construction. Currently, as the fish swim toward the spawning reach during a high flow year, the first higher velocity zone they encounter is immediately downstream of the bridge where the local hydraulic gradient increases as backwater from upstream of the bridge flows through the constriction. Prior to bridge construction, however, this local increase in hydraulic gradient may have been less pronounced and the backwater originating downstream of the bridge could have extended upstream into the spawning reach. Under these conditions, combined with historic high flows, the first high velocity zone encountered by spawning fish would have been farther upstream within the spawning reach. Suitable egg and larval habitat may have been available at this upstream location, which likely had a coarse substrate and multiple gravel bars that were largely devoid of vegetation prior to flow regulation.

6.2 Characterization of bedload transport within the spawning reach

Spatial variation in the relation between discharge, hydraulic conditions and sediment availability influences bedload transport rates from upstream to downstream. The positive relationship between bedload transport and discharge at the US transect (Figure 4.6) suggests that occasional high flow years input a pulse of sediment into the spawning reach while moderate flow years input relatively minimal sediment; a finding that is consistent with previous data (NHC, 2014; NHC, 2015). The magnitude and timing of peak sediment transport into the reach corresponds with peak flow (Figure 4.7), which concurrently corresponds to the maximum backwatered extent and minimum transport capacity within the island complex (Figure

5.9). The increased sediment availability and decreased transport capacity mid-reach produces transport-limited conditions and results in sediment deposition, primarily within secondary channels that convey the most bedload (Figure 4.8). As the hydrograph recedes and velocity (Figure 5.5), shear stress (Figure 5.7) and transport capacity (Figure 5.8) increase within the downstream portion of the spawning reach, the sediment previously stored within secondary channels is transported downstream at relatively constant, moderate rates.

It is interesting that most of bedload transported into the reach from upstream is immediately routed into the first northern secondary channel, labelled *MU-A* in Figure 4.8. While the path of bedload transport is influenced by channel shape and may be directed along topographic lows (Habersack et al., 2008), the bed elevation at the entrance of the secondary channel is 0.3 m to 0.4 m higher than the thalweg elevation. Therefore, at this location, enough force is exerted on the bed to transport sediment along an upwards local channel slope of 0.9% into the smaller channel. Once the sediment has entered this channel it becomes further divided between secondary channels but remains largely within the northern half of the island complex (Figure 6.1).

The preferential routing of sediment into secondary channel MU-A is likely caused by the presence of strong secondary flow circulation near the bed. This type of flow circulation is intensified by upstream channel curvature and is responsible for generating the lateral sediment sorting observed around meanders. In addition, given that flow velocity past the secondary channel entrance is high, the observed sediment routing may occur due to a hydraulic effect produced at channel bifurcations where most of the flow entering a secondary channel comes from the near-bed region (Bulle, 1926). This effect is a result of the vertical velocity distribution of the flow, where low velocity flow in the near-bed region has less inertia than high velocity surface flow, causing a disproportionate amount of near-bed flow, and consequently sediment, to enter the secondary channel (Vasquez, 2005). Application of a three-dimensional flow and sediment transport model would be useful to fully resolve the local hydrodynamic patterns driving the flow-sediment separation at this location.

In addition to spatial components, a temporal component influences bedload transport rates within and downstream of the island complex. Sediment transport rates were high within the main secondary channel ML-B at the peak of the annual hydrograph (600-700 m^3/s) (Table 4.3), despite the low transport capacity at this location during high flows. This likely reflects the time needed for the sediment that was transported into the reach, past the US transect, to travel downstream to the ML-B transect.

Sediment transport within the ML-B channel then decreased as flows receded to 400-500 m^3/s and upstream sediment input decreased. However, a second period of high transport was observed later in the year on August 4th, during a discharge of 218 m^3/s. This second period of high sediment transport likely occurred as sediment deposits were re-mobilized by the locally increasing transport capacity associated with receding flows. The temporal lag between mid-reach deposition during high flow and sediment re-mobilization during low flow is reflected

by progressively increasing transport rates downstream of the island complex throughout the tailing end of the receding hydrograph (Figure 4.7).

Hysteresis in the discharge-bedload transport relation at the US transect (Figure 4.6) suggests the availability of bedload sediment within the active width of the channel became limited during the rising limb of the hydrograph. This may have occurred because the amount of sediment input from bank erosion during high flow was limited and confined to localized erosion of terrace scarps due to post-regulation vegetation encroachment and bank stabilization (Rood and Neill, 1987; NHC and McAdam, 2003a). Alternatively, the sediment that had been input to the Nechako River by its tributaries during the spring freshet may have become depleted.

Given the prolonged period of competent flow, sediment previously stored within the channel upstream of the spawning reach may have been transported considerable distances between depositional areas characterized by marked reductions in hydraulic gradient. This is supported by the composition of the bedload because coarse sand can be easily entrained and transported in saltation at high velocity, especially over a channel bed that has become armoured in response to flow regulation (Church, 1995). It is plausible that the supply of readily available sediment within the 35-45 km segment of river between the spawning reach and the next upstream depositional area (NHC, 2013) began to deplete after approximately 90 days of rising discharge (300 m^3/s exceeded 60% of the time). Data collected in 2014, when daily maximum discharge reached only 325 m^3/s, did not show any hysteresis and transport rates generally plotted along the rising limb trend of the 2015 hydrograph (NHC, 2016).

The grain size of the bedload did not significantly coarsen with increasing discharge or transport rate (Figure 4.5) and contained very little gravel large enough (>8 mm) to provide suitable larval habitat. The lack of a rapid increase in bedload grain size suggests that the bed armor around the US transect did not become mobile during peak flow. The only fully mobile size fraction (Wilcock and McArdell, 1993; Church and Hassan, 2002) at the US transect during high flow was 2 mm sand. The ratio between the proportion of 2 mm sand within the bedload to its proportion on the bed surface was over 7.5 for flows exceeding 597 m^3/s, indicating that upstream sediment sources are important in supplying bedload material. This ratio dropped to below 0.5 for the 2.8 mm size class and ranged between approximately 0.3 and 0.1 for all coarser grain size intervals. During peak flow in 2015, the mean shear velocity within the upstream area of the reach was sufficient to partially suspend grains finer than 1 mm, as indicated by a Rouse number [2] of 1.6, 1.9 and 2.8 for sediment sized 0.5 mm, 1.0 mm and 2.0 mm, respectively. Bedload transport at this location can therefore be characterized as sand overpassing a relatively coarse, largely static bed surface.

[2]The Rouse number is a non-dimensional number indicating the mode of sediment transport. It is expressed as the ratio of particle settling velocity to shear velocity multiplied by the von Karman constant.

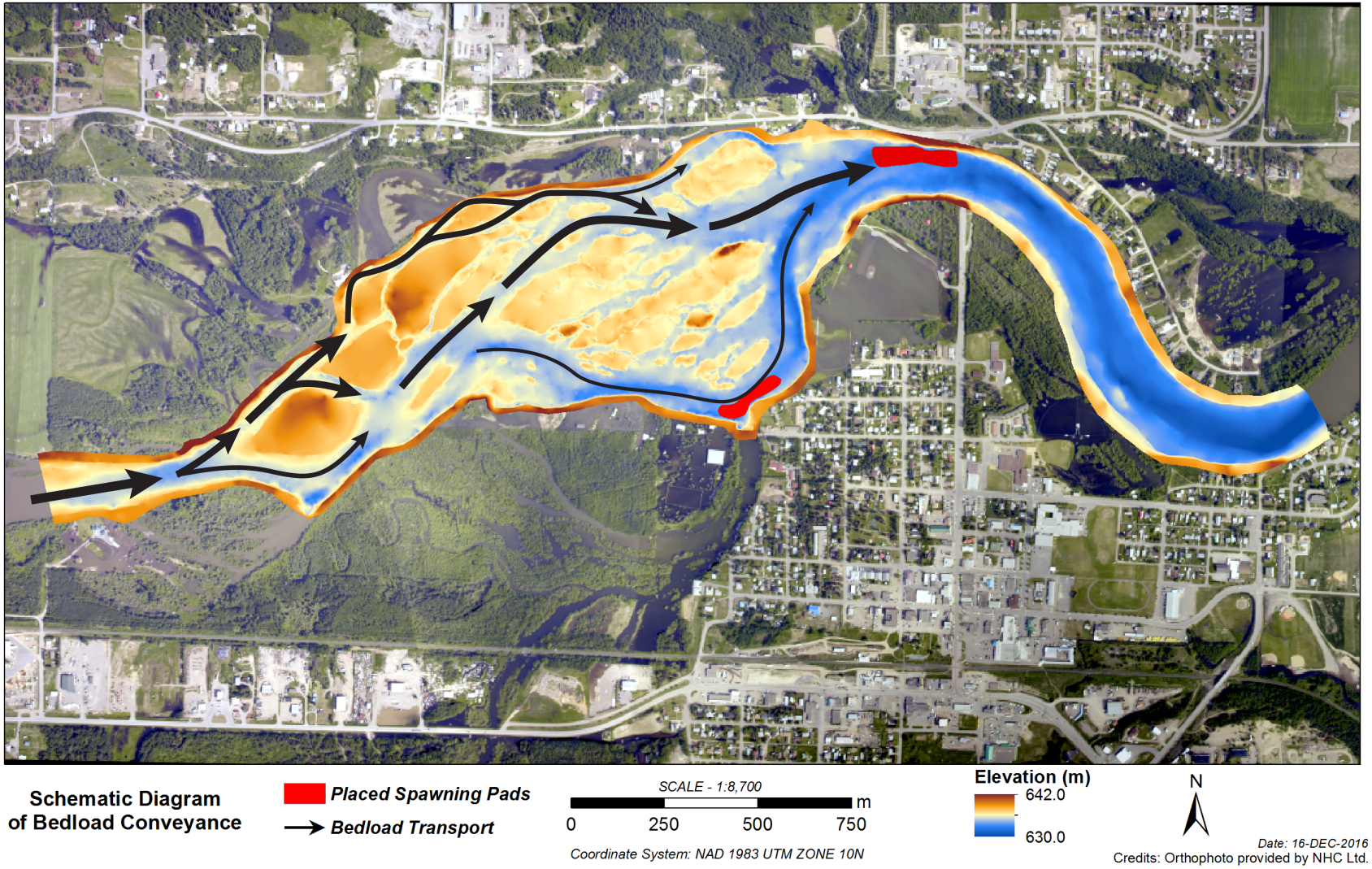

Figure 6.1: Schematic representation of bedload sediment transport through the spawning reach (arrow width represents magnitude of transport).

The mobility of coarse grains is limited by the low overall magnitude of shear stress within the reach. During the peak 2015 flow of 675 m^3/s, hydrodynamic simulations indicate that the highest shear stresses were 14-19 N/m^2. The spatially averaged mean shear stress within the upstream high velocity area was 12 N/m^2. Varying the Shields parameter from 0.06 to 0.03, the maximum mobile grain size would have been 14-39 mm, with a mobile grain size of 18-25 mm using the commonly applied Shields value of 0.047 for gravel. This traditional approach suggests that flow was not competent to mobilize the D_{50} (36 mm) grain size of the bed surface at the upstream location, which would have required a threshold shear stress of 27 N/m^2. By accounting for the reduction in critical shear stress associated with a 12% sand content of the substrate (Wilcock and Crowe, 2003), the D_{50} grain size would have been mobilized at a shear stress of 9 N/m^2. However, the higher estimate obtained using the traditional Shields approach is considered a better representation of the system because sand is overpassing a coarse, structured bed, rather than constituting a significant proportion of the surficial grain size distribution.

The morphology of the spawning reach, containing numerous mid-channel bars and low-elevation islands, reflects the depositional legacy of the area. Even prior to flow regulation, it was a threshold-type channel (using classification from Church, 2006) with infrequent, low-intensity sediment transport due to its very mild channel gradient and rapid expansion in total channel width. Although the amount of coarse substrate within the area has always been relatively limited due to low shear stress and the high proportion of fines contained within the surrounding glaciolacustrine sediment, gravel transport and deposition was likely more active during the pre-regulation era due to more extensive bank erosion upstream, increased mobilization of tributary fans and greater overall stream power within the Upper Nechako system. In addition, increased flow conveyance and floodplain storage prior to the construction of the Burrard Ave. Bridge may have maintained higher velocity flow within the mainstem channel. Thus, larval habitat within the spawning reach may have historically (i.e. prior to bridge construction and flow regulation) been maintained by freshet flows having sufficient stream power to mobilize the surface of unvegetated gravel deposits and spatially segregate coarse and fine sediment in flow convergence zones and around meander bends.

6.3 Implications for larval habitat and restoration

Backwatering and sediment deposition during high flow is discordant with the conceptual model of freshet-spawning sturgeon utilizing deep, high-velocity habitat over coarse heterogenous substrate devoid of fine sediment. Clearly, the functional relation between fluvial ecology and geomorphology has been altered, evidenced by recruitment failure since 1967 (McAdam et al., 2005). The reduction in stream power from the regulated flow regime is problematic for restoration objectives because it significantly limits the maximum mobile grain size. Even during a relatively high flow of 775 m^3/s, moderate shear stresses throughout the spawning reach suggest gravel substrates are rarely mobilized to release infilled fines. While the addition of coarse

substrate within the spawning area has been used as a restorative measure in the past (NWSRI, 2012), selecting an appropriate grain size and location to place the substrate is limited by the reduced competence of the river and by the active channel width conveying sand as bedload.

The development of backwater upstream of the Burrard Ave. Bridge poses another challenge to habitat restoration because flows exceeding 275-325 m^3/s do not significantly increase shear stress or transport capacity over the downstream spawning pad. Historically, increased floodplain storage and greater side-channel conveyance past the current bridge location may have maintained higher flow velocity and shear stress within the mainstem channel during larger pre-regulation flows. However, additional modelling is needed to test this hypothesis. Under the current dynamics, increasing discharge shifts areas with moderate transport capacity progressively upstream except for in the area immediately upstream of the bridge where hydraulic gradient increases with backwater. This upstream shift probably occurred historically as well due to backwater development downstream of the bridge location, but backwatering may have affected less of the spawning reach since the control was further downstream. Either way, the mid-reach deposition observed during high flow in 2015 is an issue because it becomes a significant source of sediment that supplies the relatively constant, moderate transport rates infilling the substrate at the downstream spawning location.

The current state of the Nechako system is the outcome of channel adjustment to nearly 65 years of imposed flow and sediment regimes. It is unlikely that historical fluvial dynamics can be restored on a large scale due to community flooding risk and to the underlying geomorphic change that has already occurred. Consequently, habitat restoration within the spawning reach is constrained by the present fluvial context. An effective restoration strategy will need to account for, and work with the present day sediment transport processes within the reach.

Site selection may benefit from the fact that a few secondary channels convey most of the bedload trough the anabranching reach with very little sediment being transported in the deeper mainstem channel. Areas that have a high flow to bedload conveyance ratio indicate locations that may be able to maintain a coarse substrate with minimal infilling. Consistency in the location of the active width within the mainstem channel also provides guidance regarding locations that are, or are not suitable for restorative measures like gravel addition. Substrate restoration may also benefit from the wide range of hydraulic conditions available within the reach during a given discharge and from the inversing relation between discharge and bedload transport from upstream to downstream. An appropriate design discharge may therefore be used to site restoration in locations that combine appropriate local hydraulics with a spatial avoidance of bedload transport.

6.4 Limitations

Sampling bedload transport must ideally account for the inherent variability of sediment transport rates that fluctuate through space and time (Gomez, 1991; Habersack et al., 2008). The intention of this study was to characterize geomorphic processes over the largest spatial and

temporal scales possible. Consequently, the number of sample replicates and the length of time during which each sample was collected were constrained. In this regard, the accuracy of bedload data presented herein is limited by relatively short sampling durations of 300 seconds per location. However, this was considered acceptable given the high sampling frequency throughout the study period. The selected sampling schedule generated robust data as indicated by the strong relation at the US transect location (Figure 4.6) and the agreement between predicted and observed rates (NHC, 2016).

A second limitation with collecting bedload data is sampling bias. Helley-Smith samplers can over- or under-sample different size fractions depending on the ratio between the size of the maximum mobile grain and the opening of the sampler. Sampling efficiency greatly decreases for ratios above 0.1 (Sterling and Church, 2002) to 0.2 (Emmett, 1980). The largest three clasts collected in 2015 were 45 mm, sampled at the US transect during peak flow. To reduce bias during this period (Vericat et al., 2006), a sampler with a 203.2 mm opening was used, translating to a ratio of 0.22. More commonly, however, the maximum mobile grain size within the reach was 11.2 mm and was collected with a 76.2 mm opening sampler corresponding to a ratio of 0.15. This suggests that coarse bedload was likely underrepresented in the samples and that sediment finer than medium sand may have been overrepresented due to the collection of suspended material (Sterling and Church, 2002). Additional bias may have occurred due to tilting and perching of the sampler on coarse substrate (Vericat et al., 2006), especially while sampling on the downstream spawning pad.

Numerical modelling requires the explicit specification of several, often unknown, parameters that can contribute to errors or biases. For example, channel roughness affects modelled shear stress both directly through its calculation and indirectly through its influence on flow velocity (Lane et al., 1999). In this study, the lack of recent WSE data collected over different flows prevented any assessment of how the influence of boundary roughness changes with discharge. Consequently, a single roughness value calibrated to the water surface at 525 m^3/s was used for all simulations. Although this method unrealistically assumes roughness does not spatially and temporally change with discharge, it does increase the comparability of model output between different flows and reduces the effect that varying roughness has on estimated shear stress. Use of a single roughness value was also considered acceptable due to the hydraulic smoothness of the channel and to the low grain size to depth ratio, or relative roughness, for most flows.

Additional error can result from the spatial interpolation required to generate input data over the entire model domain (Pasternack et al., 2006). To produce the reach-scale DEM, interpretation and manual digitization of the thalweg was required in several locations due to channel complexity and spacing interval between bathymetry transects. Significant interpolation was also necessary to specify the grain size distribution and sand content of the bed surface using 30 underwater images collected at six locations. The photo-sieving method itself was limited by water turbidity, image resolution (1.76 pixels per 1.0 mm) and the area of substrate covered per image (627.3 cm^2).

Other limitations in this study stem from the difficulty in capturing the influence of bedforms on local hydrodynamics and sediment transport rates. Bedform migration limits the accuracy of bedload sampling because of the temporal variation in sediment transport that occurs as ripples, sand sheets and dunes travel downstream. The development of bedforms is also an issue for modelling because it introduces greater form drag within the channel that could result in slower than average flows in some locations, and faster than average flows in others. Lastly, the influence of bedforms on transport capacity is not captured by sediment transport functions. Given the large proportion of sand within the island complex, these limitation may be of particular relevance within secondary channels and within the downstream portion of the study reach.

Finally, the analysis related to sediment transport capacity was limited by several key factors. Firstly, the modelled shear stress that was used to calculate the capacity represented the total shear stress, rather than the skin drag. The skin drag is the proportion of the total shear stress responsible for grain mobility, which is the proportion that should be applied in sediment transport functions. Secondly, the sparseness of data on substrate composition throughout the reach significantly limited the accuracy of capacity estimates because the Wilcock and Crowe (2003) transport function is strongly influenced by the grain size distribution of the bed surface. The estimated transport capacity in this study is intended as a reference to identify downstream trends, rather than as a predictive value, due to the combination of these limiting factors.

Chapter 7

Conclusion

Flow regulation has altered the fluvial processes that link flow and sediment transport to ecological integrity within the Nechako River. Geomorphic change within a critical white sturgeon spawning reach has decreased the quality and availability of early rearing habitat. Efforts to restore the habitat continue to be negatively impacted by progressive sedimentation of the restored spawning substrate. This study, conducted within the framework of the Nechako White Sturgeon Recovery Initiative, was intended to advance our understanding of reach-scale fluvial dynamics to contribute to the knowledge base supporting future habitat restoration design.

High flows in 2015 presented an opportunity to sample bedload sediment transport over the course of the flood hydrograph. Results from bedload sampling indicate that the rate at which sediment was transported into the reach past the upstream-most sampling transect was positively correlated with discharge. This relation was non-linear and transport rates increased rapidly once flows exceeded about 400 m^3/s. Data collected at this location also showed hysteresis in the transport rates, suggesting the availability of bedload sediment within the channel upstream of the US transect became limited during the period of high flow.

The relation between discharge and bedload transport weakened with downstream distance until no relation was observed at the LP transect. The timing of maximum sediment transport past each sampling location also had a downstream trend, where peak sediment transport occurred progressively later throughout the year from upstream to downstream. Maximum sediment transport past the LP transect occurred during a discharge of 81 m^3/s at the tailing end of the receding hydrograph limb in late August. However, the maximum transport rates within the downstream portion of the reach remained low and relatively constant compared to those sampled upstream.

Sediment was primarily transported through the island complex by a subset of secondary channels with only a minimal amount of bedload transported by the mainstem channel. These active secondary channels conveyed disproportionately large amounts of sediment compared to flow. Upstream and downstream of the anastomosed reach, where the channel has a single-thread morphology, the cross-channel location having the highest transport rates remained spatially consistent throughout the year. Bedload was conveyed past the US and LP transects

within a 50-m portion of the total channel width and the highest transport rates generally occurred within a 20-m subsection near the left bank.

Results from hydrodynamic modelling used to supplement data analysis indicate that flow through the spawning reach becomes non-uniform once discharge exceeds 225-275 m^3/s. The non-uniform water surface profile develops upstream of the Burrard Ave. Bridge because the bridge sufficiently constricts the channel to reduce conveyance of moderate to high flows. Velocity, shear stress and transport capacity within the downstream portion of the spawning reach do not increase with discharge due to this backwater effect and to the rapid expansion in total channel width that occurs once secondary channels become wetted. Rather, the areas of maximum shear stress and transport capacity shift from mid-reach to upstream locations with increasing discharge. Over the range of simulated flows, however, the magnitude of maximum shear stress within the reach remained below 23 N/m^2.

This study identified several challenges for successful habitat restoration posed by the current fluvial dynamics within the spawning reach. Firstly, the development of backwater is problematic because high flows do not increase velocity or shear stress within the downstream portion of the reach. Given that discharge and sediment transport are positively correlated upstream, high flow years including 2015 can input a large amount of sediment that becomes deposited mid-reach due to the drop in shear stress and transport capacity caused by the backwater. The deposited sediment is then available to be moved at a constant, relatively moderate bedload transport rate over the downstream spawning pad. The low magnitude of shear stresses within the reach is also problematic because it does not get high enough to move coarse particles and coarse grain mobility is a key mechanism needed to release infilled fines from interstitial voids. Low stream competence is an issue for restorative measures like gravel addition because it constrains the size of placed substrate to a relatively narrow range and makes the substrate prone to infilling.

Although it is unlikely that historical fluvial dynamics can be restored on a large scale, it may be possible to locally improve the quality of sturgeon habitat within the Nechako critical spawning reach by optimizing restoration design based on advantageous fluvial and sedimentological dynamics. Site selection may benefit from the disproportionate amount of flow and sediment conveyed through different channels and from the spatially consistent locations with highest transport. Site selection may also take advantage of the wide range of hydraulic conditions available within the reach during a given flow and of the contrasting relations between bedload transport, velocity and discharge from upstream to downstream. Successful restoration of larval habitat will likely result from siting locations that avoid preferential pathways of sediment transport while maintaining appropriate local hydrodynamics during the design discharge.

Bibliography

Ashmore, P. Channel morphology and bed load pulses in braided, gravel-bed streams. *Geografiska Annaler. Series A. Physical Geography*, pages 37–52, 1991. → pages 2

Ashmore, P. and Parker, G. Confluence scour in coarse braided streams. *Water Resources Research*, 19(2):392, 1983. → pages 3

Ashmore, P., Bertoldi, W., and Tobias Gardner, J. Active width of gravel-bed braided rivers. *Earth Surface Processes and Landforms*, 36(11):1510–1521, 2011. → pages 3, 4

Bennett, W., Edmondson, G., Williamson, K., and Gelley, J. An investigation of the substrate preference of white sturgeon (Acipenser transmontanus) eleutheroembryos. *Journal of Applied Ichthyology*, 23(5):539–542, 2007. → pages 2

Bertoldi, W., Zanoni, L., and Tubino, M. Assessment of morphological changes induced by flow and flood pulses in a gravel bed braided river: The Tagliamento River (Italy). *Geomorphology*, 114(3):348–360, 2010. → pages 4

Beschta, R. L. and Jackson, W. L. The intrusion of fine sediments into a stable gravel bed. *Journal of the Fisheries Board of Canada*, 36(2):204–210, 1979. → pages 3

Best, J. L. Sediment transport and bed morphology at river channel confluences. *Sedimentology*, 35(3):481–498, 1988. → pages 3

Biron, P., Carver, R., and Carre, D. Sediment transport and flow dynamics around a restored pool in a fish habitat rehabilitation project: Field and 3D numerical modelling experiments. *River Research and Applications*, 28(7):926–939, 2012. → pages 5

Boavida, I., Santos, J., Katopodis, C., Ferreira, M., and Pinheiro, A. Uncertainty in predicting the fish-response to two-dimensional habitat modeling using field data. *River Research and Applications*, 29(9):1164–1174, 2013. → pages 5

Brown, R. A. and Pasternack, G. B. Comparison of methods for analysing salmon habitat rehabilitation designs for regulated rivers. *River Research and Applications*, 25(6):745–772, 2009. → pages 5

Buffington, J. M. and Montgomery, D. R. Effects of sediment supply on surface textures of gravel-bed rivers. *Water Resources Research*, 35(11):3523–3530, 1999. → pages 2

Bulle, H. Untersuchungen uber die Geschiebeableitung bei der Spaltung von Wasserlaufen. *VDI Verlag, Berlin*, 1926. → pages 47

Church, M. Geomorphic response to river flow regulation: Case studies and time-scales. *Regulated Rivers: Research & Management*, 11(1):3–22, 1995. → pages 1, 3, 48

Church, M. Bed material transport and the morphology of alluvial river channels. *Annu. Rev. Earth Planet. Sci.*, 34:325–354, 2006. → pages 50

Church, M. and Hassan, M. A. Mobility of bed material in Harris Creek. *Water Resources Research*, 38(11), 2002. → pages 3, 48

Coutant, C. C. A riparian habitat hypothesis for successful reproduction of white sturgeon. *Reviews in Fisheries Science*, 2010. → pages 2

Crossman, J. and Hildebrand, L. Evaluation of spawning substrate enhancement for white sturgeon in a regulated river: Effects on larval retention and dispersal. *River Research and Applications*, 30(1):1–10, 2014. → pages 1, 4

Crowder, D. and Diplas, P. Using two-dimensional hydrodynamic models at scales of ecological importance. *Journal of hydrology*, 230(3):172–191, 2000. → pages 5, 156

DFO. Recovery strategy for white sturgeon (Acipenser transmontanus) in Canada [Final]. *Species at Risk Act Recovery Strategy Series*, pages 1–252, 2014. → pages 1, 4

Dietrich, W. E. and Smith, J. D. Bed load transport in a river meander. *Water Resources Research*, 20(10):1355–1380, 1984. → pages 3

Dietrich, W. E. and Whiting, P. Boundary shear stress and sediment transport in river meanders of sand and gravel. *River meandering*, pages 1–50, 1989. → pages 3

Dumont, P., DAmours, J., Thibodeau, S., Dubuc, N., Verdon, R., Garceau, S., Bilodeau, P., Mailhot, Y., and Fortin, R. Effects of the development of a newly created spawning ground in the Des Prairies River (Quebec, Canada) on the reproductive success of lake sturgeon (Acipenser fulvescens). *Journal of Applied Ichthyology*, 27(2):394–404, 2011. → pages 4

Eaton, B. and Lapointe, M. Effects of large floods on sediment transport and reach morphology in the cobble-bed sainte marguerite river. *Geomorphology*, 40(3):291–309, 2001. → pages 2

Emmett, W. W. A field calibration of the sediment-trapping characteristics of the Helley-Smith bed-load sampler. Technical report, US Govt. Print. Off. (No. 1139), 1980. → pages 52

Fissel, D. B. and Jiang, J. 3D numerical modeling of flows at the confluence of the Columbia and Pend d'Oreille rivers. In *Estuarine and Coastal Modeling: proceedings of the eighth international conference*, pages 928–941, 2008. → pages 4, 6

Gard, M. Comparison of spawning habitat predictions of PHABSIM and RIVER2D models. *International Journal of River Basin Management*, 7(1):55–71, 2009. → pages 5

Gendron, M., Lafrance, P., and Lahaye, M. Assessment of spawning activity on the man-made spawning ground downstream from the Beauharnois Power Dam. Technical report, Environnement Illimit Inc. prepared for Hydro-Qubec, Division Production, 2002. → pages 4, 5

Gibson, S., Abraham, D., Heath, R., and Schoellhamer, D. Vertical gradational variability of fines deposited in a gravel framework. *Sedimentology*, 56(3):661–676, 2009. → pages 3

Golder. White sturgeon spawning at Waneta, 2005 investigations. Technical report, Golder Associates Ltd. prepared for Teck Cominco Metals and BC Hydro (No. 05-1480-030F), 2006. → pages 4, 6

Gomez, B. Bedload transport. *Earth-Science Reviews*, 31(2):89–132, 1991. → pages 3, 51

Grant, G. E., Schmidt, J. C., and Lewis, S. L. A geological framework for interpreting downstream effects of dams on rivers. *A peculiar river*, pages 203–219, 2003. → pages 1

Greig, S., Sear, D., and Carling, P. The impact of fine sediment accumulation on the survival of incubating salmon progeny: implications for sediment management. *Science of the total environment*, 344(1):241–258, 2005. → pages 2

Habersack, H., Seitz, H., and Laronne, J. B. Spatio-temporal variability of bedload transport rate: Analysis and 2D modelling approach. *Geodinamica Acta*, 21(1-2):67–79, 2008. → pages 3, 47, 51

Hassan, M. A. and Church, M. Experiments on surface structure and partial sediment transport on a gravel bed. *Water Resources Research*, 36(7):1885–1895, 2000. → pages 2

Hassan, M. A., Egozi, R., and Parker, G. Experiments on the effect of hydrograph characteristics on vertical grain sorting in gravel bed rivers. *Water Resources Research*, 42 (9), 2006. → pages 2, 3

Hassan, M. A., Smith, B. J., Hogan, D. L., Luzi, D. S., Zimmermann, A. E., and Eaton, B. C. 18 Sediment storage and transport in coarse bed streams: scale considerations. *Developments in Earth Surface Processes*, 11:473–496, 2007. → pages 2

Hatfield, T., Coopper, T., and McAdam, S. *Scientific information in support of identifying critical habitat for SARA listed white sturgeon populations in Canada: Nechako, Columbia, Kootenay and Upper Fraser (2009).* Fisheries and Oceans Canada, Science Branch, 2013. → pages 2

Hildebrand, L., McLeod, C., and McKenzie, S. Status and management of white sturgeon in the Columbia River in British Columbia, Canada: An overview. *Journal of Applied Ichthyology*, 15(4-5):164–172, 1999. → pages 2

Hildebrand, L., Drauch Schreier, A., Lepla, K., McAdam, S., McLellan, J., Parsley, M., Paragamian, V., and Young, S. Status of white sturgeon (acipenser transmontanus richardson, 1863) throughout the species range, threats to survival, and prognosis for the future. *Journal of Applied Ichthyology*, 32(S1):261–312, 2016. → pages 1, 2

Hoey, T. Temporal variations in bedload transport rates and sediment storage in gravel-bed rivers. *Progress in physical geography*, 16(3):319–338, 1992. → pages 2

Johnson, J., LaPan, S., Klindt, R., and Schiavone, A. Lake sturgeon spawning on artificial habitat in the St Lawrence River. *Journal of Applied Ichthyology*, 22(6):465–470, 2006. → pages 1, 5

Kerr, S. J., Davison, M. J., and Funnell, E. *A review of lake sturgeon habitat requirements and strategies to protect and enhance sturgeon habitat.* Ontario Ministry of Natural Resources, 2011. → pages 4, 5

Kock, T. J., Congleton, J. L., and Anders, P. J. Effects of sediment cover on survival and development of white sturgeon embryos. *North American Journal of Fisheries Management*, 26(1):134–141, 2006. → pages 2

KTOI. *Kootenai River habitat restoration project master plan: A conceptual feasibility analysis and design framework*. Kootenai Tribe of Idaho, Bonners Ferry, ID, 2009. → pages 1, 4, 5

LaHaye, M., Branchaud, A., Gendron, M., Verdon, R., and Fortin, R. Reproduction, early life history, and characteristics of the spawning grounds of the lake sturgeon (Acipenser fulvescens) in Des Prairies and L'Assomption rivers, near Montreal, Quebec. *Canadian Journal of Zoology*, 70(9):1681–1689, 1992. → pages 4

Lane, S., Bradbrook, K., Richards, K., Biron, P., and Roy, A. The application of computational fluid dynamics to natural river channels: Three-dimensional versus two-dimensional approaches. *Geomorphology*, 29(1):1–20, 1999. → pages 5, 6, 52

Lapointe, M., Eaton, B., Driscoll, S., and Latulippe, C. Modelling the probability of salmonid egg pocket scour due to floods. *Canadian Journal of Fisheries and Aquatic Sciences*, 57(6): 1120–1130, 2000. → pages 2

Lisle, T. E. Sediment transport and resulting deposition in spawning gravels, north coastal California. *Water resources research*, 25(6):1303–1319, 1989. → pages 2, 3

Lisle, T. E., Nelson, J. M., Pitlick, J., Madej, M. A., and Barkett, B. L. Variability of bed mobility in natural, gravel-bed channels and adjustments to sediment load at local and reach scales. *Water Resources Research*, 36(12):3743–3755, 2000. → pages 3

Logan, B., McDonald, R., Nelson, J., Kinzel, P., and Barton, G. Use of multidimensional modeling to evaluate a channel restoration design for the Kootenai River, 2011. → pages 6

Lytle, D. A. and Poff, N. L. Adaptation to natural flow regimes. *Trends in ecology & evolution*, 19(2):94–100, 2004. → pages 1

McAdam, D. S. O. Retrospective weight-of-evidence analysis identifies substrate change as the apparent cause of recruitment failure in the upper Columbia River white sturgeon (Acipenser transmontanus). *Canadian Journal of Fisheries and Aquatic Sciences*, 72(8): 1208–1220, 2015. → pages 2, 4, 6

McAdam, S. O. Effects of substrate condition on habitat use and survival by white sturgeon (Acipenser transmontanus) larvae and potential implications for recruitment. *Canadian Journal of Fisheries and Aquatic Sciences*, 68(5):812–822, 2011. → pages 1, 2

McAdam, S. O., Walters, C. J., and Nistor, C. Linkages between white sturgeon recruitment and altered bed substrates in the Nechako River, Canada. *Transactions of the American Fisheries Society*, 134(6):1448–1456, 2005. → pages 1, 2, 4, 50

McDonald, R., Nelson, J., Paragamian, V., and Barton, G. Modeling the effect of flow and sediment transport on white sturgeon spawning habitat in the Kootenai River, Idaho. *Journal of Hydraulic Engineering*, 136(12):1077–1092, 2010. → pages 3, 4, 5, 6

Nanson, G. C. and Knighton, A. D. Anabranching rivers: Their cause, character and classification. *Earth surface processes and landforms*, 21(3):217–239, 1996. → pages 8

NHC. Preliminary substrate investigation: Nechako River at Vanderhoof. Technical report, NHC Ltd. prepared for BC Ministry of Environment (No. 34203), 2006. → pages 9, 37

NHC. Nechako River at Vanderhoof hydrodynamic model upgrade: Final Report. Technical report, NHC Ltd. prepared for BC Ministry of Environment (No. 34623), 2008. → pages 6, 37

NHC. Nechako sturgeon spawning gravel september: 2011 substrate assessment. Technical report, NHC Ltd. prepared for Ministry of Forests, Lands and Natural Resource Operations, 2012. → pages 1, 4, 5, 9, 10

NHC. Nechako sturgeon spawning gravel: September 2012 substrate assessment. Technical report, NHC Ltd. prepared for Ministry of Forests, Lands and Natural Resource Operations, 2013. → pages 9, 48

NHC. Nechako River 2013 sediment transport investigations. Technical report, NHC Ltd. prepared for Ministry of Forests, Lands and Natural Resource Operations, 2014. → pages 7, 9, 10, 46, 101, 151

NHC. 2014 sediment transport investigation on the Vanderhoof reach of the Nechako River. Technical report, NHC Ltd. prepared for Ministry of Forests, Lands and Natural Resource Operations, 2015. → pages 7, 10, 14, 46, 101, 151

NHC. 2015 sediment transport investigation on the Vanderhoof reach of the Nechako River. Technical report, NHC Ltd. prepared for Ministry of Forests, Lands and Natural Resource Operations, 2016. → pages 10, 14, 48, 52, 151

NHC and McAdam, S. Nechako River geomorphic assessment Phase I: Historical analysis of Lower Nechako River. Technical report, NHC Ltd. prepared for BC Ministry of Water, Land and Air Protection, 2003a. → pages 9, 10, 48

NHC and McAdam, S. Nechako River geomorphic assessment Phase II: Detailed analyses of potential white sturgeon habitat sites. Technical report, NHC Ltd. prepared for BC Ministry of Water, Land and Air Protection, 2003b. → pages 10

Nicholas, A., Ashworth, P., Kirkby, M., Macklin, M., and Murray, T. Sediment slugs: Large-scale fluctuations in fluvial sediment transport rates and storage volumes. *Progress in Physical Geography*, 19(4):500–519, 1995. → pages 2

NWSRI. Nechako White Sturgeon Recovery Initiative 2011-2012 Annual Report. *Accessed from http://nechakowhitesturgeon.org*, 2012. → pages 1, 4, 10, 51

Paragamian, V. Kootenai River white sturgeon: Synthesis of two decades of research. *Endangered Species Research*, 17(2):157–167, 2012. → pages 2

Paragamian, V., McDonald, R., Nelson, G. J., and Barton, G. Kootenai River velocities, depth, and white sturgeon spawning site selection-a mystery unraveled? *Journal of Applied Ichthyology*, 25(6):640–646, 2009. → pages 2, 4

Parsley, M. J. and Beckman, L. G. White sturgeon spawning and rearing habitat in the lower Columbia River. *North American Journal of Fisheries Management*, 14(4):812–827, 1994. → pages 2

Pasternack, G. B., Wang, C. L., and Merz, J. E. Application of a 2D hydrodynamic model to design of reach-scale spawning gravel replenishment on the Mokelumne River, California. *River Research and Applications*, 20(2):205–225, 2004. → pages 5, 156

Pasternack, G. B., Gilbert, A. T., Wheaton, J. M., and Buckland, E. M. Error propagation for velocity and shear stress prediction using 2D models for environmental management. *Journal of Hydrology*, 328(1):227–241, 2006. → pages 5, 52, 156

Perrin, C. J., Rempel, L. L., and Rosenau, M. L. White sturgeon spawning habitat in an unregulated river: Fraser River, Canada. *Transactions of the American Fisheries Society*, 132(1):154–165, 2003. → pages 2, 4

Plouffe, A. and Levson, V. Late Quaternary glacial and interglacial environments of the Nechako River-Cheslatta Lake area, central British Columbia. *Canadian Journal of Earth Sciences*, 38(4):719–731, 2001. → pages 9

Powell, D. M. Patterns and processes of sediment sorting in gravel-bed rivers. *Progress in Physical Geography*, 22(1):1–32, 1998. → pages 3

Rhoads, B. L. and Kenworthy, S. T. Flow structure at an asymmetrical stream confluence. *Geomorphology*, 11(4):273–293, 1995. → pages 3

Rood, K. Nechako River substrate quality and composition. Technical report, Nechako Fisheries Conservation Program (No. M89-7), 1998. → pages 10

Rood, K. Identification and ranking of sources contributing sediment to the upper Nechako River. Technical report, Nechako Fisheries Conservation Program (No. RM89-7), 1999. → pages 9, 10

Rood, K. and Neill, C. A study of some aspects of the geomorphology of the Nechako River. Technical report, Reid Crowther and Partners Ltd and NHC Ltd. prepared for Fisheries and Oceans Canada, 1987. → pages 9, 48

Roy, A. and Bergeron, N. Flow and particle paths at a natural river confluence with coarse bed material. *Geomorphology*, 3(2):99–112, 1990. → pages 3

Shen, Y. and Diplas, P. Application of two-and three-dimensional computational fluid dynamics models to complex ecological stream flows. *Journal of Hydrology*, 348(1):195–214, 2008. → pages 5, 6

Sterling, S. M. and Church, M. Sediment trapping characteristics of a pit trap and the Helley-Smith sampler in a cobble gravel bed river. *Water Resources Research*, 38(8), 2002. → pages 52

Trencia, G. and Collin, P.-Y. Rapport d'aménagement d'une frayère pour le poisson à la Rivière Chaudière. *Ministère des Ressources Naturelles et de la Faune, Direction de l'aménagement de la faune Chaudière-Appalaches, Charny, Québec*, 2006. → pages 4

Vasquez, J. Two-dimensional numerical simulation of flow diversions. In *17th Canadian Hydrotechnical Conference: Hydrotechnical Engineering: Cornerstone Of A Sustainable Environment, Edmonton, Alberta*, 2005. → pages 47

Vericat, D., Church, M., and Batalla, R. J. Bed load bias: Comparison of measurements obtained using two (76 and 152 mm) Helley-Smith samplers in a gravel bed river. *Water Resources Research*, 42(1), 2006. → pages 15, 52

Wheaton, J. M., Pasternack, G. B., and Merz, J. E. Spawning habitat rehabilitation-I. Conceptual approach and methods. *International Journal of River Basin Management*, 2 (1):3–20, 2004a. → pages 5, 6

Wheaton, J. M., Pasternack, G. B., and Merz, J. E. Spawning habitat rehabilitation-II. Using hypothesis development and testing in design, Mokelumne River, California, USA. *International Journal of River Basin Management*, 2(1):21–37, 2004b. → pages 5

Wilcock, P. R. and Crowe, J. C. Surface-based transport model for mixed-size sediment. *Journal of Hydraulic Engineering*, 129(2):120–128, 2003. → pages 33, 50, 53, 136

Wilcock, P. R. and McArdell, B. W. Surface-based fractional transport rates: Mobilization thresholds and partial transport of a sand-gravel sediment. *Water Resources Research*, 29 (4):1297–1312, 1993. → pages 48

Winemiller, K. O. Life history strategies, population regulation, and implications for fisheries management. *Canadian Journal of Fisheries and Aquatic Sciences*, 62(4):872–885, 2005. → pages 1, 2

Zimmermann, A. E. and Lapointe, M. Intergranular flow velocity through salmonid redds: sensitivity to fines infiltration from low intensity sediment transport events. *River Research and Applications*, 21(8):865–881, 2005. → pages 2

Appendix A

Real-Time Kinematic (RTK) Survey on the Nechako River

A.1 Methods

*This section provides supplementary information to section **3.1 Bathymetry, topography and water surface elevation** in the thesis; previously described aspects have been omitted.*

A.1.1 Configurations

Table A.1: Configurations used for RTK surveying.

Parameter	Selected Configuration
Datum	NAD83 (Canadian Spatial Reference System)
Version (Epoch)	V4.0.0 (2002.0)
Geoid	HTv2.0
Coordinate system	UTM 10 N
Survey style	RTK Fixed (resolved ambiguity)
Base RTK initialization	Known Point (Keyed In)
Rover RTK initialization	On-The-Fly
Establishing control	Static Point observation off GCM
SNR mask	7
Elevation mask	10 degrees
Logging interval - Control point	600 second (Control)
Logging interval - Topographic point	10 second (TOPO)
Logging interval - Survey point	3 second (Fast-Static)

A.1.2 Data collection

Geodetic Control Monument (GCM) 653659, accessed through MASCOT government database, was located approximately 8 km southeast of the spawning reach. This benchmark was therefore

used to position a spike on the property of the Nechako White Sturgeon Conservation Center (NWSCI) using a 600-second Control Point logging interval (Figure A.1). This spike remained fixed in the ground for the duration of the survey, allowing for rapid and precise reinstallation of the base-station (Figure A.2).

Channel bathymetry was surveyed between May 12-15th, 2015, a period during which discharge increased from 510 m^3/s to 533 m^3/s. Two longitudinal profiles of bed and water surface elevation were collected on May 14th at a discharge of 523 m^3/s; one within the mainstem and the other within a secondary channel to the north. Figure A.3 shows the installation used to conduct the survey, with the RTK GPS received mounted on top of the survey-grade Sonar-Mite echo sounder. Banklines and bar topographies were surveyed on foot from August 25th to September 6th, 2015, during a discharge of 64 m^3/s to 118 m^3/s (Figure A.4). These surveys were done during low flow to mesh the topographic and bathymetric data and delineate shapefiles for bottom-of-bank (BOB), top-of-bank (TOB) and bar contours, which were submerged at high flow. Overall, 64,594 points were surveyed, consisting of 83 bar elevation points, 3,042 bank elevations points and 61,469 bed elevation points.

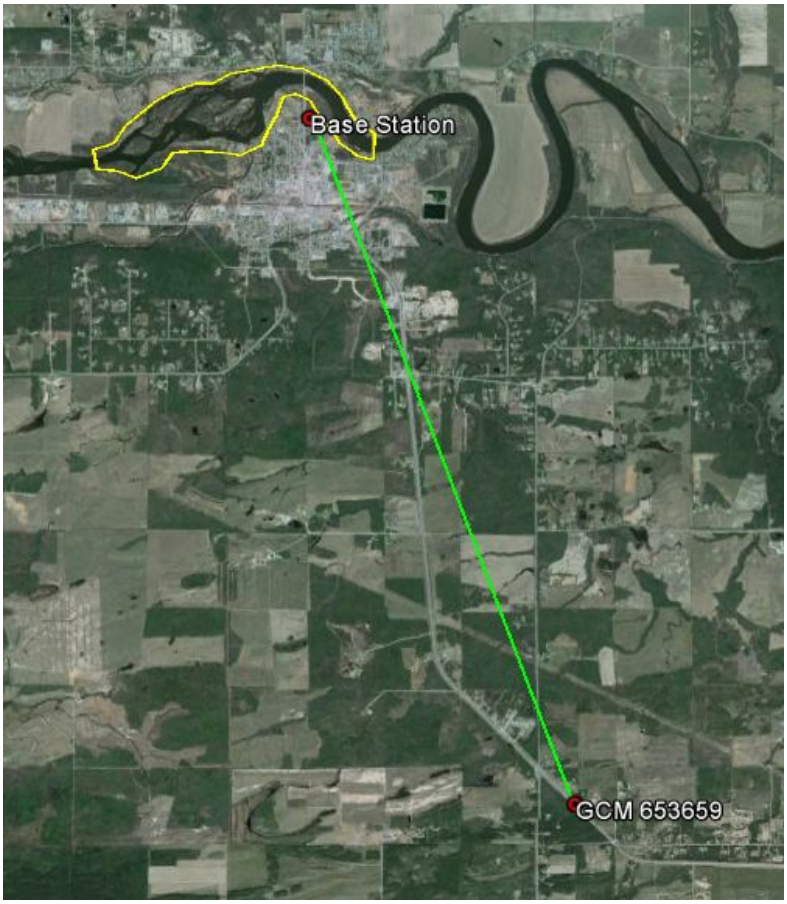

Figure A.1: Establishing local control using GCM 653659, study reach outlined in yellow (Google Earth image).

Figure A.2: RTK base-station receiver and radio positioned over the spike in front of the NWSCI.

Figure A.3: Installation used for bathymetric survey, showing the RTK rover receiver mounted on top of the survey-grade SonarMite echo sounder.

Figure A.4: Surveying top-of-bank topography.

A.1.3 Data processing

Analysis was required to verify and correct the base-station location that was obtained using the baseline observation from GCM 653659. To do so, these coordinates were compared to PPP coordinates obtained using the CSRS-PPP service offered by the Geodetic Survey Division of Natural Resources Canada (NRCAN, 2013). The CSRS-PPP process requires that raw GNSS data logged by the base-station be converted to Receiver Independent Exchange (RINEX) Format prior to submission to NRCAN. Once the data is submitted, along with the height of the GPS head and the antenna type, the PPP data is processed and a summary report will be returned to the user containing a computed position, standard deviation and accuracy of the positioning.

PPP reports were generated for the four longest duration base-station observations, which ranged from about 4 hours to over 11 hours (Figure A.5 - Figure A.8). Only long observations were used because PPP accuracy increases with the duration of the observation, which must exceed four hours to achieve centimeter-scale accuracy (NRCAN, 2013). Results of the PPP reports are shown and compared to the spike location obtained using the GCM baseline in Table A.2. The survey data were post-processed by shifting the spike coordinates, and hence the entire survey, by 0.359 m to the south and 0.786 m to the east to match the Northing and Easting obtained from the PPP results averaged over 33 hours of data logging. The PPP results were considered more accurate than the GCM baseline location because GCM 653659 had not been maintained recently and was located near a highway ditch, leading to the possibility of it being disturbed during roadworks, snow plowing, etc. The GCM baseline and PPP results were in good agreement regarding the elevation of the base-station, but for consistency, it too was corrected to match the PPP results by decreasing it 0.007 m.

Table A.2: Comparison of control point location obtained using PPP and GCM baseline methods.

Method	Date	Duration	Northing (m)	Easting (m)	Elevation (m)
PPP	5/12/2015	8h 56m	5986529.484	433953.101	639.041
PPP	5/13/2015	11h 24m	5986529.484	433953.123	639.012
PPP	5/14/2015	4h 10m	5986529.472	433953.105	639.046
PPP	5/15/2015	9h 31m	5986529.478	433953.116	639.032
PPP	Average		5986529.480	433953.111	639.033
GCM			5986529.839	433952.325	639.040
Difference			0.359	- 0.786	0.007

CSRS-PPP (V 1.05 34613)

30001

Data Start	Data End	Duration of Observations
2015-05-12 18:13:30.000	2015-05-13 03:10:00.000	8h 56m 30.00s
Apri / Aposteriori Phase Std		**Apri / Aposteriori Code Std**
0.015m / 0.012m		2.0m / 1.673m
Observations	**Frequency**	**Mode**
Phase and Code	L1 and L2	Static
Elevation Cut-Off	**Rejected Epochs**	**Observation & Estimation Steps**
10.000 degrees	-0.04 %	1.00 sec / 30.00 sec
Antenna Model	**APC to ARP**	**ARP to Marker**
TRM60158.00	L1= 0.085 m L2= 0.081 m	1.376 m

(APC = antenna phase center; ARP = antenna reference point)

Estimated Position for 07091321.15o

	Latitude (+n)	Longitude (+e)	Ell. Height
NAD83(CSRS) (2002)	54° 01' 22.1068''	-124° 00' 29.3569''	626.501 m
Sigmas(95%)	0.007 m	0.010 m	0.037 m
Apriori	54° 01' 22.156''	-124° 00' 29.466''	629.558 m
Estimated - Apriori	-1.527 m	1.995 m	-3.057 m

Orthometric Height CGVD28 (HTv2.0)

639.041 m

(click here for model and accuracy)

95% Error Ellipse (cm)
semi-major: 1.224cm
semi-minor: 0.924cm
semi-major azimuth: 89° 35' 14.42''

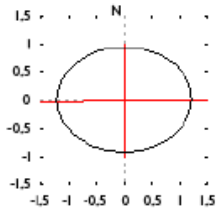

UTM (North) Zone 10

5986529.484m (N) 433953.101m (E)

Scale Factors
0.99965353 (point)
0.99955524 (combined)

(Coordinates from RINEX file used as apriori position)

Figure A.5: PPP report for observation 1 (8 hours and 56 minutes).

CSRS-PPP (V 1.05 34613)

30001

Data Start	Data End	Duration of Observations
2015-05-13 14:33:30.000	2015-05-14 01:58:00.000	11h 24m 30.00s
Apri / Aposteriori Phase Std		**Apri / Aposteriori Code Std**
0.015m / 0.013m		2.0m / 1.757m
Observations	**Frequency**	**Mode**
Phase and Code	L1 and L2	Static
Elevation Cut-Off	**Rejected Epochs**	**Observation & Estimation Steps**
10.000 degrees	-0.03 %	1.00 sec / 30.00 sec
Antenna Model	**APC to ARP**	**ARP to Marker**
TRM60158.00	L1= 0.085 m L2= 0.081 m	1.328 m

(APC = antenna phase center; ARP = antenna reference point)

Estimated Position for 07091330.15o

	Latitude (+n)	Longitude (+e)	Ell. Height
NAD83(CSRS) (2002)	54° 01' 22.1068''	-124° 00' 29.3557''	626.472 m
Sigmas(95%)	0.005 m	0.008 m	0.029 m
Apriori	54° 01' 22.102''	-124° 00' 29.345''	629.720 m
Estimated - Apriori	0.139 m	-0.186 m	-3.248 m

Orthometric Height CGVD28 (HTv2.0)

639.012 m

(click here for model and accuracy)

95% Error Ellipse (cm)
semi-major: 1.049cm
semi-minor: 0.590cm
semi-major azimuth: 79° 9' 27.63''

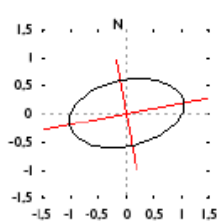

UTM (North) Zone 10

5986529.484m (N) 433953.123m (E)

Scale Factors
0.99965353 (point)
0.99955524 (combined)

(Coordinates from RINEX file used as apriori position)

Figure A.6: PPP report for observation 2 (11 hours and 24 minutes).

CSRS-PPP (V 1.05 34613)

30001

Data Start	Data End	Duration of Observations
2015-05-14 14:23:30.000	2015-05-14 18:34:00.000	4h 10m 30.00s
Apri / Aposteriori Phase Std		**Apri / Aposteriori Code Std**
0.015m / 0.013m		2.0m / 1.644m
Observations	**Frequency**	**Mode**
Phase and Code	L1 and L2	Static
Elevation Cut-Off	**Rejected Epochs**	**Observation & Estimation Steps**
10.000 degrees	-0.07 %	1.00 sec / 30.00 sec
Antenna Model	**APC to ARP**	**ARP to Marker**
TRM60158.00	L1= 0.085 m L2= 0.081 m	1.315 m

(APC = antenna phase center; ARP = antenna reference point)

Estimated Position for 07091340.15o

	Latitude (+n)	Longitude (+e)	Ell. Height
NAD83(CSRS) (2002)	54° 01' 22.1064''	-124° 00' 29.3567''	626.506 m
Sigmas(95%)	0.008 m	0.020 m	0.048 m
Apriori	54° 01' 22.094''	-124° 00' 29.423''	628.195 m
Estimated - Apriori	0.382 m	1.200 m	-1.688 m

Orthometric Height CGVD28 (HTv2.0)

639.046 m

(click here for model and accuracy)

95% Error Ellipse (cm)
semi-major: 2.491cm
semi-minor: 0.891cm
semi-major azimuth: 80° 16' 50.50''

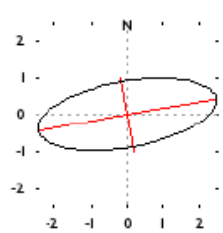

UTM (North) Zone 10

5986529.472m (N) 433953.105m (E)

Scale Factors
0.99965353 (point)
0.99955524 (combined)

(Coordinates from RINEX file used as apriori position)

Figure A.7: PPP report for observation 3 (4 hours and 10 minutes).

CSRS-PPP (V 1.05 34613)

30001

Data Start	Data End	Duration of Observations
2015-05-15 15:03:00.000	2015-05-16 00:34:30.000	9h 31m 30.00s
Apri / Aposteriori Phase Std		**Apri / Aposteriori Code Std**
0.015m / 0.013m		2.0m / 1.698m
Observations	**Frequency**	**Mode**
Phase and Code	L1 and L2	Static
Elevation Cut-Off	**Rejected Epochs**	**Observation & Estimation Steps**
10.000 degrees	-0.02 %	1.00 sec / 30.00 sec
Antenna Model	**APC to ARP**	**ARP to Marker**
TRM60158.00	L1= 0.085 m L2= 0.081 m	1.384 m

(APC = antenna phase center; ARP = antenna reference point)

Estimated Position for 07091350.15o

	Latitude (+n)	Longitude (+e)	Ell. Height
NAD83(CSRS) (2002)	54° 01' 22.1066''	-124° 00' 29.3561''	626.492 m
Sigmas(95%)	0.005 m	0.009 m	0.029 m
Apriori	54° 01' 22.073''	-124° 00' 29.481''	629.588 m
Estimated - Apriori	1.029 m	2.281 m	-3.095 m

Orthometric Height CGVD28 (HTv2.0)

639.032 m

(click here for model and accuracy)

95% Error Ellipse (cm)
semi-major: 1.076cm
semi-minor: 0.583cm
semi-major azimuth: 85° 35' 17.74''

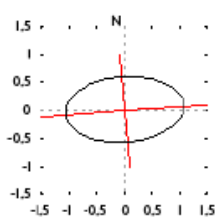

UTM (North) Zone 10

5986529.478m (N) 433953.116m (E)

Scale Factors
0.99965353 (point)
0.99955524 (combined)

(Coordinates from RINEX file used as apriori position)

Figure A.8: PPP report for observation 4 (9 hours and 31 minutes).

A.2 Limitations

Overall, RTK surveying was an efficient technique to collect data on the morphology of the study reach. However, operational issues related to signal and communication interference became problematic in vegetated areas. This resulted in low survey point density and limited accuracy on islands and along banklines within the upstream portion of the study reach.

A.3 References

Natural Resources Canada, Surveyor General Branch. 2013. Guidelines for RTK/RTN GNSS surveying in Canada (Version 1.1). *Accessed from www.nrcan.gc.ca.*

Natural Resources Canada. 2016. Height reference system modernization. *Accessed from www.nrcan.gc.ca.*

Trimble. 2003. Real-time kinematic surveying; Training Guide. (Revision D). Part Number 33142-40. *Accessed from www.gisresources.com.*

Trimble. 2004. Trimble 5700/5800 GPS receiver; User Guide. (Revision A), Version 2.21. *Accessed from www.ngs.noaa.gov.*

United States Geological Survey. 2014. Hurricane storm-surge GNSS surveying campaigns; Surveying methods. *Accessed from http://water.usgs.gov.*

Appendix B

Velocity and Discharge Measurement in the Nechako River using an Acoustic Doppler Current Profiler (ADCP)

B.1 Methods

*This section provides supplementary information to section **3.2 Flow velocity and discharge** in the thesis; previously described aspects have been omitted.*

B.1.1 Data collection

Data were collected from May 12-15th, 2015, during a rising discharge of approximately 510 m^3/s to 533 m^3/s. To collect the data, a Teledyne RDI RiverRay Acoustic Doppler Current Profiler (ADCP) raft was tethered to a wooden boom off the side of a motorized boat (Figure B.1). The boat was operated at the slowest and most constant speed possible across all transects (Figure B.2 - Figure B.10). However, it proved difficult to maintain speeds inferior to the flow velocity along near-bank vegetated areas and across transect TRH, where flow velocity was well below 1.0 m/s over most the transect (Figure B.9).

Compass calibrations were performed on each day prior to data collection, except for the first day when two calibrations were done. Calibrations were performed within a low-velocity bay located along the right bank in the upstream part of the reach (432125 E, 5986020 N). Compass error for each of these calibrations was 1.2°, 1.8°, 0.6° and 0.9°.

Each transect began and ended as close to the vegetated bankline as possible. It was then necessary to estimate the remaining wetted channel distance because significant portions of bankline and low-lying islands were submerged due to the high-flow conditions at the time

(Figure B.11). These distances were estimated by eye and subsequently input to the ADCP software to estimate overbank discharge.

On May 13th, two moving bed tests were performed at near transect TRA within the upstream, high-velocity end of the reach. These tests included one stationary test and one cross-channel loop test; neither test detected a moving bottom.

Figure B.1: Teledyne RDI RiverRay ADCP raft tethered to a wooden boom to collect velocity profiles.

Legend for Figures B.2 to B.10;

- *Red: Water velocity referenced to the Bottom Track*
- *Blue: Water velocity referenced to the GGA GPS string*
- *Green: Water velocity referenced to the VTG GPS string*
- *Orange: Boat velocity referenced to the Bottom Track*
- *Purple: Boat velocity referenced to the GGA GPS string*
- *Black: Boat velocity referenced to the VTG GPS string*

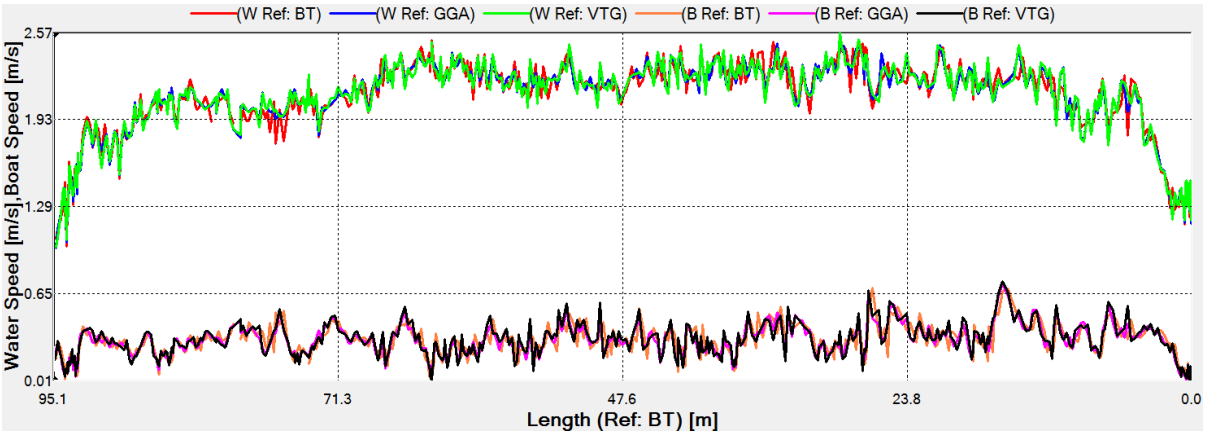

Figure B.2: Boat speed versus flow velocity across transect TRA.

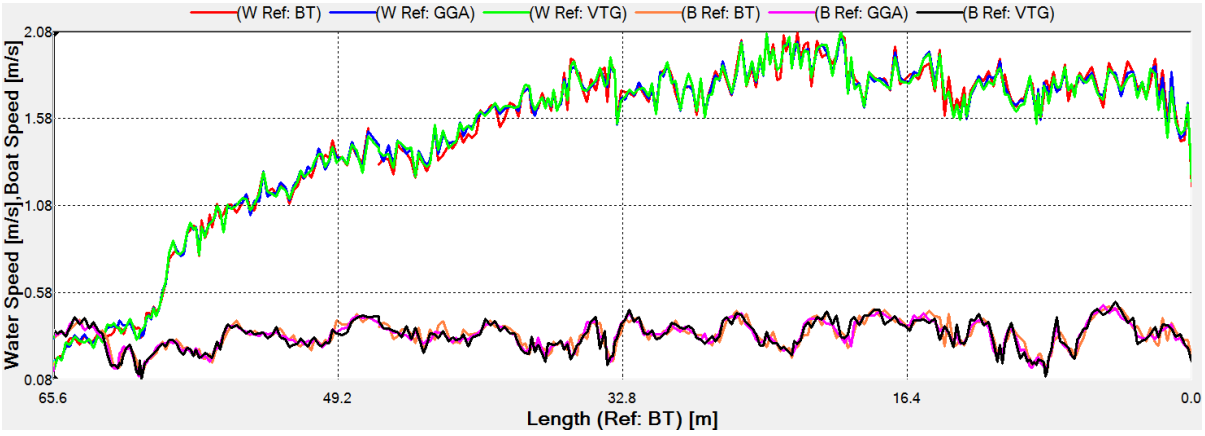

Figure B.3: Boat speed versus flow velocity across transect TRB.

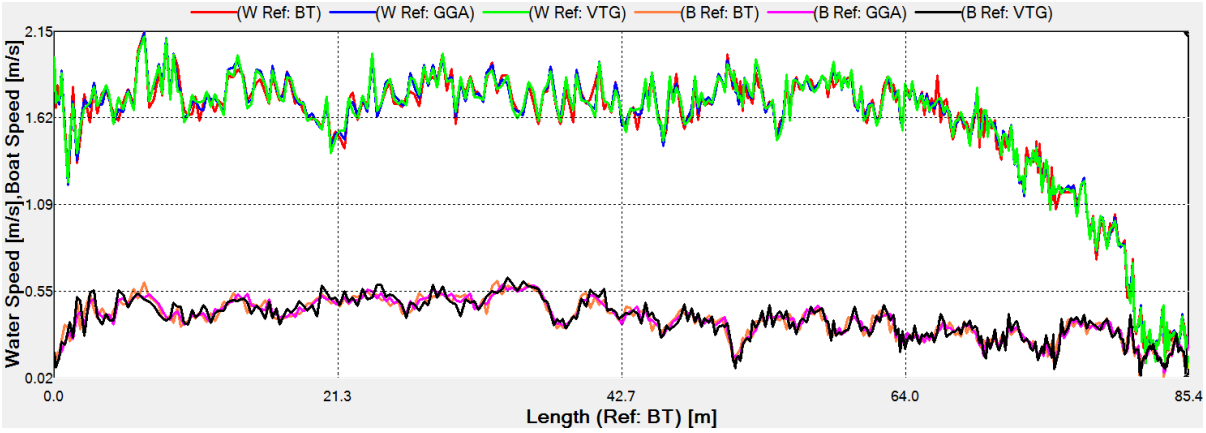

Figure B.4: Boat speed versus flow velocity across transect TRC.

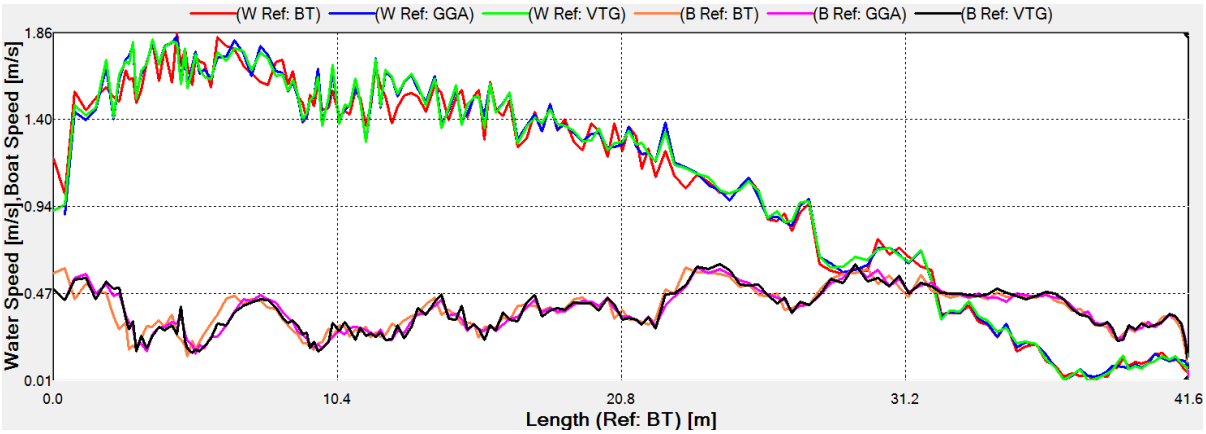

Figure B.5: Boat speed versus flow velocity across transect TRD.

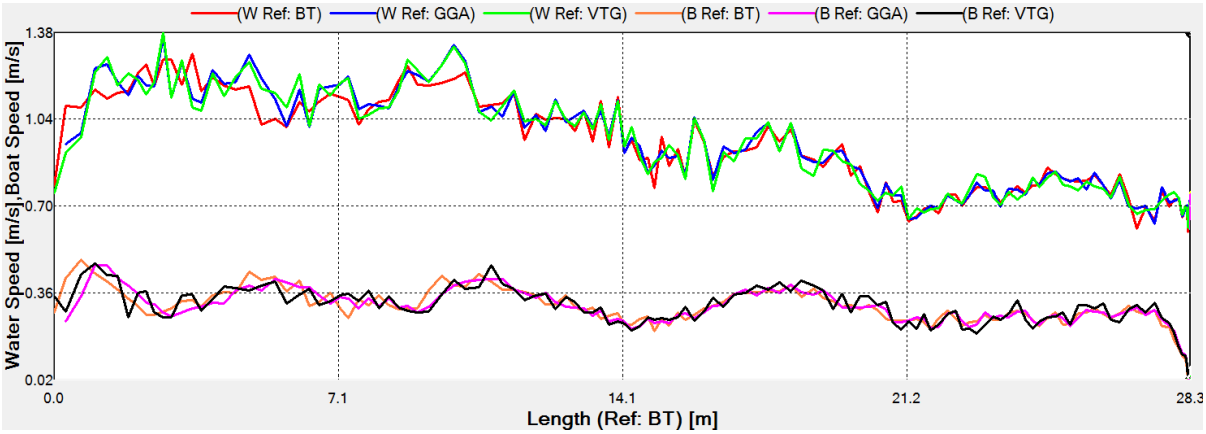

Figure B.6: Boat speed versus flow velocity across transect TRE.

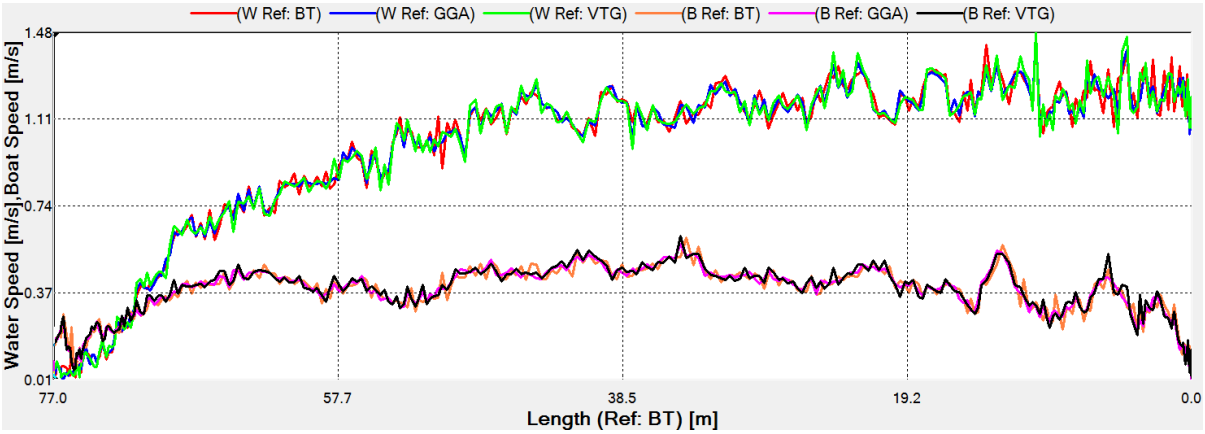

Figure B.7: Boat speed versus flow velocity across transect TRF.

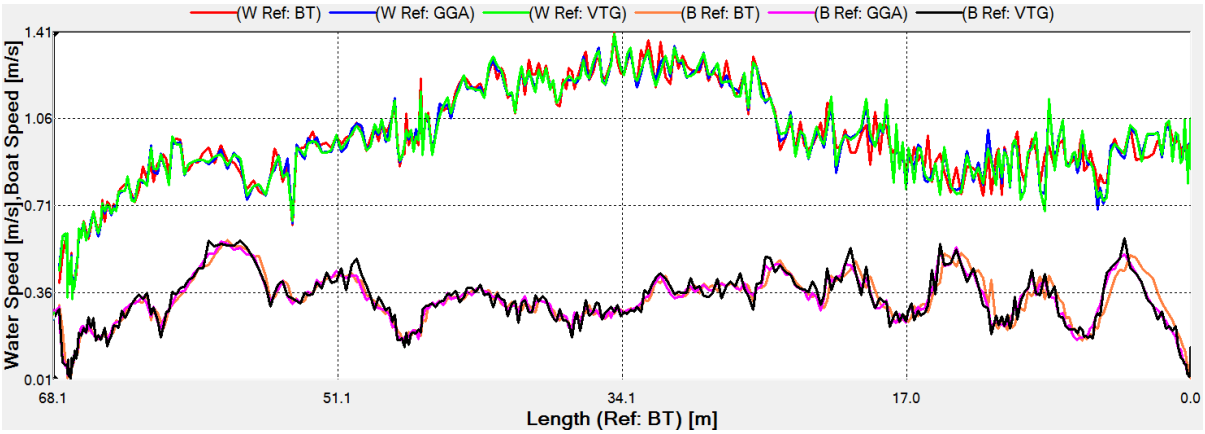

Figure B.8: Boat speed versus flow velocity across transect TRG.

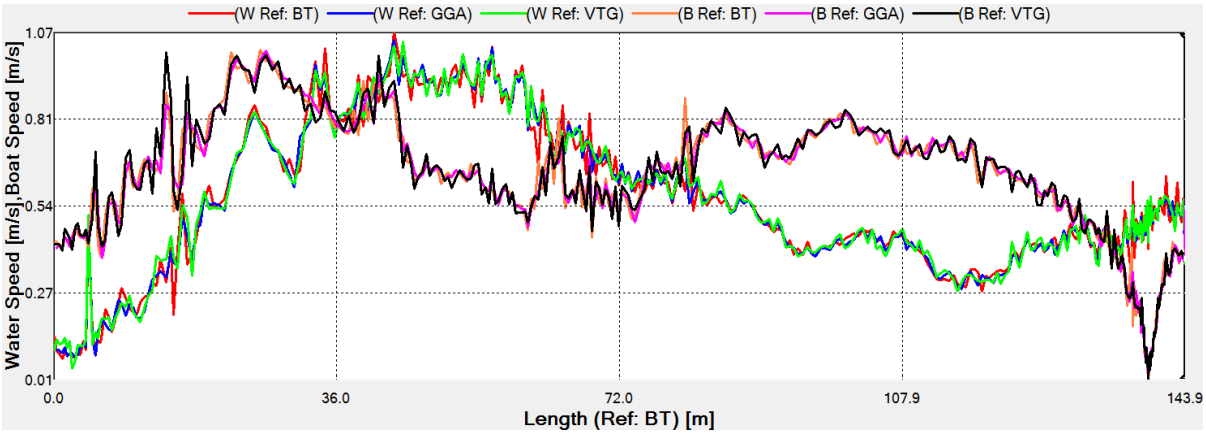

Figure B.9: Boat speed versus flow velocity across transect TRH.

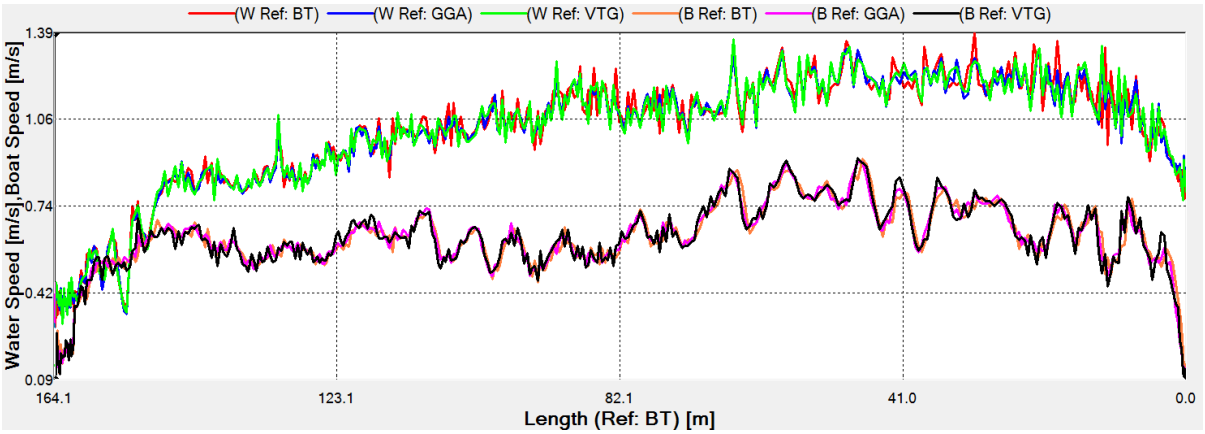

Figure B.10: Boat speed versus flow velocity across transect TRI.

Figure B.11: Banklines and low-lying islands were submerged during data collection, making it difficult to estimate wetted channel width.

B.1.2 Data processing

Using the Teledyne RDI WinRiver II software, the raw data were first processed by setting the magnetic variation to 17.3° for all transects based on alignment of the GPS ship track with the ADCP Bottom Track (BT) referenced path at transect TRH (Figure B.12). This transect was selected because sampled bedload transport rates were very low, suggesting that the bed at this location was very unlikely to be mobile. Good agreement between the ship tracks at transect TRC indicates that the magnetic variation applied was appropriate for the upstream extent of the reach as well.

Discharge and velocity were referenced to the BT for all transects except TRA and TRB, which were referenced to the GGA sentence from the GPS receiver because the bed was sufficiently mobile in local areas to offset the two ship tracks (Figure B.13 - Figure B.14). However, bed mobility was relatively minor and had a minimal influence on total estimated discharge, with the BT-referenced and GPS-referenced discharge estimates varying by 1.4% and 2.0% at the TRA and TRB transects, respectively.

To estimate total discharge, WinRiver II was configured to fit a power function to the near-surface and near-bed data to estimate the flux through these regions. No data is available within these regions due to the required blanking distance from the transducer and to bed and side-lobe interference (Mueller and Wagner, 2009). All transects were then cropped to

exclude poor quality data in shallow, low-velocity and vegetated near-bank areas. To estimate flux through the near-shore areas, bank geometry was assumed to have a triangular slope. Additional configurations regarding discharge estimation and data screening are presented in Figure B.15.

Each transect was replicated a minimum of four times during data collection. If the percent difference of estimated discharge between consecutive passes was over 5%, the pass would be flagged as an outlier, discarded and repeated. Only one replicate from each transect is shown in Figure B.16 - Figure B.24. Discharge summary statistics for each transect are presented in Figure B.25.

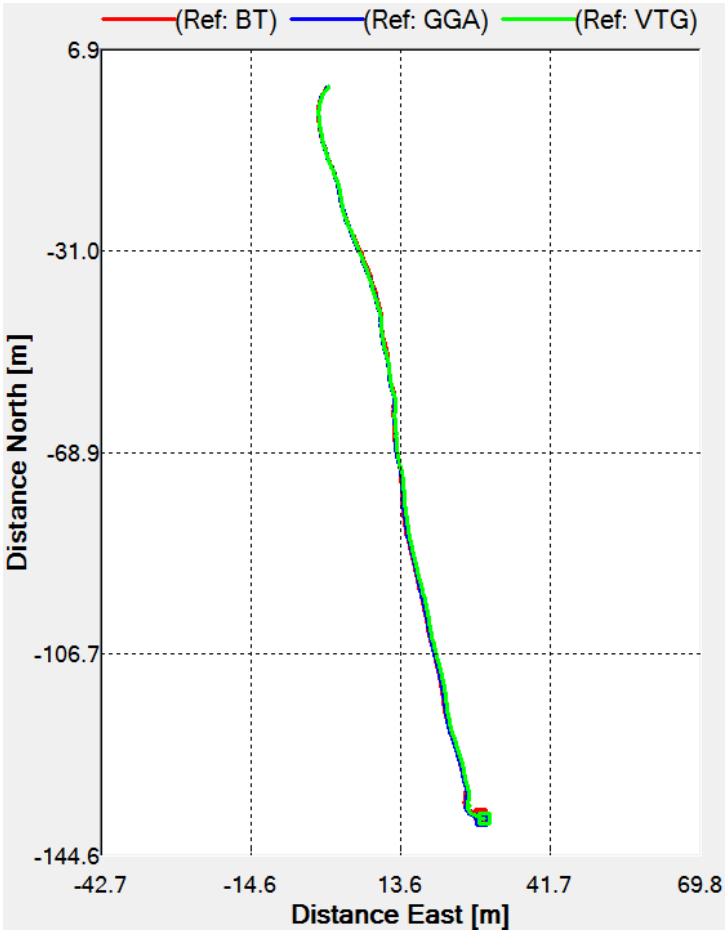

Figure B.12: TRH used to set magnetic variation to 17.3° by aligning GPS and BT ship tracks.

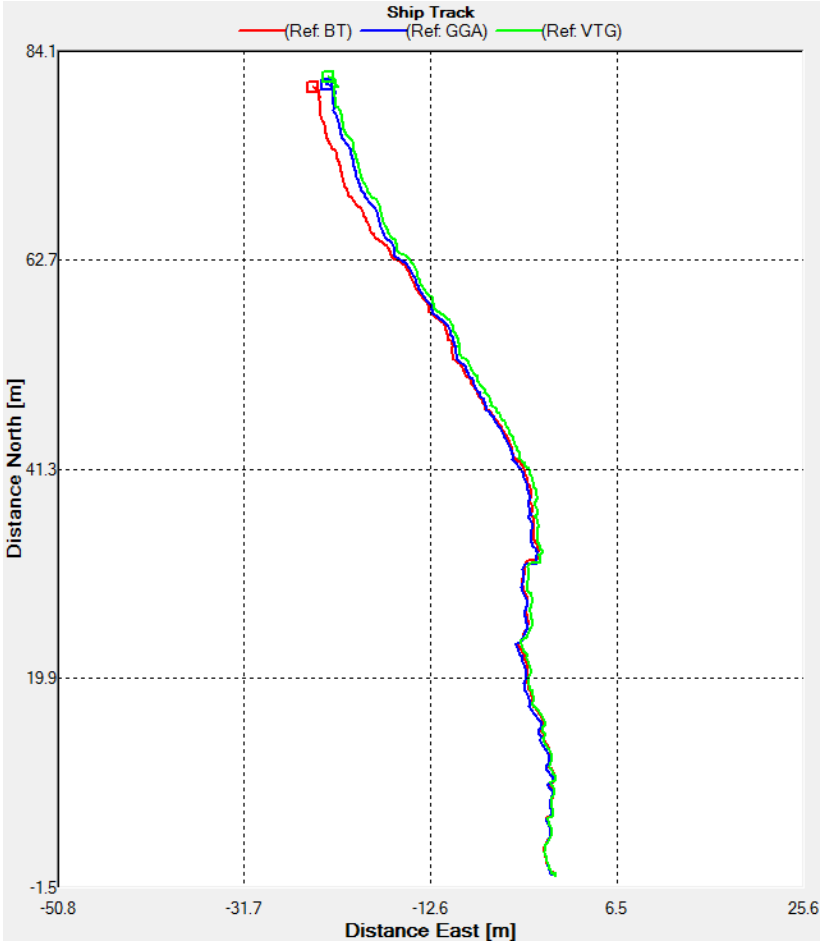

Figure B.13: Moving bed offsetting GPS and BT ship tracks at transect TRA.

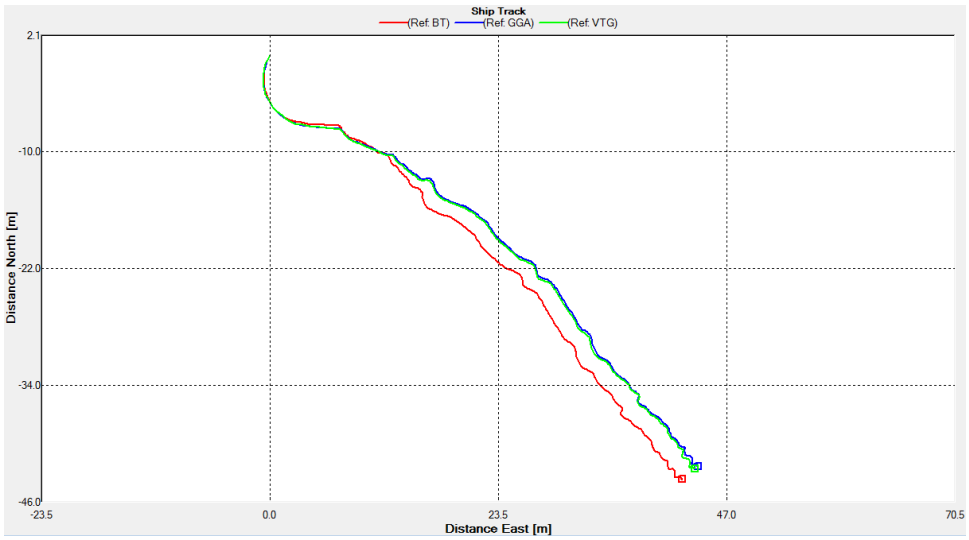

Figure B.14: Moving bed offsetting GPS and BT ship tracks at transect TRB.

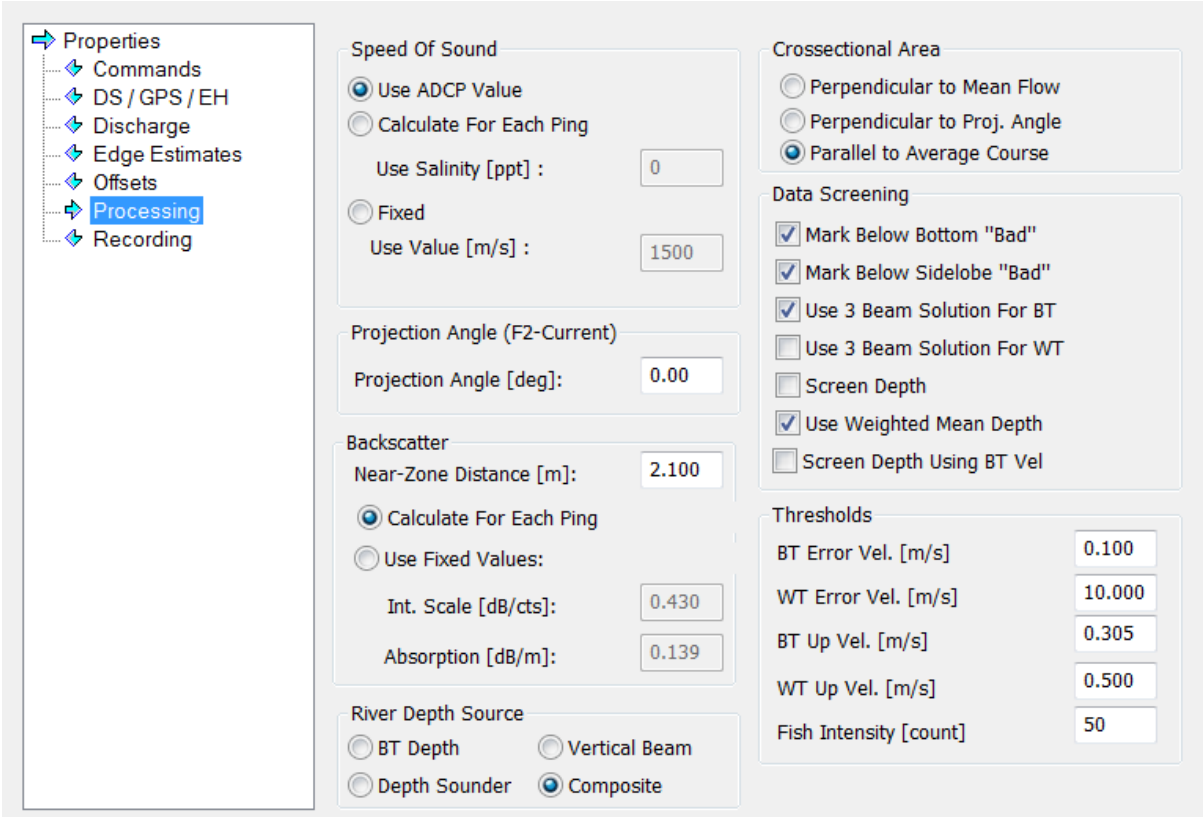

Figure B.15: Additional configurations used in WinRiver II for data processing.

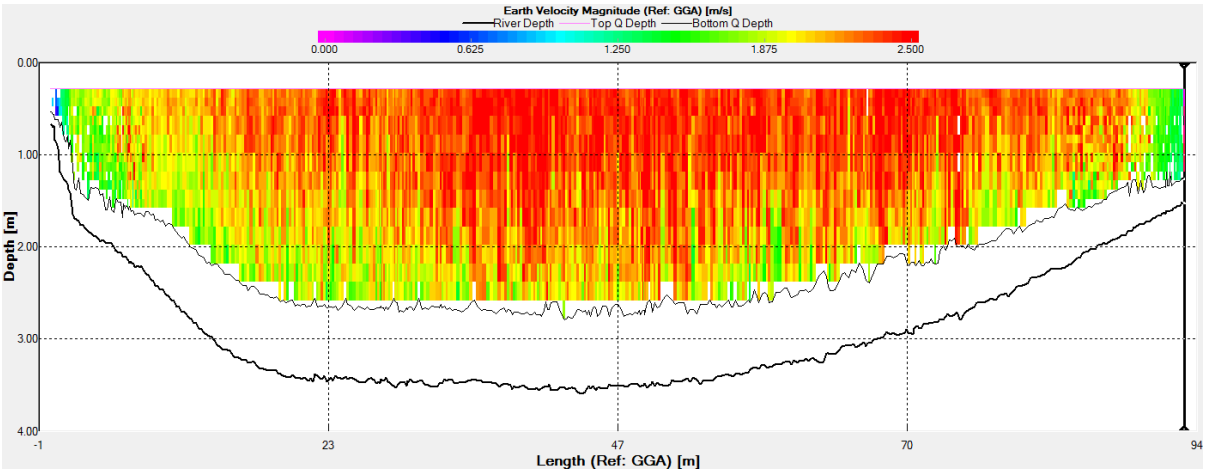

Figure B.16: Cross-channel velocity profile at transect TRA.

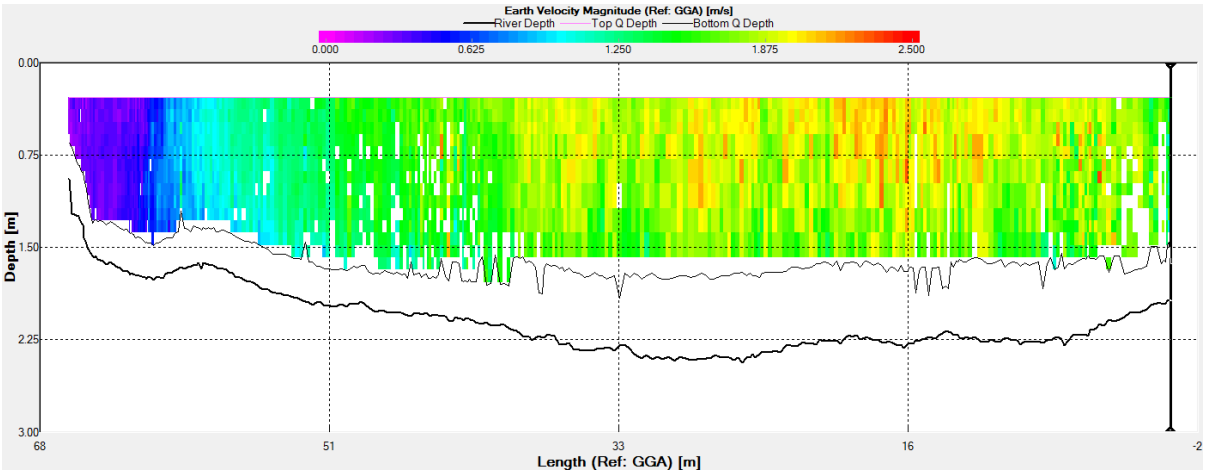

Figure B.17: Cross-channel velocity profile at transect TRB.

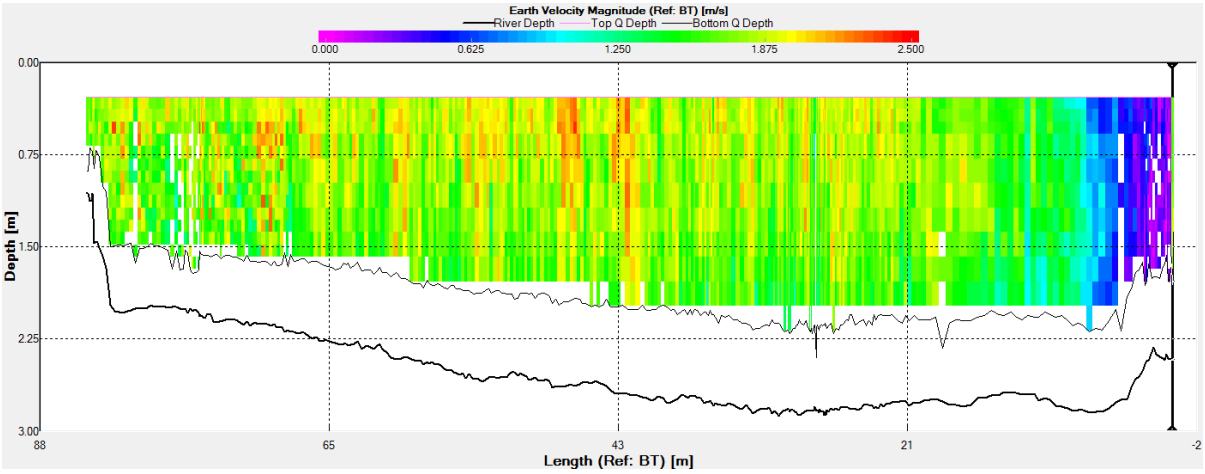

Figure B.18: Cross-channel velocity profile at transect TRC.

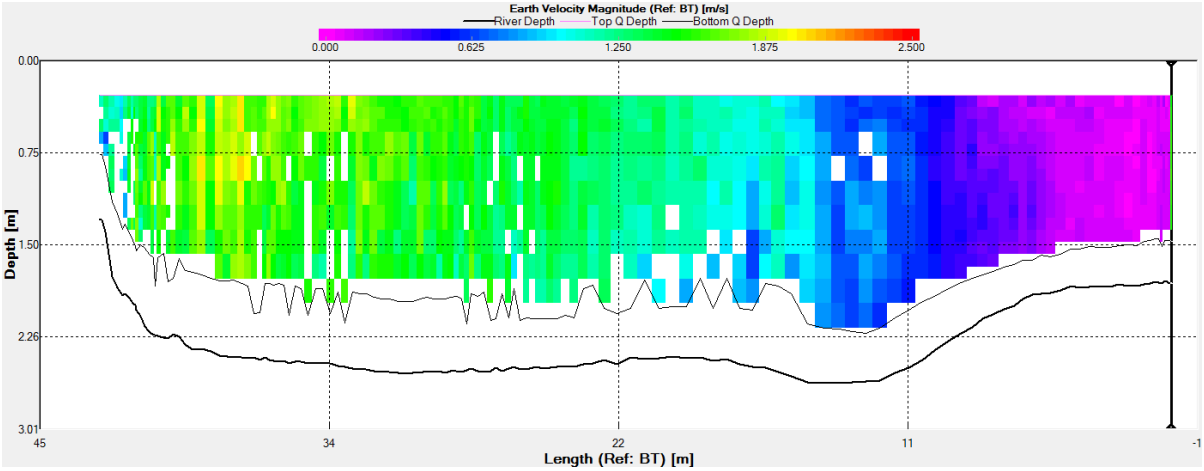

Figure B.19: Cross-channel velocity profile at transect TRD.

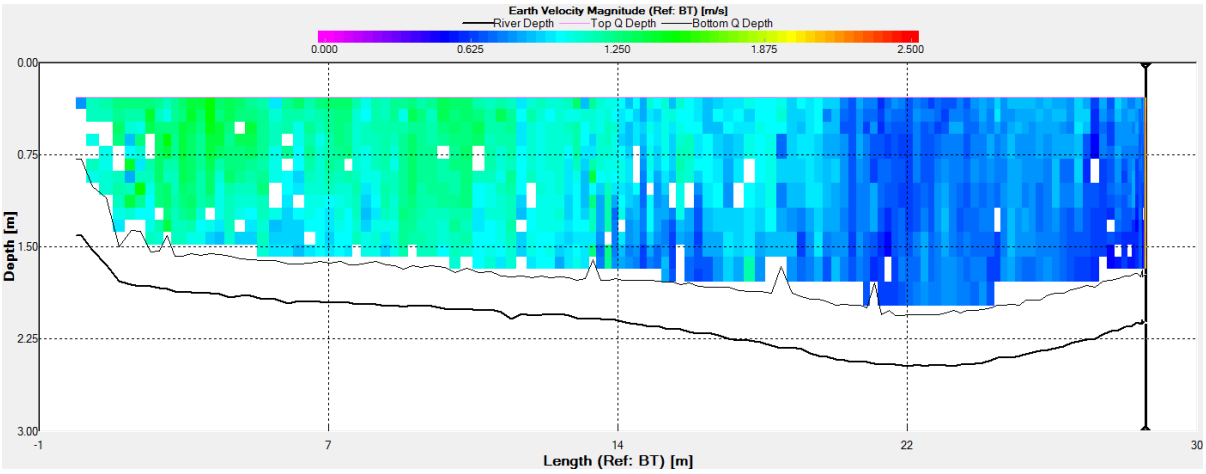

Figure B.20: Cross-channel velocity profile at transect TRE.

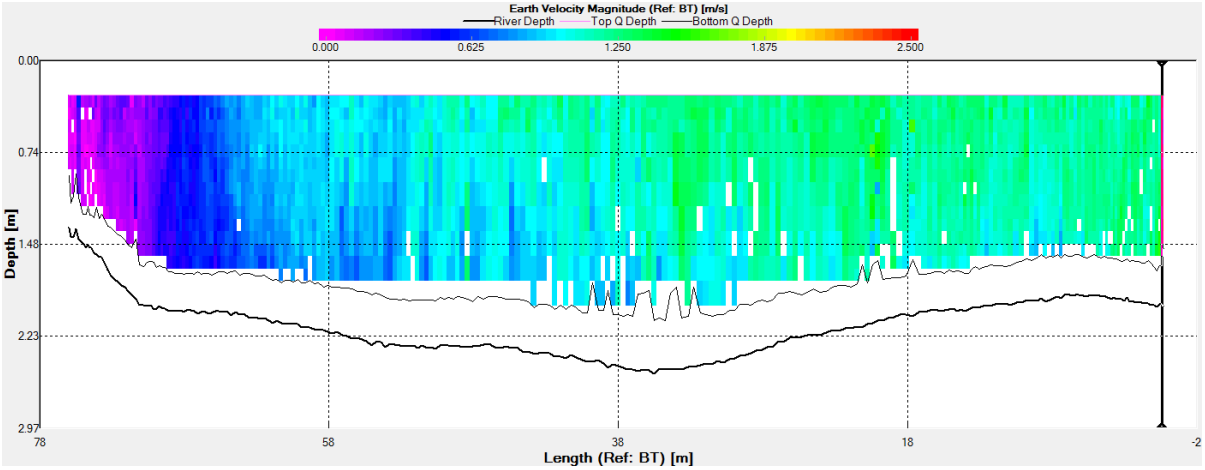

Figure B.21: Cross-channel velocity profile at transect TRF.

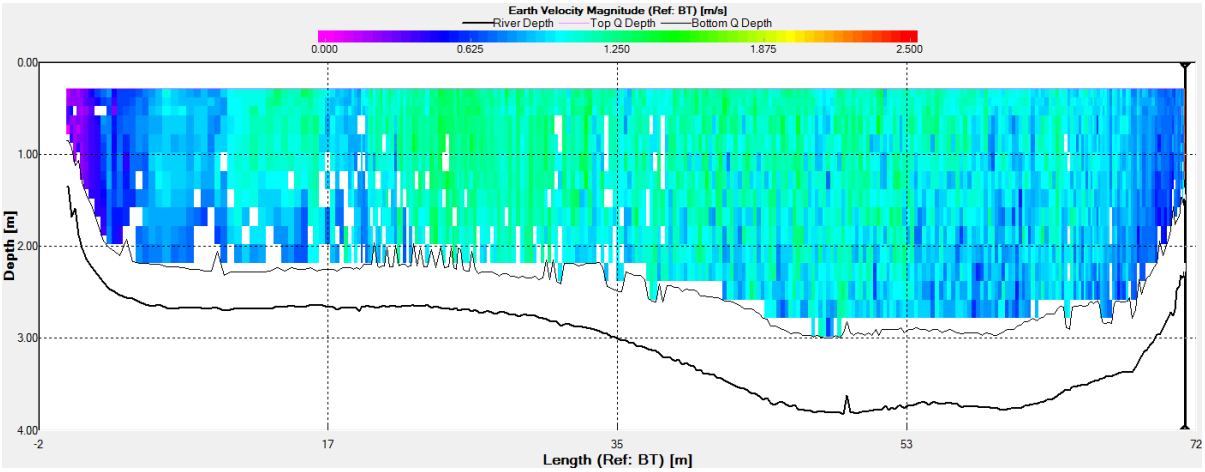

Figure B.22: Cross-channel velocity profile at transect TRG.

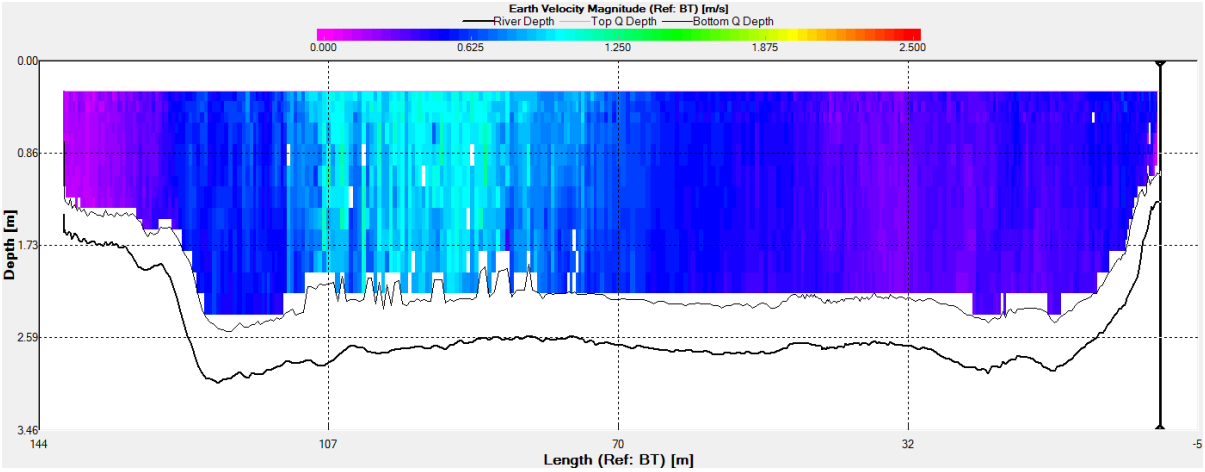

Figure B.23: Cross-channel velocity profile at transect TRH.

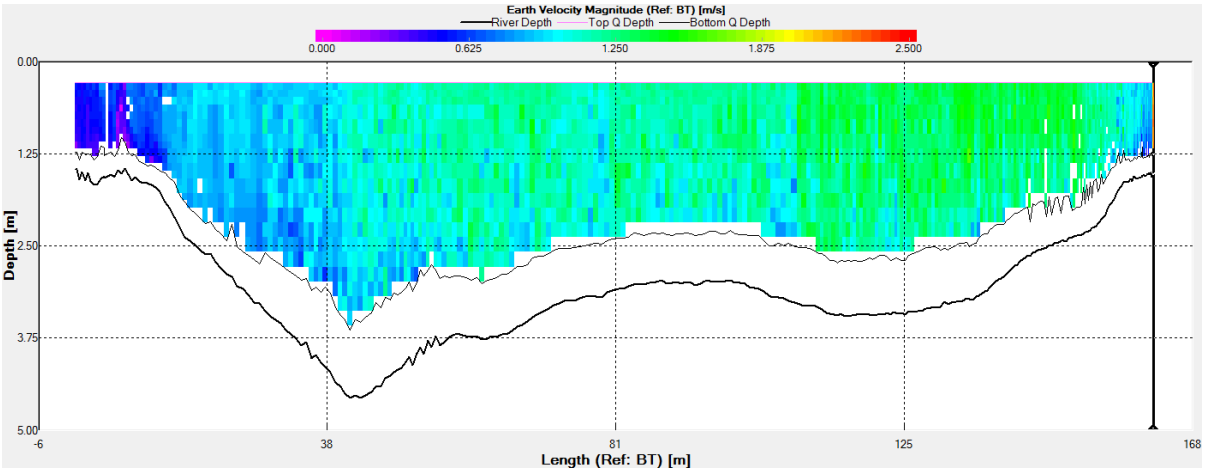

Figure B.24: Cross-channel velocity profile at transect TRI.

Transect	# of Ens.	Total Q (m^3/s)	Meas. Q (m^3/s)	Top Q (m^3/s)	Bottom Q (m^3/s)	Left Q (m^3/s)	Right Q (m^3/s)	Left Dist. (m)	Right Dist. (m)	Width (m)	Total Area (m^2)	Q/Area (m/s)	Boat Speed (m/s)	Flow Speed (m/s)
TRA - Avg.	459	497.9	327.8	53.7	111.3	0.7	4.4	1.3	6.0	90.8	250.9	2.0	0.29	2.10
TRA - SD	41	2.2	1.1	0.2	1.0	0.4	0.3	0.3	0.0	0.6	1.8	0.0	0.02	0.03
TRB - Avg.	351	196.6	117.1	28.4	44.6	0.2	6.2	1.4	6.0	68.3	134.8	1.5	0.28	1.48
TRB - SD	50	1.7	0.6	0.3	0.9	0.1	0.5	0.5	0.0	0.4	0.4	0.0	0.03	0.08
TRC - Avg.	357	306.0	189.2	38.4	70.7	6.7	1.0	8.0	4.5	89.7	204.8	1.5	0.35	1.57
TRC - SD	23	4.9	2.2	0.5	2.1	0.9	0.5	0.0	0.0	0.6	1.8	0.0	0.03	0.06
TRD - Avg.	185	95.8	60.2	12.4	21.8	1.2	0.1	1.5	4.3	47.7	104.0	0.9	0.36	1.03
TRD - SD	56	3.1	1.8	0.6	1.1	0.6	0.3	0.0	0.5	5.5	8.6	0.1	0.04	0.05
TRE - Avg.	155	59.5	36.9	8.3	8.9	3.1	2.2	4.5	4.7	37.2	68.3	0.9	0.26	0.96
TRE - SD	24	2.0	1.3	0.3	0.3	0.1	0.3	0.0	0.0	0.6	1.2	0.0	0.02	0.05
TRF - Avg.	295	153.6	102.2	21.9	24.8	0.0	4.6	2.0	5.5	80.5	164.5	0.9	0.37	0.98
TRF - SD	41	3.2	2.5	0.5	0.3	0.1	0.2	0.0	0.0	1.3	2.3	0.0	0.05	0.05
TRG - Avg.	301	190.6	130.1	19.3	37.5	1.0	2.6	5.0	4.1	75.3	213.9	0.9	0.33	0.94
TRG - SD	17	6.1	3.8	0.5	1.9	0.3	0.4	0.0	0.0	0.3	2.3	0.0	0.02	0.05
TRH - Avg.	291	195.0	136.5	23.6	33.3	0.7	0.9	10.0	5.0	154.6	375.0	0.5	0.72	0.49
TRH - SD	66	3.6	3.4	0.5	3.7	0.2	0.5	0.0	0.0	0.4	3.0	0.0	0.19	0.01
TRI - Avg.	353	502.6	344.3	51.7	103.2	1.1	2.3	5.0	5.5	171.0	499.5	1.0	0.69	1.03
TRI - SD	61	10.4	6.6	1.0	3.2	0.2	0.2	0.0	0.0	0.6	1.4	0.0	0.12	0.03

Figure B.25: Summary statistics for ADCP transects.

Data were subsequently exported from WinRiverII and imported into the USGS Velocity Mapping Toolbox (VMT), which is a Matlab-based software for ADCP data processing and visualization (available at https://hydroacoustics.usgs.gov). This software was used to read the ASCII output file from WinRiver II and convert it to CSV file formats. To avoid averaging the raw data at this stage, the grid node spacing within the VMT working environment was set to the typical average bin size of the ADCP data. The specified grid size had a 0.3 m horizontal node spacing and a 0.1 m vertical node spacing. The smoothing window was set to 1 in both horizontal and vertical directions. Once the data were refit to a common grid, depth-averaged velocities were exported.

Files exported from VMT were then imported to the R software environment for further data processing. Firstly, the raw data were filtered to remove any bad points that had been assigned error values. Then, the depth-averaged data were binned into 5-m distance intervals across each transect. These 5-m distance intervals were determined using a straight cross-channel distance, and therefore may include over 5 m of data if the ship track was particularly curvilinear. Within each bin, the mean coordinates, depth-averaged velocity, depth and specific discharges value were calculated and exported. The binned depth-averaged velocities, including the standard deviation within each bin, are plotted in Figure B.26 - Figure B.34.

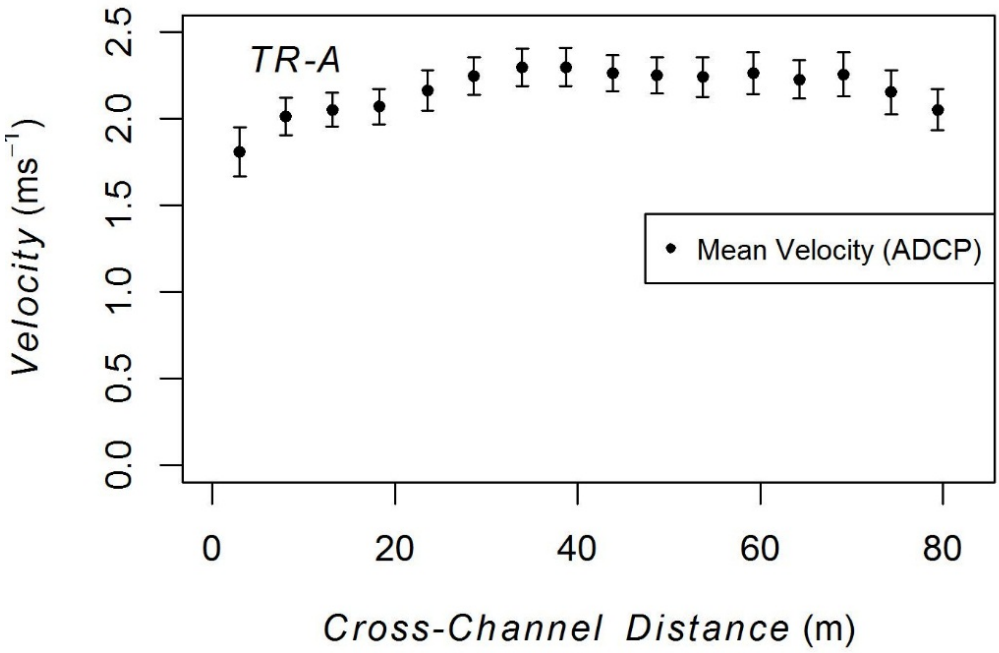

Figure B.26: Mean and standard deviation of depth-averaged velocity across-transect TRA.

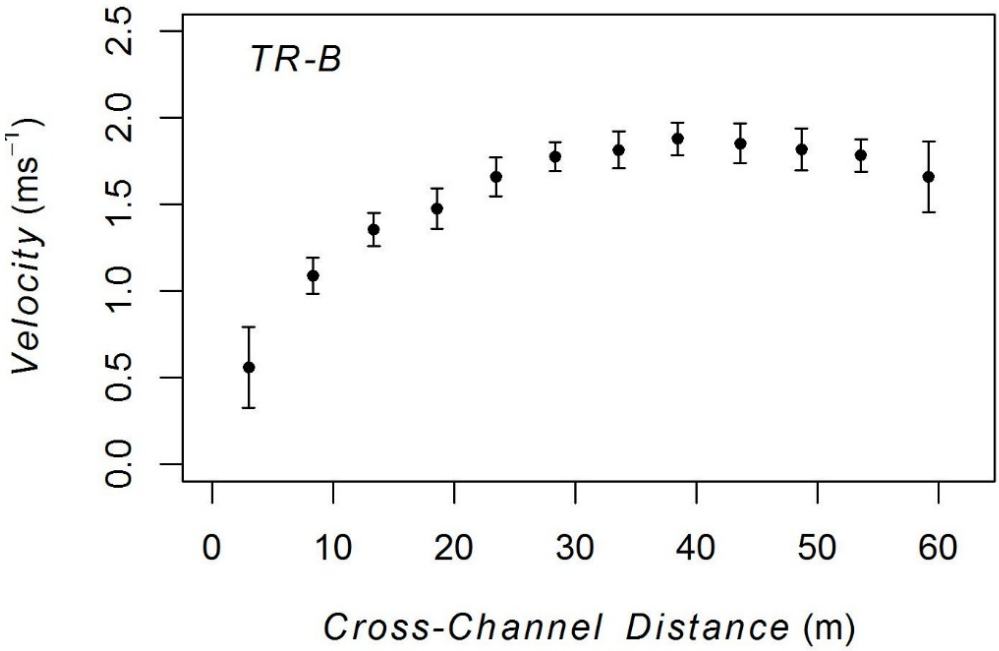

Figure B.27: Mean and standard deviation of depth-averaged velocity across-transect TRB.

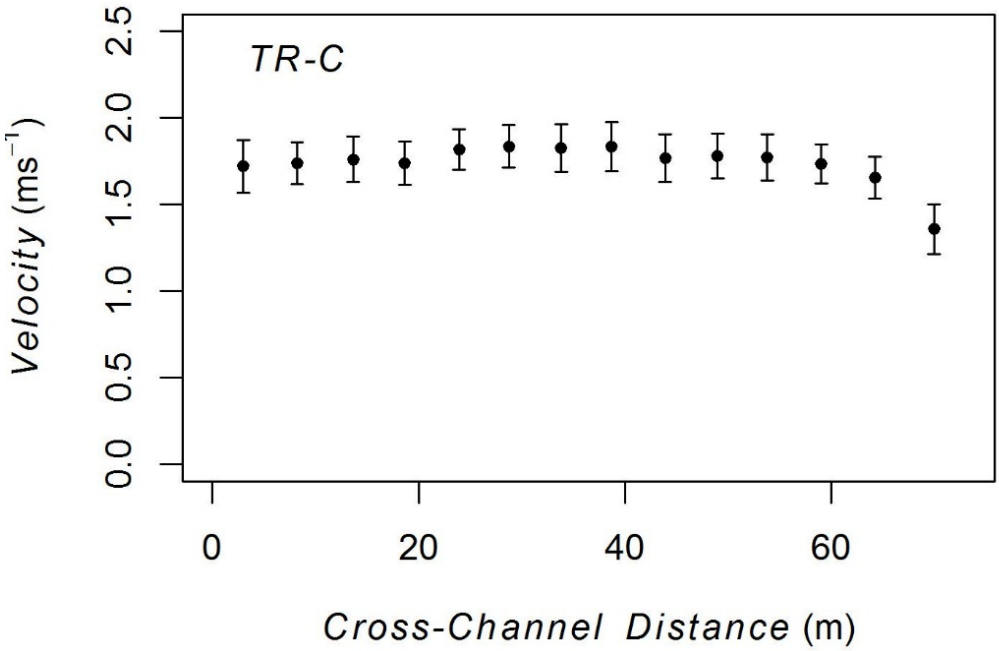

Figure B.28: Mean and standard deviation of depth-averaged velocity across-transect TRC.

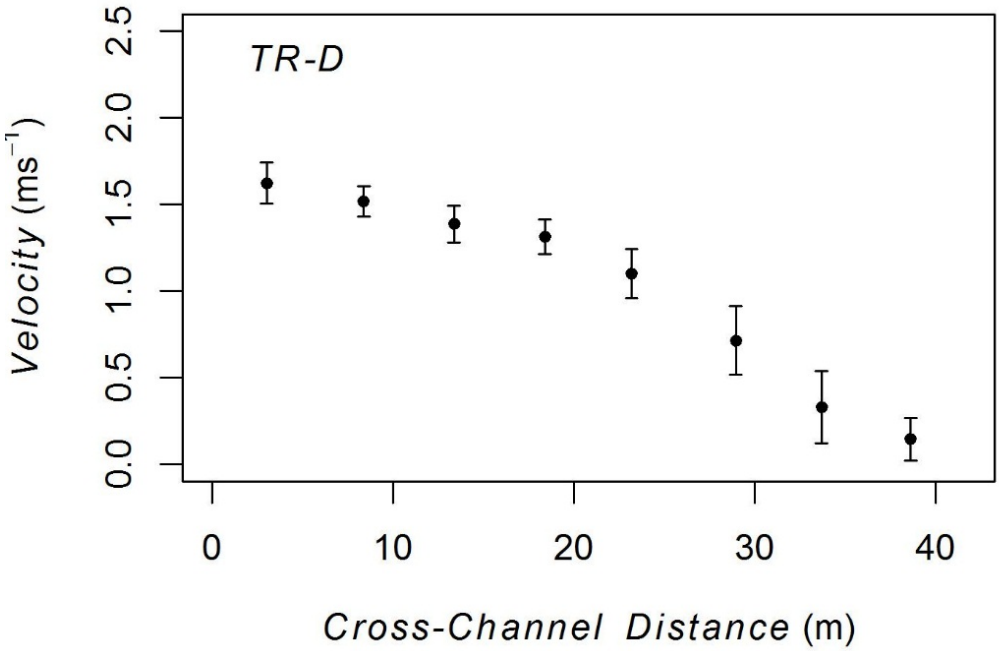

Figure B.29: Mean and standard deviation of depth-averaged velocity across-transect TRD.

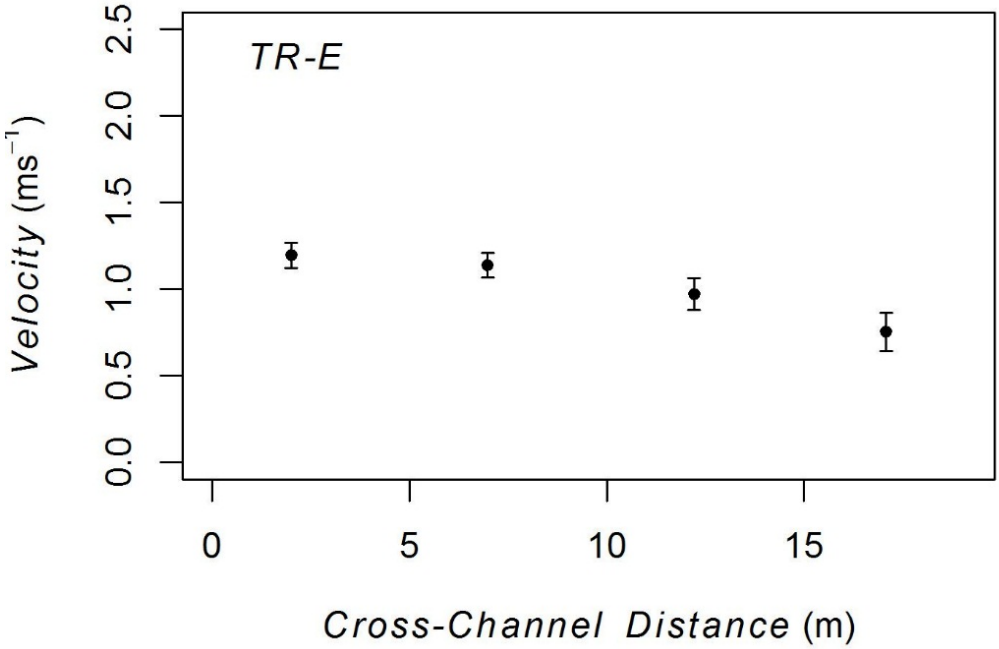

Figure B.30: Mean and standard deviation of depth-averaged velocity across-transect TRE.

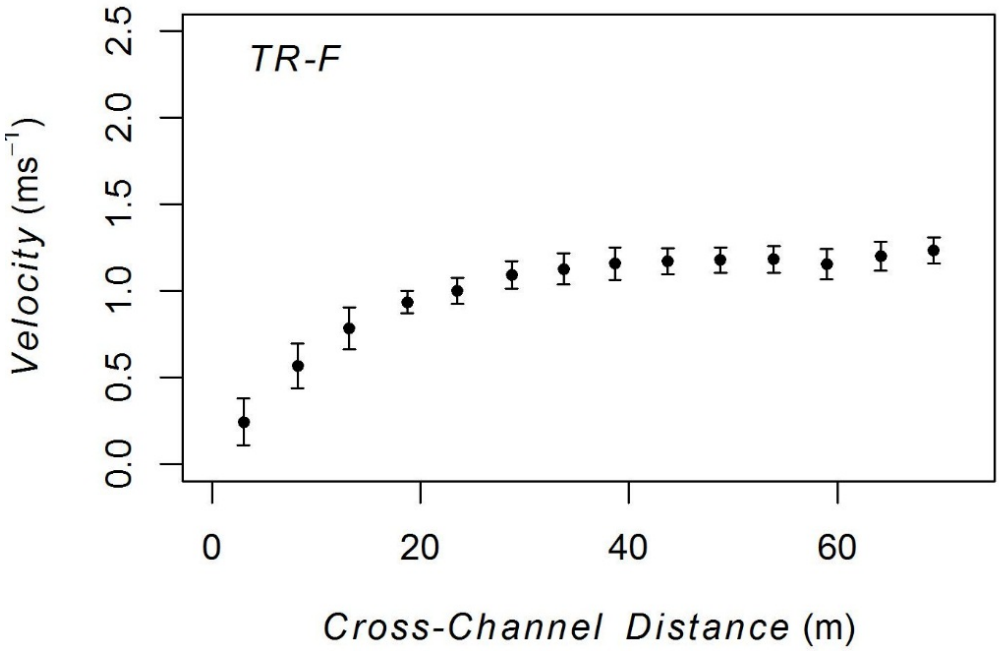

Figure B.31: Mean and standard deviation of depth-averaged velocity across-transect TRF.

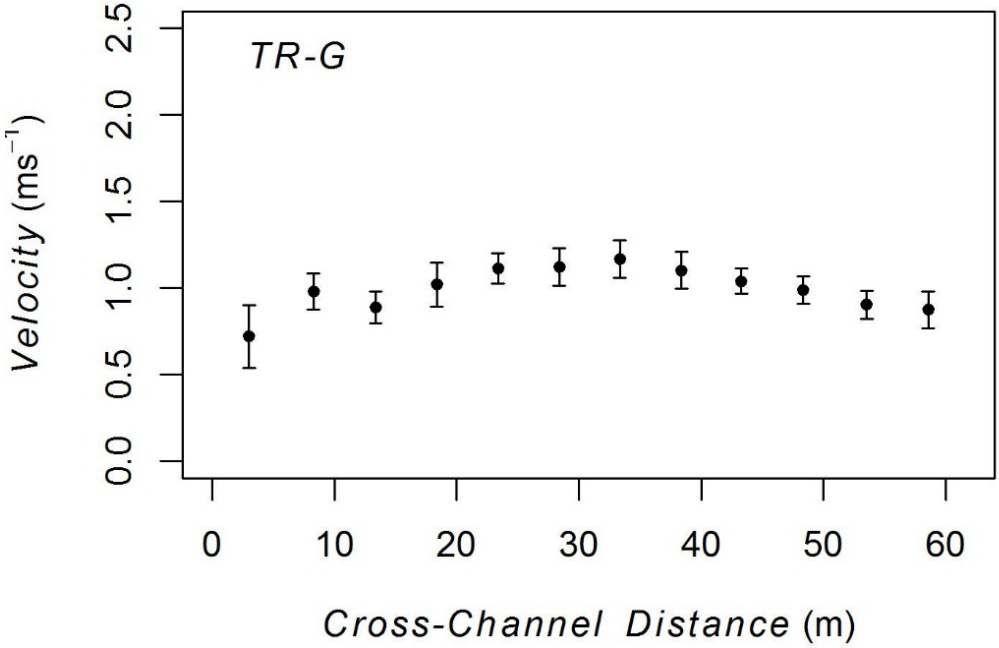

Figure B.32: Mean and standard deviation of depth-averaged velocity across-transect TRG.

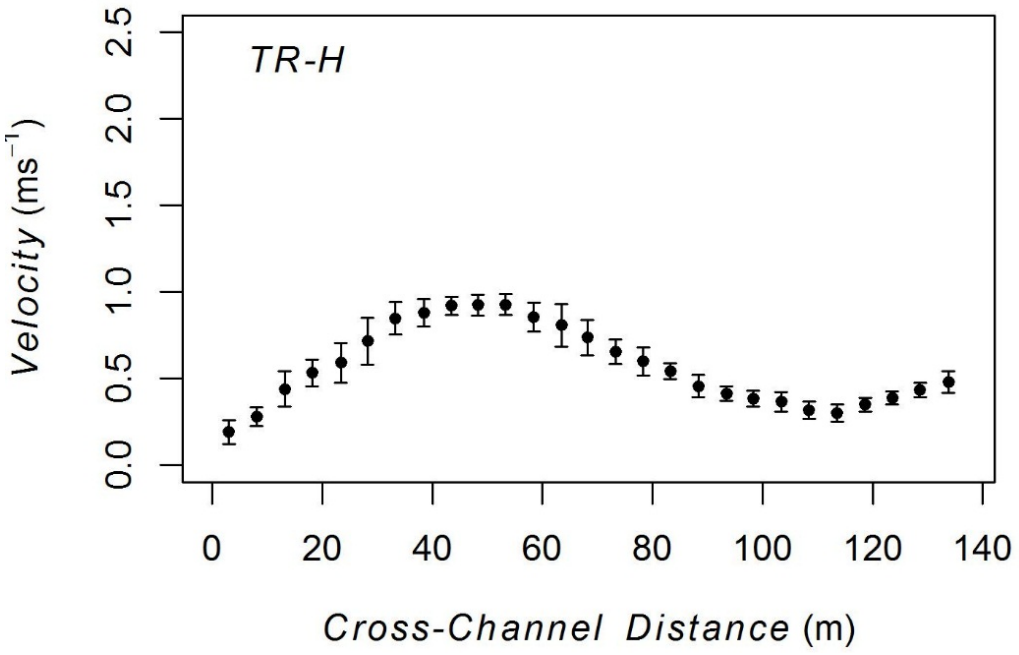

Figure B.33: Mean and standard deviation of depth-averaged velocity across-transect TRH.

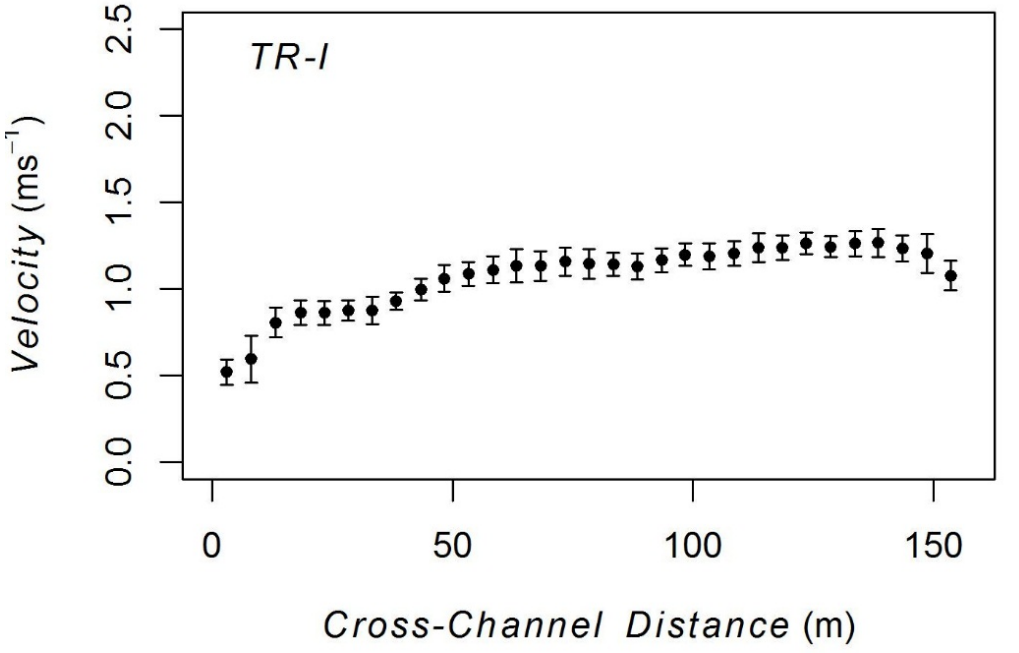

Figure B.34: Mean and standard deviation of depth-averaged velocity across-transect TRI.

B.2 Limitations

Maintaining a slow and constant boat speed was not trivial during data collection because flow velocities reached over 2.5 m/s. A jet-boat was used to collect data on May 12-13th, sometimes making it difficult to transition from high-velocity flow to near-bank eddies at constant speeds due to the momentum of the large boat. However, the boat operator was highly proficient and achieved well. The other potential complication when using a jet-boat is magnetic interference with the ADCP compass (Mueller et al., 2007). This was addressed with regular, daily compass calibrations. Lastly, the accuracy of total discharge estimates were limited due to the difficultly in specifying the total wetted width of the channel. Total channel width was difficult to assess because high flow conditions were causing extensive overbank flow. Given that the flow in overbank areas was generally low velocity, due to significant vegetation, this limitation is considered to have had a relatively minimal impact.

B.3 References

Mueller, D.S., and Wagner, C.R. 2009. Measuring discharge with acoustic Doppler current profilers from a moving boat: U.S. Geological Survey Techniques and Methods 3A22, 72 p. *Accessed from http://pubs.water.usgs.gov.*

Mueller, D.S., Wagner, C.R., and Winkler, M.F. 2007. Best practices for measuring discharge with Acoustic Doppler Current Profilers. USGS Publications.

Appendix C

Bedload Sampling Protocol

The following excerpt is presented with permission from NHC and MFLNRO and was obtained from:

NHC. 2015. 2014 Sediment Transport Investigation on the Vanderhoof Reach of the Nechako River. Prepared for Ministry of Forests, Lands and Natural Resource Operations. March 2, 2015.

C.1 Methodology

The samples will be collected with a Helley-Smith bedload sampler. A Helley-Smith sampler with a 76.2 mm wide opening and 0.125 mm mesh bag is to be used to monitor sediment transport rates. In general, one sample is to be collected from each vertical over a duration of 300 seconds (5 minutes). If transport rates are exceptionally high and the bag over-fills, additional samples are to be collected for shorter duration periods.

- Begin sampling at the first location where the water depth is sufficient for boat access.
- Take a photo of the site that shows conditions of the river. Take photos facing upstream, downstream and of each bank.
- Navigate the boat as close as possible to the GPS point (within 5 m of the point) and drop the anchor.
- Allow the boat to come to rest on the anchor. The amount of rope required will vary depending on flow but should be around 15 m. Record an estimate of how much rode is let out in the field notes.
- Attach a clean sample bag onto the Helley-Smith.
- Slowly lower the sampler to the river bed. The tail of the sampler should make contact with the bed first, followed by the nozzle.

- As soon as the sampler is resting flat on the bed, start the timer.
- Collect sediment for 300 seconds (5 minutes).
- During sediment collection, it is essential that the cable to the sampler remains slack and the boat does not pull on the sampler causing it to dredge up material. If this occurs, the sampler should be brought to surface, the sample bag flushed clean, and the collection started again.
- As soon as 300 seconds has been reached, the sampler should be raised back to the surface.
- Check if the sample has an unexpected amount of sediment in it. This could indicate that the sampler nose-dived into the bottom or was dragged along the bed. If this is suspected, flag the sample and collect an additional one. If you are confident this happened, discard the sample and collect another sample.
- Bedload transport is highly variable in space and time so adjacent locations may collect very different amounts. Make notes on any observed sheets or streams of mobile bed material.
- Check that the sample bag is not over-filled (over 40% full of sediment).
- Using a squeezable water bottle, wash any sediment that is stuck in the opening or upper parts of the sample bag into the back of the bag.
- Carefully transfer the sediment from the sample bag to a Ziploc. Use the water bottle to wash the sediment stuck to the collection bag, and then carefully drain off the excess water from the Ziploc.
- Label the Ziploc with the site and station number, the length of the sample, and the date and time. If multiple samples were taken for one station, this should also be included.
- If the sample bag is more than 40% full, it is likely that the hydraulic efficiency of the sampler has been reduced and a biased sample has been collected. The sample must be discarded and a new sample collected.
- If the bag is only slightly over-filled, attempt to collect two samples of 150 seconds or three samples for 100 seconds.
- If there is a tiny bit or no sediment, the sample from the next vertical can be included. In this case, do not replace the bag but just go to the next location. This is likely only suitable when sampling during low river discharge.

Appendix D

Geographic Information System (GIS) Data Processing and Analysis

D.1 Data processing

A speed of sound correction was applied to all surveyed depths using the temperature of the water at the time of data collection. The corrected depth value and the distance from the transducer to the RTK GPS head were subtracted from the RTK elevation to obtain bed elevation. The distance from the transducer to the water surface was added to the corrected depth to obtain the water surface elevation (WSE). The processed bathymetric data were combined with the topographic data and imported to ArcGIS. Data from the bankline survey was imported separately to ArcGIS from AutoCAD as polylines.

A triangulated irregular network (TIN) of bed elevation and a TIN of WSE were created using the banklines as hardlines and the survey extent as a hardclip. Both TINs were manually adjusted by connecting nodes on large triangulated wedges. The bed elevation TIN also required the connection of TIN nodes along the thalweg, especially in areas with low surveyed point density. The TINs were then converted to 1-m resolution rasters with common processing extents. Finally, the rasters were differenced to produce a depth map, which was clipped to exclude vegetated islands and overbank areas. The DEM of bed elevation was coarsened to a resolution of 2 m and exported to be used for hydrodynamic modelling, along with shapefiles of banklines and bar contours.

D.2 Maps

Figure D.1 presents the TIN of bed elevation that was used to generate the reach-scale DEM (Figure D.2). The interpolated water surface during data collection (525 m^3/s) in Figure D.3 was differenced with the DEM to produce the depth map presented in Figure D.4.

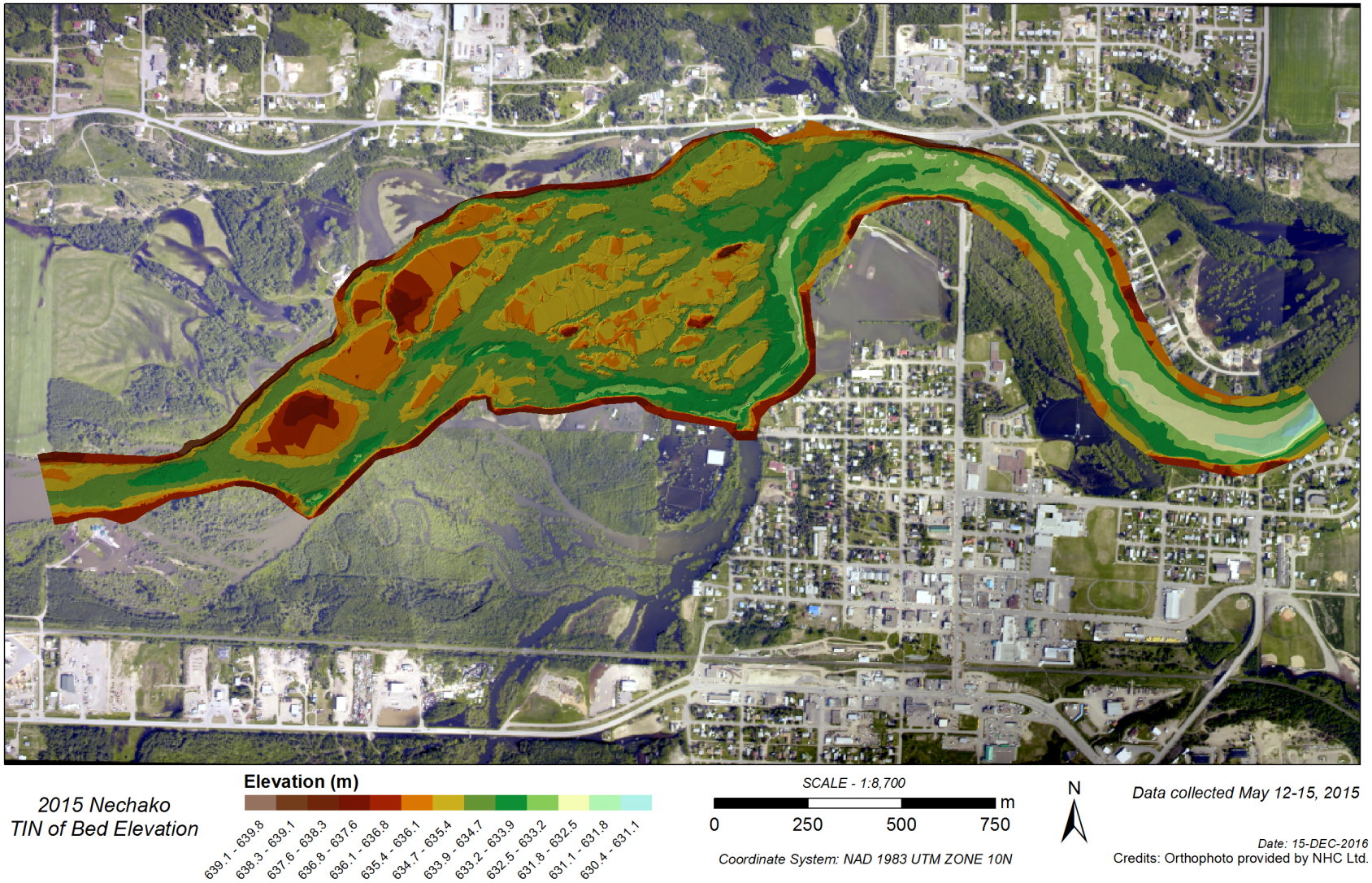

Figure D.1: TIN generated from surveyed elevations.

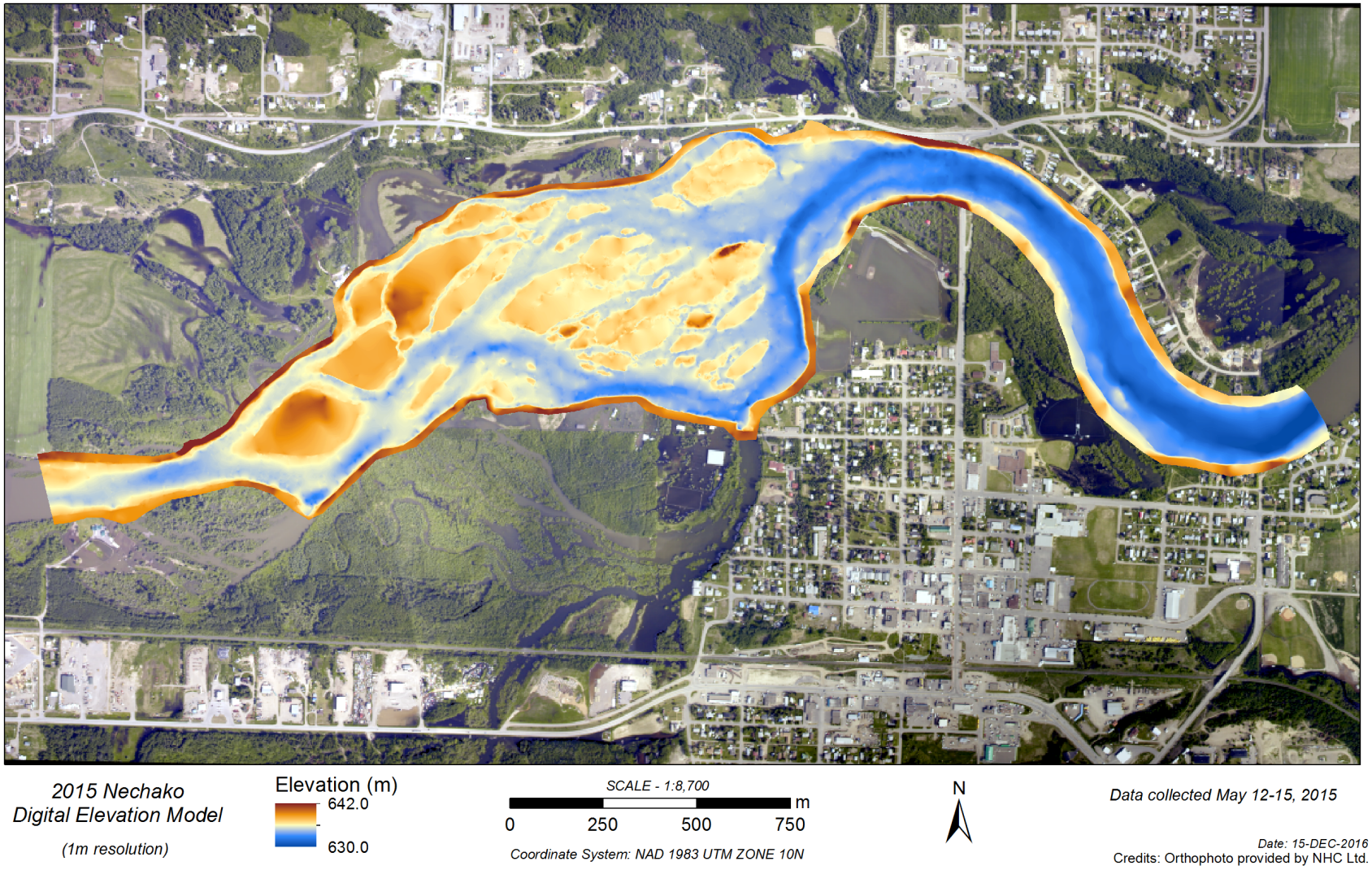

Figure D.2: 2015 DEM.

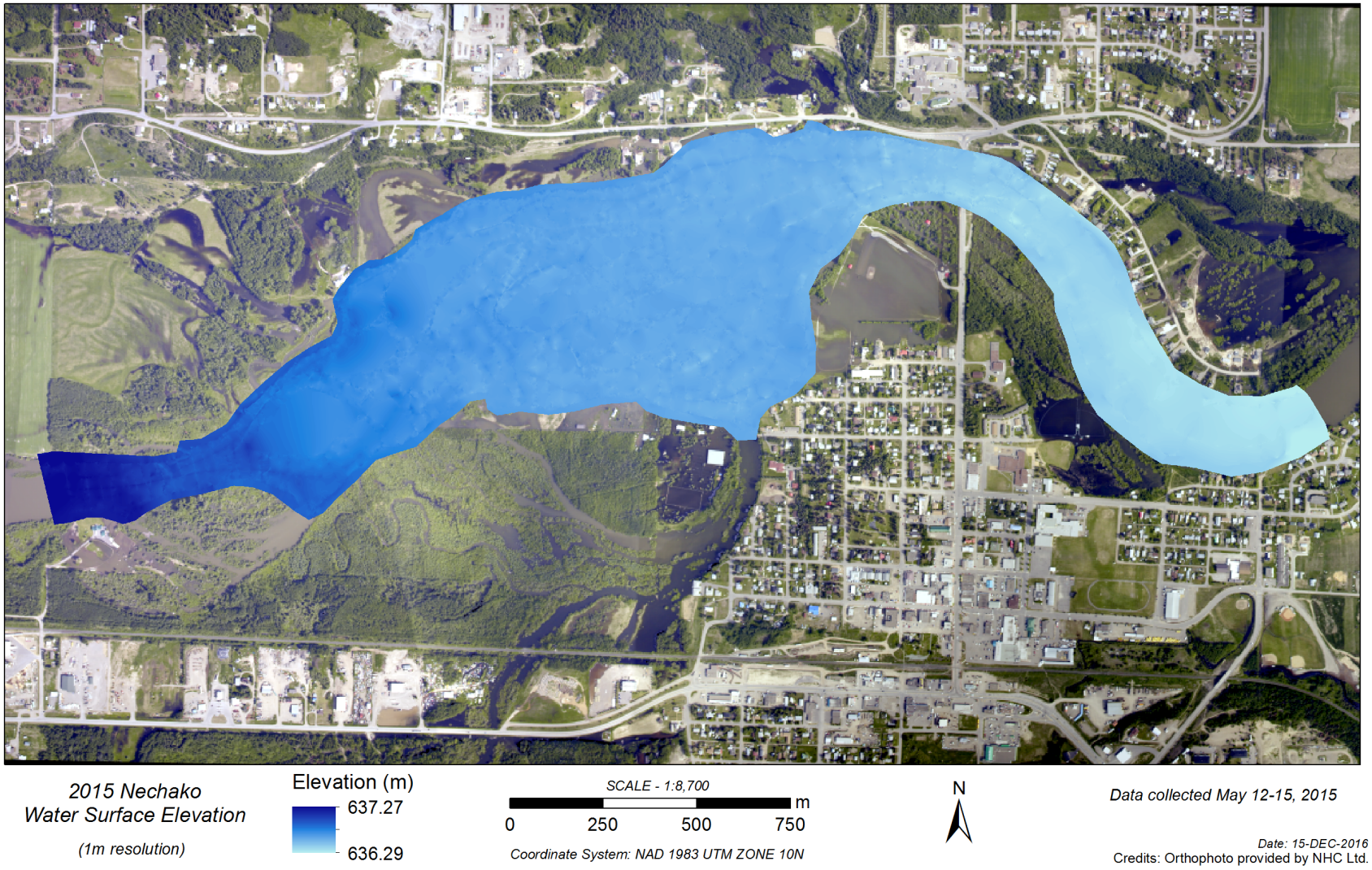

Figure D.3: Water surface elevation during a discharge of 525 m^3/s.

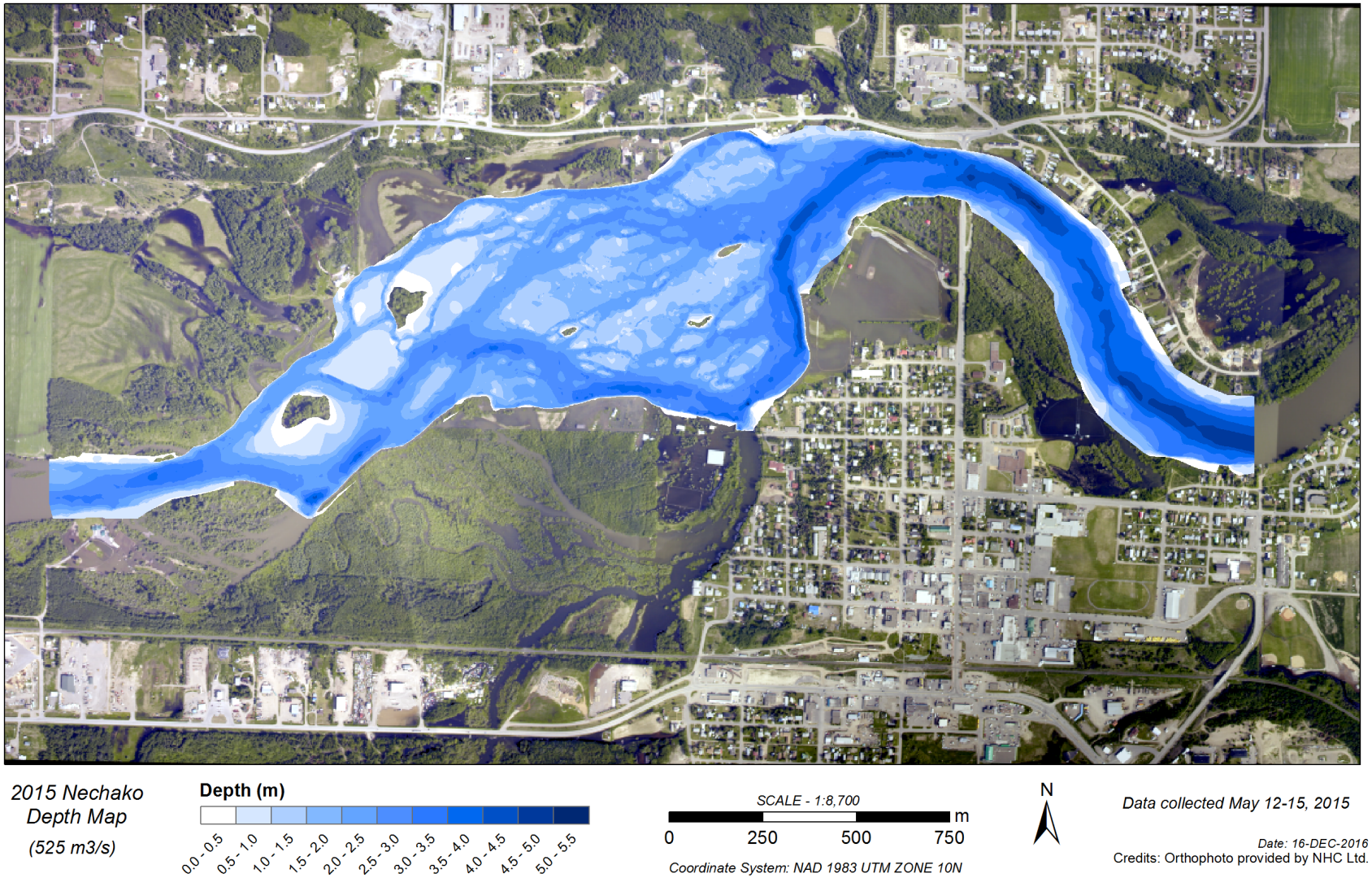

Figure D.4: Water depth during a discharge of 525 m^3/s.

Appendix E

Analysis of Annual Sediment Load using a Rating Curve Approach

The following excerpt is presented with permission from NHC and MFLNRO and was obtained from:

NHC. 2016. 2015 Sediment Transport Investigation on the Vanderhoof Reach of the Nechako River. Prepared for Ministry of Forests, Lands and Natural Resource Operations. January 31, 2016.

E.1 Bedload sediment transport

Data collected at the Upper Site suggests that the supply of bedload sediment became limited during the period of peak annual flow in June. This supply limitation is shown by the hysteresis in Figure E.1, where sediment transport declines at a greater rate per unit discharge during the receding limb of the hydrograph. Two separate bedload-discharge rating curves were developed for the Upper Site in order to accurately represent these different transport rates. The rising and falling limb rating curves were applied to the 2015 hydrograph, resulting in an estimated annual sediment load of 9,250 m^3. Predicted daily bedload transport at the Upper Site is in surprisingly good agreement with measured values given the inherent variability associated with sediment transport processes (Figure E.2).

Bedload transport at the Lower Patch showed no clear relation with discharge and therefore no rating curve could be used to derive the 2015 annual sediment load (Figure E.3). Rather, the estimated load of 3,050 m^3 was obtained by interpolating daily transport rates between sampled days. The Lower Patch bedload rate remained relatively constant between 100-300 g/s/transect for the majority of 2015, until the greatest transport rate of 1,384 g/s/transect was sampled on August 31st at a discharge of approximately 80 m^3/s.

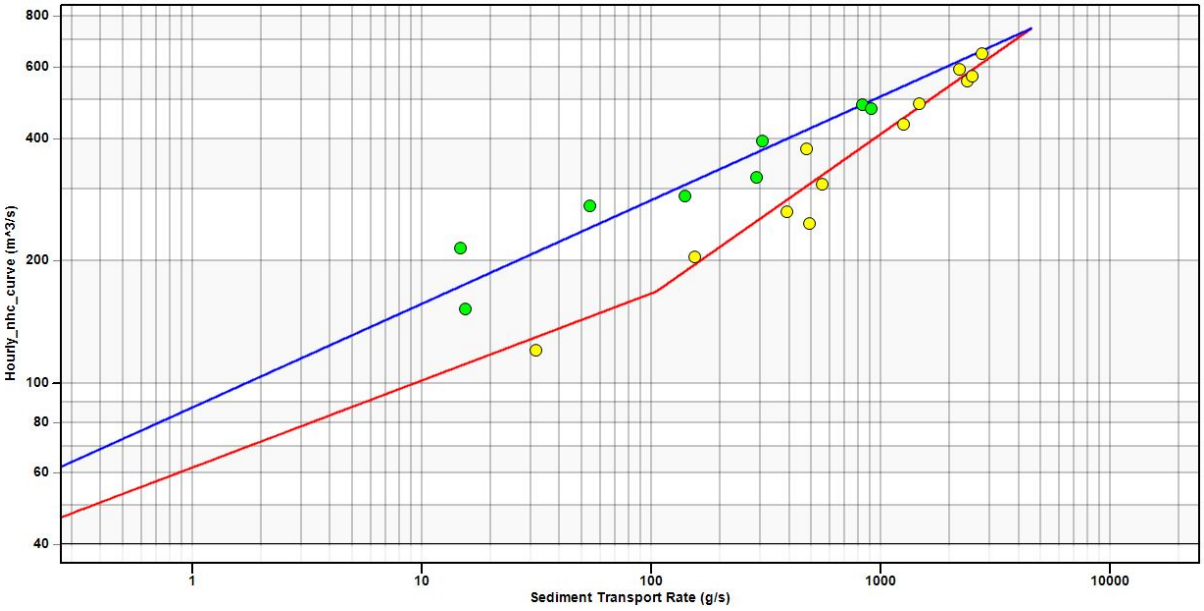

Figure E.1: Bedload rating curves developed for the Upper Site showing hysteresis (rising limb shown in red, receding limb in blue).

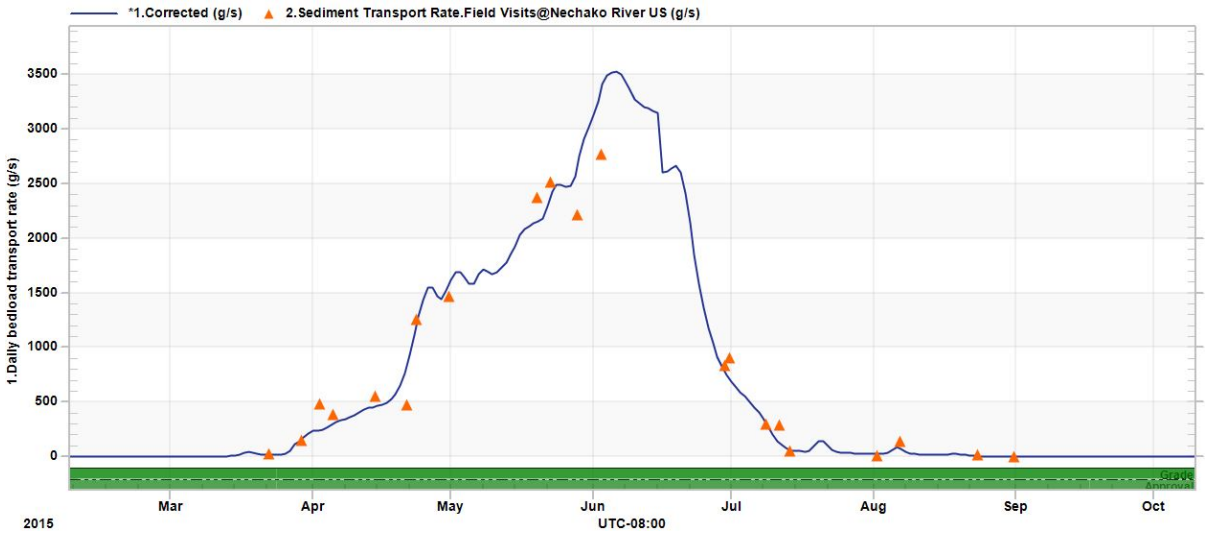

Figure E.2: Predicted versus observed bedload transport rate at Upper Site in 2015.

The maximum daily bedload transport rate is predicted to have been roughly 2.5 times greater at the Upper Site than Lower Patch, translating to values of 190 m^3/day and 75 m^3/day respectively. The daily bedload rate at the Upper Site exceeded 75 m^3/day for 61 consecutive days between April 25th and June 24th, 2015. The significant difference in bedload transport between the upstream and downstream extent of the reach suggests 6,200 m^3 of sediment has been stored within the reach in this year. This net storage is interesting because previous years have observed the opposite trend with more sediment being output from the reach than input (NHC, 2014; NHC, 2015).

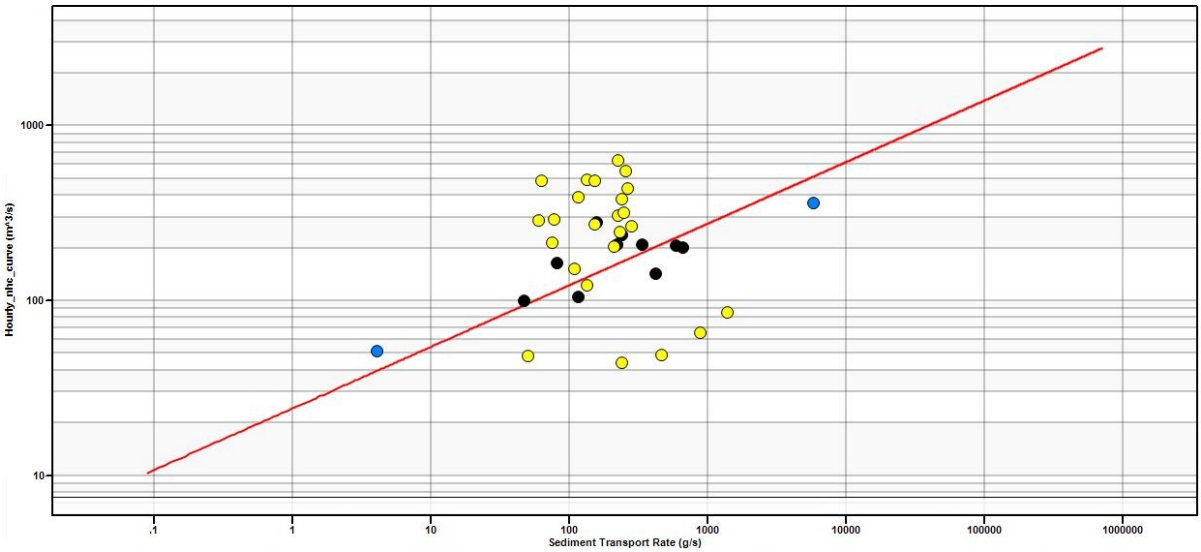

Figure E.3: Bedload transport at the Lower Patch showing no clear relation with discharge in 2015. Samples taken in 2015 are yellow, 2014 are black and 2013 are blue. The rating curve used in 2014 is shown in red.

Appendix F

Bedload Sediment Transport through the Nechako Spawning Reach

F.1 Data processing

Sampled transport rates were binned into 100 m^3/s discharge intervals. If a location was sampled more than once during the discharge interval, the mean transport rate was calculated. Figures F.1 to F.7 plot the bedload transport rate through different channels, sampled throughout the 2015 flood hydrograph.

F.2 Maps

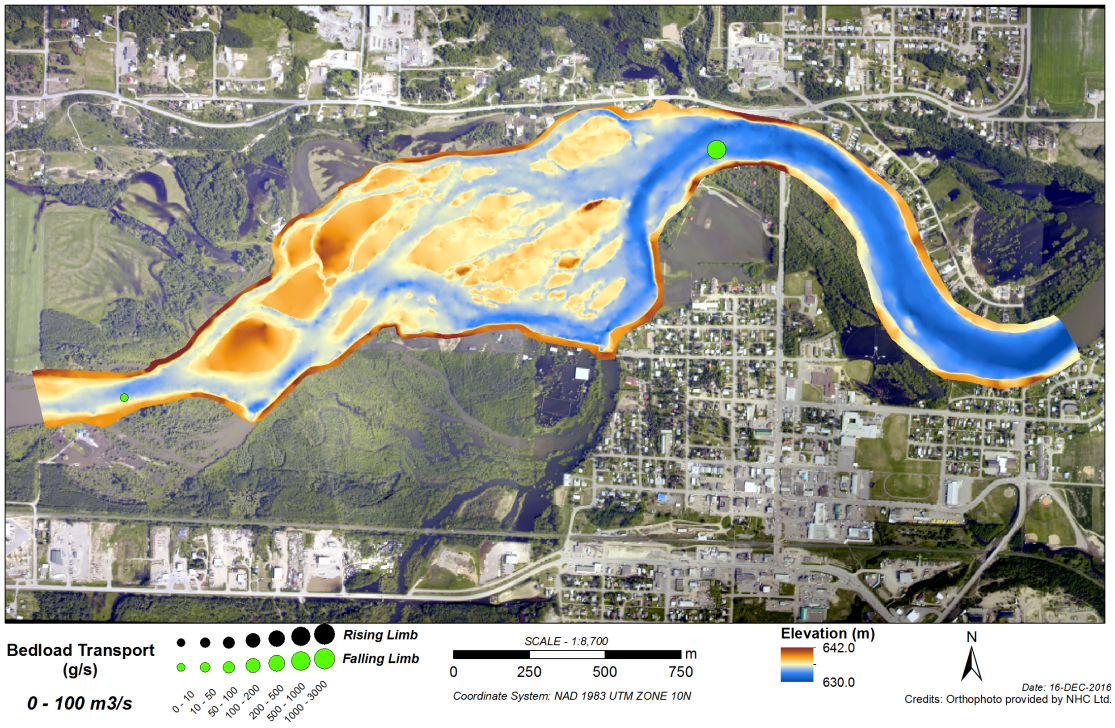

Figure F.1: Sampled transport rates (discharge below 100 m^3/s).

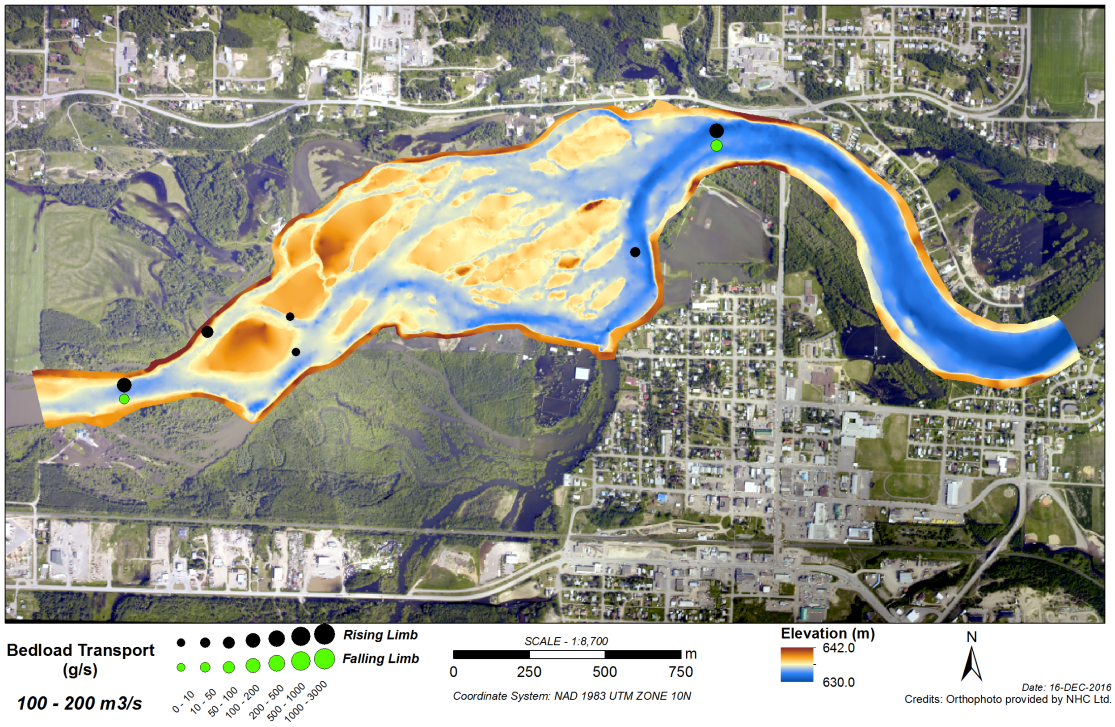

Figure F.2: Sampled transport rates (100-200 m^3/s).

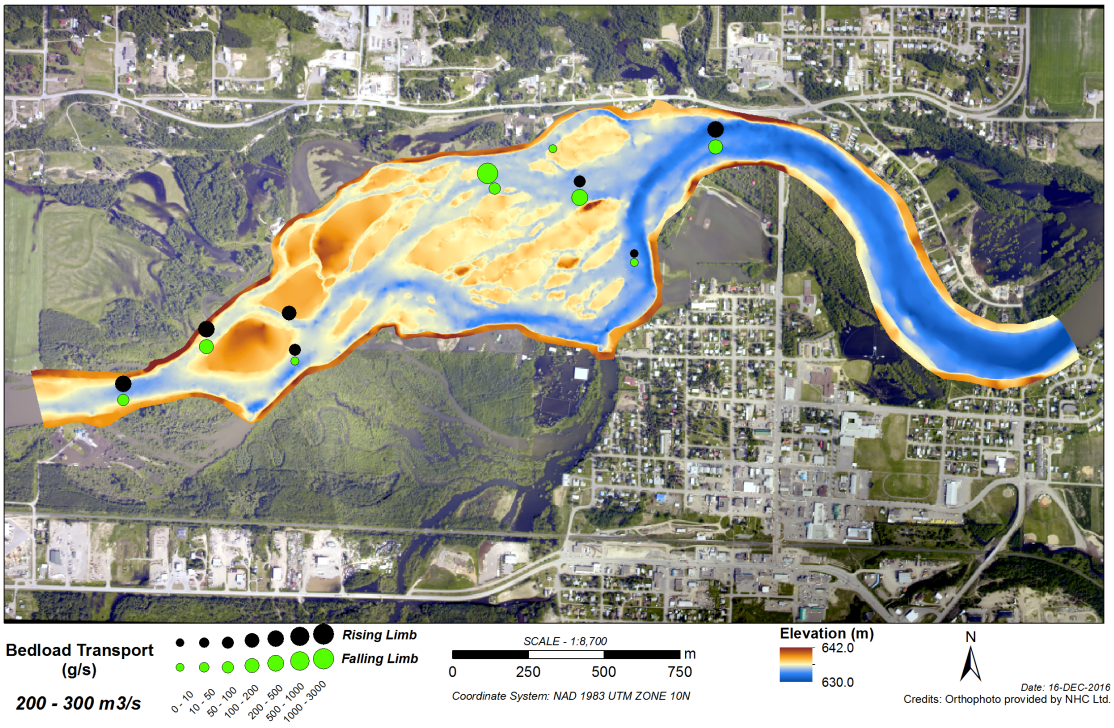

Figure F.3: Sampled transport rates (200-300 m^3/s).

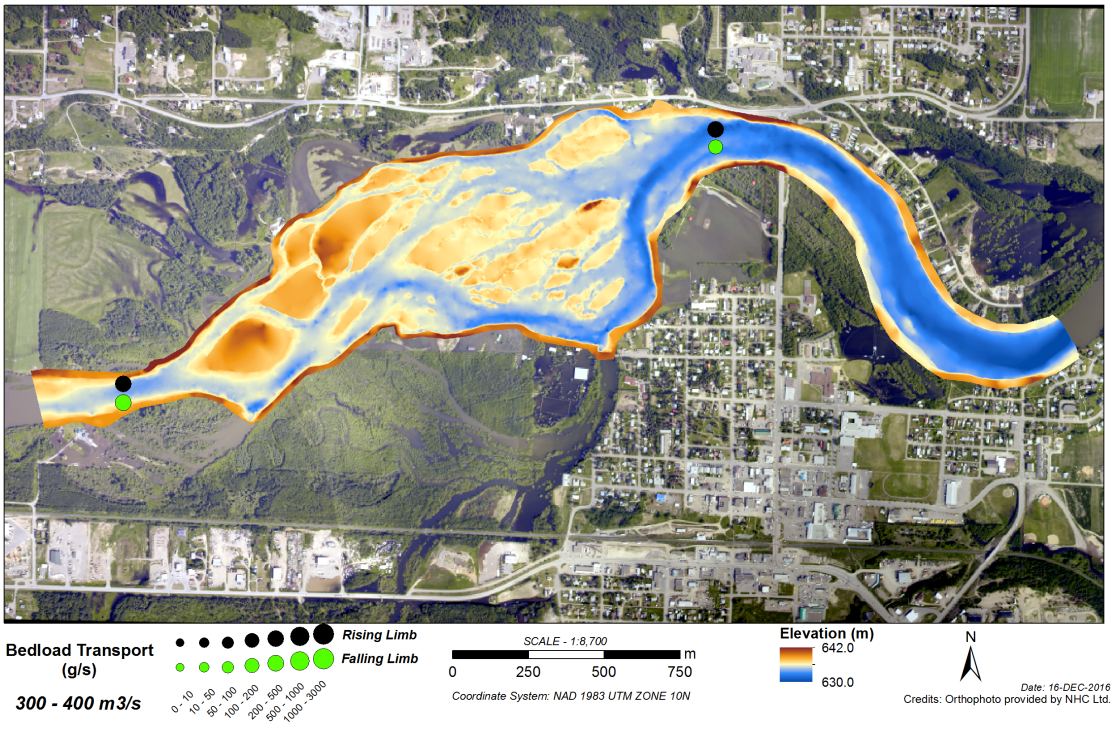

Figure F.4: Sampled transport rates (300-400 m^3/s).

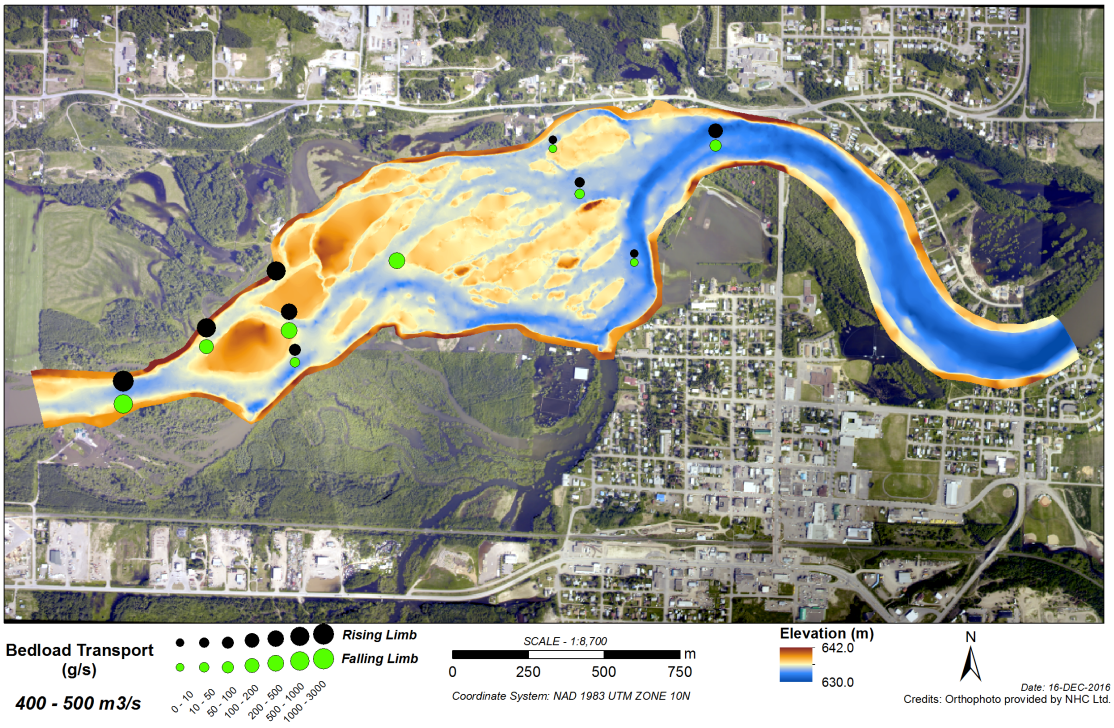

Figure F.5: Sampled transport rates (400-500 m^3/s).

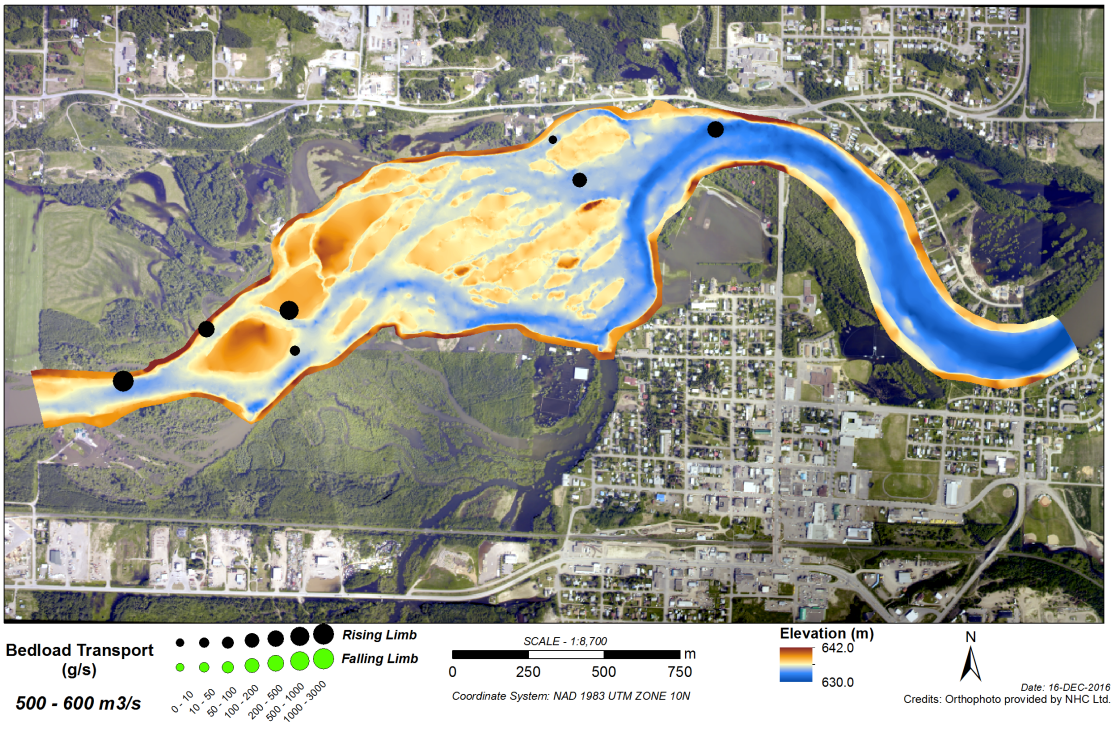

Figure F.6: Sampled transport rates (500-600 m^3/s).

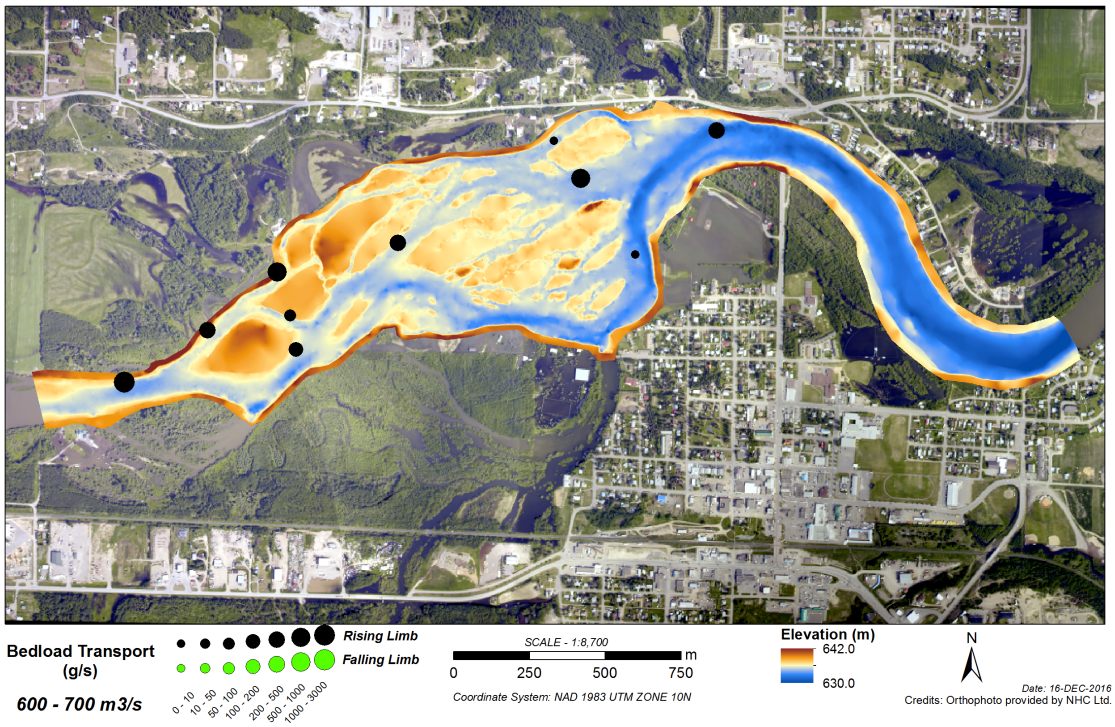

Figure F.7: Sampled transport rates (600-700 m^3/s).

Appendix G

Two-Dimensional Flow Modelling of the Nechako River using Nays2DH

G.1 Methods

*This section provides supplementary information to section **5 Modelling** in the thesis; previously described aspects have been omitted.*

G.1.1 Configurations

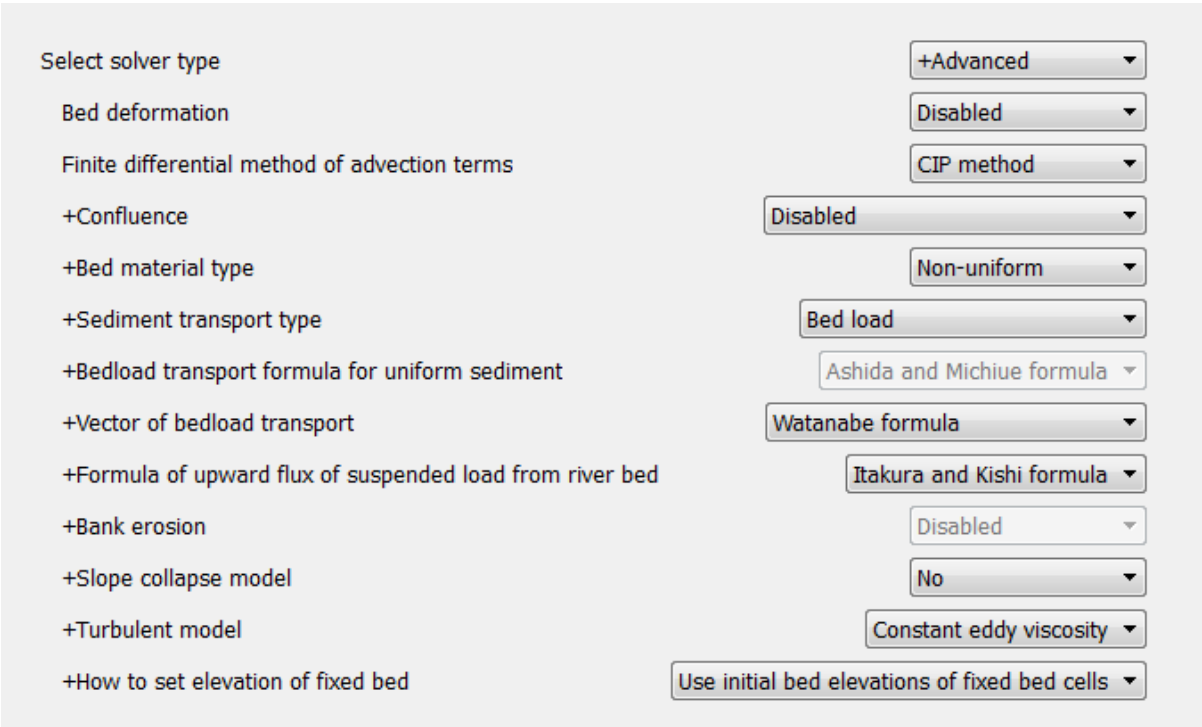

Figure G.1: Solver type calculation conditions.

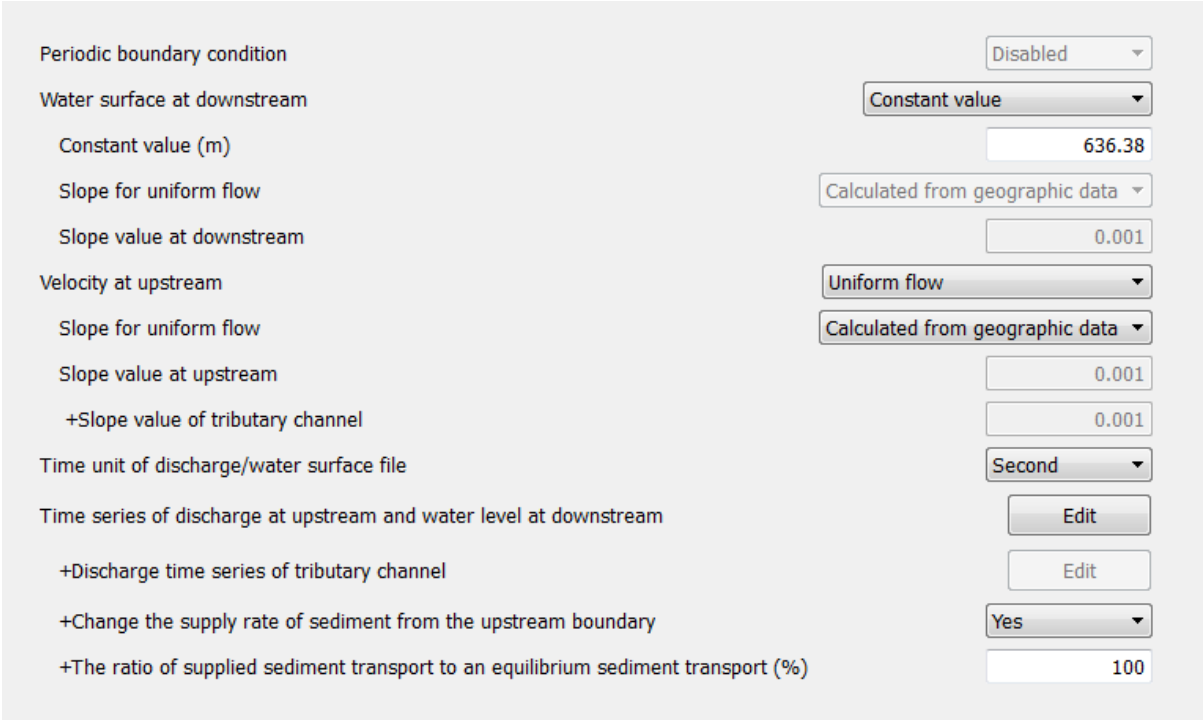

Figure G.2: Boundary conditions (for simulated discharge of 523 m^3/s).

The mesh was created from a polygonal centerline and defined domain width of 900 m. The curvilinear centerline was drawn down the middle of the reach, rather than along the main southern channel, to avoid pinching of the mesh in meanders. The length of the modelling domain is 3,300 m, resulting in a total of 118,440 cells for a 5-m resolution mesh. Elevation was imported to the model from the DEM created in ArcGIS and overbank areas with no data were assigned a high elevation of 638 m (Figure G.3). Shapefiles of bar contours and banklines from the RTK survey were imported and assigned different vegetation densities to locally increase drag (Figure G.4). The model domain was separated into five regions (Figure G.5), each with a unique grain size distribution that was assigned based on the results of photo-sieving. Although it was preferable to use only one value of Manning's roughness for the entire channel to reduce its influence on modelled shear stress, three polygons were drawn and assigned slightly higher roughness values within a hydrodynamically complex area to increase model stability, especially during high-flow simulations (Figure G.6).

A stage-discharge rating curve was developed to specify the water surface elevation at the downstream extent of the model domain. This was necessary because flow is non-uniform during moderate to high discharge and therefore the model could not use uniform flow calculations to set the downstream boundary condition. The rating curve (Figure G.7) was developed by iteratively adjusting the input WSE until good agreement was achieved between modelled output and measured stage at WSC Gauge 08JC001, located approximately 1 km upstream of the model boundary (Figure G.8).

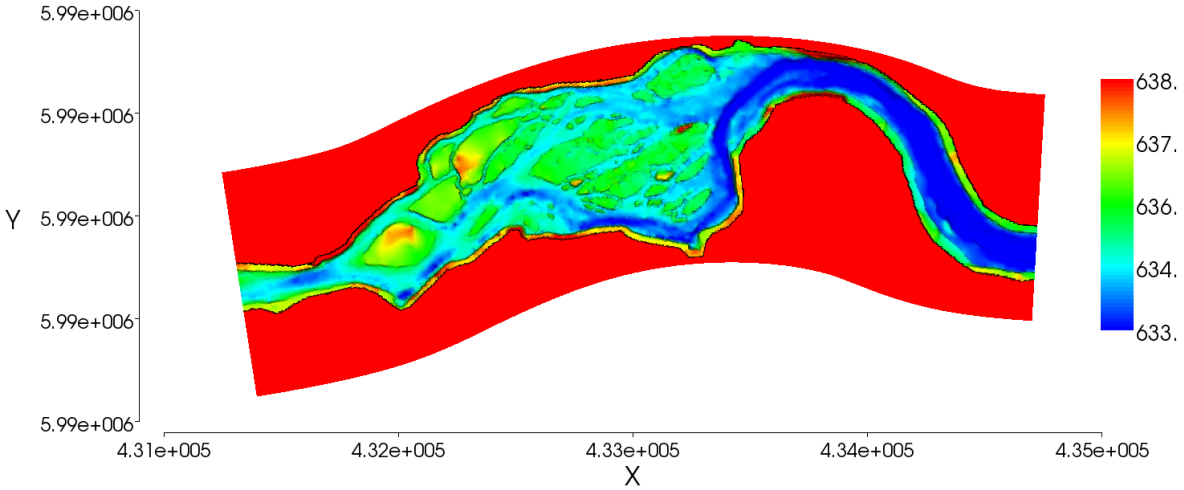

Figure G.3: Entire modelling domain showing elevation in meters.

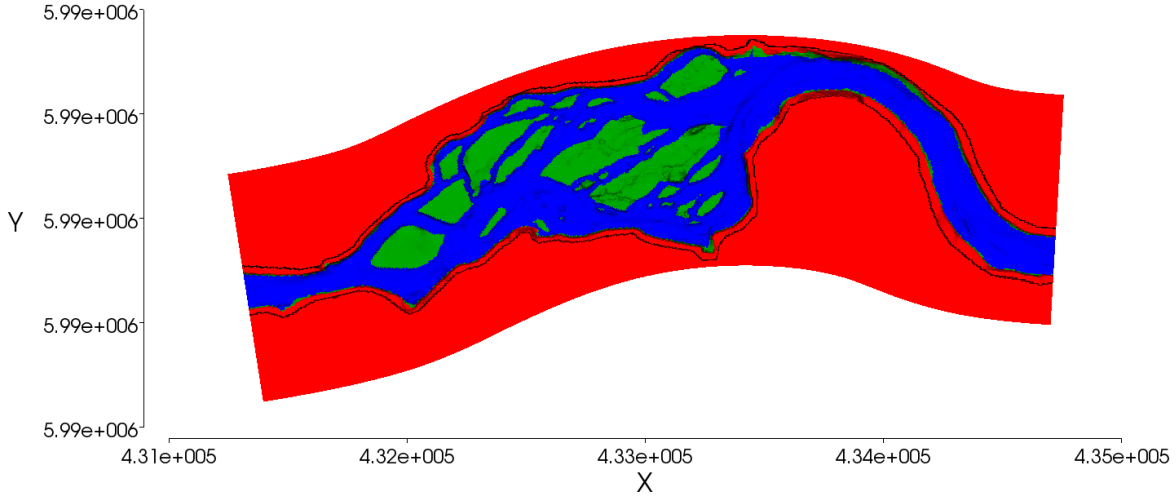

Figure G.4: Vegetation density specified using shapefiles of bar contours and banklines, bars (green) were assigned a vegetation density of 0.1 stems/m^2 and overbank areas (red) were assigned a vegetation density of 2 stems/m^2.

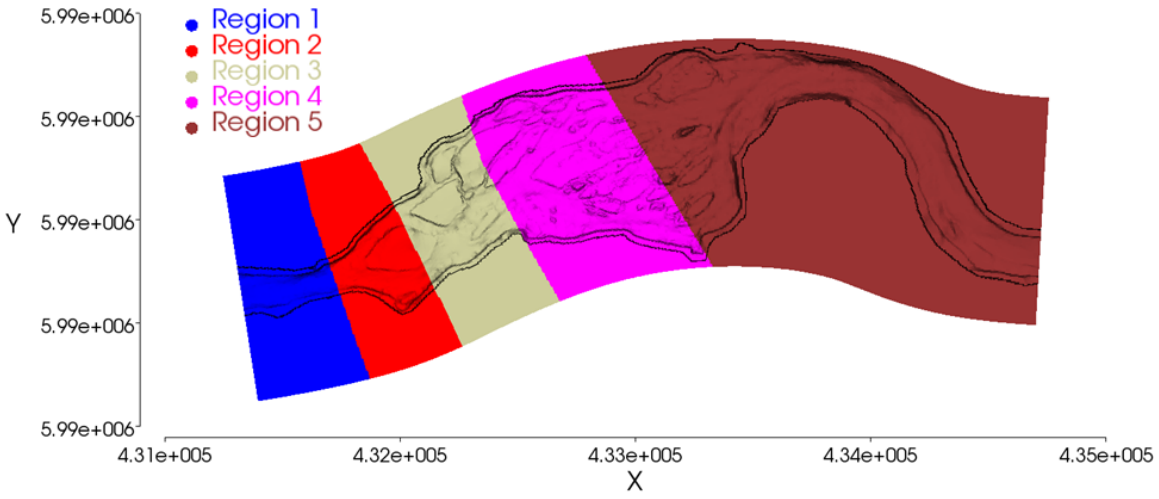

Figure G.5: Specific grain size distributions were input to the model for each region based on the results of photo-sieving underwater photos.

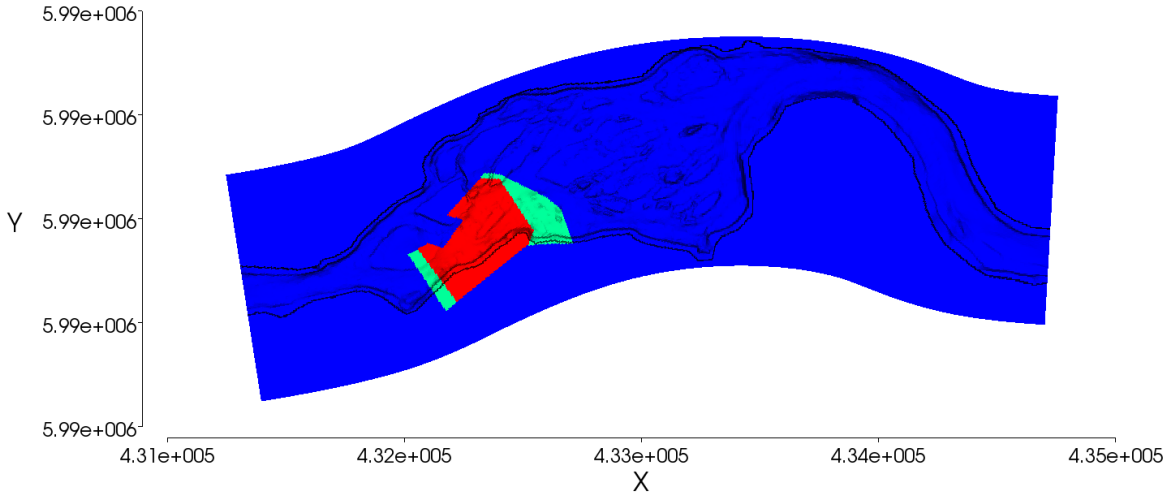

Figure G.6: Manning's roughness used for the entire domain in blue (n = 0.0215) with additional polygons added for numerical stability during high flow simulations in green (n = 0.022) and in red (n = 0.024).

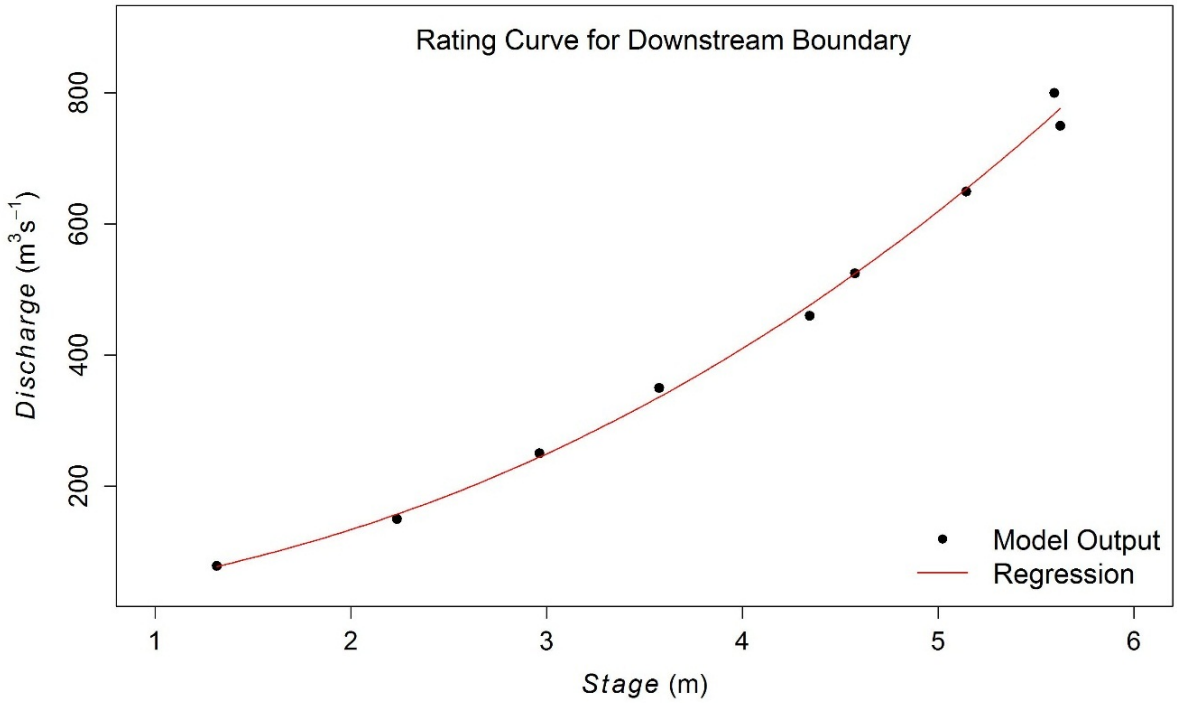

Figure G.7: Rating curve developed to specify WSE at the downstream extent of the model domain.

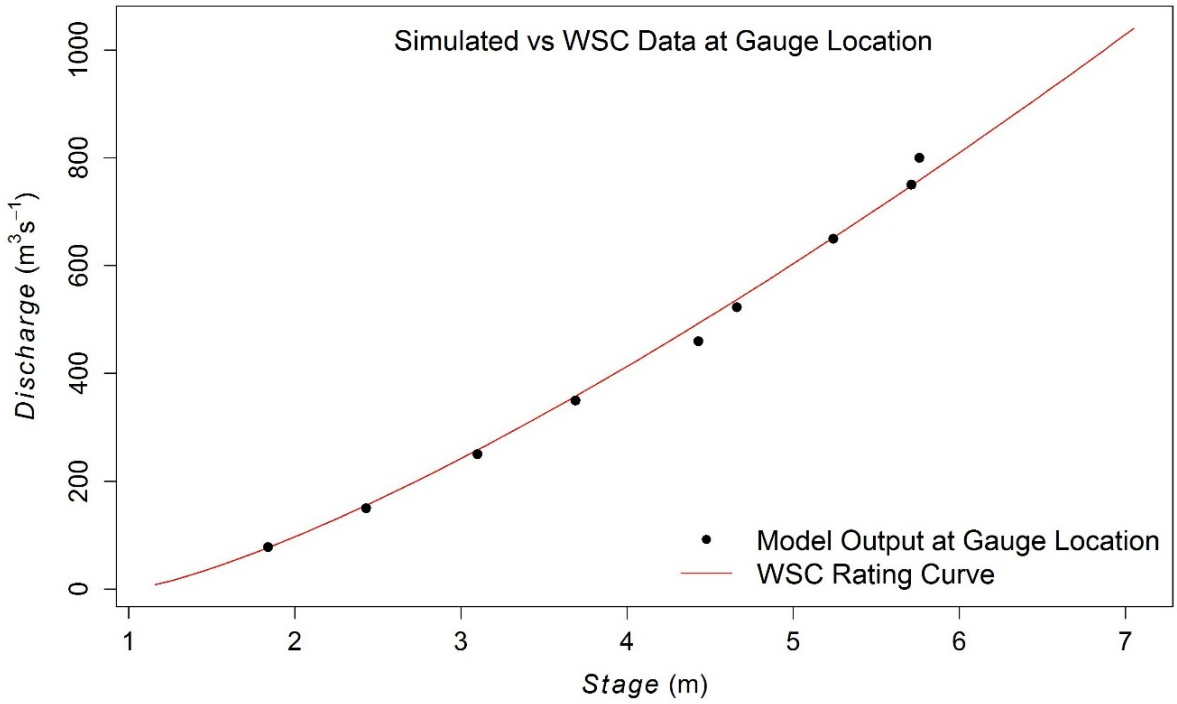

Figure G.8: Modelled vs measured stage at the WSC gauge used to develop the downstream rating curve.

G.1.2 Processing the grain size data

The grain size distributions for Regions 1-5 were obtained by photo-sieving a series of 30 underwater images taken across transects US, MU-A, MU-B, MU-D, M-A and LP. Figures G.9 to G.13 provide examples of one photo from each transect. Images were photo-sieved using a Wolman Pebble Count approach, where 100 grains were measured within the image frame at fixed intervals. The finest size class used for classification was sand, so all grains sized 2 mm or finer were included within the 2 mm fraction. The resulting grain size distribution for Region 1 through Region 5 are presented in Figures G.14 to G.18

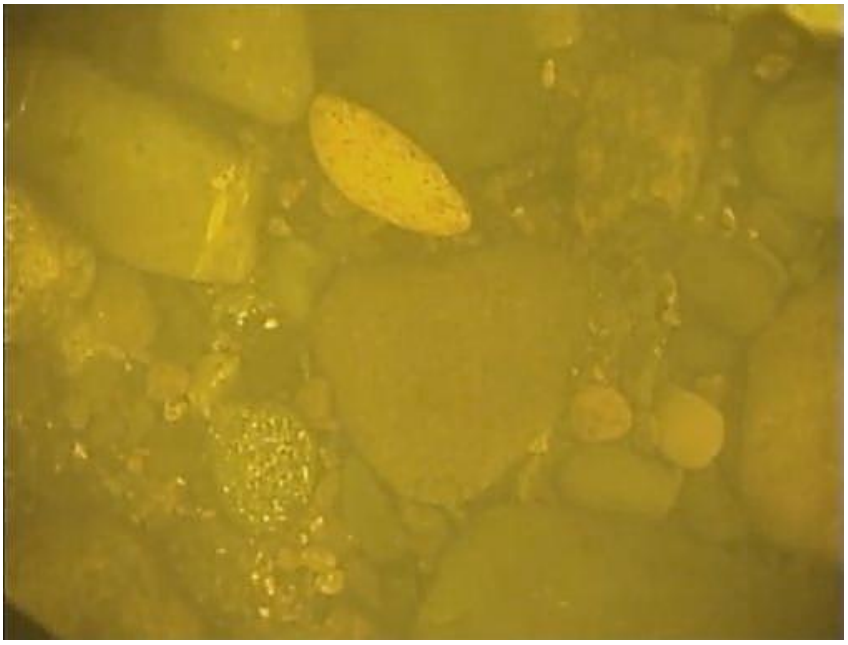

Figure G.9: Region 1 grain size distribution obtained by photo-sieving images at the US transect.

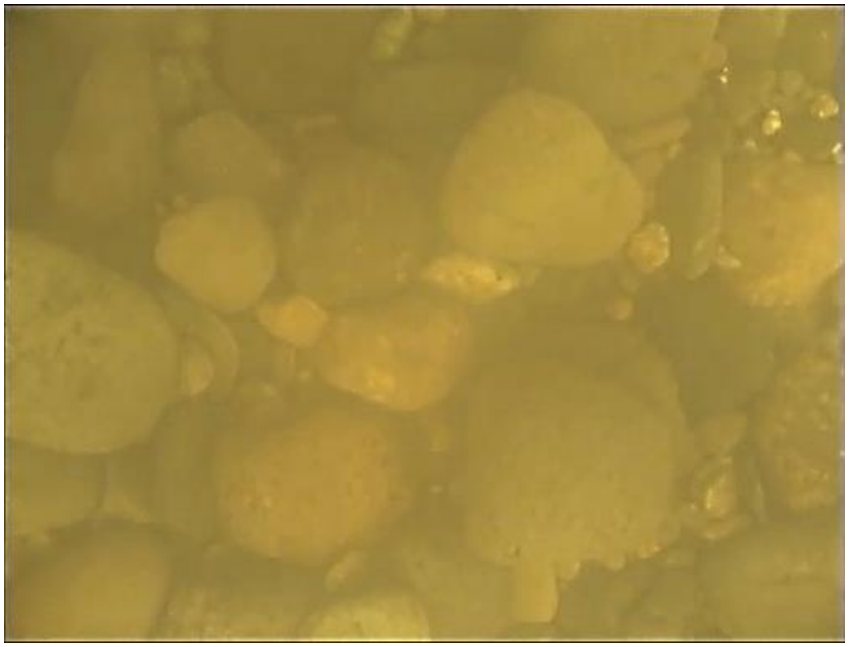

Figure G.10: Region 2 grain size distribution obtained by photo-sieving images at the MU-A transect.

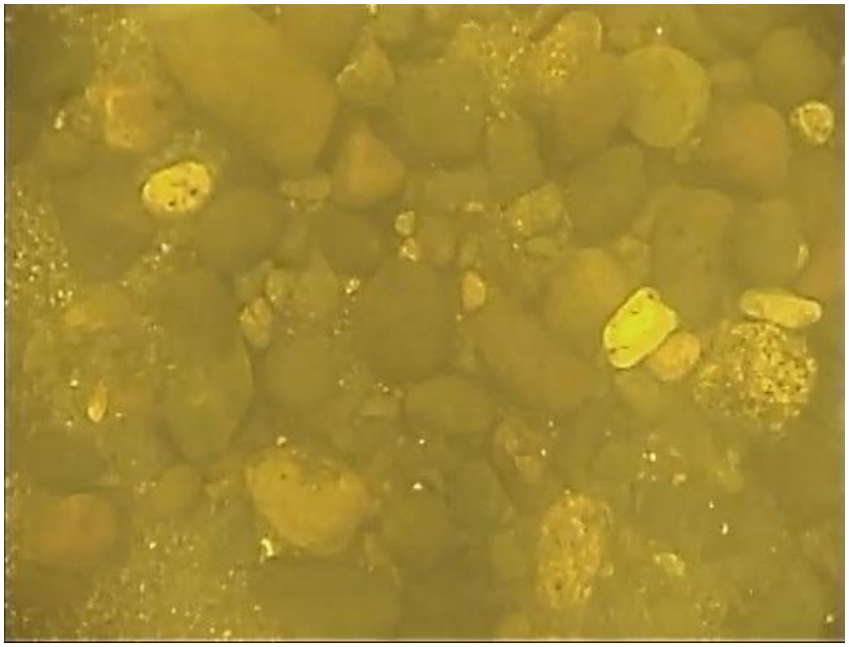

Figure G.11: Region 3 grain size distribution obtained by photo-sieving images at the MU- B and MU-D transects.

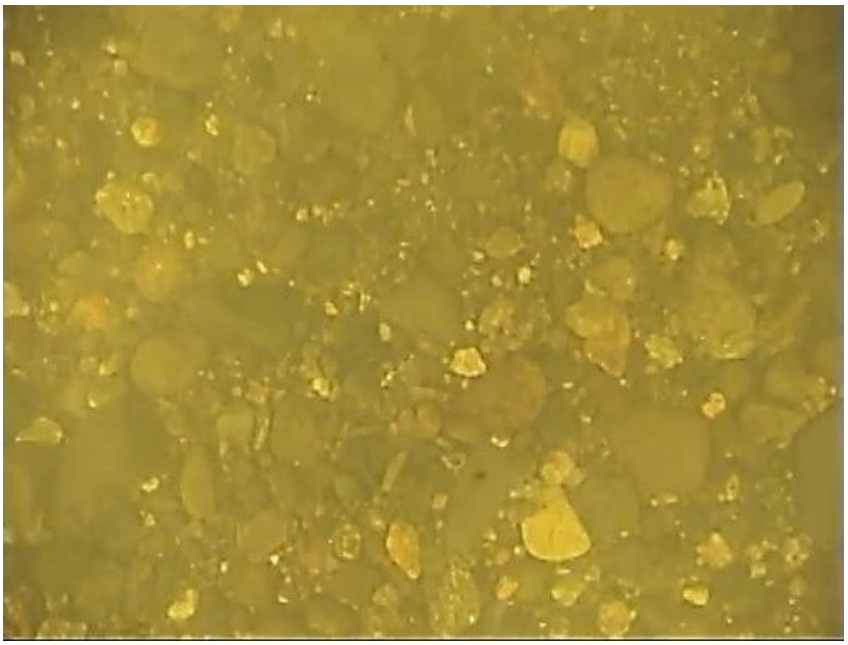

Figure G.12: Region 4 grain size distribution obtained by photo-sieving images at the M-A transect.

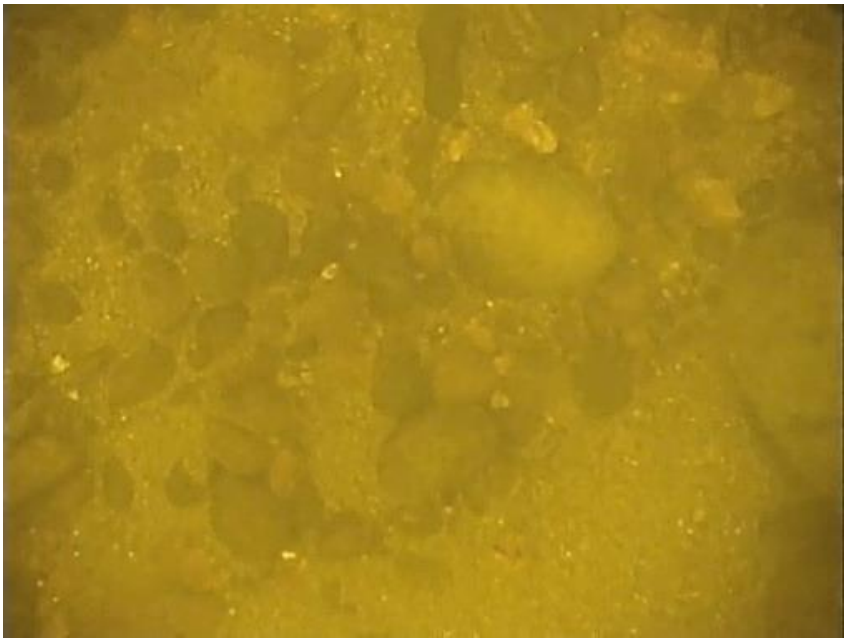

Figure G.13: Region 5 grain size distribution obtained by photo-sieving images at the LP transect.

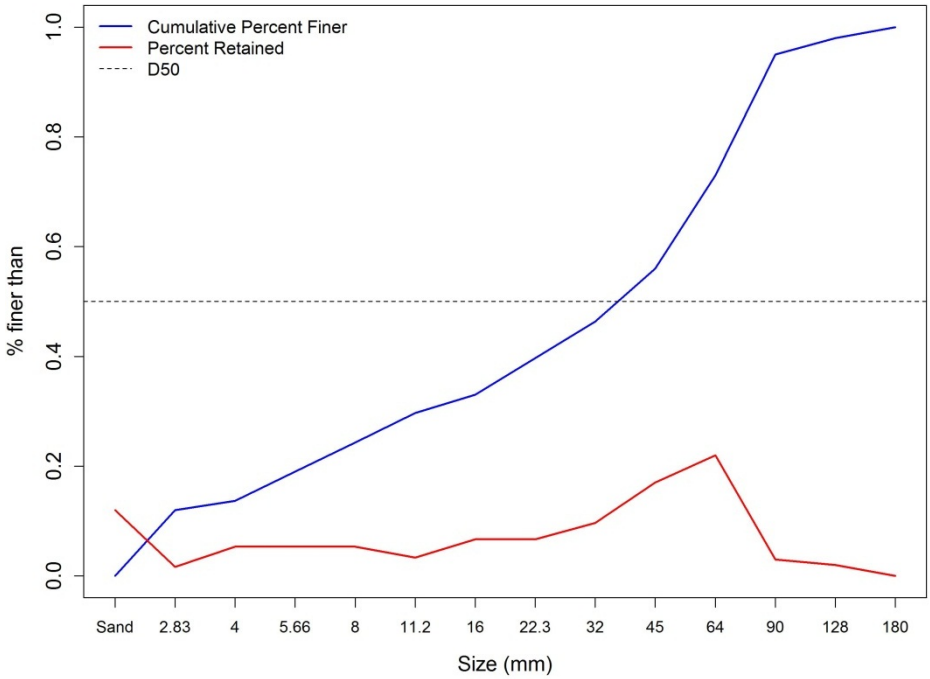

Figure G.14: Region 1 grain size distribution.

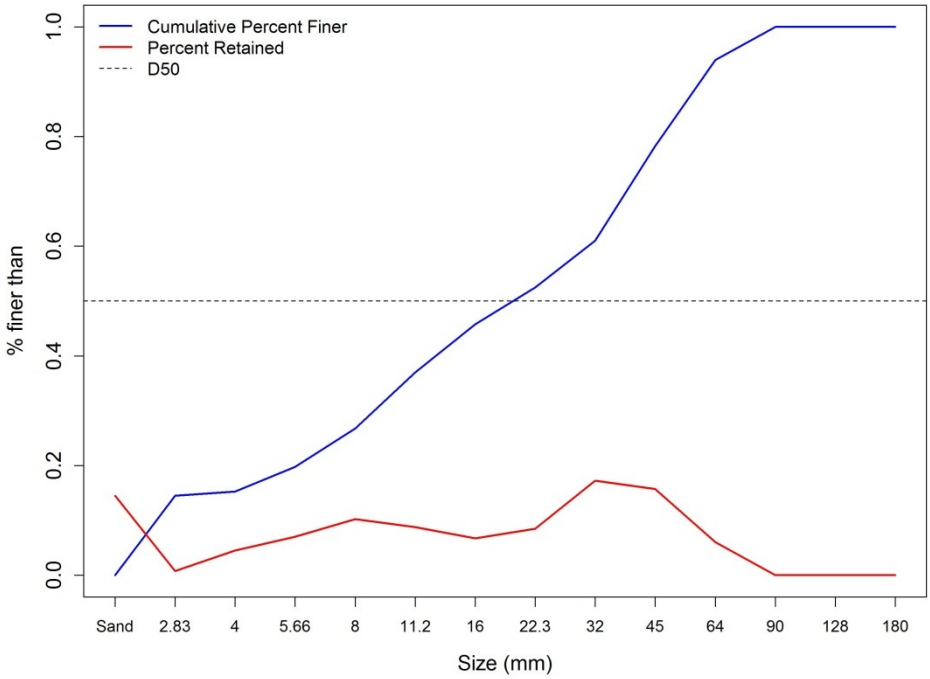

Figure G.15: Region 2 grain size distribution.

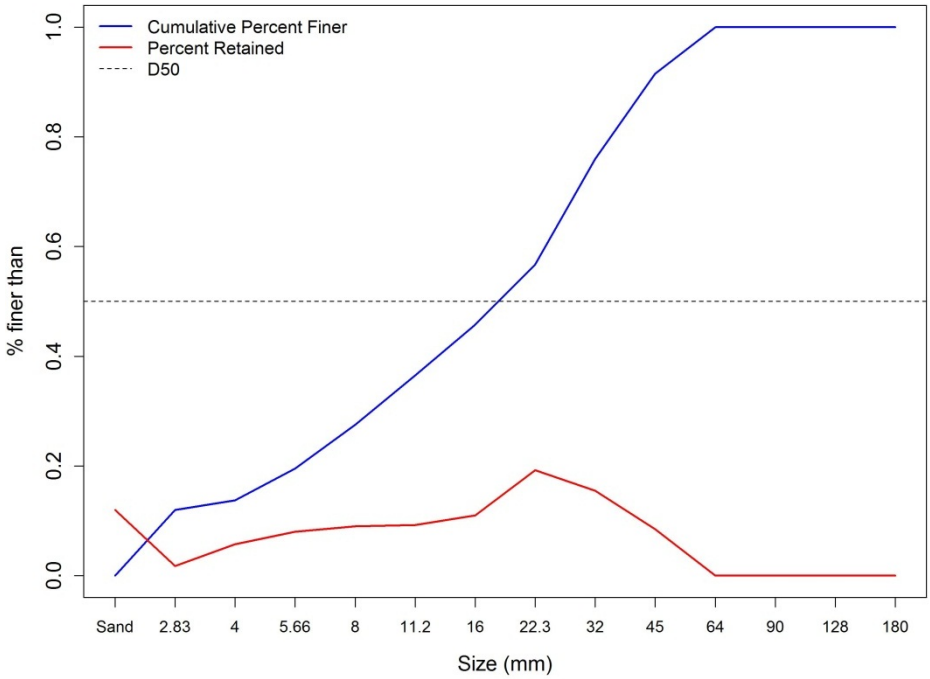

Figure G.16: Region 3 grain size distribution.

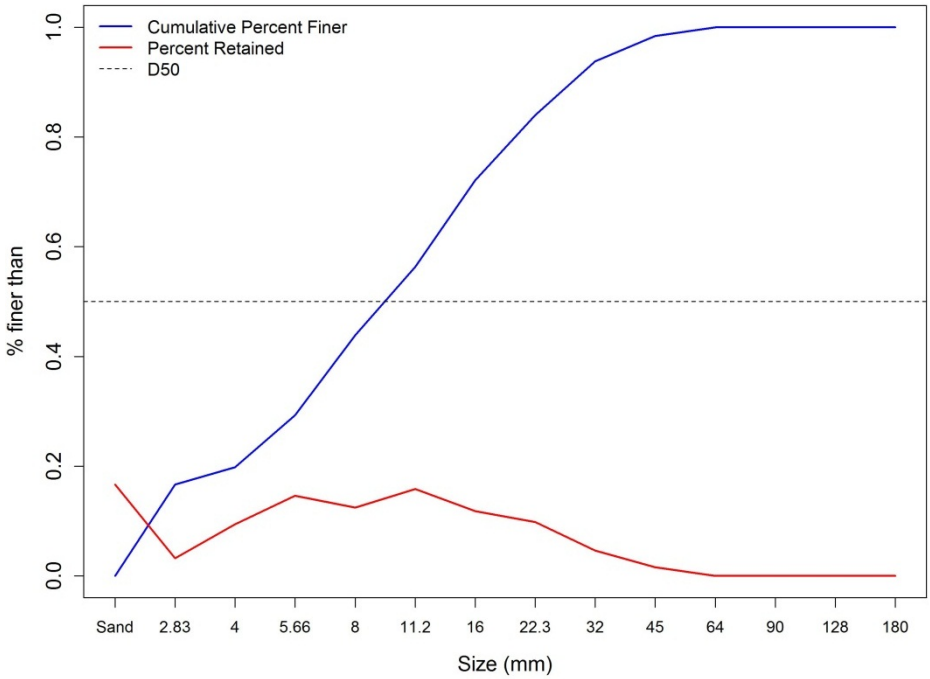

Figure G.17: Region 4 grain size distribution.

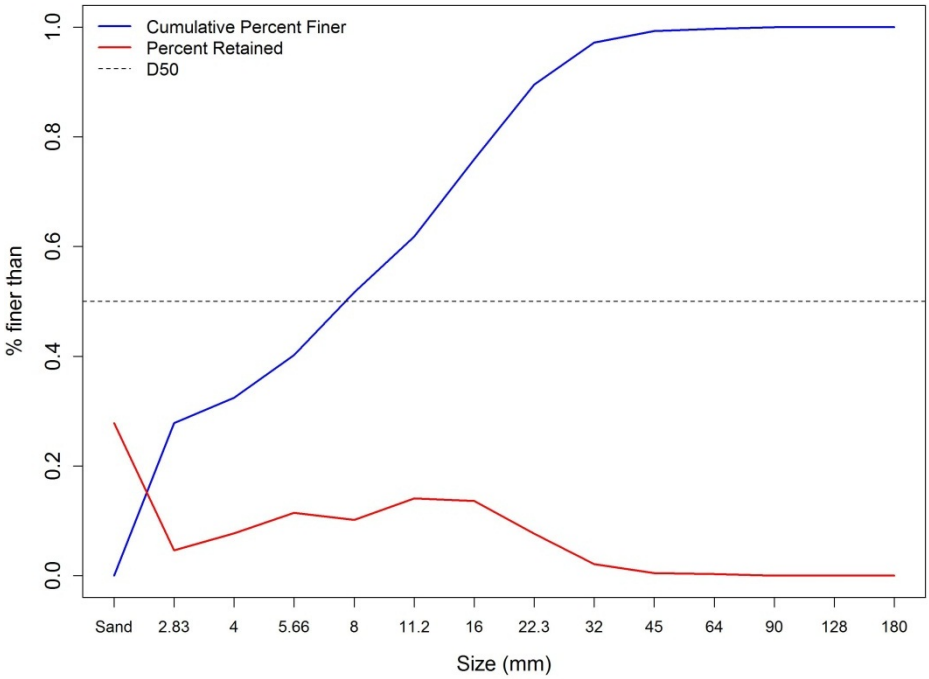

Figure G.18: Region 5 grain size distribution.

G.1.3 Processing the model output

The first step in processing the model output was averaging the last 1,000 seconds of each simulation. A discharge of 523 m^3/s was used to validate the model against WSE and velocity data collected with the ADCP. Modelled WSE profiles (presented in section **5.2 Calibration and Validation** in the thesis) were validated by comparing each data point to the value within the nearest 5 m grid cell from the model output. This same approach was used to validate the model against cross-channel binned velocity and depth data. For each of the 9 ADCP transects, absolute error and percent error was calculated for velocity, depth and specific discharge within each cross-channel bin. Results from the model validation are presented as a series of plots; simulated versus observed velocity is presented in Figures G.19 to G.27, and simulated versus observed depth in Figures G.28 to G.36. The cross-channel errors for each transect were then averaged into a mean absolute and mean absolute percent error (Table 5.1 within the thesis).

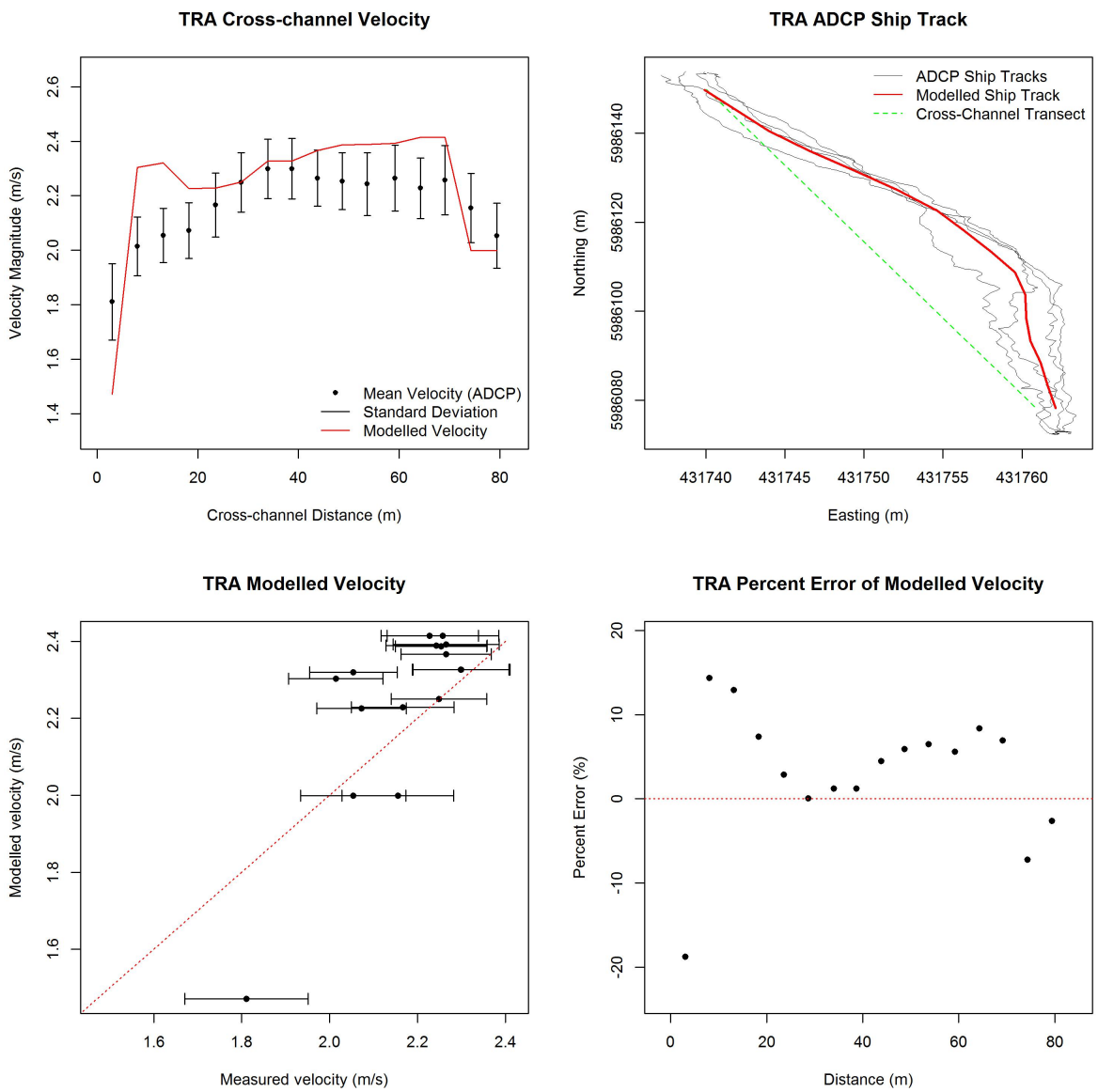

Figure G.19: Model velocity validation at transect TRA.

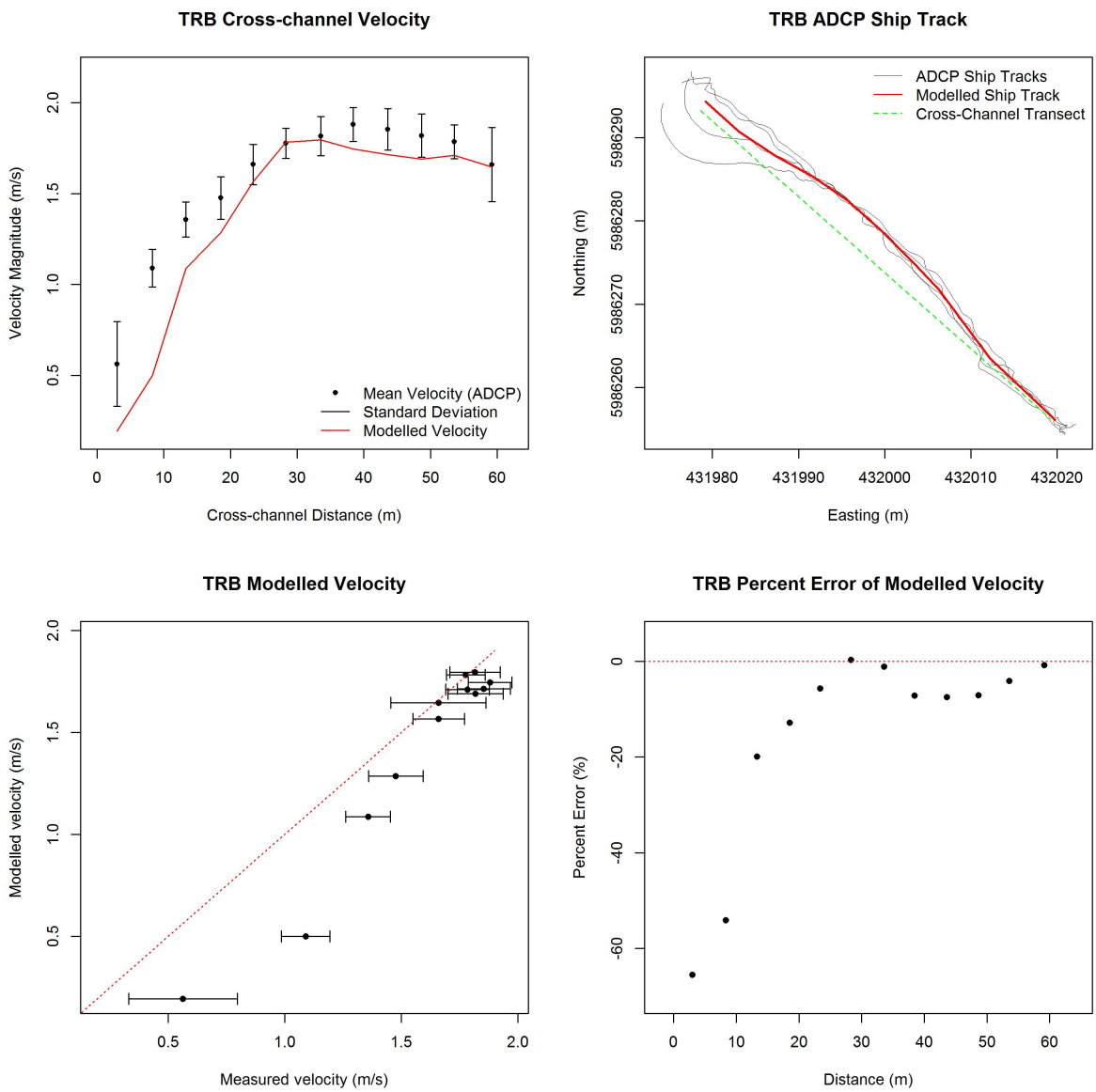

Figure G.20: Model velocity validation at transect TRB.

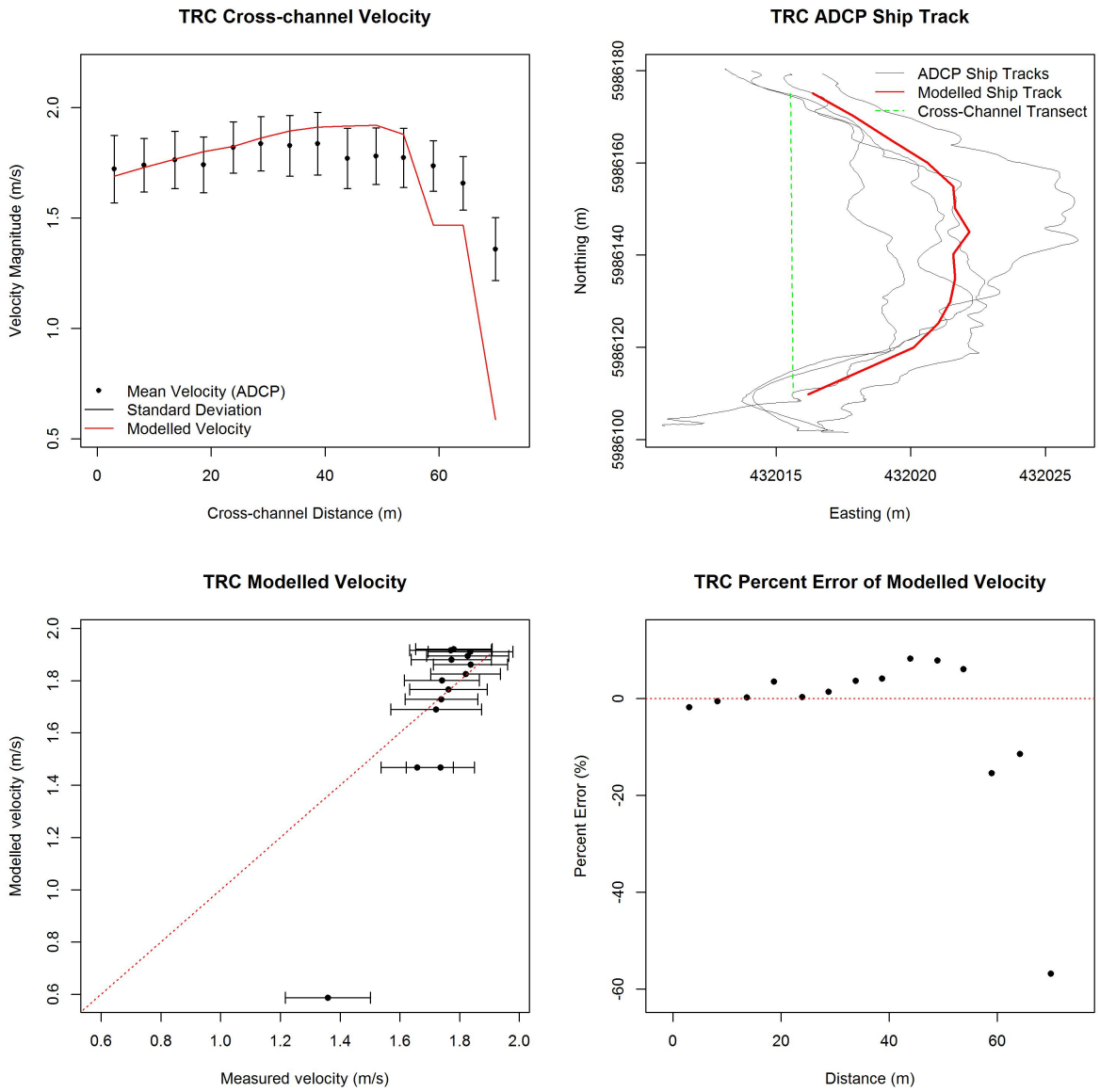

Figure G.21: Model velocity validation at transect TRC.

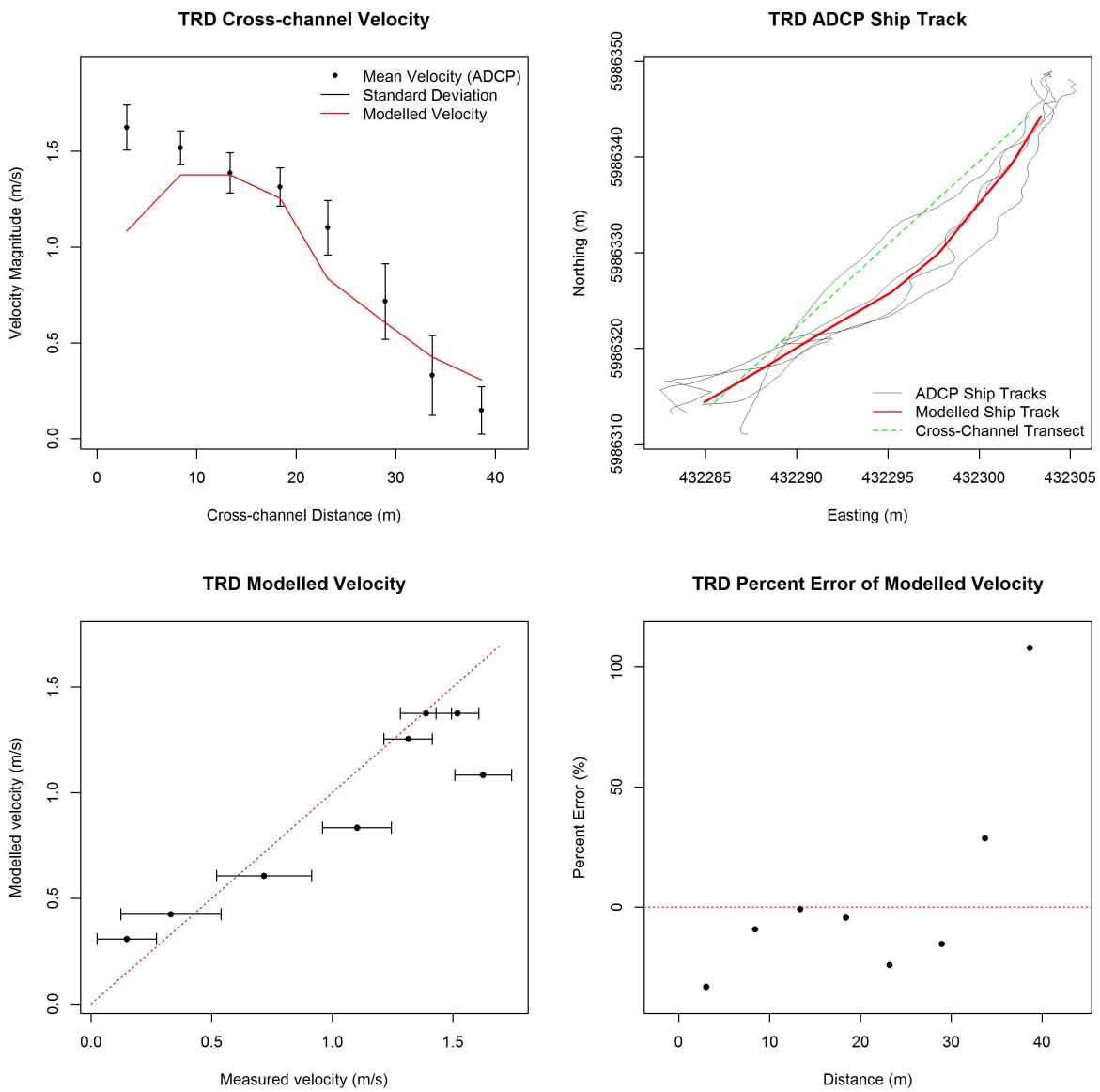

Figure G.22: Model velocity validation at transect TRD.

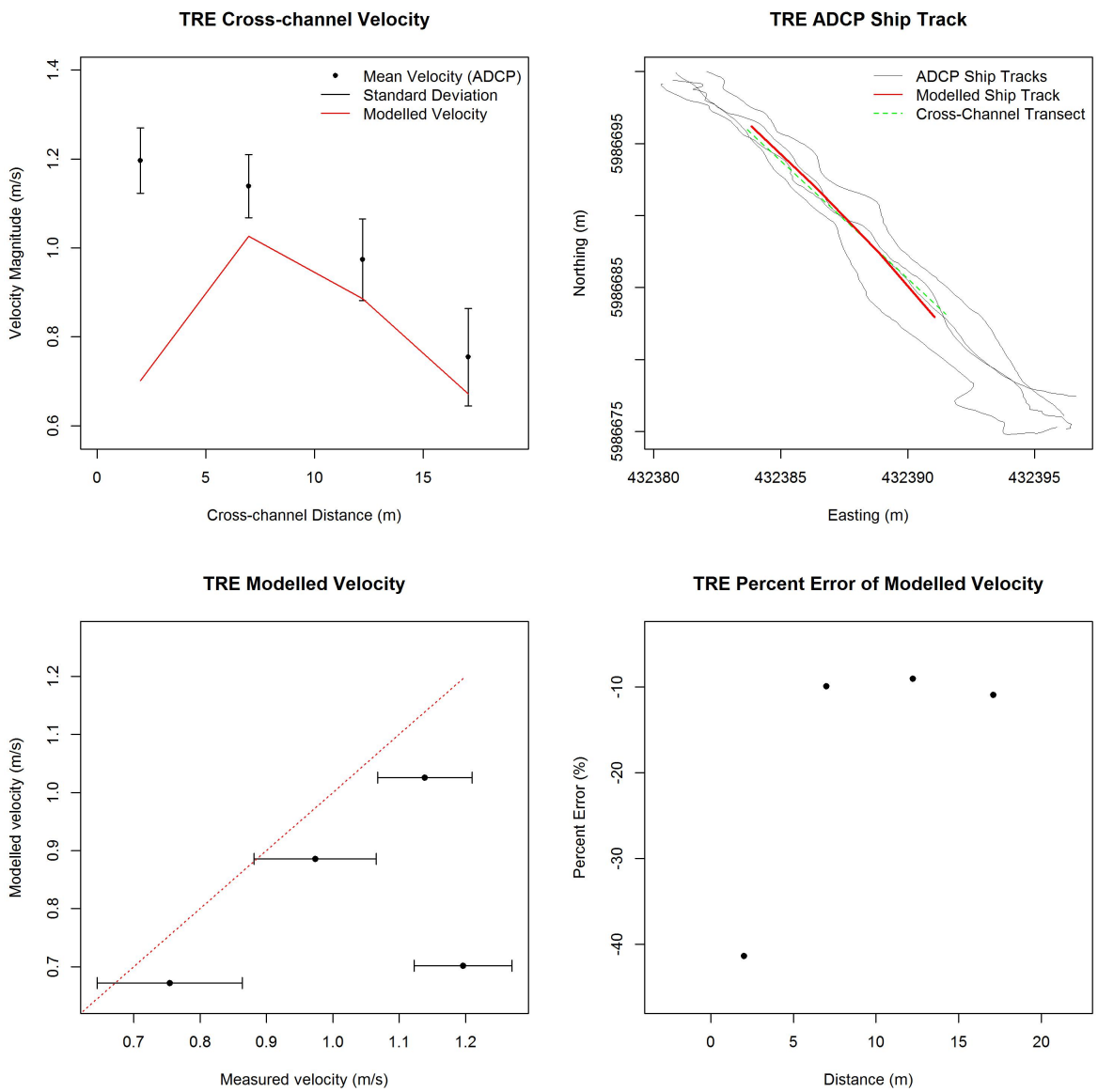

Figure G.23: Model velocity validation at transect TRE.

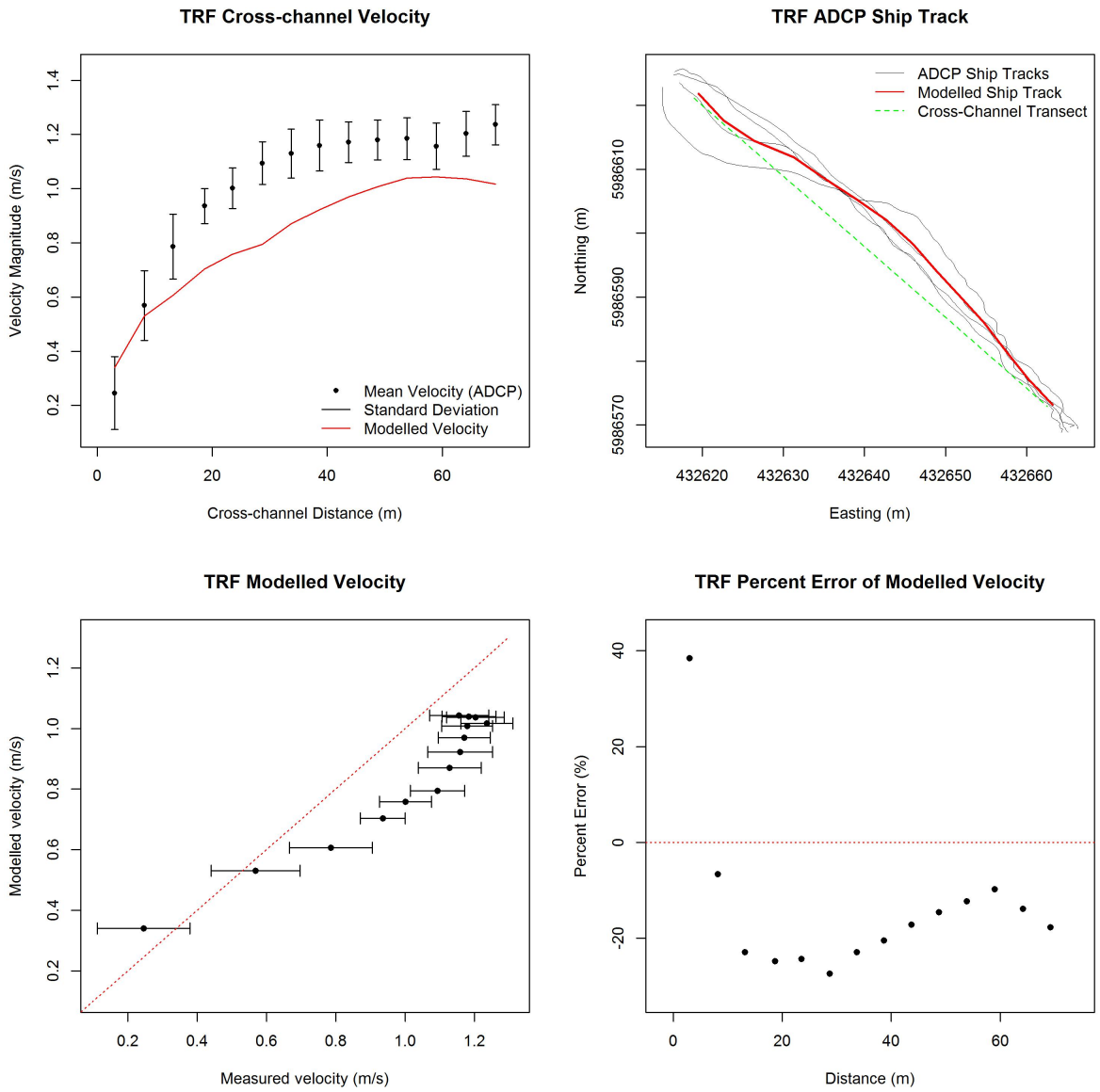

Figure G.24: Model velocity validation at transect TRF.

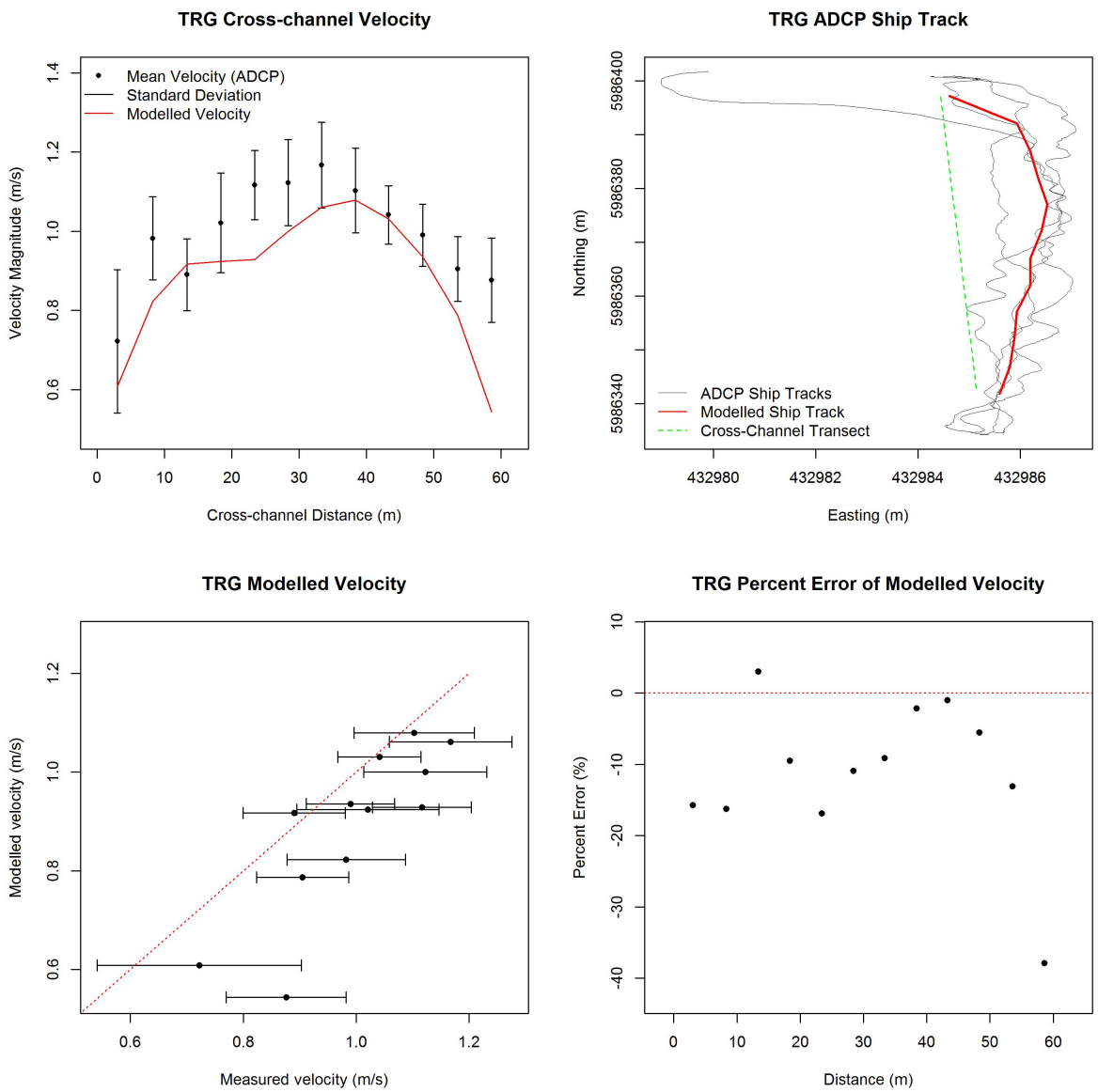

Figure G.25: Model velocity validation at transect TRG.

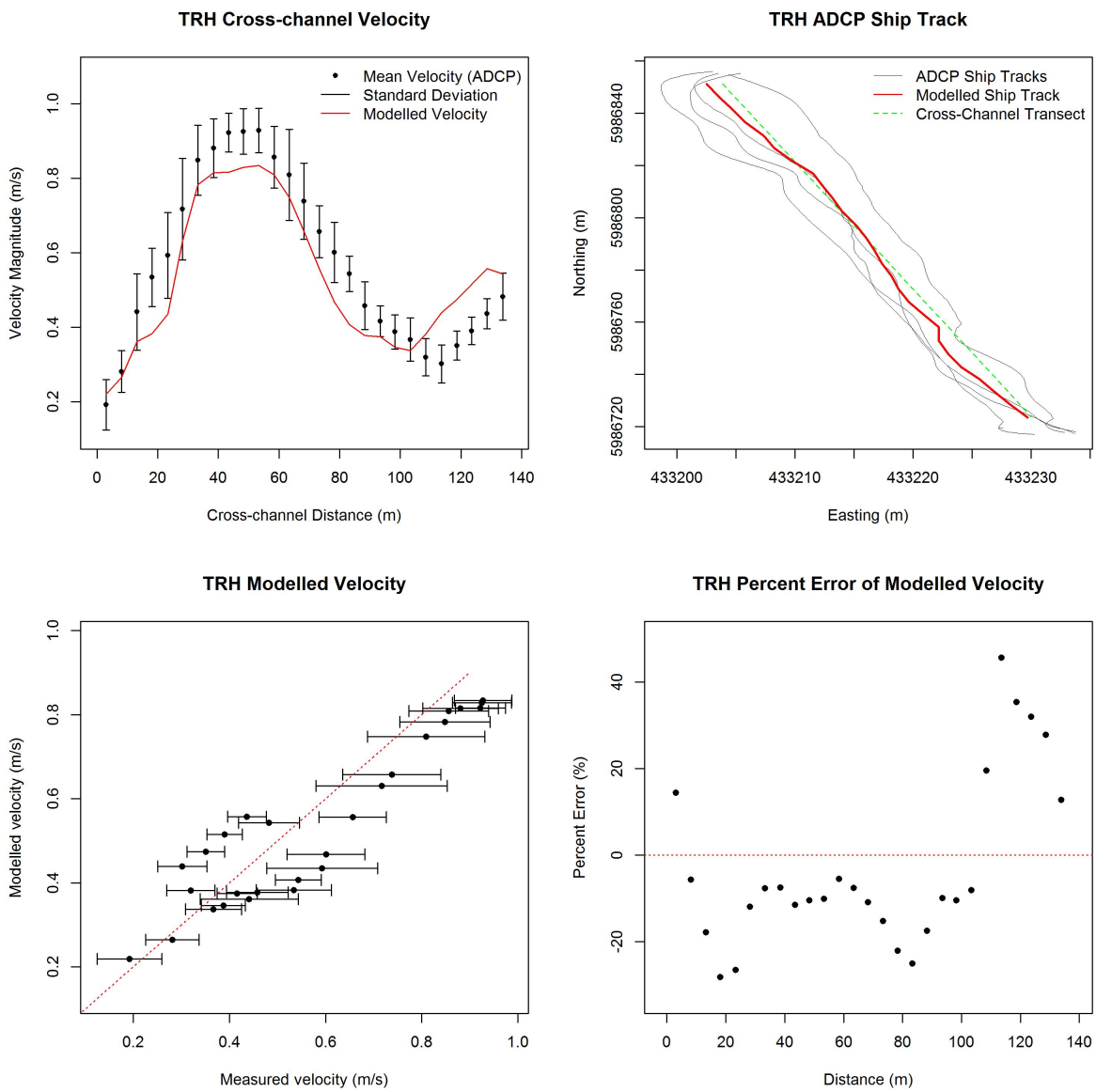

Figure G.26: Model velocity validation at transect TRH.

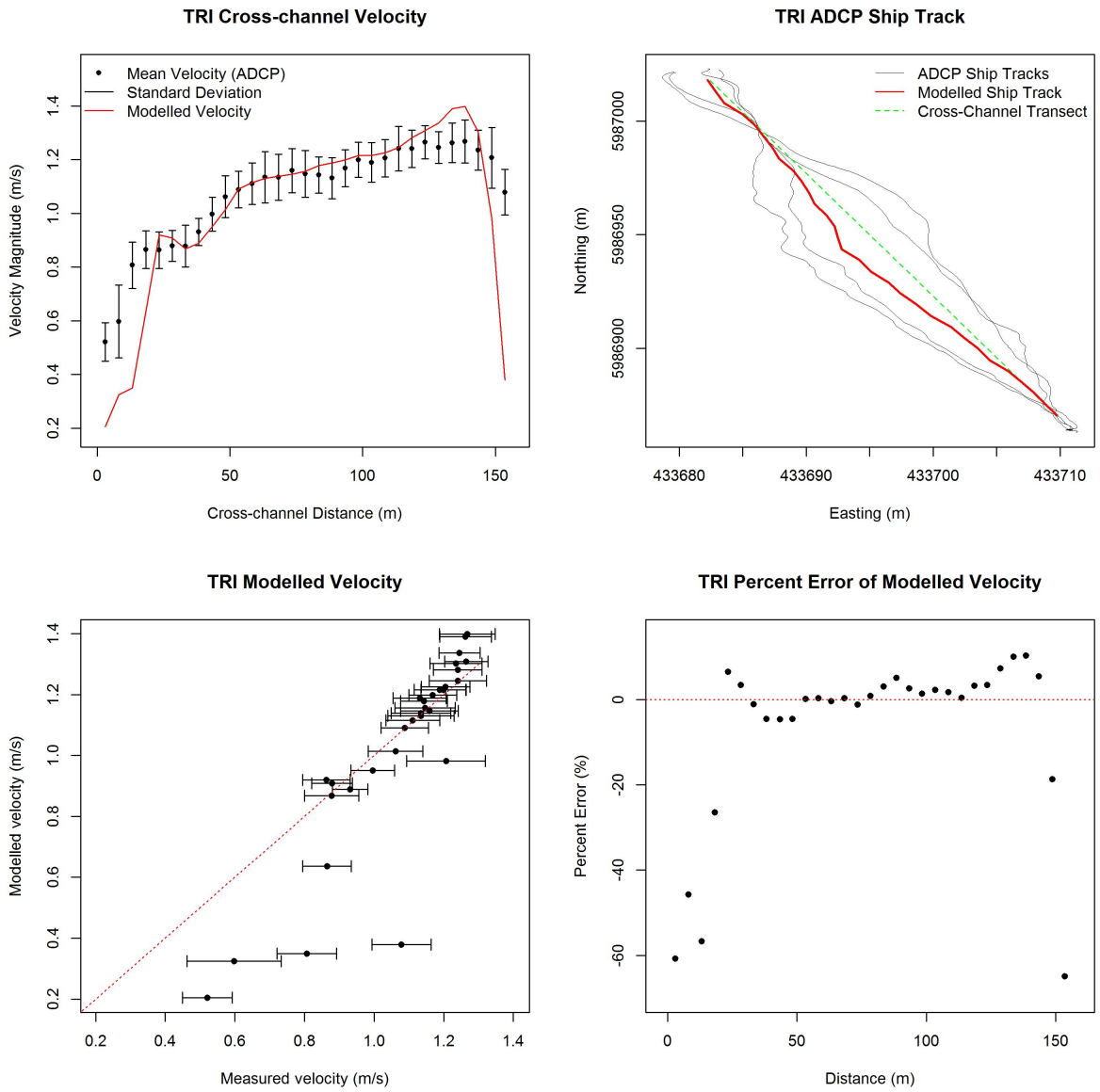

Figure G.27: Model velocity validation at transect TRI.

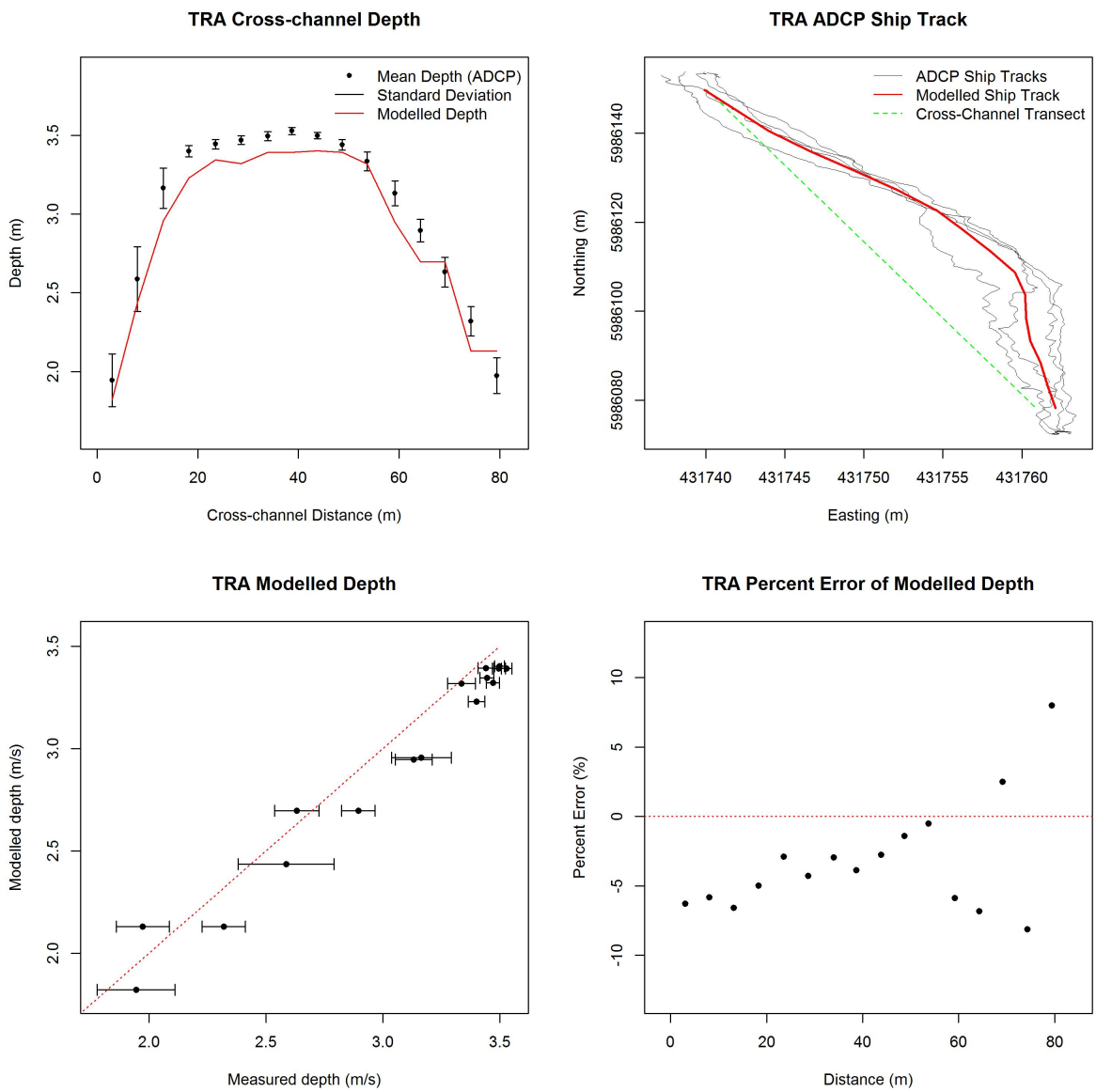

Figure G.28: Model depth validation at transect TRA.

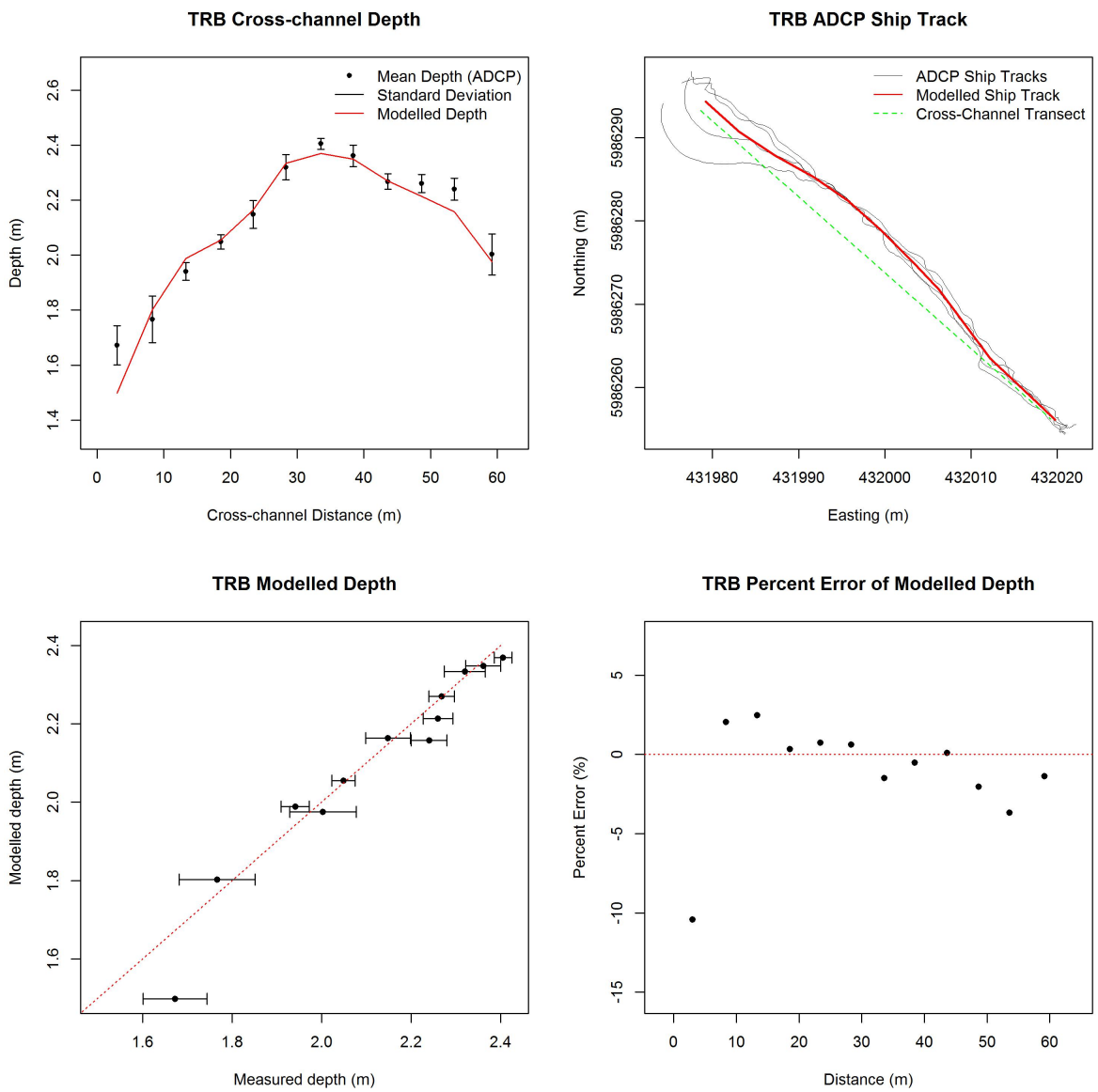

Figure G.29: Model depth validation at transect TRB.

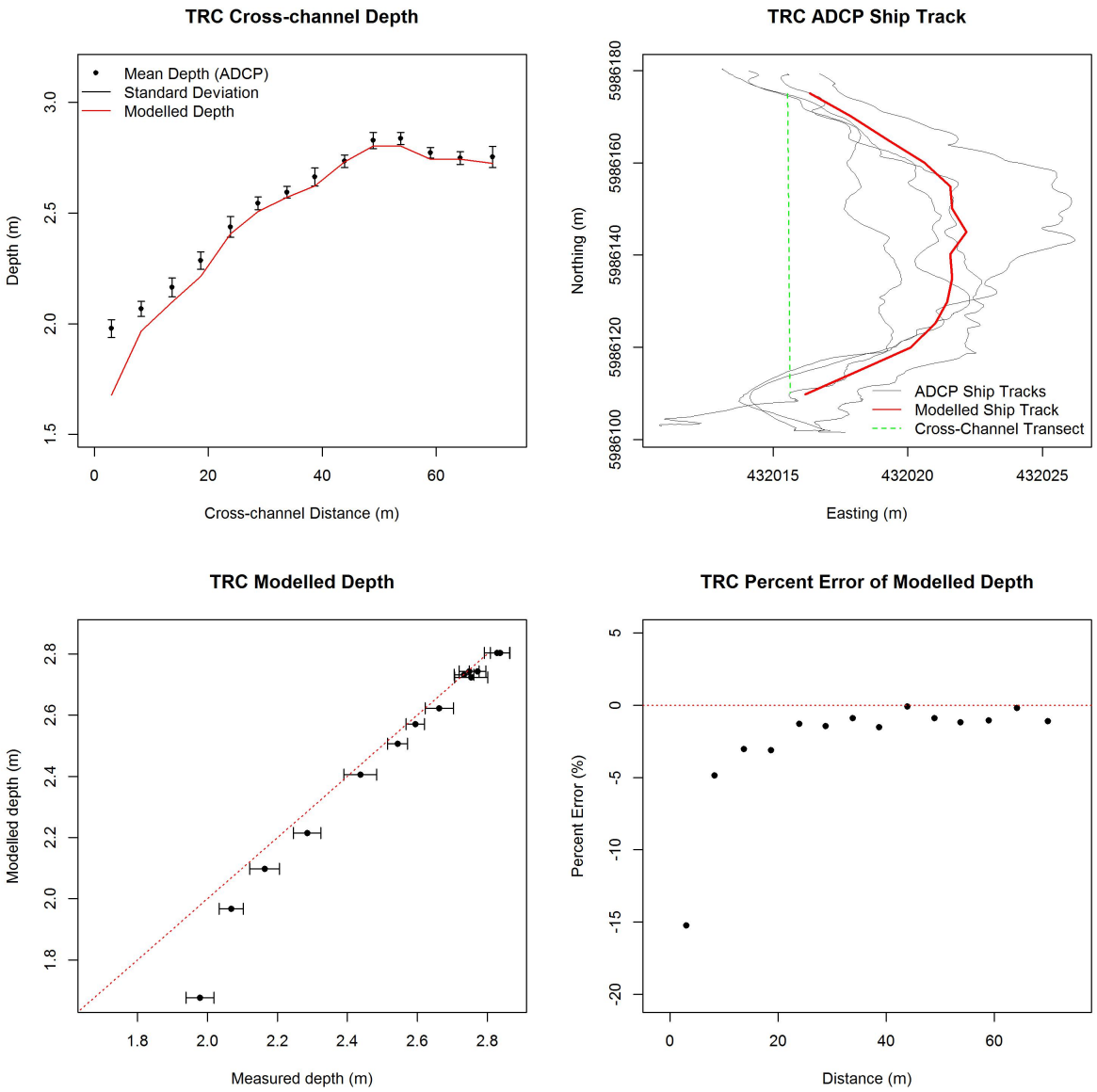

Figure G.30: Model depth validation at transect TRC.

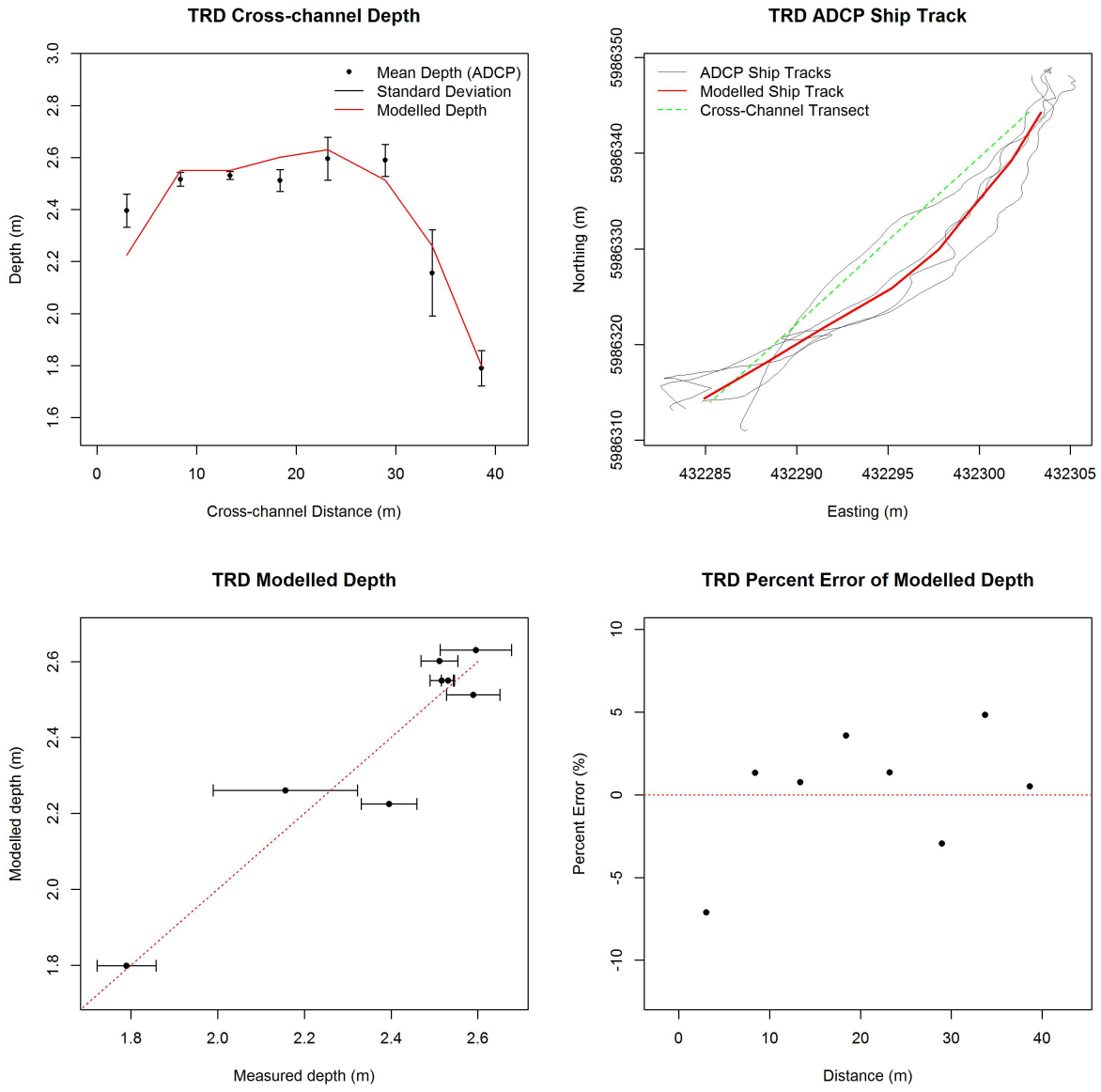

Figure G.31: Model depth validation at transect TRD.

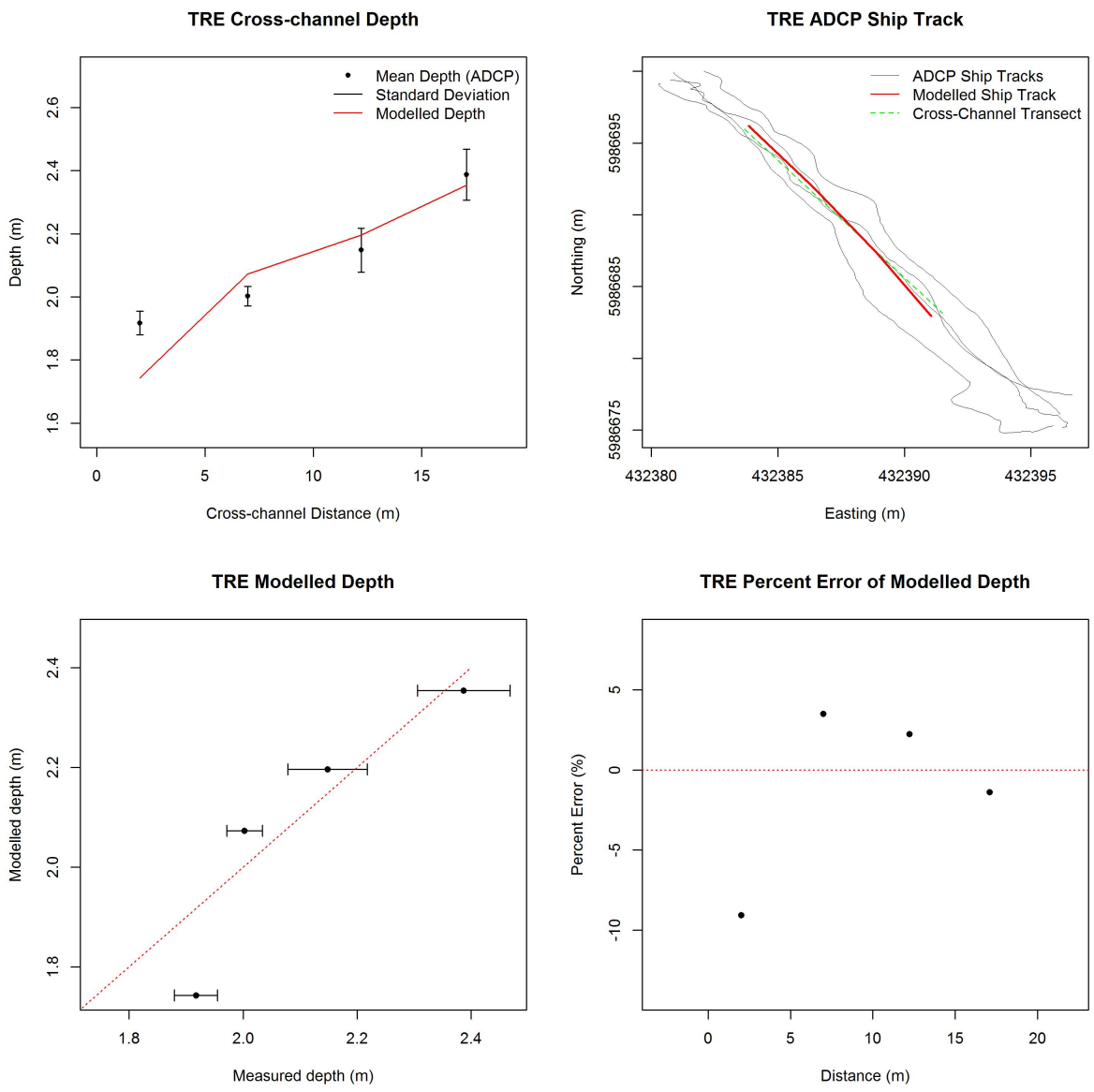

Figure G.32: Model depth validation at transect TRE.

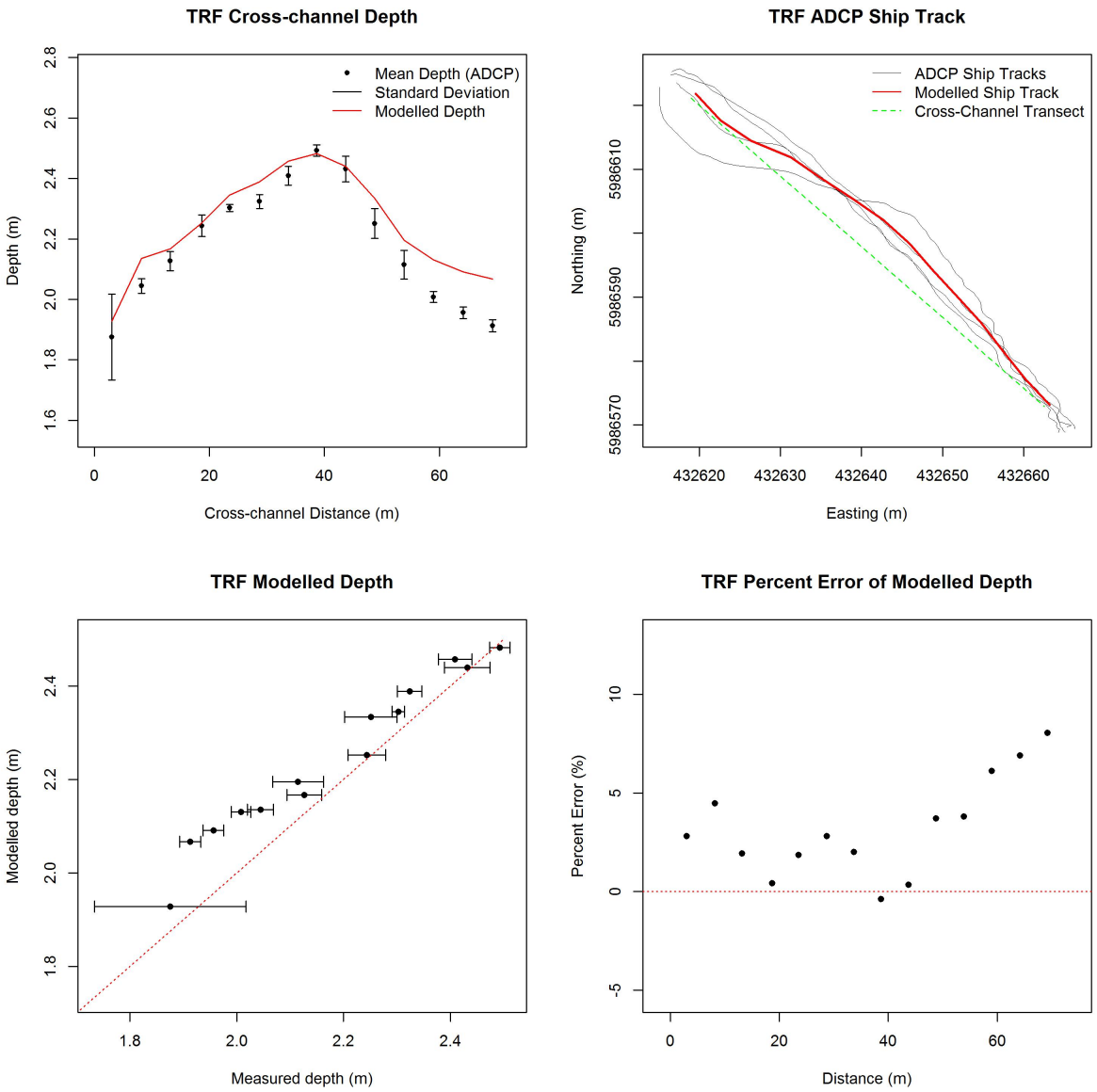

Figure G.33: Model depth validation at transect TRF.

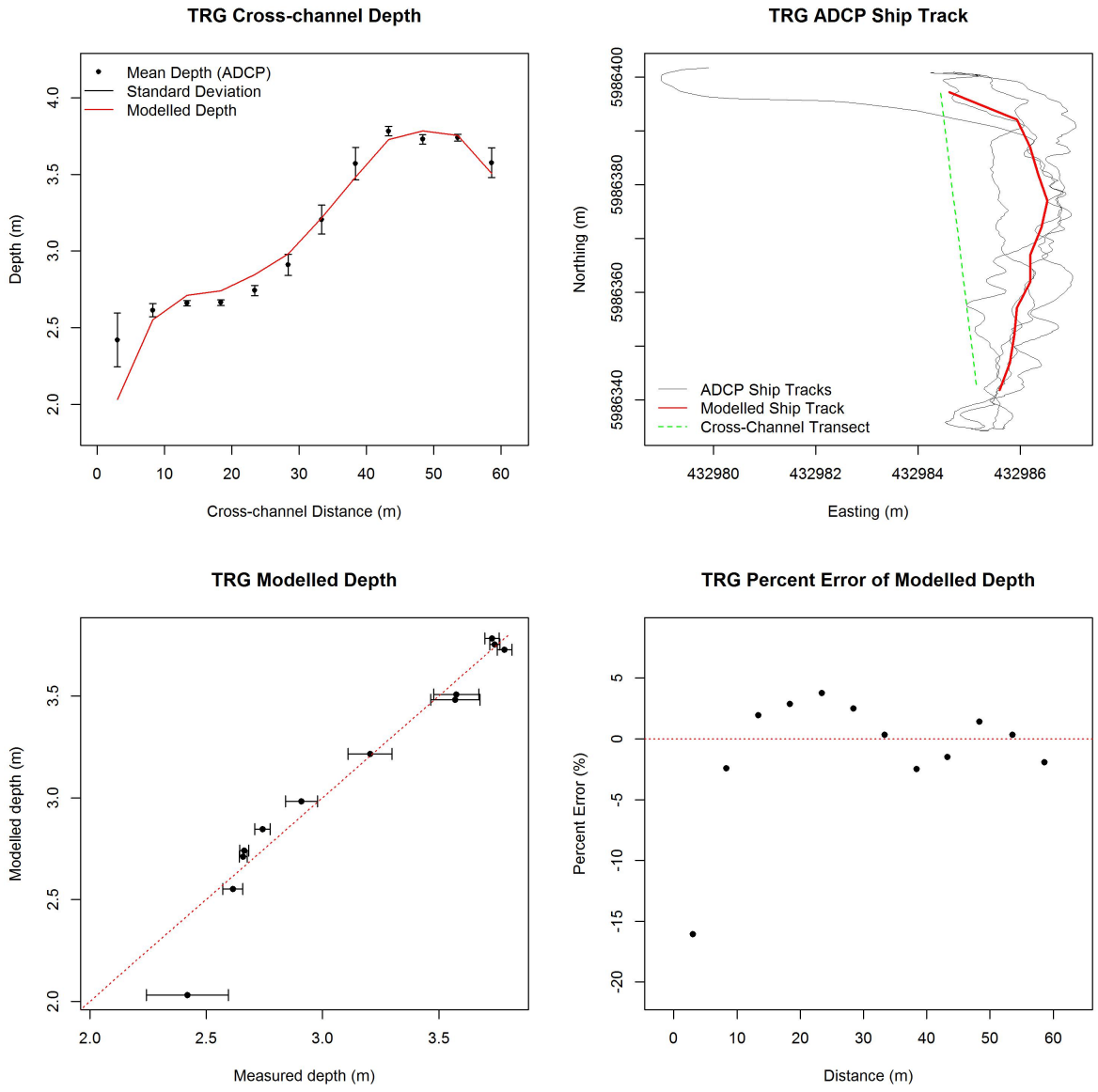

Figure G.34: Model depth validation at transect TRG.

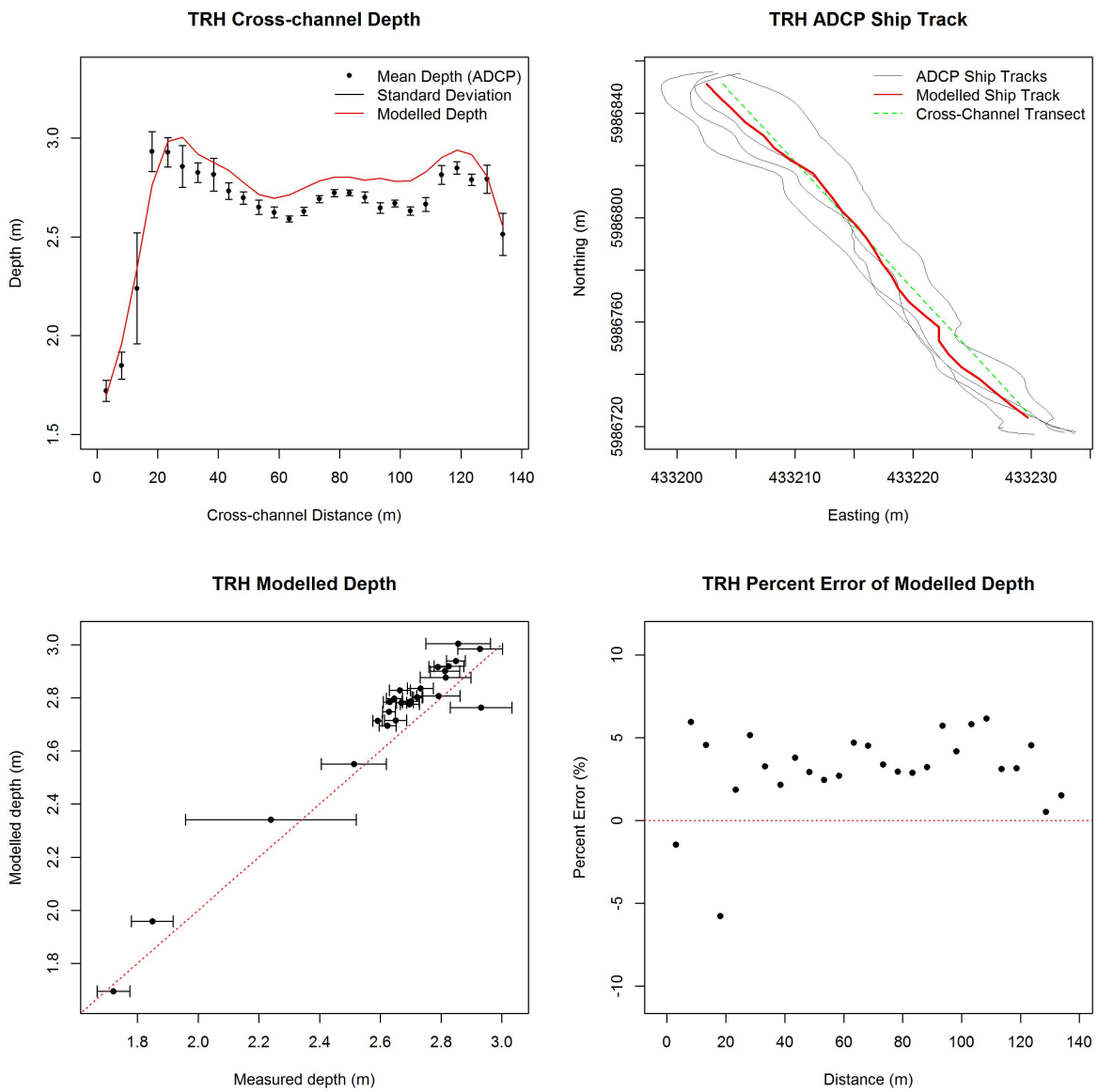

Figure G.35: Model depth validation at transect TRH.

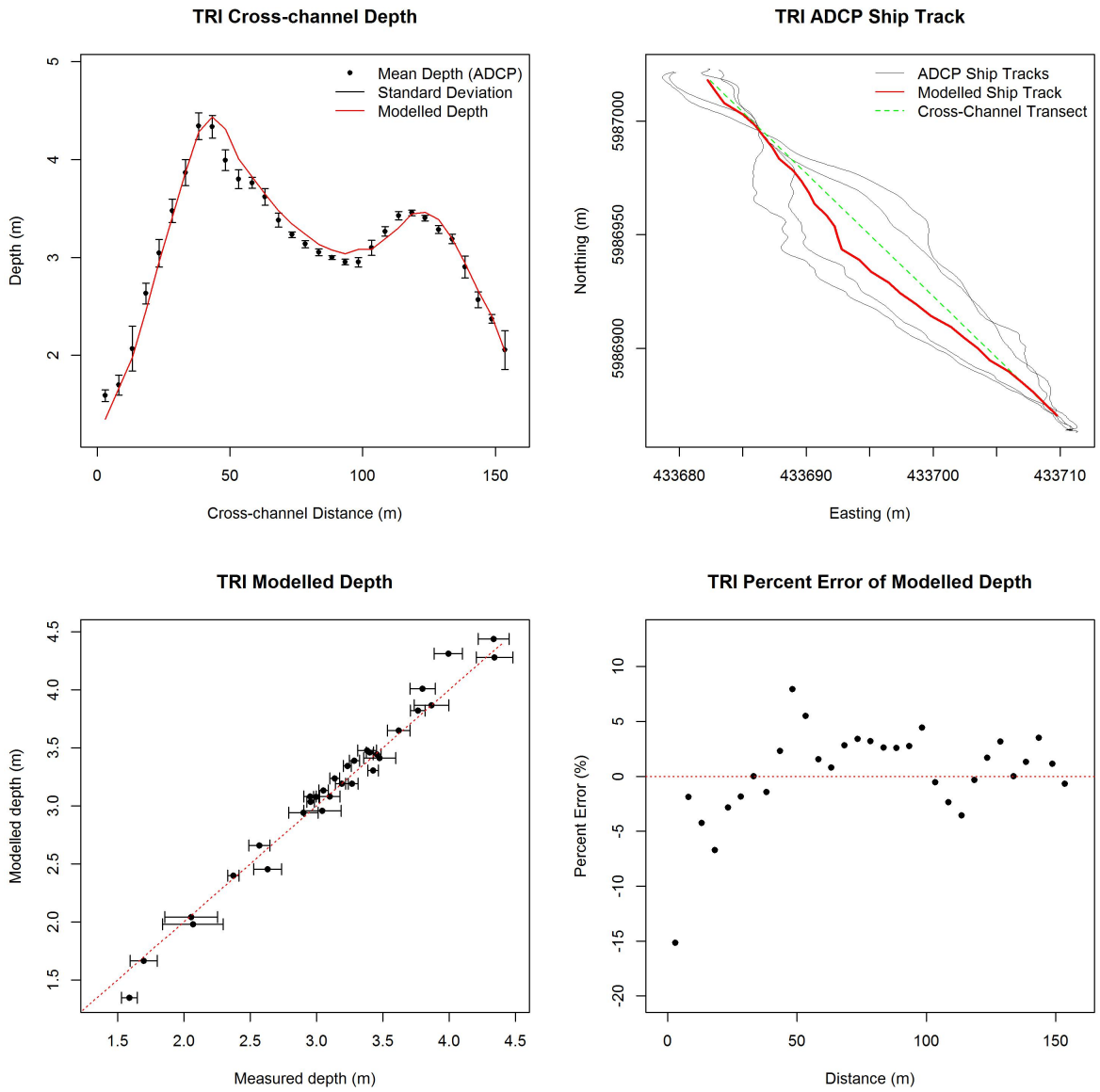

Figure G.36: Model depth validation at transect TRI.

For each simulated discharge, modelled shear stress was used to calculate sediment transport capacity using the Wilcock and Crowe (2003) transport function. First, the model output was filtered to remove areas with less than 10 cm depth. Then, a shear stress raster with a 10-m grid resolution was interpolated to the dimensions of the wetted channel (i.e. $>$ 10 cm depth). To assign a grain size distribution to each cell within the raster, size fractions and substrate characteristics (percent sand and geometric mean grain size) were interpolated between Regions 1-5 and mapped to a common grid. Each raster was then cropped to remove areas outside of the surveyed bottom-of-bank bankline and shear velocity was calculated for each cell. The result of this process is a single gridded data frame, where each cell contains the necessary attributes to apply the sediment transport function.

The calculated unit transport rate of each size fraction was then multiplied by the cell size to obtain volumetric fractional transport rates. These fractional rates were summed to obtain a total sediment transport capacity for each cell. The subsequent step in the analysis was to obtain the total cross-sectional transport capacity with downstream distance. Cross-sections were established at 30-m downstream intervals using the modelling mesh, excluding 100-m channel lengths at the upstream and downstream extent of the model domain to avoid boundary effects. Transport capacity was extracted from each grid cell along the channel cross-sections and summed to obtain a total cross-channel capacity.

G.2 Model results

Shear stress rasters are presented in Figures G.37 to G.45, transport capacity rasters in Figures G.46 to G.54 and downstream capacity profiles in Figures G.55 to G.63. Although this analysis was conducted for every 50 m^3/s discharge interval between 45 m^3/s and 775 m^3/s, figures are only presented per 100 m^3/s simulated discharge interval.

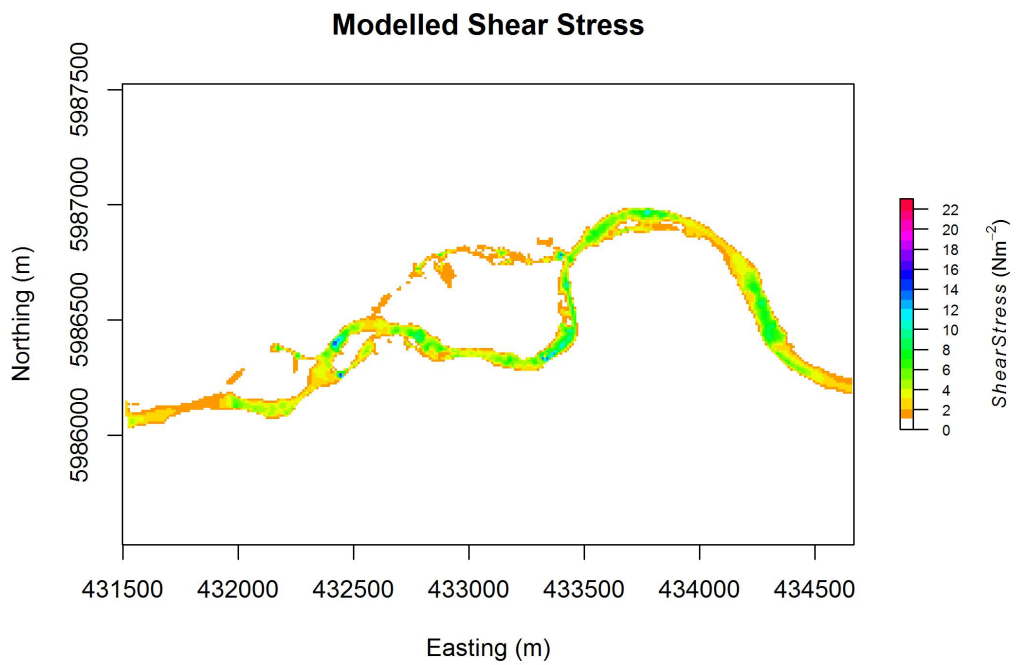

Figure G.37: Simulated shear stress during a discharge of 45 m^3/s.

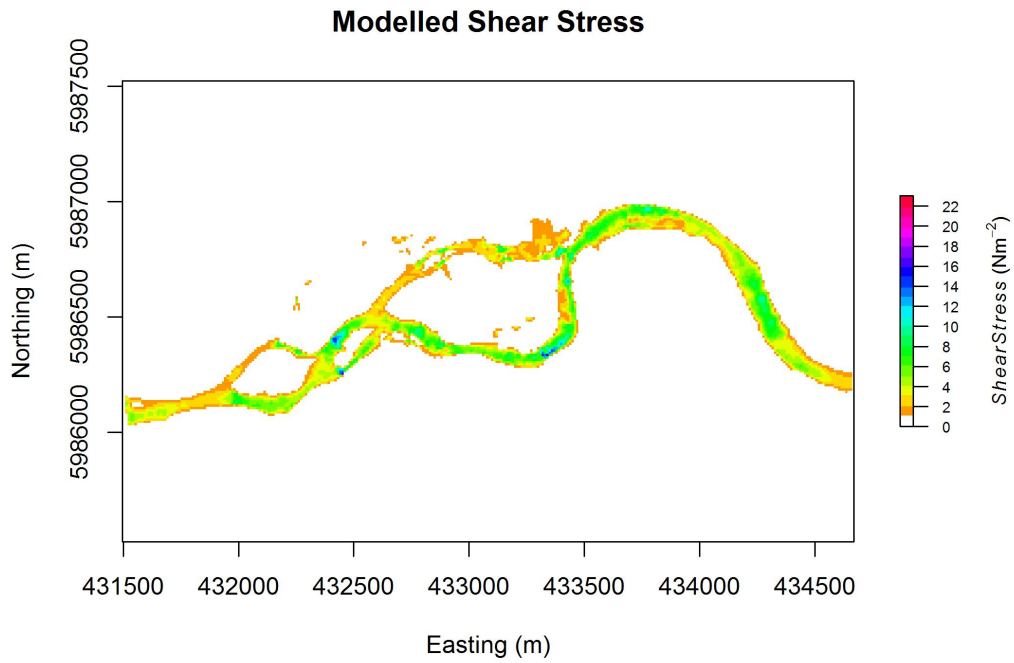

Figure G.38: Simulated shear stress during a discharge of 75 m^3/s.

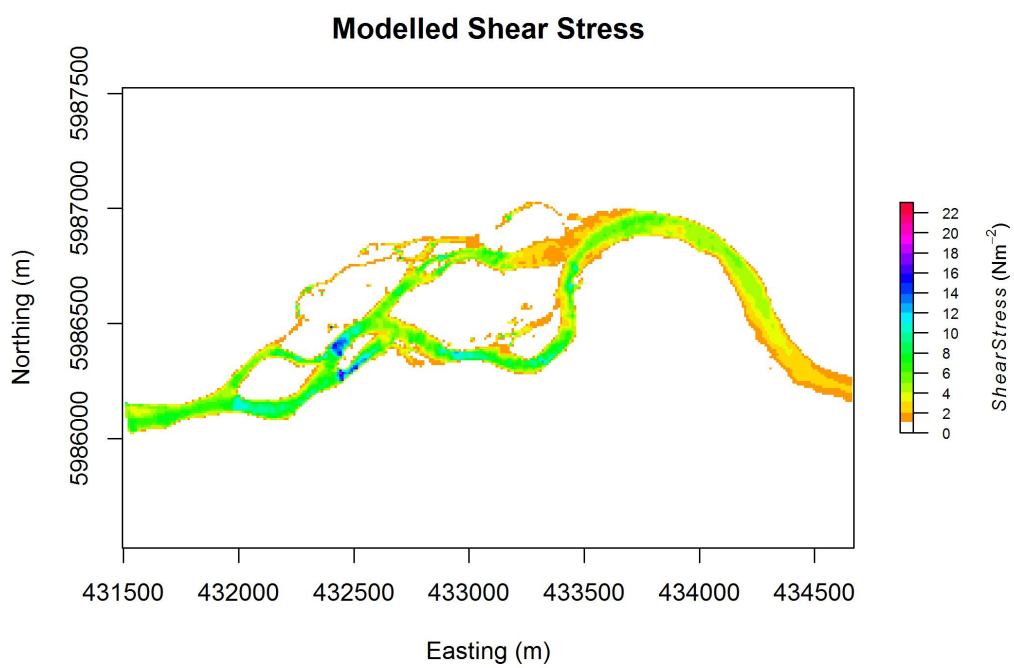

Figure G.39: Simulated shear stress during a discharge of 175 m^3/s.

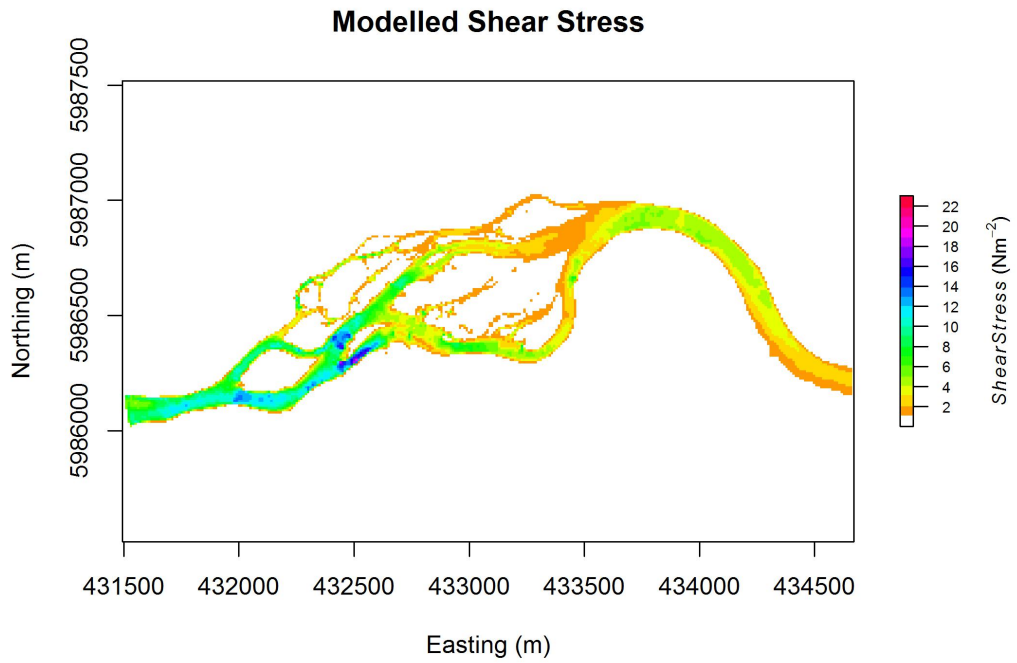

Figure G.40: Simulated shear stress during a discharge of 275 m^3/s.

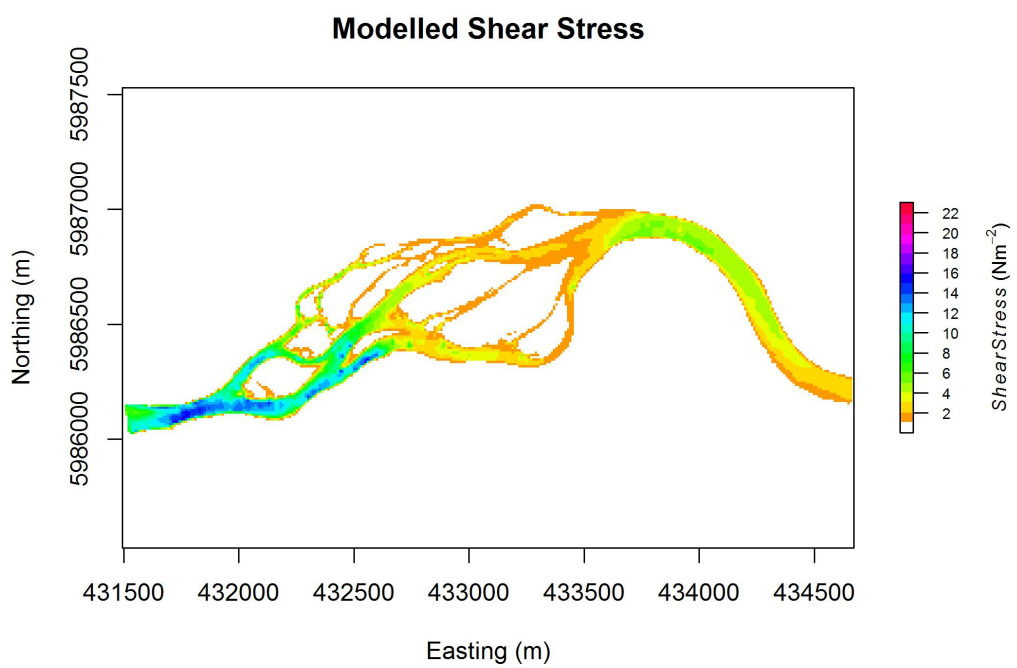

Figure G.41: Simulated shear stress during a discharge of 375 m^3/s.

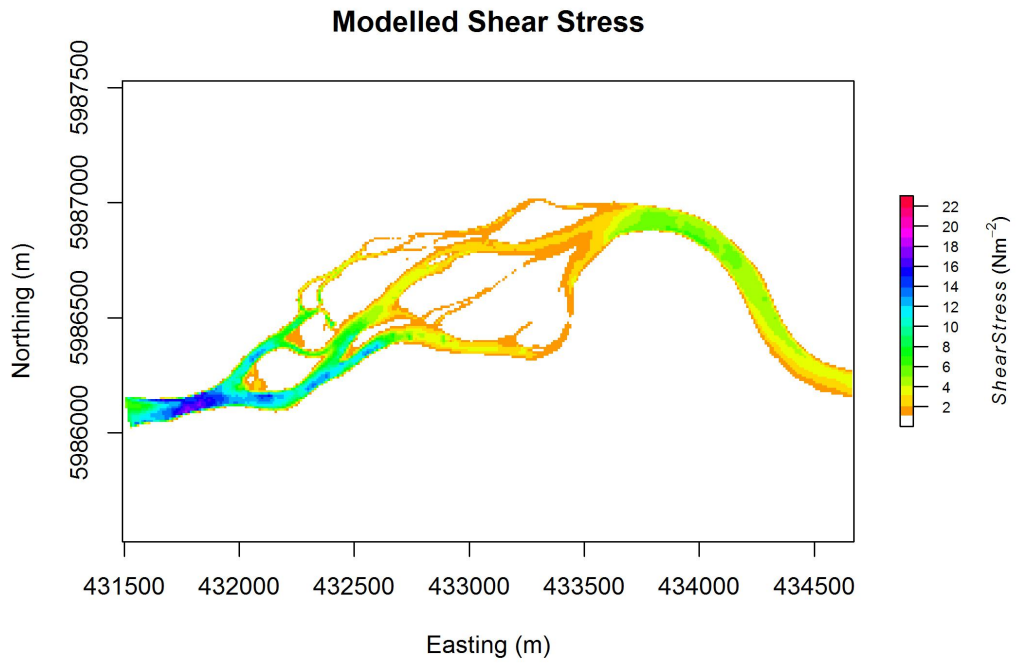

Figure G.42: Simulated shear stress during a discharge of 475 m^3/s.

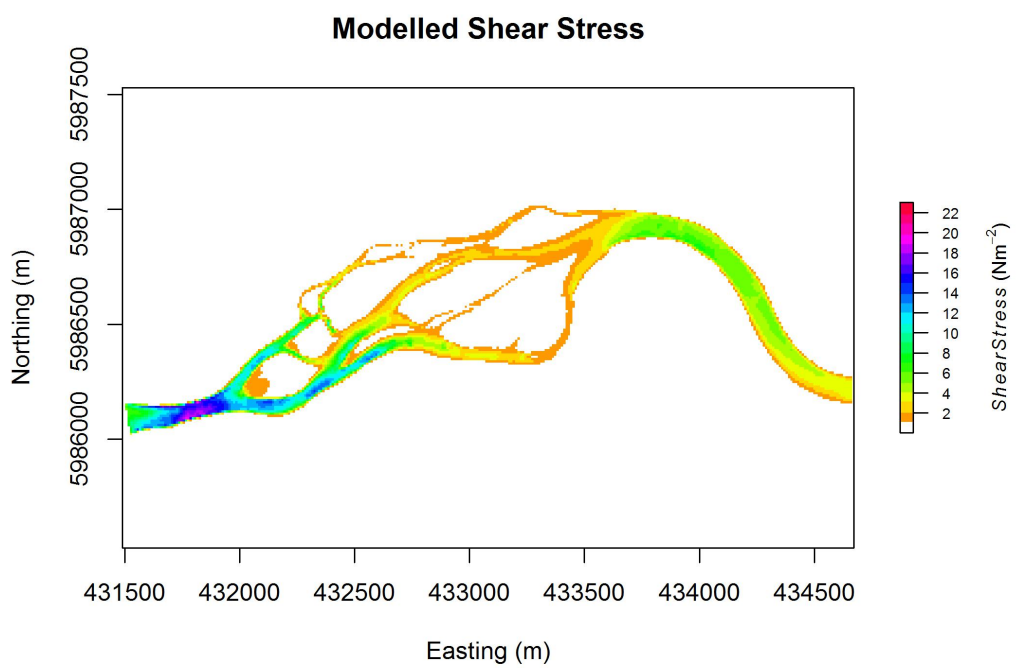

Figure G.43: Simulated shear stress during a discharge of 575 m^3/s.

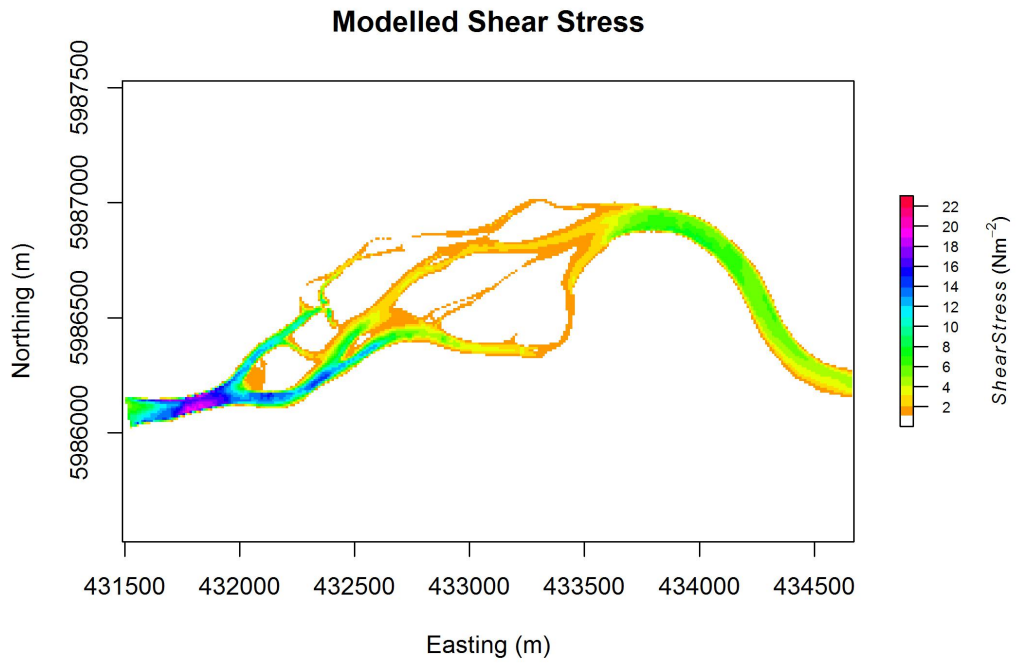

Figure G.44: Simulated shear stress during a discharge of 675 m^3/s.

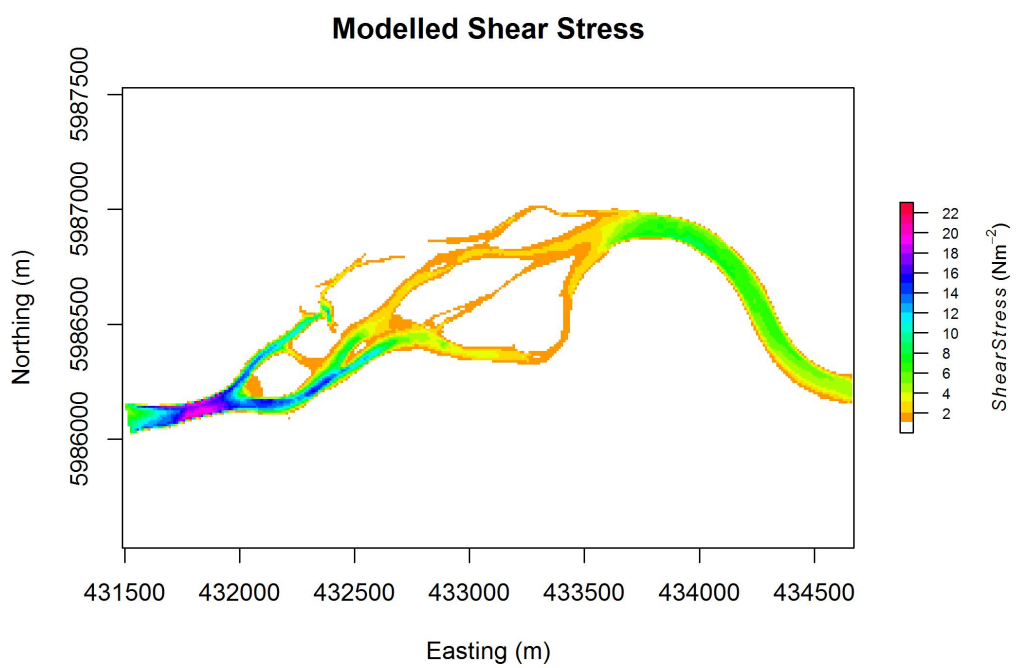

Figure G.45: Simulated shear stress during a discharge of 775 m^3/s.

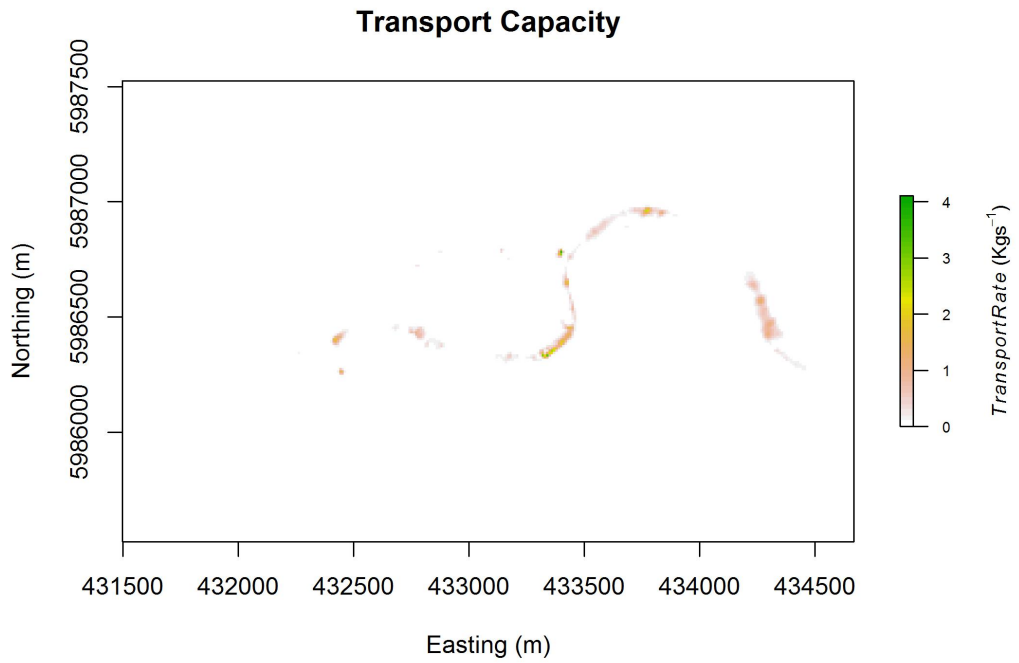

Figure G.46: Estimated sediment transport capacity during a discharge of 45 m^3/s.

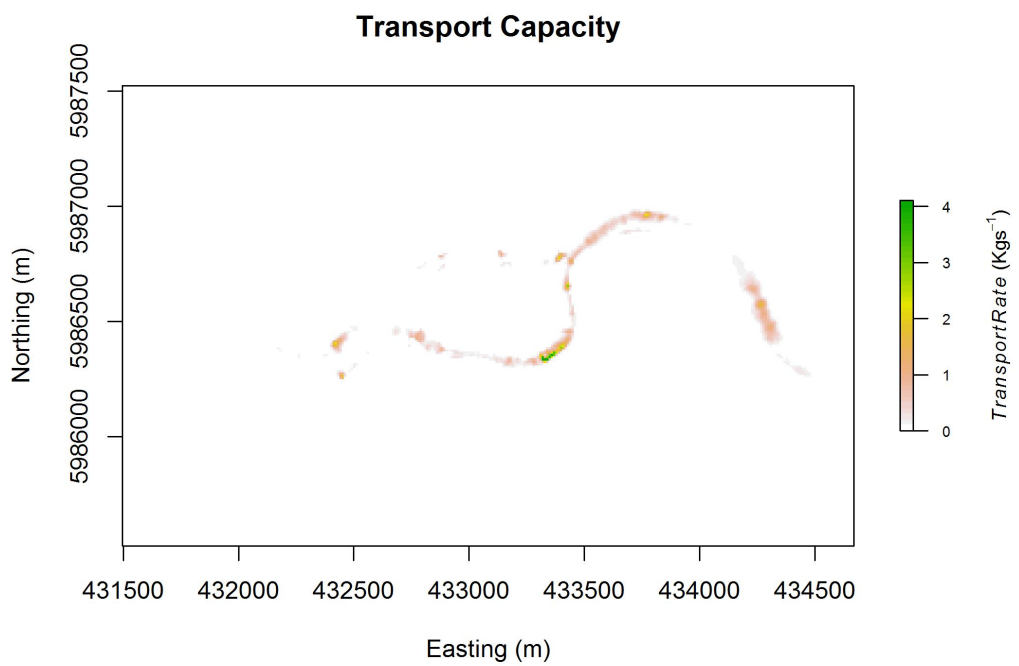

Figure G.47: Estimated sediment transport capacity during a discharge of 75 m^3/s.

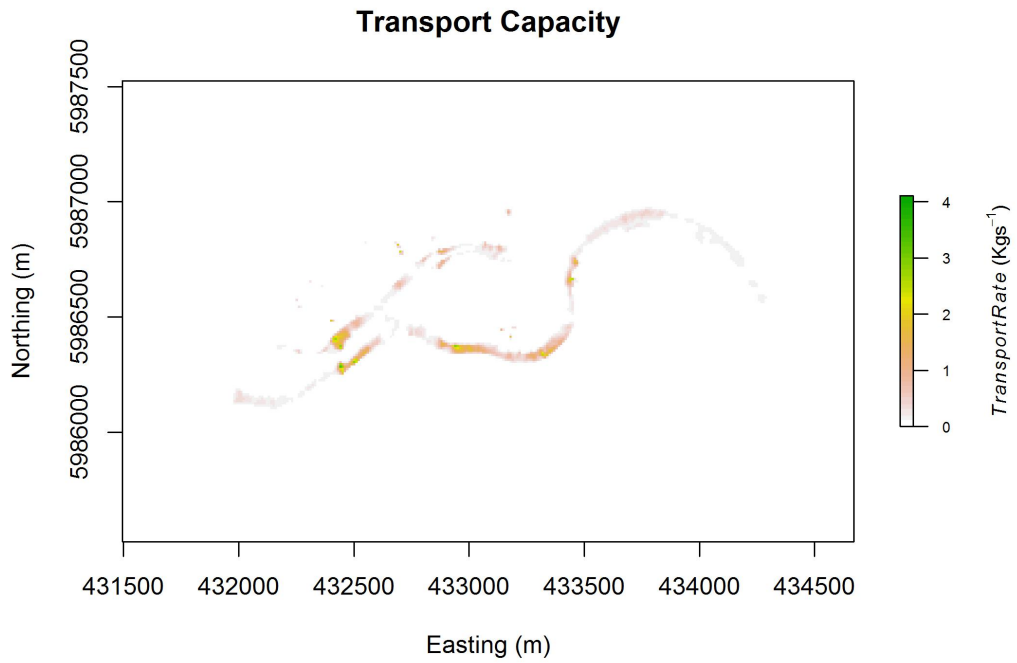

Figure G.48: Estimated sediment transport capacity during a discharge of 175 m^3/s.

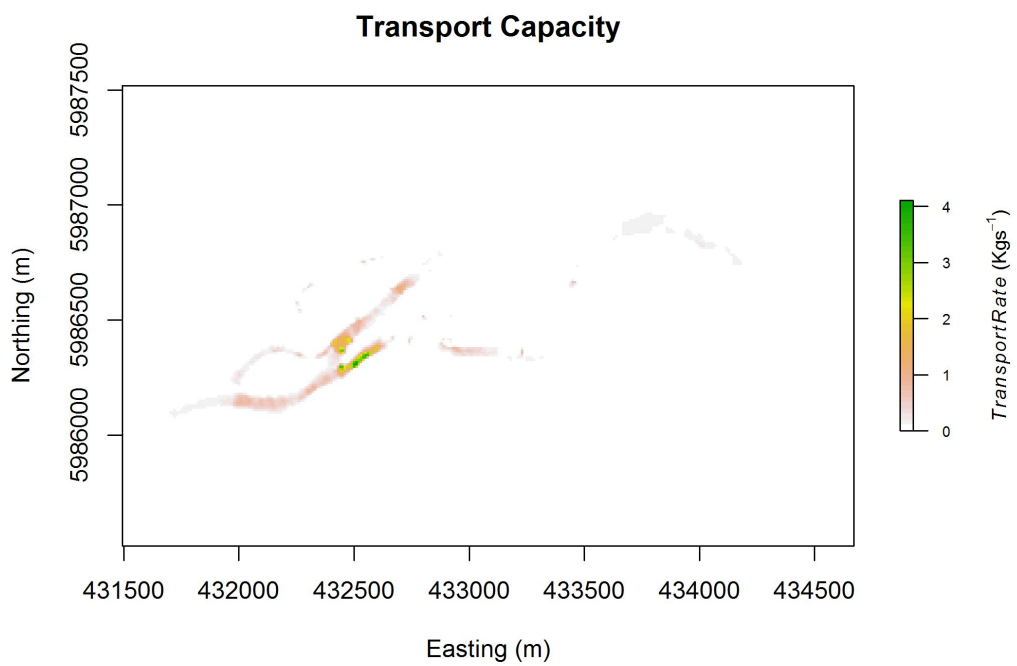

Figure G.49: Estimated sediment transport capacity during a discharge of 275 m^3/s.

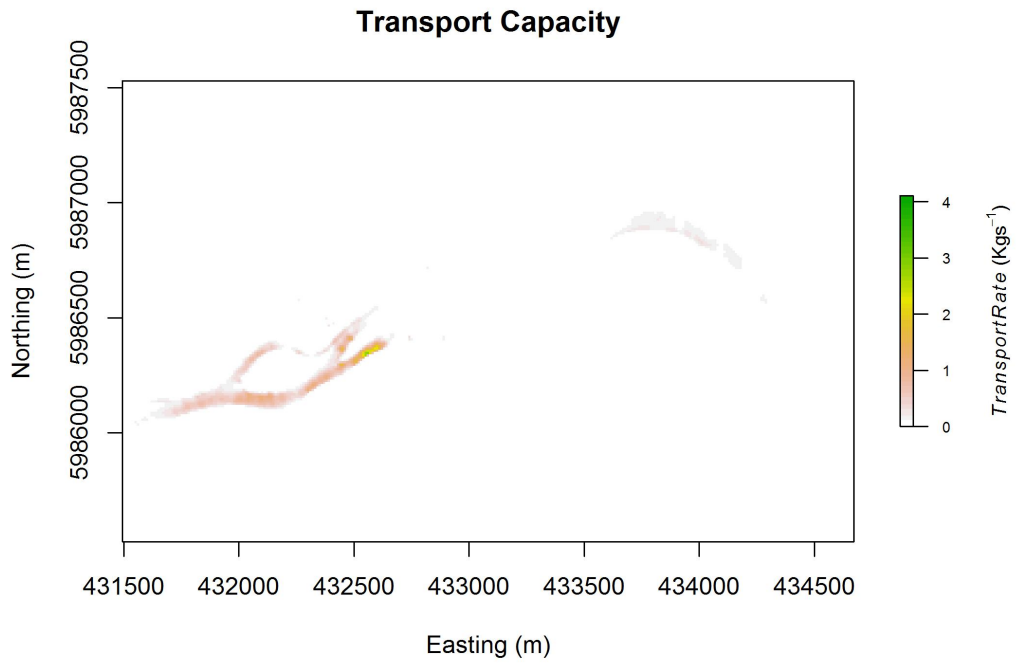

Figure G.50: Estimated sediment transport capacity during a discharge of 375 m^3/s.

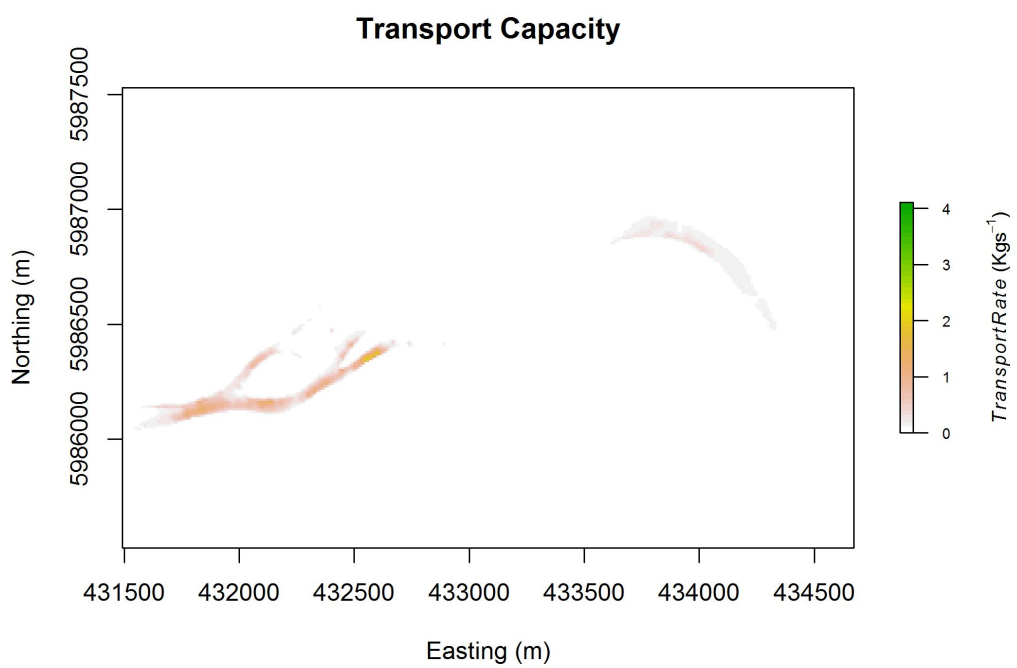

Figure G.51: Estimated sediment transport capacity during a discharge of 475 m^3/s.

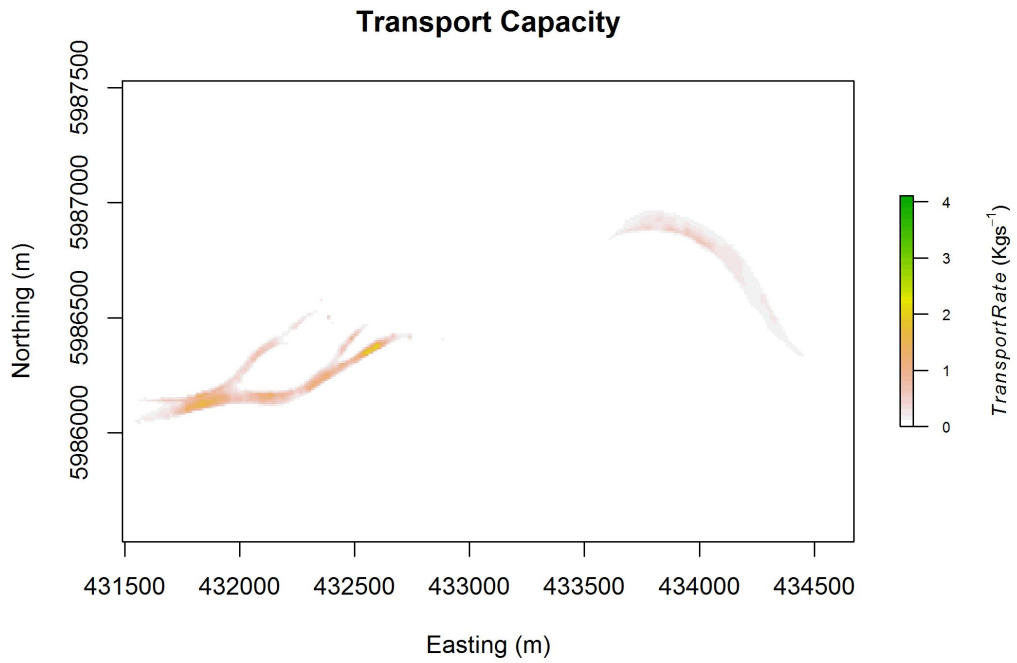

Figure G.52: Estimated sediment transport capacity during a discharge of 575 m^3/s.

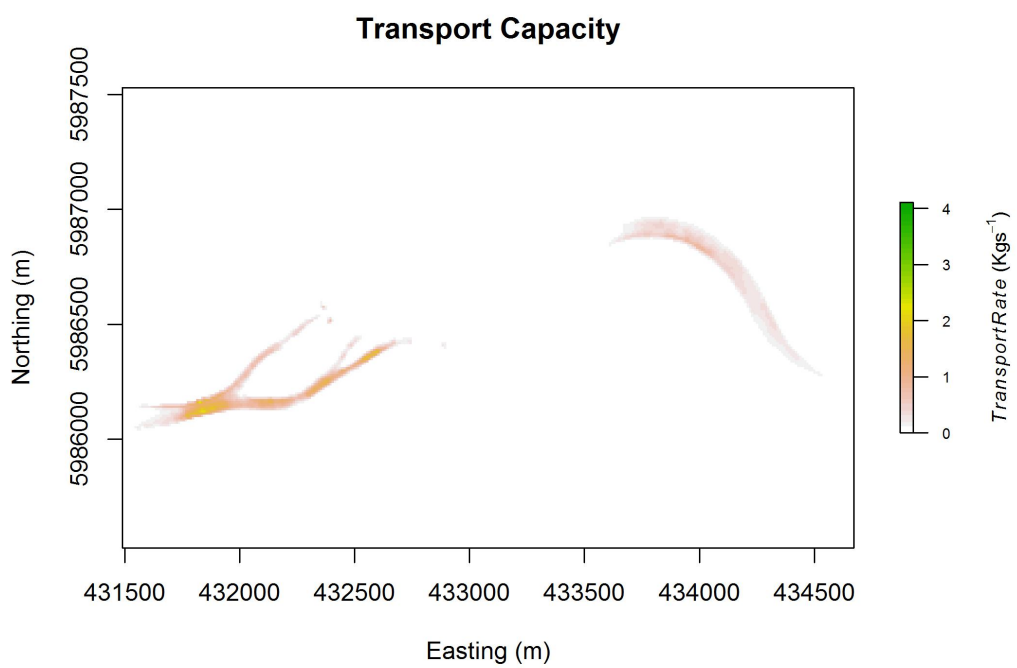

Figure G.53: Estimated sediment transport capacity during a discharge of 675 m^3/s.

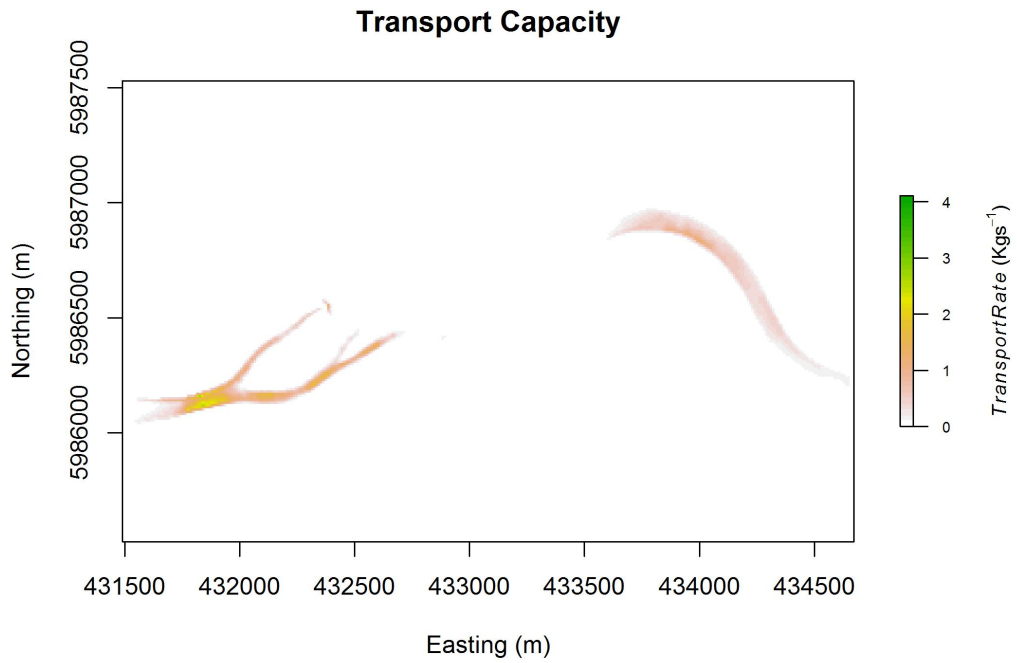

Figure G.54: Estimated sediment transport capacity during a discharge of 775 m^3/s.

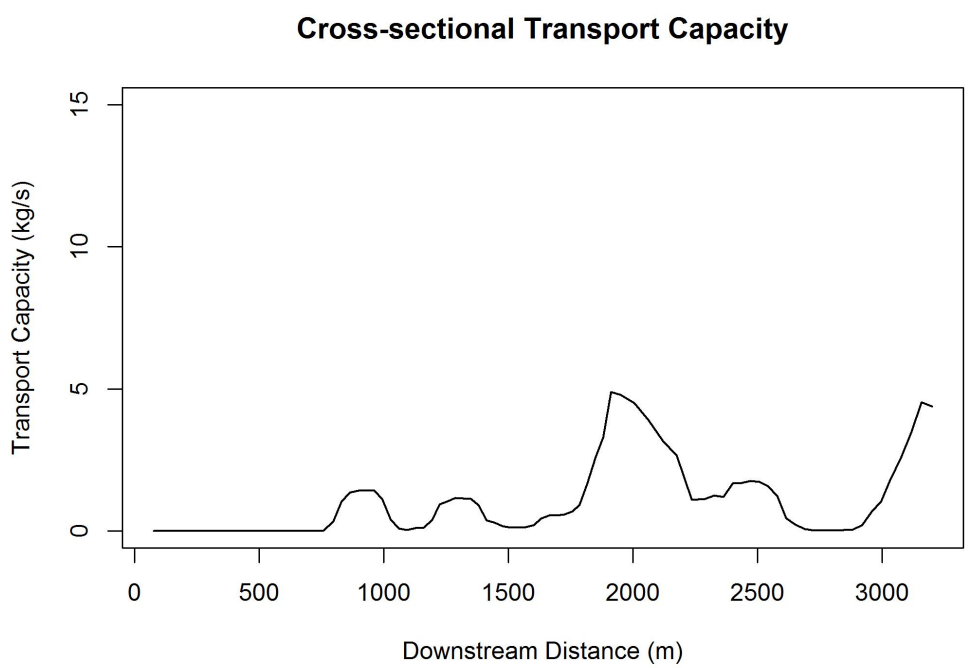

Figure G.55: Profile of downstream transport capacity during a discharge of 45 m^3/s.

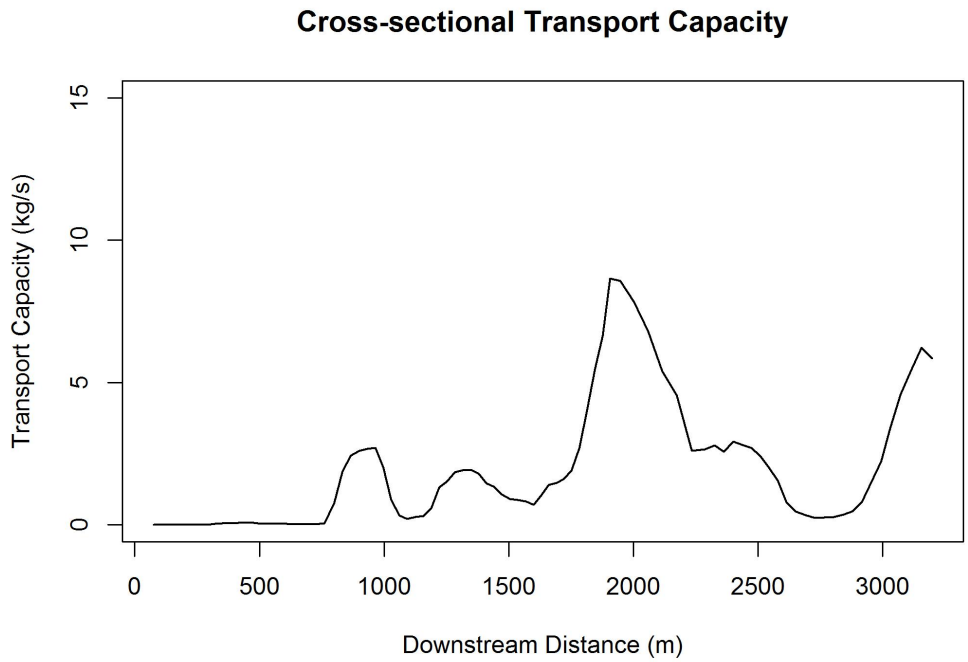

Figure G.56: Profile of downstream transport capacity during a discharge of 75 m^3/s.

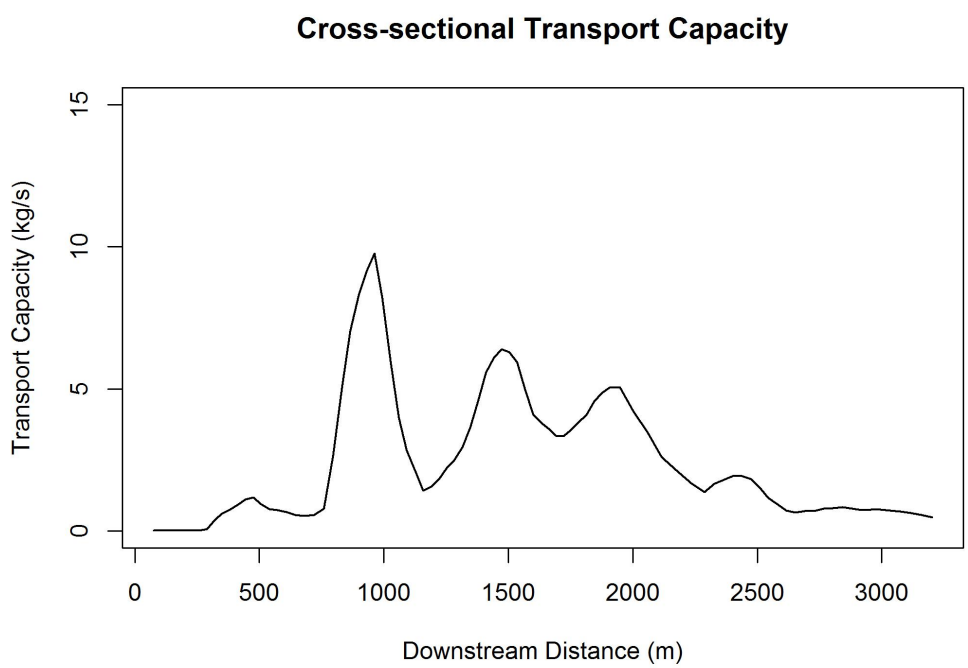

Figure G.57: Profile of downstream transport capacity during a discharge of 175 m^3/s.

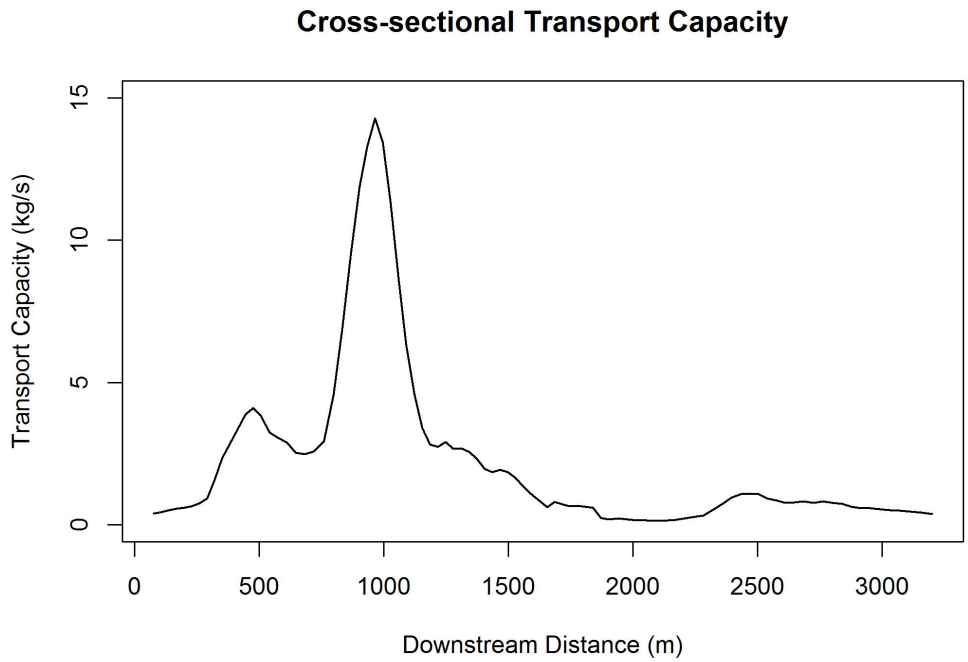

Figure G.58: Profile of downstream transport capacity during a discharge of 275 m^3/s.

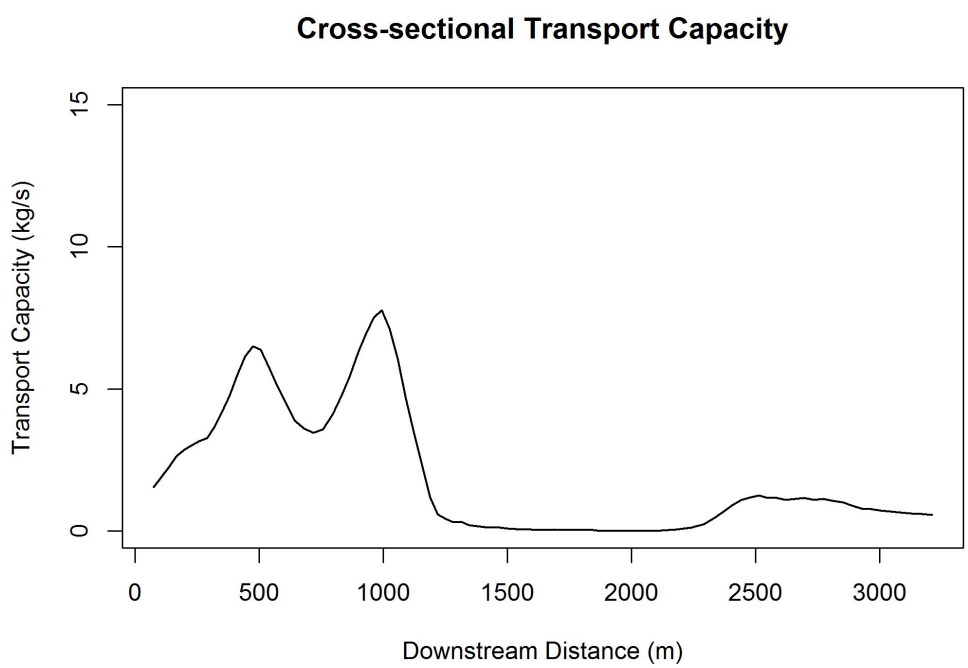

Figure G.59: Profile of downstream transport capacity during a discharge of 375 m^3/s.

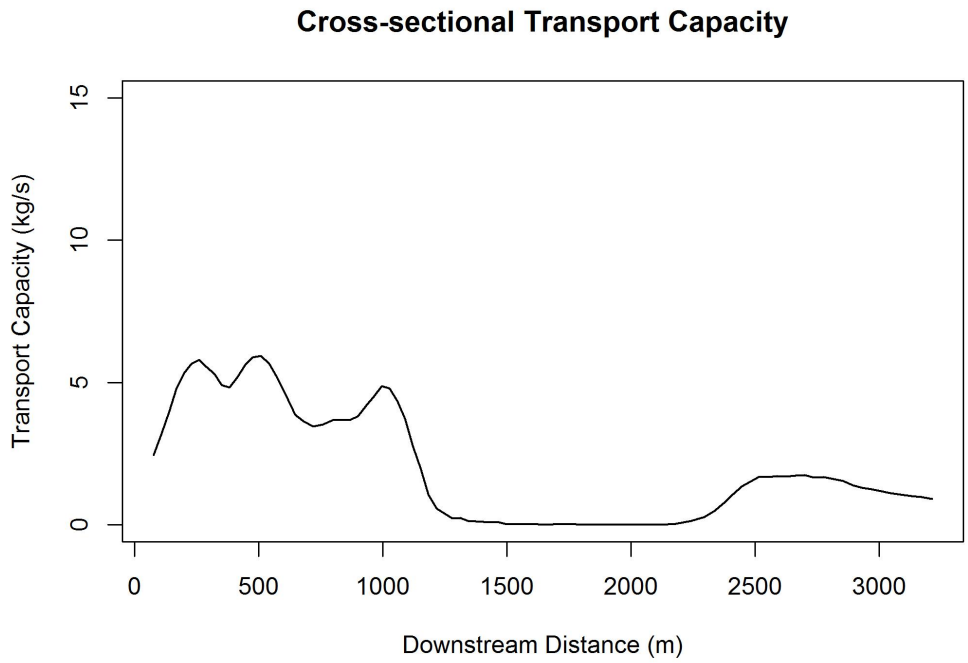

Figure G.60: Profile of downstream transport capacity during a discharge of 475 m^3/s.

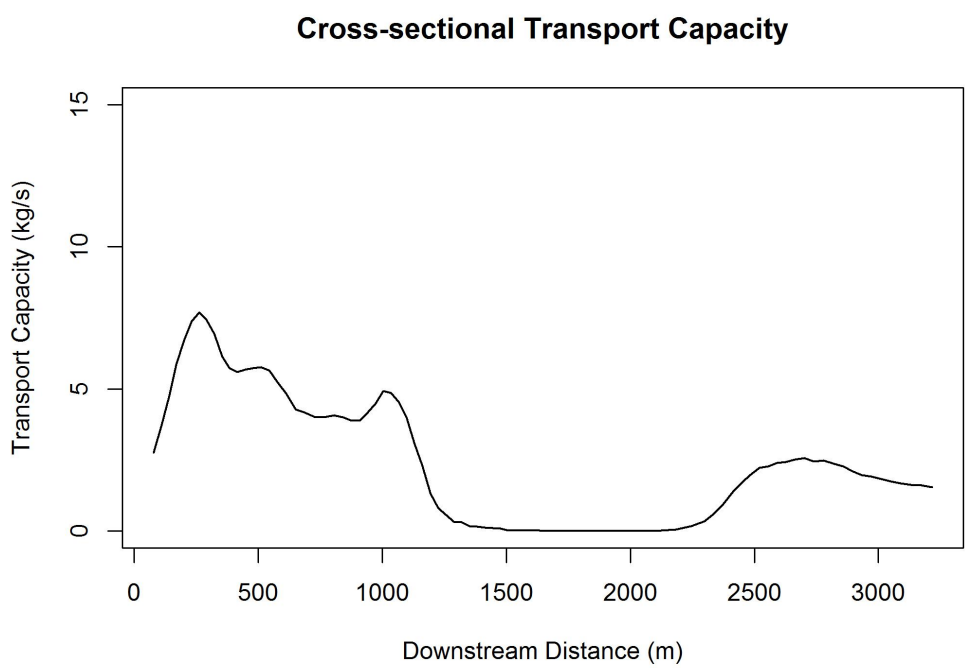

Figure G.61: Profile of downstream transport capacity during a discharge of 575 m^3/s.

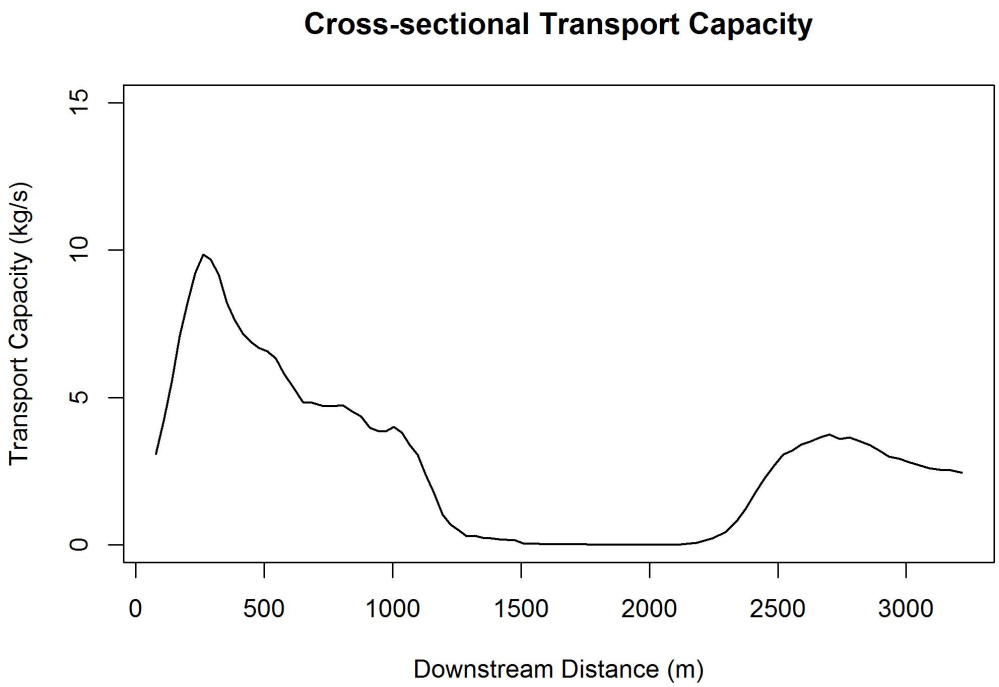

Figure G.62: Profile of downstream transport capacity during a discharge of 675 m^3/s.

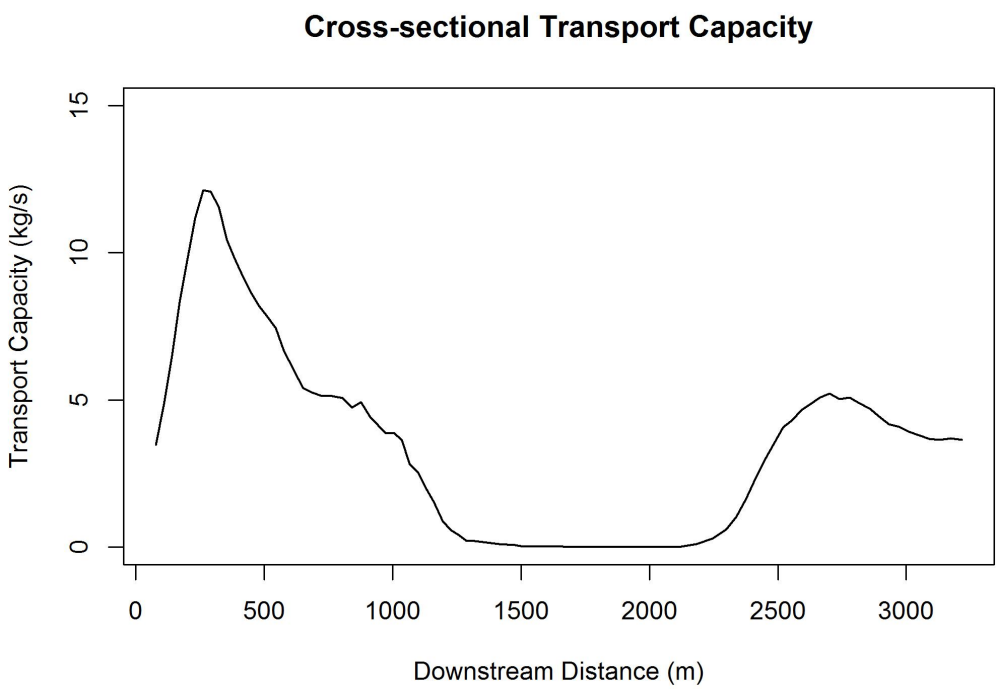

Figure G.63: Profile of downstream transport capacity during a discharge of 775 m^3/s.

To explore possible relations between flow and sediment transport through the spawning reach, the cumulative transport capacity was plotted for three downstream locations over a series of hydrographs. This was motivated by previous investigations (NHC, 2014; NHC, 2015; NHC, 2016) which observed a discrepancy between the amount of sediment transported into and out of the reach depending on the annual hydrograph. The three locations correspond to upstream (US bedload transect), mid-reach and downstream (LP bedload transect) locations. At each location, transport capacity was averaged over a 90-m downstream distance to reduce the effect of local variations. This was repeated for all simulated discharge intervals. Daily flow data were downloaded from WSC gauge 08JC001 and binned into 50 m^3/s intervals, corresponding to the simulated discharge intervals. The transport capacity at each location was multiplied by the flow duration within each bin to obtain the cumulative transport capacity. The analysis was done for three hydrograph sequences of three years each. The sequences included three low-flow years (1954-1956) which occurred during the period of reservoir infilling (Figure G.64), three typical hydrograph years (2002-2004) (Figure G.65) and the past three years (2014-2016) (Figure G.66) which included the high flow in 2015. The 2015 flood was the only year where capacity was greater within the upstream part of the reach than downstream (Figure G.67).

To remove the effect that varying the grain size distribution has on estimated capacity, the same analysis was done with a single grain size distribution assigned to the entire reach. The single grain size distribution was obtained by taking the mean of all GSD data collected at all locations, and had a D_{50} of 13.6 mm and 17% sand. Results from this analysis are presented in the same order as was previously shown; 1954-1957 (Figure G.68), 2002-2004 (Figure G.69), 2014-2016 (Figure G.70) and 2015 (Figure G.71). By using the single GSD, transport rates at the US transect greatly increase because the mean GSD is finer than observed substrate composition.

It is important to note that this analysis is not intended to predict future sediment loads or estimate historic loads with any degree of accuracy. Rather, it is intended as an interpretive tool to better understand reach-scale sediment dynamics.

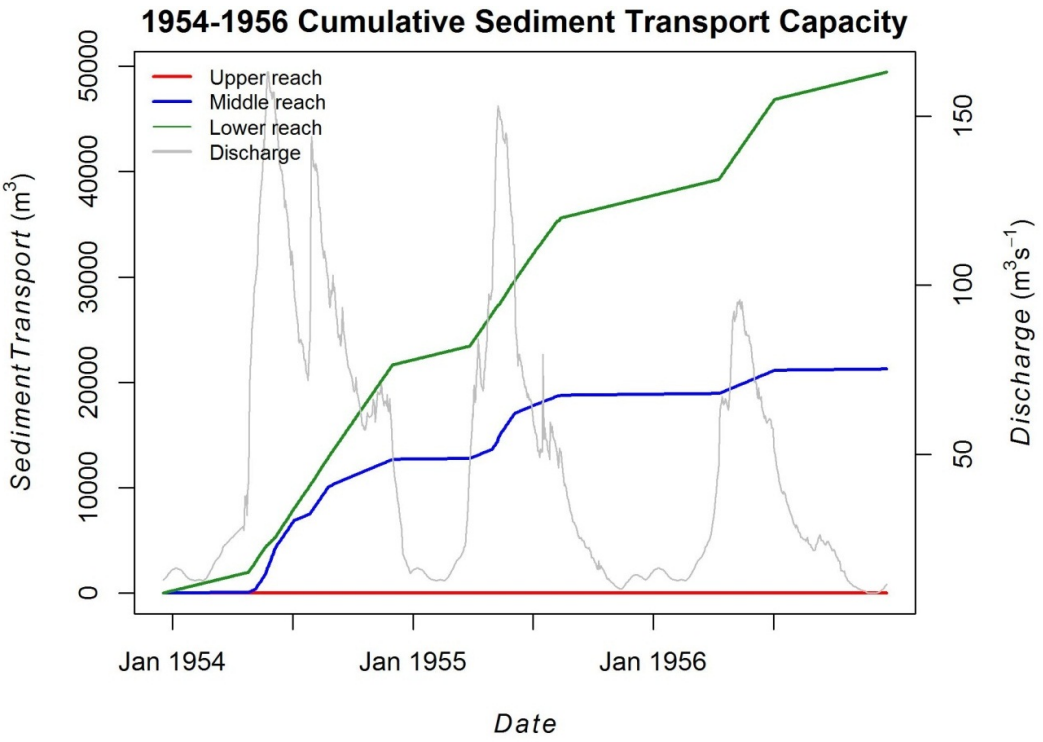

Figure G.64: Cumulative transport capacity for a sequence of low-flow hydrographs.

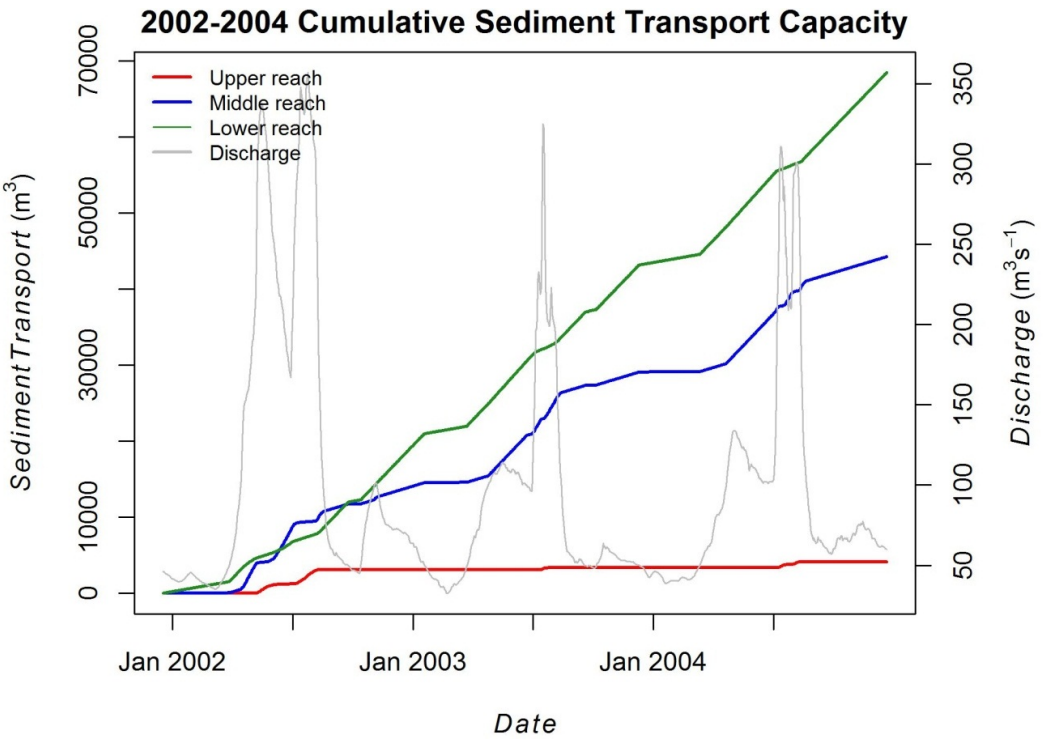

Figure G.65: Cumulative transport capacity for a sequence of typical hydrographs.

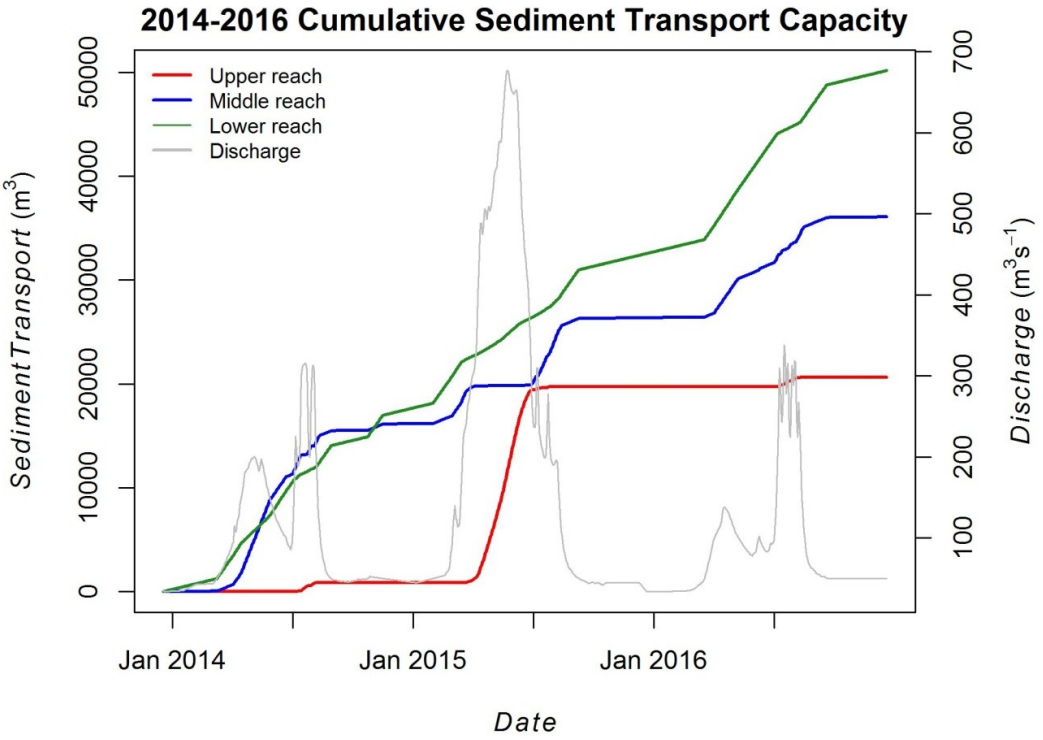

Figure G.66: Cumulative transport capacity for a sequence containing a high flow hydrograph.

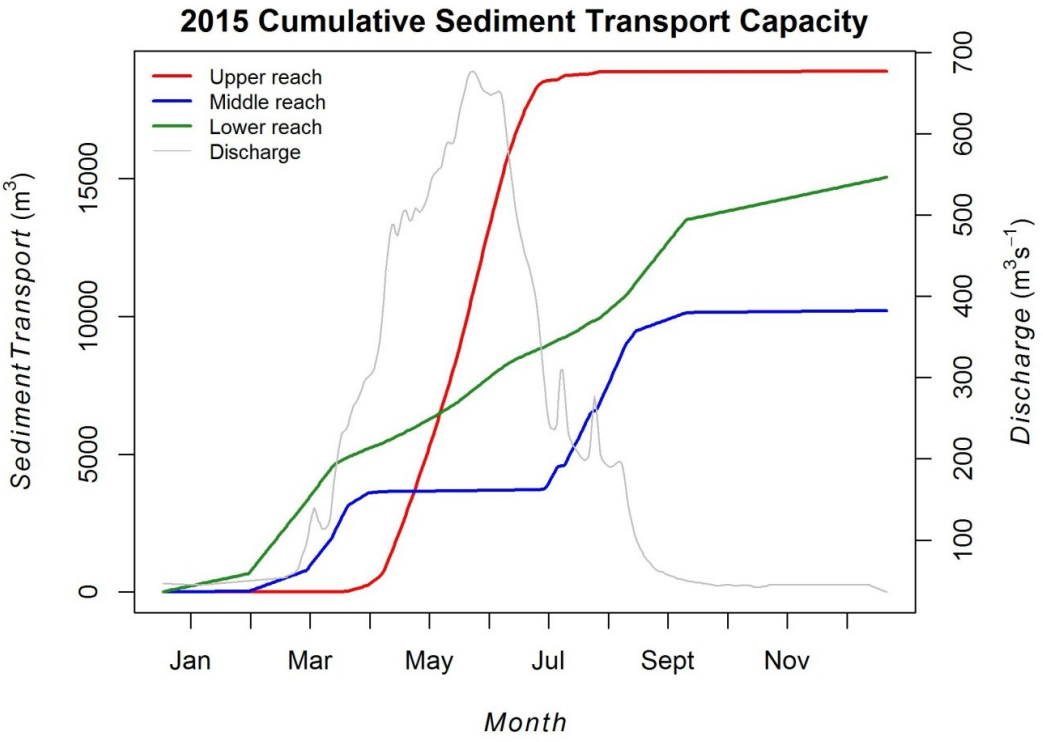

Figure G.67: Cumulative transport capacity for the 2015 flood.

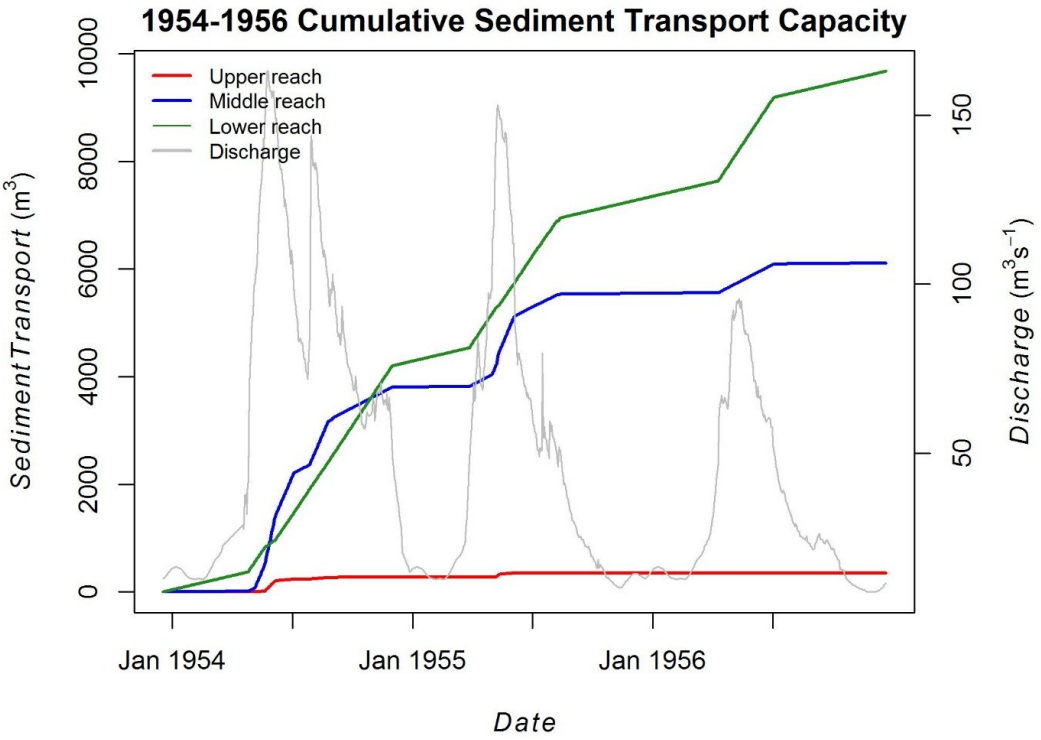

Figure G.68: Cumulative transport capacity (uniform GSD) for a sequence of low-flow hydrographs.

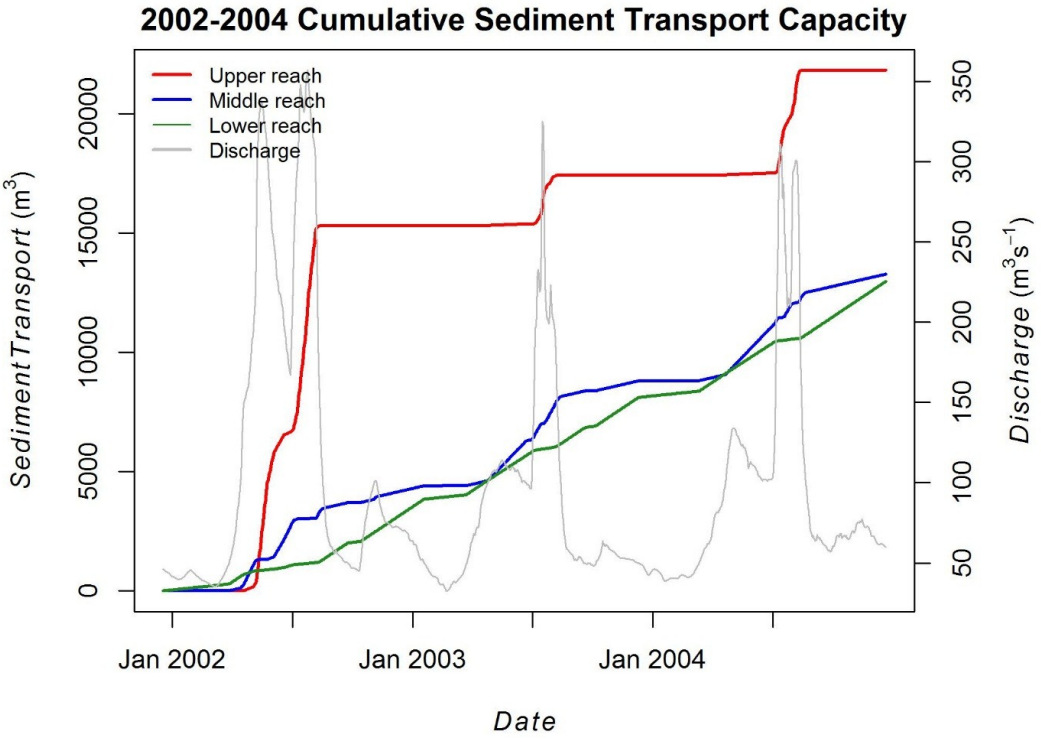

Figure G.69: Cumulative transport capacity (uniform GSD) for a sequence of typical hydrographs.

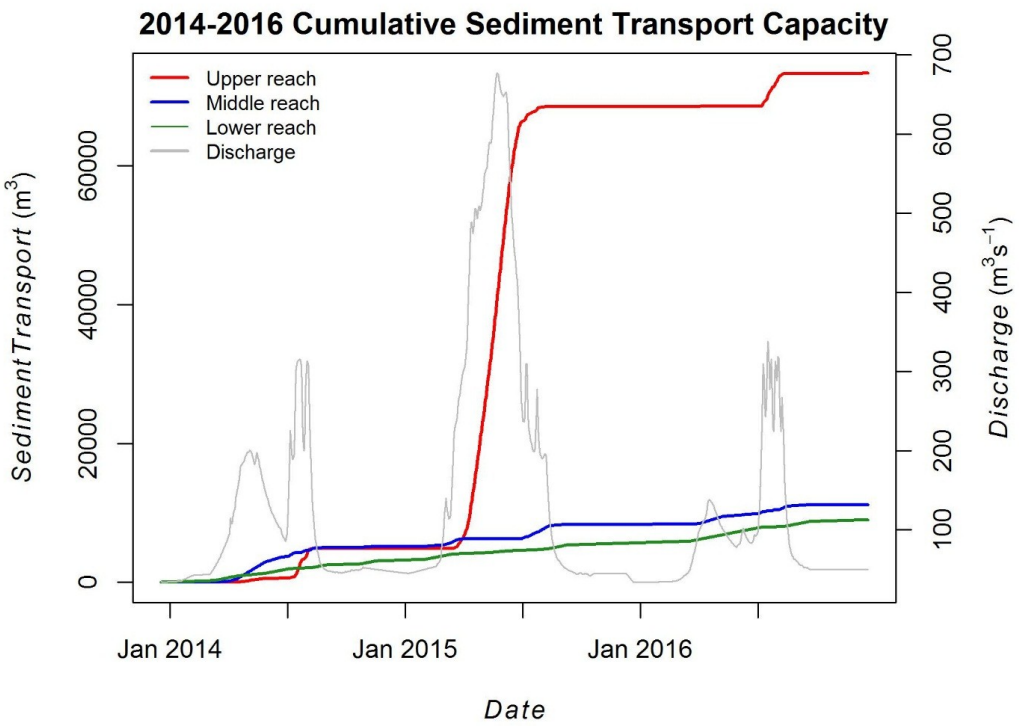

Figure G.70: Cumulative transport capacity (uniform GSD) for a sequence containing a high flow hydrograph.

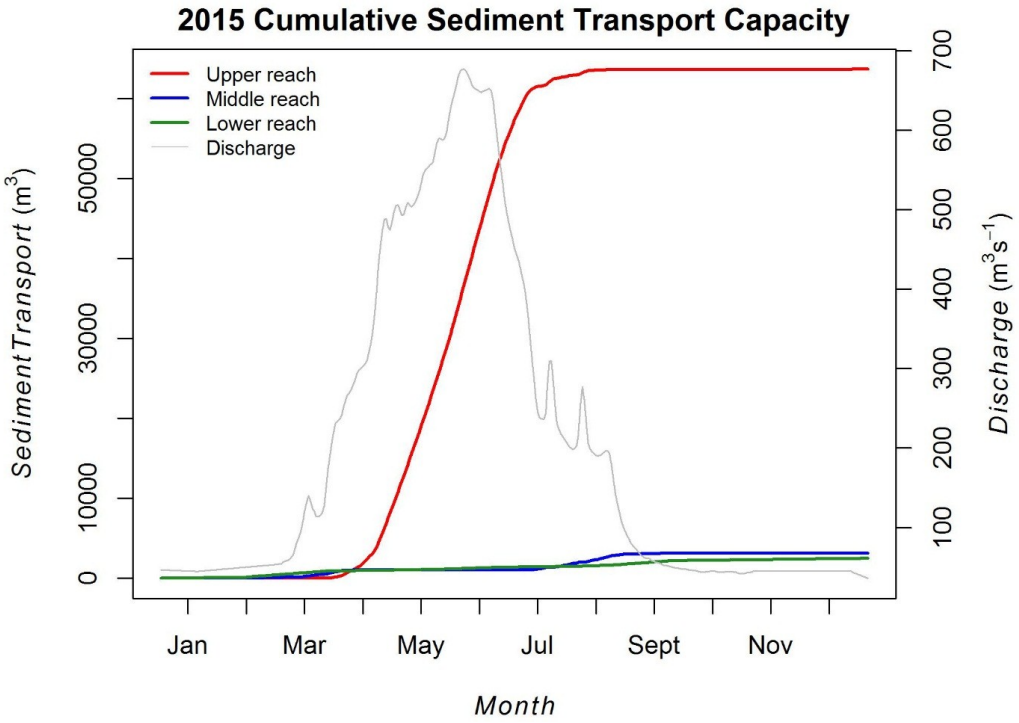

Figure G.71: Cumulative transport capacity (uniform GSD) for the 2015 flood.

G.3 Limitations

The accuracy of model performance is limited in areas that have relatively low surveyed point densities. These areas required considerable interpolation between data points to produce the DEM. Spatial interpolation is likely to misrepresent complex channel geometry and may generate artefacts that affect simulation output. The error produced by DEM creation and survey point density has been documented elsewhere and remains a limiting factor for 2-dimensional modelling projects (Pasternack et al., 2004; Pasternack et al., 2006). Possible simulation error caused by DEM interpolation can be seen as locally high shear stresses within the middle of the reach (at approximately 432500 m E, 5986400 m N) for flows between 125-275 m^3/s (Figures G.37 to G.40).

Mesh resolution is another factor that limits model performance (Crowder and Diplas, 2000), especially within some of the smaller secondary channels. The 5-m resolution used herein was chosen a compromise between spatial detail and reasonable computation times. Given that the purpose of the model was to explore reach-scale dynamics, rather than to evaluate small to meso-scale restorative measures or local habitat conditions, the resolution of the analysis is considered acceptable.

The accuracy of sediment transport capacity is limited by numerous factors. Firstly, calculation results are very sensitive to the grain size distribution of the bed surface and the percent sand content. The data used to define these characteristics was not very robust because underwater images were only taken at a few downstream locations, only a few images were taken per location, the area covered per image was relatively small (especially for coarse substrate) and visibility was relatively poor due to water turbidity. Attributing a grain size distribution to all cells within the model domain required extensive interpolation and is only representative of the very general trend of downstream fining.

In addition, the grain size of the substrate may not be representative of the sediment being transported as bedload. This was the case at the upstream end of the reach, where sand is transported over a coarse static bed rather than constituting a fraction of it. In contrast, the high sand content within the bed at the downstream end of the reach may cause sediment to be transported as migrating bedforms. The development of bedforms increases the importance of form drag and decreases the proportion of the total shear stress exerted as skin drag; the proportion responsible for grain mobility within sediment transport functions *(note that total shear stress was used to calculate capacity in this study, which is another significant limitation)*. Neither the model nor the sediment transport function capture the effect of bedforms on local hydrodynamics and sediment transport.

G.4 References

Crowder, D.W., and Diplas, P. 2000. Using two-dimensional hydrodynamics models at scales of ecological importance. Journal of Hydrology, 230, 172-191.

NHC. 2014. Nechako River 2013 Sediment Transport Investigations. Prepared by Northwest Hydraulic Consultants for the Ministry of Forests, Lands and Natural Resource Operations, North Vancouver BC. 48 pp.

NHC. 2015. 2014 Sediment Transport Investigation on the Vanderhoof Reach of the Nechako River. Prepared for Ministry of Forests, Lands and Natural Resource Operations, North Vancouver BC. 29 pp.

NHC. 2016. 2015 Sediment Transport Investigation on the Vanderhoof Reach of the Nechako River. Prepared for Ministry of Forests, Lands and Natural Resource Operations. North Vancouver BC. 38 pp.

Pasternack, G. B., Wang, C. L., and Merz, J. E. 2003. Application of a 2D hydrodynamic model to design of reach scale spawning gravel replenishment on the Mokelumne River, California. River Research and Applications, 19, 1-21.

Pasternack, G., Gilbert, A., Wheaton, J. and Buckland, E. 2006. Error propagation for velocity and shear stress prediction using 2D models for environmental management. Journal of Hydrology. 328, 227-241.